UNIVERSITÀ DEL PIEMONTE ORIENTALE

UNIVERSITA' DEGLI STUDI DEL
PIEMONTE ORIENTALE
"AMEDEO AVOGADRO"

Dipartimento di Scienze ed Innovazione Tecnologica
PhD thesis in chemical sciences (cycle XXVIII)

Theoretical modeling of gas adsorption in microporous aromatic polymers

Candidate: Lorenzo Canti

Supervisor: Prof. Maurizio Cossi

Coordinator: Prof. Domenico Osella

Ai miei genitori Giorgio Canti e Rossella Palazzeschi,
alla mia fidanzata e futura moglie, Alessandra Poggi
ed ai miei fratelli Guido e Gianni.

ACRONYMS

Abbreviaton	Meaning
ANG	Adsorbed Natural Gas
BASF	BadischeAnilin undSodaFabrik
BET	Branauer, Emmet, Teller
BSSE	Basis Set Superposition Error
CC	Coupled Cluster
CCS	Carbon Capture And Storage
CI	Cross-linked Index
CMP	Conjugated Microporous Polymer
CNG	Compressed Natural Gas
CR	Crystalline Rate
DFT	Density Functional Theory
DOE	Department Of Energy
EDX	Energy Dispersive X-ray Analysis
FDA	Formaldehyde Dimethyl Acetal
FF	Force Field
FHM	Fully Hypercrosslinked Model
FTIR	Fourier Transform Infrared Spectroscopy
GCMC	Grand Canonical Monte Carlo
HCP	Hyper-Crosslinked Polymer
IUPAC	International Union of Pure and Applied Chemistry
LNG	Liquefied Natural Gas
MOF	MetalOrganic Frameworks
MOPAC	Molecular Orbital PACkage
MOVE	Methane Opportunities for Vehicular Energy
MP2	Second order MollerPlessett perturbation theory
mPAF	microPorous Aromatic Framework
NG	Natural Gas
NLDFT	Non Local Density Functional Theory
PAF	Porous Aromatic Framework
PIM	Polymers Of Intrinsic Microporosity
PSD	Pore Size Distribution
PXRD	Powder X-Ray Diffraction
QSDFT	Quenched Solid Density Functional Theory
RBP	Random Branched Polymer
RCSP	Random Core/Shell Polymer
RHP	Random Hybrid Polymer
SBU	Secondary Building Unit
SSA	Specific Surface Area
STP	Standard Temperature and Pressure
TGA	Thermal Gravimetric Analysis
TPM	Tetraphenylmethane

ABSTRACT

This PhD dissertation deals with the modeling of new microporous organic polymer, characterized and synthesized by the physical-chemistry group of our department, and the identification of their storage properties.
Microporous materials (with pores of less than 2 nm in diameter) have recently attracted considerable attention due to the variety of their possible applications, including heterogeneous catalysis and gas purification, separation and storage. This research work is part of an industrially driven project that aims at the synthesis and characterization of microporous aromatic polymers to be used for H_2 and CH_4 storage and CO_2 capture.
In Chapter 1, the properties required for the storage of hydrogen, methane and carbon dioxide are described; argon and nitrogen adsoprtion is considered for the porosimetric material determination, with particular attention to the high surface area and for the high microporous volume.
Among the materials with suitable properties, porous carbons, MOFs (Metal Organic Frameworks) and organic microporous polymers have been widely studied.
The latter can be divided in different subclasses, which have in common a structure formed by light elements (H, B, C, O and Si) linked by strong covalent bonds. Normally, they show high thermal and chemical stability, and they can be synthesized with a wealth of organic reactions and building blocks, which provide flexibility for the material design to achieve desirable pore properties.
This PhD thesis has been focused on the modeling and the determination of the storage properties of the porous aromatic frameworks (PAF) and microporous aromatic frameworks (mPAF), two classes of materials that can be obtained by different synthetic strategies: the Yamamoto homo-coupling reaction used to synthesize PAF materials and the Friedel-Crafts reaction suitable to obtain mPAF polymer. These coupling reactions lead to the formation of new C-C bonds starting from precursors with specific functionalities. These materials and their syntheses will be discussed in Chapter 2.
In Chapters 3, the theory behind quantum mechanics and computation programs used in this work was briefly presented.
In Chapter 4 the three-dimensional structure and the adsorption properties of PAF (Porous Aromatic Framework), i.e. a class of microporous adsorbent materials with a high thermal and hydrothermal stability and a high surface area, were discussed. Some members of this class, indicated with the acronym "PAF-30n", where n is the number of polyaromatic ligands ranging from 1 to 4, were considered.
It has been necessary to proceed in various steps, starting from the development of a force field which best represents the guest-guest and host-guest interactions, comparing results with high level quantum calculations (MP2). Based on this model, the Lennard - Jones parameters of a standard force fields were optimized.
The force fields so optimized were employed in Grand-Canonical Monte Carlo calculations simulating the adsorption isotherms of gas in solid matrices with good precision and at various temperatures.
Besides the simulation of PAF materials, we modeled some functionalized PAF also, to explore the possibility to increase CO_2 capture, a pressing environmental issue.
In Chapter 5 the mPAF material was modeled. This material was synthesized in our De-

partment with Friedel-Crafts reaction between tetraphenylmethane (TPM) and formaldehyde dimethyl acetale (FDA) and it shows very interesting properties.
All the periodic molecular models are defined as networks of tetraphenylmethane moieties connected by methylene bridges in para position. In contrast to the crystalline structure of PAF, this material presents an amorphous morphology due to polymerization defects.
For this reason, experimental isotherms of the material were analyzed and several structural models, both crystalline and amorphous, were defined.
A good agreement between the experimental sample and the theoretical models was found through the pore size and the comulative pore volume analysis based on N_2 isotherms.
Moreover these results allowed to estimate the storage potential of this new material through the comparison with other adsorbent material uptakes presents in the literature.

Contents

1 Gas Storage in Porous Polymers

1.1 Introduction

Porous materials have captured the worldwide attention, in these years.Interest, investments and efforts in scientific research and technological development around the world are rapidly increasing. These materials possess surface, structural, and bulk properties that make them relevant in various fields such as ion exchange, [1,2] adsorption (for separation), [3,4] catalysis [5, 6], and gas storage. [7–10]
In this introduction chapter the main storage systems for hydrogen, methane and carbon dioxide, as well as their porosity and surface area, will be described in relation to the main classes of porous materials that have been proposed for gas storage.

1.2 Gas storage

The growing world population and the increasing standard of living increase the concerns over the sustainability of oil reserves: the supply of economically usable hydrocarbon resources in the world is limited, and the demand for hydrocarbon fuels is increasing.
In the current hydrocarbon economy, transportation is fuelled primarily by petroleum. The burning of hydrocarbon fuels has an adverse effect on the environment as it is responsible for the increase in the earth's atmosphere of CO_2 and other pollutants.
A number of potential solutions for conservation and remediation of the environment due to CO_2 increment are cutting edge research topics.
These include work in CO_2 capture and storage, [11] as well as the use of cleaner fuels, such as natural gas (CH_4) [12] or hydrogen (H_2). [13, 14]

1.2.1 H_2 Capture

Hydrogen energy is one of the alternative energy candidates which are being considered as a replacement for fossil fuels. Hydrogen can be produced from a various sources including coals, natural gases, and ultimately water. It is non-toxic and environmentally clean energy as water would only remain after the cyclic usage of the energy.
The automobile industry, one of the main potential applications of hydrogen energy, requires stored hydrogen for mobile applications. Therefore, methods to store H_2 with appropriate weight and volume are important for successful applications.
The development of a hydrogen storage device having light weight and high capacity is a necessary condition to enable fuel cell vehicles to replace fossil fuel vehicles.
More importantly, the developed vehicle should be operated at temperatures of 323 - 423 Kelvin and pressures of 1 - 100 bar. The vehicle should also have a fast recharge/discharge cycle.
Unfortunately, molecular hydrogen that can be used as fuel does not occur naturally in convenient tanks.
It needs to be produced by steam reforming of hydrocarbons, water electrolysis or by other

methods. [15, 16]
Possible approaches for hydrogen storage include: [17]

- Physical storage of compressed hydrogen gas in high pressure tanks (up to 700 bar);
- Physical storage of cryogenic hydrogen (cooled to -253^0 C, at pressures of 6-350 bar) in insulated tanks;
- Storage in advanced materials within the structure or on the surface of certain materials as well as in chemical compounds that can undergo a chemical reaction to release hydrogen.

Hydrogen has a very high energy content by weight (about three times higher than gasoline), but it has a very low energy content by volume (liquid hydrogen is about four times lower than gasoline). Currently, hydrogen is stored either in high pressure tanks or in liquid form in cryogenic tanks.
As far as the interaction/adsorption of hydrogen with/on a material is concerned, there are mainly three different approaches: [17]

- **Physisorption**: hydrogen remains molecular and binds weakly on the surface of the most common porous materials with a binding energy in the meV range. Hence, it desorbs already at very low temperatures. Sorbent materials belonging to this category are carbon-based materials such as nanotubes, fullerenes, graphene, mesoporous silica, metal-organic frameworks (MOFs), covalent organic frameworks (COFs), and clathrates. [19–21]
- **Chemisorption**: H_2 molecule dissociates into individual atoms, migrates into the material, and binds chemically with a binding energy lying in the 2-4 eV range. As the bonding is strong, the desorption takes place at higher temperatures. Complex hydrides, which are light metal hydrides, are the main class of materials where hydrogen is held in strong covalent bonds. [22, 23]
- **H_2 weakened but not broken**: The strength of interaction is intermediate between physisorption and chemisorption (binding energy in the 0.1-0.8 eV range). This type of adsorption concerns carbon-based nanostructured materials such as nanotubes, fullerenes and graphenes doped with metals and transition metals. [24–26]

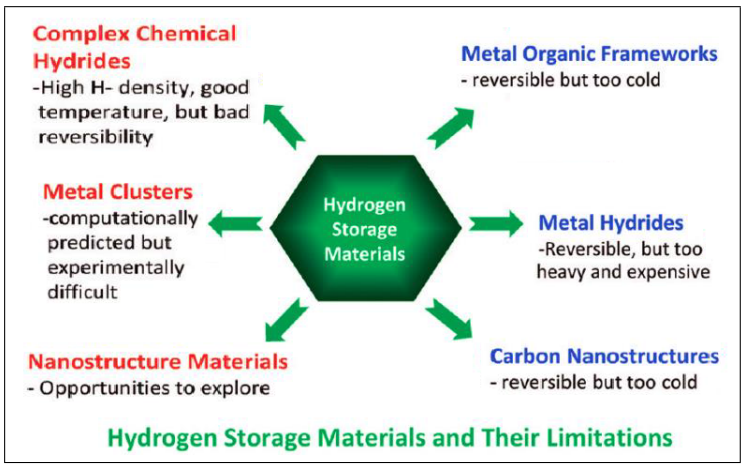

Figure 1.1: Summary of various hydrogen storage materials and their limitations. [18]

Figure 1.1 summarizes the different types of materials being studied for hydrogen storage. [18]
Metal hydrides are reversible under ambient conditions but are too heavy.
Simple chemical hydrides are reversible but only at very high pressure and temperature.
Complex chemical hydrides have high hydrogen density but suffer from poor reversibility.
Nanostructured materials are very promising but are yet to emerge as practical materials. In fact they offer good reversibility but require very low temperatures of storage. The kinetic of hydrogen adsorption by microporous materials is very rapid, which is a practical advantage for hydrogen storage, but low temperatures are required to achieve significant capacities at useful storage pressures.
In practice, low temperature storage requires cooling, which inevitably makes heavier the storage unit and is therefore a significant disadvantage. In order to achieve high volumetric capacities, adsorbed hydrogen must be stored at relatively high densities within the pores.
For these reasons, the hydrogen adsorption capacity of microporous materials at ambient temperature is currently too low for practical use. [27] The actual research in this field is to enhance the interaction of hydrogen with the materials to reach an adsorption capacity sufficiently high for real applications.

1.2.2 CH_4 Capture

Economical and environmental considerations have also boosted interest in Natural gas (NG) as a fuel for transportation, and especially as a replacement for petrol (gasoline).
In the generation of energy from methane, the major concern is the production of CO_2, though it is comparatively less than other fossil fuels (gasoline or diesel). Indeed, methane has a gravimetric heat of combustion (55.5 MJ/kg) comparable to that of gasoline (44.7 MJ/kg), but it boasts the smallest amount of CO_2 per unit of heat produced among fossil fuels, and it is naturally abundant. However, the lack of efficient storage methods has so far prevented the widespread use of NG in motor vehicles.
The two common methods of NG storage currently used are:

- liquefaction at low temperature (down to 120 K)
- compression to 200-300 bar at room temperature.

The volumetric energy density of Liquefied Natural Gas (LNG) is lower (22.2 MJ/l, 112 K) than that of gasoline (34.2 MJ/l) but requires the storage in expensive cryogenic vessels and it suffers from boil-off losses.
On the other hand, Compressed Natural Gas (CNG) necessitates the use of heavy, thick-walled cylindrical storage tanks and multi-stage compressors to achieve a reasonable volumetric energy density, which is actually only 27% (9.2 MJ/l) with respect to gasoline. [28]
Despite efforts to improve cylinders and compressors, the amount of NG stored in a CNG tank permits for only a short driving autonomy on light-duty passenger vehicles, and high pressure storage on vehicles has been associated to safety concerns. [29]
In order to take advantage of the benefits that the use of NG in vehicles may offer, attractive alternatives to CNG and LNG are needed. It has been suggested that porous adsorbents represent a safer, simpler, and potentially more cost-effective method for storing NG at ambient temperature and reasonable pressures (around 35 bar) in the form of adsorbed NG (ANG). [30]
Similarly to hydrogen storage, also for CH_4 the adsorption can be physical (weak van der Waals forces) or chemical (significant covalent interactions) depending on the type and on the strength of the interaction between methane molecules and the material surface sites. From an application standpoint, the primary difference between physisorption and chemisorption is

the significant disparity in binding energies. For reversible gas storage and delivery, moderate binding energies (measured as heat of adsorption) are required to maximize energy efficiency of the system. Therefore, physisorptive materials are best suited for this application, as chemisorptive materials would require a substantial amount of external heat to release the adsorbed gas.

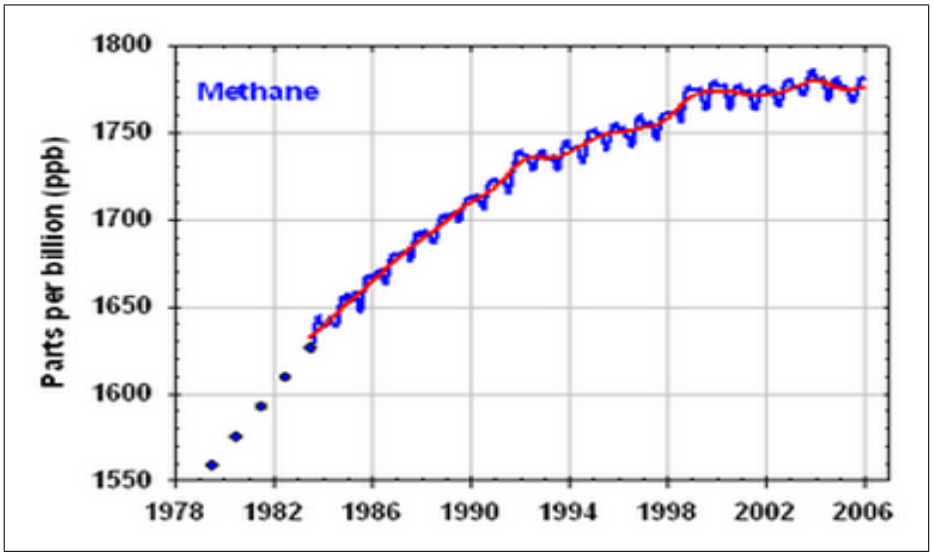

Figure 1.2: The increment of CH_4 emissions during the period 1978-2006 [31]

To address the need for better technologies to combat the growing increase of emissions in the atmosphere CH_4, in 1993, the U.S. Department of Energy (DOE) set the methane storage target as 150 cm^3 (STP)/ cm^3 at 298 K and 35 bar. [32, 33]
As a result of efforts by a number of researchers, some MOFs exhibited considerably high methane uptakes, which exceeded the above DOE target. [34]
In 2012, the U.S. DOE initiated a Methane Opportunities for Vehicular Energy (MOVE) Program, and re-set several targets to guide the research on adsorbent-based methane storage [35]. The major target is that the adsorbent-level volumetric energy density should exceed 12.5 MJ/L and 9.2 MJ/L after packing losses (25%), at room temperature and low pressure (less than 35 bar). This corresponds to a volumetric storage capacity of 0.25 g/cm^3 or 350 cm^3 (STP)/ cm^3 for the adsorbent material. Even assuming no packing loss, the volumetric storage capacity still needs to be higher than 260 cm^3 (STP)/ cm^3. [36] Clearly, this is an ambitious target, which none of the currently known adsorbent materials meet. In fact, even for the previously widelyreferred, much lower target of 150 cm^3 (STP)/ cm^3, there are only few materials known to reach this value. [37, 38] Additionally, DOE set a target concerning the gravimetric energy density, 0.5 g (methane)/g (adsorbent), or 700 cm^3 (STP)/ g, which is equally challenging.
The ideal sorbent should also show resistance to impurities typically encountered in natural gas sources with a lifetime of at least 100 fillrelease cycles, and it should be cost effective approaching, $10/kg sorbent, in addition to other system level targets such as desorption rates, tank abuse tests, etc. [29]
About the storage measures, there are several volumetric measures used to quantify the fundamental characteristics of an underground storage facility and the gas contained within it.
For some of these measures, it is important to distinguish between the characteristic of a

facility such as its capacity, and the characteristic of the gas within the facility such as the actual inventory level. These measures are as follows:

- **Total gas storage capacity** is the maximum volume of gas that can be stored in an underground storage facility in accordance with its design, which comprises the physical characteristics of the reservoir, installed equipment, and operating procedures particular to the site.
- **Total gas in storage** is the volume of storage in the underground facility at a particular time.
- **Base gas (or cushion gas)** is the volume of gas intended as permanent inventory in a storage reservoir to maintain adequate pressure and deliverability rates throughout the withdrawal season.
- **Working gas capacity** refers to total gas storage capacity minus base gas.
- **Working gas** is the volume of gas in the reservoir above the level of base gas. Working gas is available to the marketplace.
- **Deliverability** is most often expressed as a measure of the amount of gas that can be delivered (withdrawn) from a storage facility on a daily basis. Also referred to as the deliverability rate, withdrawal rate, or withdrawal capacity, deliverability is usually expressed in terms of millions of cubic feet per day (MMcf/day). Occasionally, deliverability is expressed in terms of equivalent heat content of the gas withdrawn from the facility, most often in dekatherms per day (a therm is 100,000 Btu, which is roughly equivalent to 100 cubic feet of natural gas; a dekatherm is the equivalent of about one thousand cubic feet (Mcf)). The deliverability of a given storage facility is variable, and depends on factors such as the amount of gas in the reservoir at any particular time, the pressure within the reservoir, compression capability available to the reservoir, the configuration and capabilities of surface facilities associated with the reservoir, and other factors. In general, a facility's deliverability rate varies directly with the total amount of gas in the reservoir: it is at its highest when the reservoir is most full and declines as working gas is withdrawn.
- **Injection capacity (or rate)** is the complement of the deliverability or withdrawal rate-it is the amount of gas that can be injected into a storage facility on a daily basis. As with deliverability, injection capacity is usually expressed in MMcf/day, although dekatherms/day is also used. The injection capacity of a storage facility is also variable, and is dependent on factors comparable to those that determine deliverability. By contrast, the injection rate varies inversely with the total amount of gas in storage: it is at its lowest when the reservoir is most full and increases as working gas is withdrawn.

1.2.3 CO_2 Capture and Storage (CCS)

Beside the development of technologies for the use of methane [39] and hydrogen [40] as clean fuels, industrial technologies for carbon dioxide capture are vital in environmental safety.
Due to growing levels of greenhouse gas emissions (Figure 1.3), separation of CO_2 from mixtures of gases such as the gas emitted from the combustion of fossil fuels is of great importance. [41]

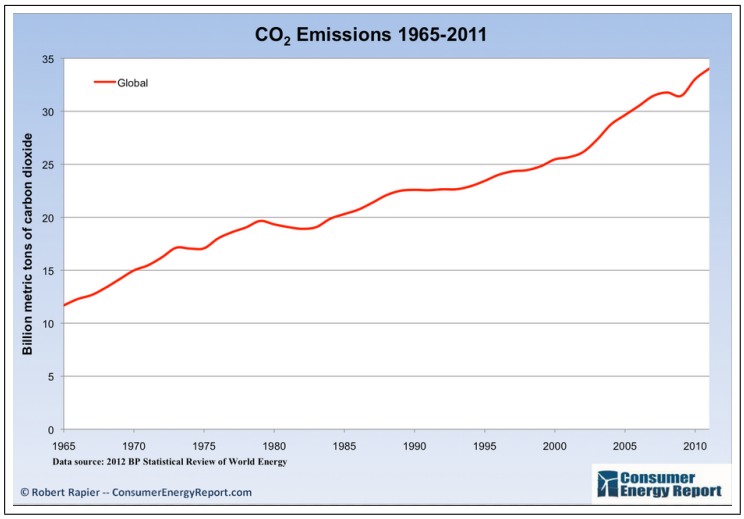

Figure 1.3: The increment of CO_2 concentration during the period 1965-2010 (at Mauna Loa Observatory), in the atmosphere. [42]

Carbon capture and storage (CCS) is an efficient way to reduce CO_2 concentration in the atmosphere. It is a three-step process including separation of CO_2 from other gases before reaching the atmosphere, CO_2 transportation, and its permanent storage. [42] Among them, the CO_2 capture is the most challenging key step for which new adsorbent materials need to be developed. Conventional adsorbent materials rely on either chemisorption or physisorption to capture CO_2.
There are three major approaches for CCS: pre-combustion capture, oxy-fuel process and post-combustion capture: [43]

- In pre-combustion, the fossil fuel is partially oxidized in a gasifier. The resulting syngas (CO and H_2) is shifted into H_2 and CO_2, which can be captured from the stream.
- Oxy-combustion occurs when the fuel is burned in the presence of oxygen. The resulting flow gas consists mainly of pure CO_2 which can be transported to the sequestration site and stored.
- The post combustion capture is based on removing CO_2 from the flow gas after combustion. Instead of being released directly into the atmosphere, flue gas is passed through a particular equipment that separates/captures most of the CO_2.

Post-combustion capture offers some advantages since existing combustion technologies can still be employed without radical changes. This makes post-combustion capture easier to implement as a retrofit option compared to the other two approaches.
Various technologies such as membrane separation, cryogenic distillation and adsorption can be used for CO_2 capture. The adsorption is the ideal way to achieve efficient CCS. It is a separation technology, able to reduce both cost and energy of post-combustion capture compared to other technologies. Selective capture and subsequent storage of carbon dioxide in porous materials has been considered as a promising new approach. [11]
The adsorbents used for CO_2 capture can be placed into two categories: physical and chemical adsorbents. [44]

- Chemisorption is a sub-class of adsorption, driven by a chemical reaction occurring at the exposed surface. Chemical adsorbents are mostly metal compounds such as metal oxides and metal salts.

- Physisorption is a process in which the electronic structure of the atom or molecule is barely perturbed upon adsorption. The major physical adsorbents reported for CO_2 adsorption include activated carbons and inorganic porous materials such as zeolites.

However, the success of this approach is dependent on the development of adsorbents with high capacity and selectivity; Ideally, this has to be environmentally benign, renewable, safe, and cost-effective. [42]
In summary, the goal remains in the development of low-cost and high-performance adsorbents for CO_2 sequestration, gas separation and energy storage applications.

1.2.4 Nitrogen and Argon Storage

Pore size analysis of mesoporous materials from adsorption isotherms is based on an adopted interpretation of the mechanisms of capillary condensation and evaporation and associated hysteresis phenomena. [45, 52]
Nitrogen is the probe gas most commonly used for pore size distributions (PSD) analysis because it is inexpensive, readily obtained, inert, and well-studied in the adsorption literature. The experimental isotherm is usually measured at the normal liquid nitrogen boiling point of 77 K, which is sufficiently below the critical temperature so that a large uptake of the adsorbate is realized. This is again a convenient choice, since liquid nitrogen is inexpensive and isothermal conditions can easily be maintained using liquid nitrogen as a cryostat. Despite these merits, there may arise situations in which a probe gas species other than nitrogen is desirable. On activated carbons that have substantial chemical heterogeneity, there may be significant interactions between the quadrupolar nitrogen molecule and various functional groups on the carbon surface.
Argon is an ideal probe gas for characterizing the pore structure of heterogeneous adsorbents, since it is a monatomic, spherical molecule with no multipolar moments and it is similar in size to nitrogen. Argon porosimetry has been used extensively for PSD analysis of activated carbons, silicas, aluminas, and mesoporous oxides. [139,140] DFT model isotherms have been computed for argon adsorption at its normal boiling point of 87 K.
This temperature is readily maintained by using liquid argon as the temperature bath for the sorption measurement.
Because liquid argon is more expensive than liquid nitrogen, however, it is convenient and economical to carry out the argon adsorption measurement at the normal liquid nitrogen boiling point of 77 K.

1.3 Adsorption Isotherms and Porosity

The adsorption of guest molecules into a solid surface plays an essential role in determining the properties of porous compounds. Depending upon the strength of the interaction, all adsorption processes can be divided into chemical and physical adsorption categories.

- **Chemical adsorption or chemisorption** involves valence forces of the same type as those operating in the formation of chemical compounds.
- **Physical adsorption or physisorption** is a general phenomenon which occurs whenever a gas (the adsorbate) is brought into contact with the surface of a solid (the adsorbent), in this case the forces involved are intermolecular forces (van der Waals) and always include the long-range London dispersion forces and the short-range intermolecular repulsion. [45]

Adsorption is described through isotherms, which correlate the amount of gas adsorbed to the pressure in the system at a constant temperature. The adsorbed gas quantity is always normalized to the mass of adsorbent to allow the comparison with other materials.
The textural analysis of powders is usually performed by physisorption of nitrogen, argon and krypton at cryogenic temperatures (77 K and 87 K). From a proper isotherm, it is possible to extract information about surface area, pore size and porosity of a given material.
IUPAC proposed to classify pores by their internal pore width:

- **Macropores** $\geq$ 50 nm widths;
- **Mesopoeres** Pores between 2 and 50 nm widths;
- **Micropores** Pores $\leq$ 2 nm widths;
  - **Supermicropores** between 0.7 and 2 nm;
  - **Ultramicropores** $\leq$ 0.7 nm;

The sorption behaviour in mesopores is distinct from the adsorption phenomena occurring in micropores. The mesopore adsorption is dominated by capillary condensation, which is responsible for a sharp adsorption enhancement around the mid relative-pressure region. Conversely the adsorption in a micropore should not be considered as that of molecules onto a solid surface but as the filling of molecules into a nanospace where a deep potential field is generated between the adsorbate molecules and the pore walls. In this case, the adsorption isotherm shows a steep rise at very low relative pressure and a plateau after saturation. [46]
Based on IUPAC classification, there are six representative adsorption isotherms that reflect the relationship between porous structure and type of sorption (Figure 1.4a). [47]

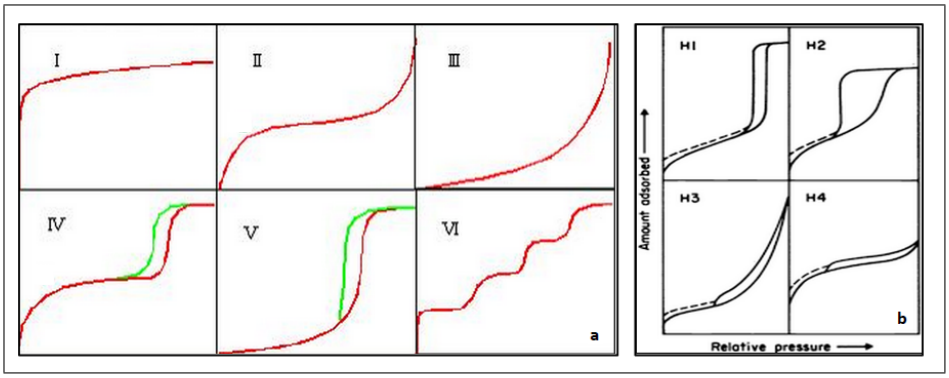

Figure 1.4: (a) Types of physisorption isotherms; (b) Types of hysteresis loops

.
These adsorption isotherms are characteristics of microporous (Type I), nonporous and macroporous (types II, III and VI), and mesoporous (type IV and V) adsorbents.
An empirical classification of hysteresis loops was given by IUPAC (Figure 1.4b), in which the shape of the hysteresis loops (types H1 - H4) is correlated to the adsorbent texture. According to this classification: [47, 48]

- Type H1 is often associated with porous materials exhibiting a narrow distribution of relatively uniform (cylindrical-like) pores.
- Materials that give rise to H2 hysteresis contain a more complex pore structure in which network effects such as pore blocking percolation and cavitation are relevant (Figure 1.5). [49–51] In case of pore blocking (sometimes called ink-bottle) desorption from the

pore body may occur only after emptying its neck. In other words, desorption from the neck triggers evaporation in the blocked pore. Thus, the vapour pressure of desorption from the pore body depends on neck size, network connectivity, and on the state of the neighbouring pores. While the mechanism of desorption involves cavitation phenomena (spontaneous nucleation and growth of gas bubbles in the metastable condensed fluid) when the neck diameter is smaller than a certain critical width (estimated to be ca. 6 nm for nitrogen at 77.4 K). In this case, the pore body empties while the pore neck remains filled.

- Isotherms with type H3 hysteresis do not exhibit any limiting adsorption at high P/P_0. This behaviour can be caused by the existence of non-rigid aggregates and in principle should not be expected to provide a reliable assessment of either the pore size distribution or the total pore volume.

- H4 hysteresis loops are generally observed with complex materials containing both micropores and mesopores.

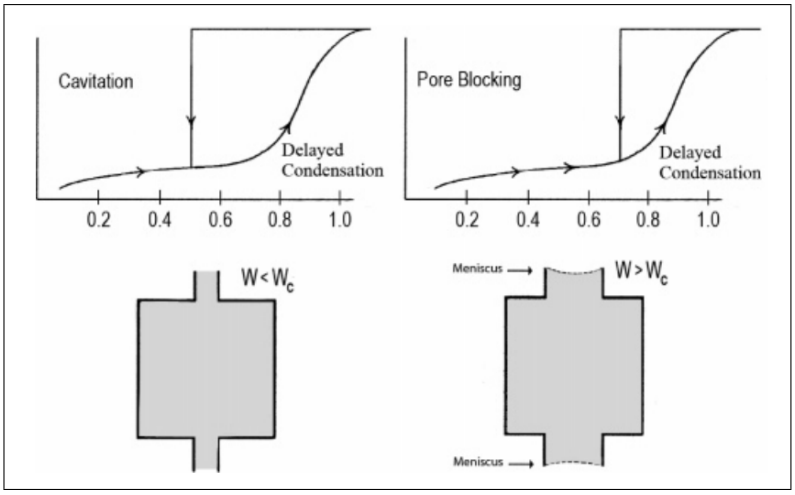

Figure 1.5: Schematic illustration of pore blocking and cavitation controlled evaporation. [48]

Great progress was achieved in the understanding of adsorption, capillary condensation, and desorption phenomena in highly ordered mesoporous materials with simple pore geometries, such as MCM and SBA-type mesoporous silica crystals. [52]
However, there are still many open questions concerning adsorption-desorption mechanisms in more complex porous systems. Fluids adsorbed in hierarchically structured micromesoporous materials exhibit a great variety of hysteretic adsorption-desorption isotherms with multiple steps related to phase transformations in adsorbed phases.
Adsorption-desorption processes involve a combination of physical mechanisms, such as delayed condensation, advanced condensation, cavitation-induced evaporation, pore blocking, and percolation, which are reflected in characteristic types of hysteresis loops formed by adsorption and desorption isotherms. [53]
The hysteresis loop causes a considerable complication for the pore structure characterization; however, if interpreted correctly, hysteresis loops can provide important information on pore network morphology, which is crucial for discriminating the physical mechanisms of phase transformation. [54]

1.4 Surface Area

The surface area is one of the most important factors for evaluating the adsorption capacity of porous materials. Adsorbents have a high effective surface area exposed, per gram of material, expressed in m^2/g. The specific surface area (SSA) is a relevant textural parameter of adsorbent materials.
Conventionally, the Brunauer-Emmett-Teller (BET) gas adsorption method has become the most widely used standard procedure for the determination of the SSA, in spite of the over simplification of the theoretical model on which is based. [45]
In particular, the BET model applied to the N_2 adsorption data at 77 K has been widely used to characterize the adsorbent material of interest. It assumes that once a monolayer becomes saturated, a further monolayer can form on top, and that the rates of adsorption and desorption are equal for each layer.
There are several methods to calculate the surface area of computational models. In this work we have taken into account mainly two methodologies: the Van der Waals surfaces and the Connolly surfaces.

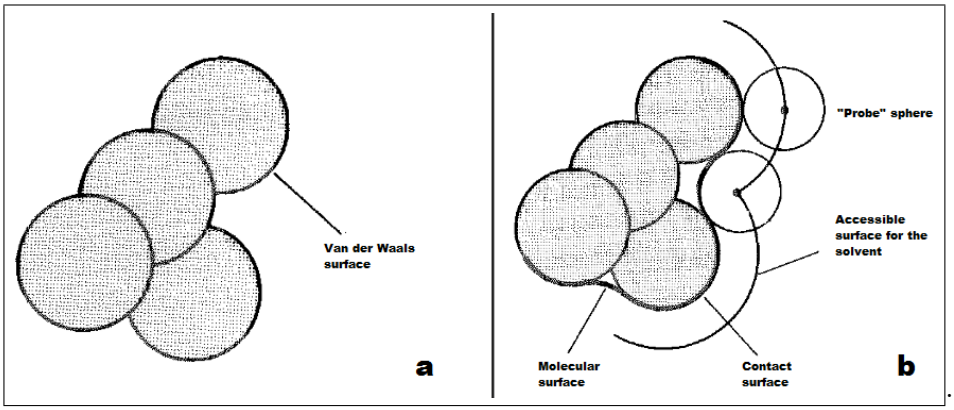

Figure 1.6: (a) Van der Waals surface and (b) Connolly surface.

.
The van der Waals surface of a molecule corresponds to the outer surfaces of the radii of van der Waals forces of the atoms. The molecular surface is generated by rolling a spherical "probe" (generally with a radius of 1.4 to represent a molecule of water) on the surface by van der Waals forces. The molecular surface is the contact surface. The accessible surface to the solvent (or Connolly) is instead drawn from the center of the probe in the same manner.

1.5 Adsorbent properties for best performance gas storage

The work of this thesis primarily concerns with the study of physical adsorption in different porous materials. Each gas and its associated applications have criteria that should be met for any gas storage material to be of use in practice.
In general, there are different sets of performance criteria for a good adsorbent as listed below: [57]

- High adsorption capacity. One of the most important parameters is the high specific surface area (SSA). However, simple considerations based on SSA are not enough to obtain an efficient material: also the sizes of the pores are of considerable importance, as adsorption predominantly occurs within the pores that are able to create a sufficiently

high attractive potential. Such a situation is met as soon as the pore walls are so close to each other that their own potential fields overlap. This affects the bonding strength of the molecules to the adsorbent surface, which is related to the isosteric heat of adsorption. [58] Thus, the most relevant properties that affect the gas adsorption capacity are SSA, surface chemical nature, and pore size. These parameters determine how much adsorbates can be accumulated per unit mass of adsorbents.

- High selectivity. For multicomponent mixtures, selectivity is highly desirable for gas separation. The selectivity of an adsorbent will depend on pore size, shape and pore size distribution as well as on the nature of the adsorbate components.

- Favorable adsorption kinetics. Adsorption kinetics is determined by the particle (crystallite) size, and by the macro-, meso and microporosity of the adsorbent. Sometimes, binder type and amount would also affect the interparticle transport and thus the global adsorption process kinetics. For a favourable kinetic, the adsorption rate should be high or controllable depending on the requirements of a particular application.

- Excellent mechanical properties. Adsorbents need to be mechanically strong and robust enough to stand attrition, erosion and crushing in adsorption columns or vessels. High bulk density and crushing strength, and attrition resistance are desirable.

- Good stability and durability in use. Adsorbents are often subject to harsh chemical environments or to high pressure and thermal conditions. A high stability in those environments/conditions is essential in ensuring long life or durable utilization.

Obviously, the practical challenges concern the preparation of high performance materials in a simple and cost effective manner and the materials should meet the above requirements/criteria as much as possible.

2 Porous materials for gas storage

2.1 Introduction

In recent years, nanoporous materials have been a core focus of scientific and technological importance because of their ability to adsorb atoms, ions and molecules.
The main classes of materials that show good performances for gas storage are: [59–66]

1. Porous Carbons
2. Porous Inorganic Materials
3. Metal Organic Framework materials (MOFs)
4. Microporous organic polymers
    - Polymers of intrinsic microporosity (PIMs)
    - Covalent organic frameworks (COFs)
    - Conjugated microporous polymers (CMPs)
    - HyperCrosslinked polymers (HCPs)
    - Porous aromatic frameworks (PAFs)
        - microPorous Aromatic Frameworks (mPAF)

2.2 Porous Carbons

Several types of porous carbons such as activated carbons, carbon nanotubes and nanofibers and microporous templated carbons have attracted interest for gas storage. [80] From a practical point of view, porous carbons are already commercially produced in large quantities for a broad range of applications and are relatively inexpensive. Among porous carbons, activated carbons are the most widely studied family. They are a form of carbon processed to have small, low-volume pores that increase the surface area available for adsorption or chemical reactions. [60] Activated is sometimes substituted with active.
Activated carbon is used in gas purification, [82–85] decaffeination, gold purification, metal extraction, [86] water purification, [88] medicine, sewage treatment, air filters in gas masks and respirators, filters in compressed air and many other applications. [89] One major industrial application involves use of activated carbon in the metal finishing field.
They are also very widely employed for purification of electroplating solutions, for example, for removing organic impurities from bright nickel plating solutions. A variety of organic chemicals are added to plating solutions for improving their deposit qualities and for enhancing properties like brightness, smoothness, ductility, etc. Due to passage of direct current and electrolytic reactions of anodic oxidation and cathodic reduction, organic additives generate unwanted breakdown products in solution. Their excessive build up can adversely affect the plating quality and physical properties of deposited metal. Activated carbon treatment removes such impurities and restores plating performance to the desired level. [62]
Due to its high degree of microporosity, just one gram of activated carbon has a surface area

in excess of 500 m^2, as determined by gas adsorption. [61] An activation level sufficient for useful application may be attained solely from high surface area; however, further chemical treatment often enhances adsorption properties.
These materials generally are prepared from a carbonaceous starting materials (coal, wood, coconut husks . etc) by a thermal treatment or chemical treatment, which can lead to polymeric systems with large surface areas, often well in excess of 1000 m^2/g and even up to > 3000 m^2/g. [81]

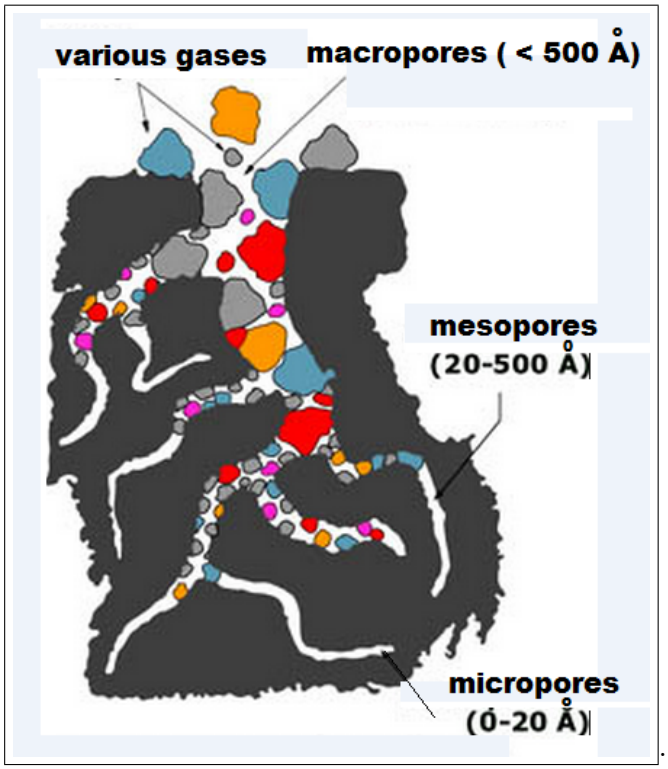

Figure 2.1: Rapresentation of the pore structure of activated carbons

.
Unfortunately, due to their method of production, most activated carbons have a wide distribution of pores sizes ranging from microporous to macroporous. Additionally, the surface of activated carbons is chemically well defined with a mixture of oxygen and nitrogen functional groups. These two factors combine to give an excellent adsorbent material for a wide range of species, though it suffers from poor selectivity for specific molecules. Moreover, improvement of the storage capacity for porous carbons is currently limited by the difficulties in increasing the surface area above 3500 m^2/g, being this parameter strongly correlated with the amount of gas that can be stored in the material.

2.3 Porous Inorganic Materials

Porous inorganic materials cover a range of solids, both oxides and nonoxides, crystalline and amorphous, that have a pore size extending from about 3 Å to over 500 Å. The main materials of this family are zeolites. Zeolites are hydrated aluminosilicate minerals made from interlinked tetrahedra of alumina (AlO_4) and silica (SiO_4).
They are solids with a relatively open, three-dimensional crystal structure built from the elements aluminum, oxygen, and silicon, with alkali or alkaline-Earth metals (such as sodium,

potassium, and magnesium) plus water molecules trapped in the gaps between them.
Zeolites form with many different crystalline structures, which have large open pores (sometimes referred to as cavities) in a very regular arrangement and roughly the same size as small molecules.
There are about 40 naturally occurring zeolites, forming in both volcanic and sedimentary rocks; according to the US Geological Survey, the most commonly mined forms include chabazite, clinoptilolite, and mordenite.
Dozens more artificial, synthetic zeolites (around 150) have been designed for specific purposes, the best known of which are zeolite A (commonly used as a laundry detergent), [67,68] zeolites X and Y (two different types of faujasites, used for catalytic cracking) [69, 70] and the petroleum catalyst ZSM-5 (a branded name for pentasil-zeolite). [71]

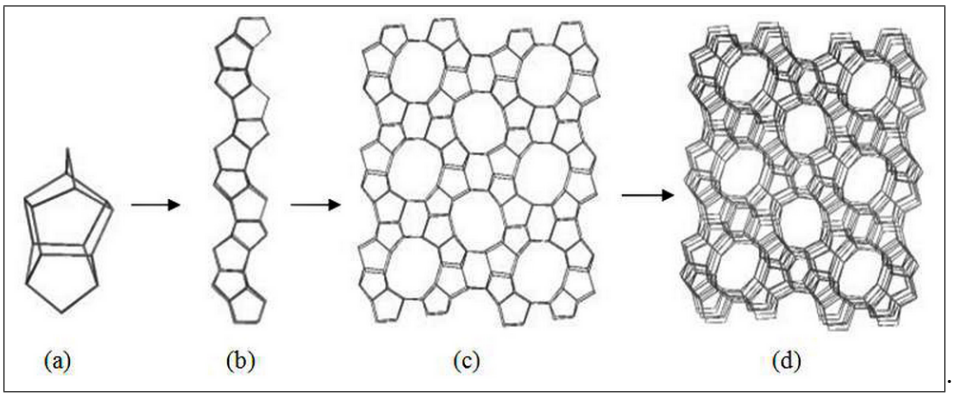

Figure 2.2: ZSM-5: (a) the pentasil unit; (b) chains of pentasil units; (c) layers of these chains; and (d) layers linked across inversion centres. [71]

.
Zeolites have a number of significant practical advantages over other microporous adsorbents in that, for example, they possess high thermal stability. [72, 73]
However, it seems unlikely that zeolites could be useful as practical gas storage media as discussed by Felderhoff et al.. [74]
The problems encountered when using zeolites as adsorbents for the storage of gas are the following: [75, 76]

- The presence of non-structural porosity given by aggregations of zeolite particles, which diminish the amount of material in the same volume and thus worsen the gas storage.
- Zeolites with hydrophilic character may preferentially adsorb traces of water found in gas mixtures, with a consequent reduction in storage capacity.
- Relatively low surface areas (<1000 m^2/g).

2.4 Metal-Organic Frameworks (MOFs)

In recent years, a new class of crystalline materials called MOFs (Metal Organic Frameworks) has been synthesized and characterized by the presence of organic functionality and adjustable pore size and porosity, all features that make them attractive for use in gas storage. [77]
In some cases, the pores are stable for the removal of the guest molecules (often solvents) and can be used for storage of hydrogen and carbon dioxide. [90, 91]

The synthesis is based on the principles of reticular chemistry, which allows the design and structure prediction. The final product using the constituent unit secondary (Secondary Building Unit, SBU) allows to obtain stable materials transforming these individual fragments in a porous lattice extended. [92]
The SBUs are clustered inorganic and / or molecular complexes formed after the coordination of ligands to metal ions by organic linkers to obtain structures, much more extensive, both bidimensional and tridimensional. [87]
The SBU are crosslinked to form the metal-organic structure through the connection of the points of extensions present in each SBU using organic binders.
The choice of the organic binder is of fundamental importance since it determines the structure of the lattice, the size of the pores and the surface area of the material. To induce porosity permanent structures rigid ligands are usually chosen, for which among all the possible systems, aromatic ones are preferred with respect to alkyl chains characterized by high flexibility.
In figure 2.3 an example of isostructural MOFs has shown, which has the same SBUs but different organic binders.

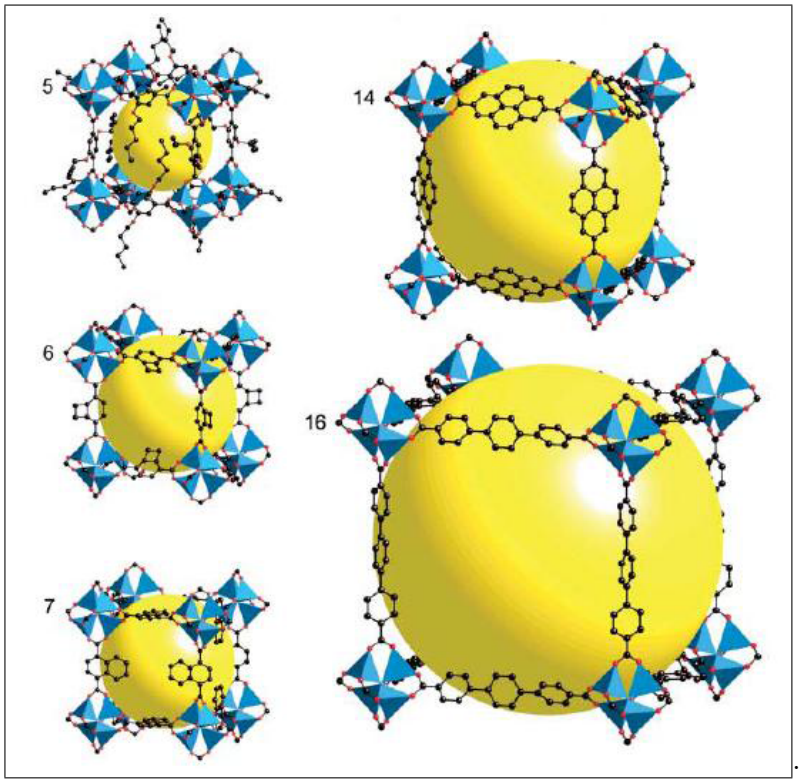

Figure 2.3: Examples of MOFs iso reticular called IRMOS synthesized by Petit et al. [78] Atoms Zinc (blue polyhedra), oxygen atoms (red spheres), carbon atoms (black spheres). The yellow spheres represent the diameter of the pores.

.
The MOFs, thanks to their porosity and high surface area, can be used in various applications, in particular, have been much studied in the last decade for their storage capacity of CH_4, H_2, CO_2. [79, 93]
However, these materials are generally less robust than zeolites and microporous carbons, because they exhibit lower thermal and chemical stability that hinder them from usage under extreme conditions.

Nevertheless, their commercialization is already under way, principally by BASF who markets a series of framework materials under the trade name Basolite TM, and so the practical application and use of these materials on an industrial scale is clearly feasible.

2.5 Microporous organic polymers

Porous Organic Polymers is another class of microporous materials of great interest in literature. They can be divided in several subclasses of polymers, which have in common the following features: [96]

- The structure is formed by light elements (H, B, C, O and Si) that are linked by strong covalent bonds (B-O, C-O, C-C, B-C, and Si-C).
- A high thermal and chemical stability to air and atmospheric moisture since they are linked by strong covalent bonds.
- Normally, they do not have a long range order. Thus, their structure is amorphous due to irreversible bond formation governed by a kinetic control.
- They can be constructed using a plethora of organic reactions and building blocks, which provides flexibility for the material design to achieve desirable pore properties. In all the materials is possible to use a wide range of organic functionalities using different synthetic strategies and a great choice of monomers that makes it easy to introduce various functional groups in the pore walls. [97]
- They show high specific surface area and microporosity, two properties of fundamental importance in gas storage. At the moment, they are the reference point for the evaluation of the capacity of an adsorbent material.

The main classes of microporous organic polymer that are considered as potential candidates for gas storage are: Polymers of Intrinsic Microporosity (PIMs), Covalent Organic Frameworks (COFs), conjugated Microporous Polymers (CMPs), Hypercrosslinked Polymers (HCPs) and Porous Aromatic Frameworks (PAFs). [98]

2.5.1 Polymers of Intrinsic Microporosity (PIMs)

Polymers of intrinsic microporosity (PIMs) are a group of polymeric materials which don't require a network of covalent bonds in order to show microporosity; indeed intrinsic microporosity in polymers is defined as a continuous network of interconnected intermolecular voids, which are formed as a direct consequence of the shape and rigidity of the component macromolecules. [99]
PIMs are amorphous solids due to their random packing and lack of long-range order, but possess surface areas in the range of 400 - 1760 m^2/g. [100] Usually they are formed by a double nucleophilic aromatic substitution reaction between a tetrahydroxylated monomer and a tetrafluorinated monomer, resulting in the formation of dioxane links between monomer units (Figure 2.4).
It is essential for the production of a microporous PIM that one of the monomers has a highly rigid and contort structure.

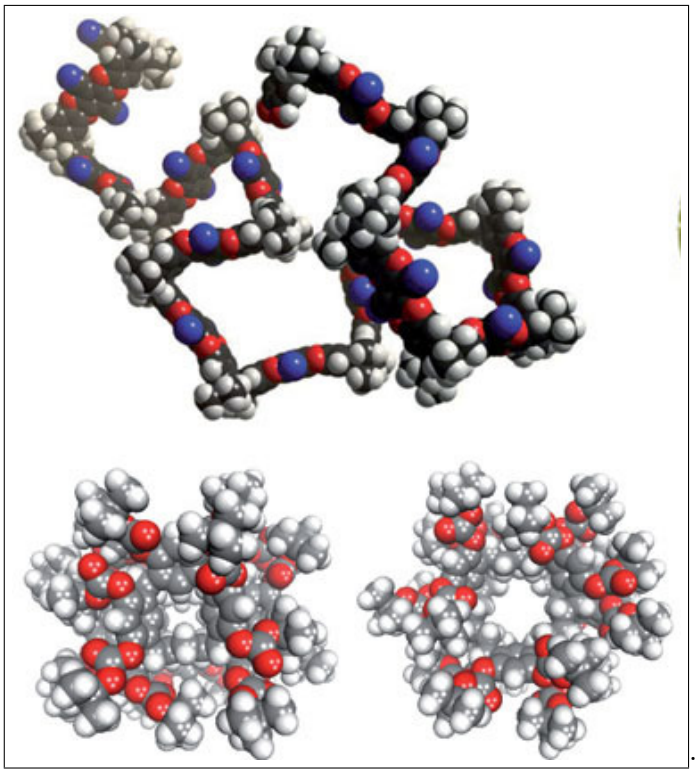

Figure 2.4: Typical molecular models of PIM polymer. [59]

Hydrogen uptakes of up to 2.7 wt%, at 10 bar and 77 K, have been reported for a triptycene-based polymer (trip-PIM). [101]

2.5.2 Covalent Organic Frameworks (COFs)

Covalent organic frameworks (COFs) are a class of crystalline porous polymers with precisely integrated organic units to create predesigned skeletons and nanopores. [105]
Being composed of light-weight elements linked by strong covalent bonds, COFs have low mass densities, possess high thermal stabilities, and provide permanent porosity. [104]
Depending on the building block dimensions, COFs can be categorized into either two-(2D) [102] or three-dimensional (3D) COFs. [103]
In 2D COFs, the covalently bound framework is restricted to 2D sheets, which stack to form a layered eclipsed structure that presents periodically aligned columns. [106] This columnar stacking structure provides a unique mean to construct ordered p systems that are difficult to create via conventional covalent and/or noncovalent approaches. The ordered columns in 2D COFs could facilitate charge carrier transport in the stacking direction, which implies that 2D COFs have potential for developing new type p-electronic and photofunctional materials for optoelectronics and photovoltaics.
In contrast, 3D COFs, formed by building blocks containing an sp_3 carbon or silane atom, characteristically possess high specific surface areas (in some cases larger than 4000 m^2/g), numerous open sites, and low densities, as low as 0.17 g/cm^3. The group of Farha et al. synthesized COFS with other 2D and 3D framework, [95] characterized by high surface areas (COF-102 (Fig.2.5a) and COF-103 (3472 and 4210 m^2/g, respectively) and very low density as for example, the COF-108 (Fig.2.5c) with a value 0.17 g/cm^3, which is currently the lowest value ever achieved by a porous crystalline material.

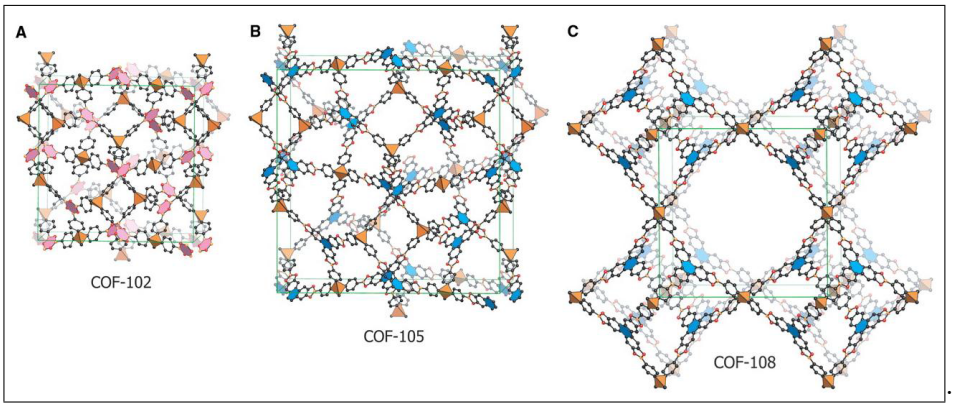

Figure 2.5: 3D Structures of (a)COF-102, (b)COF-103 and (c)COF-108. [94]

The storage capabilities of COFs for gases, such as hydrogen, methane, and carbon dioxide, have been widely investigated. [107–109]

2.5.3 Conjugated Microporous Polymers (CMPs)

Conjugated microporous polymers (CMPs) are a class of porous materials with amorphous three-dimensional organic framework made up of multiple carboncarbon bonds and/or aromatic rings that form an extended conjugated network.
CMPs were first reported in 2007 [110] and took advantage of Sonogashira-Hagihara palladium coupling to link aromatic halides to aromatic alkynes, thus forming poly(aryleneethynylene) (PAE) networks, with BET surface areas that exceed 1000 m^2/g in some cases. [111, 112]
CMPs are formed under kinetic control and display no long-range order, but their pore sizes are well-defined and can be controlled by careful selection of the monomers. [101] Surface areas can also be controlled by changing the linker length, with the number of micropores decreasing with increasing linker length. This behavior can be explained by the extra flexibility granted to the framework by longer linkers, that allow a more efficient packing and decrease the available surface area. [113]
Thanks to the study on PAEs it was discovered that:

- similarly to the crystalline materials, such as MOFs and COFS, the surface area and pore distribution can be modulated according to the type of organic linker that connects the monomers
- the structural order is not a prerequisite for controlling of microporosity.

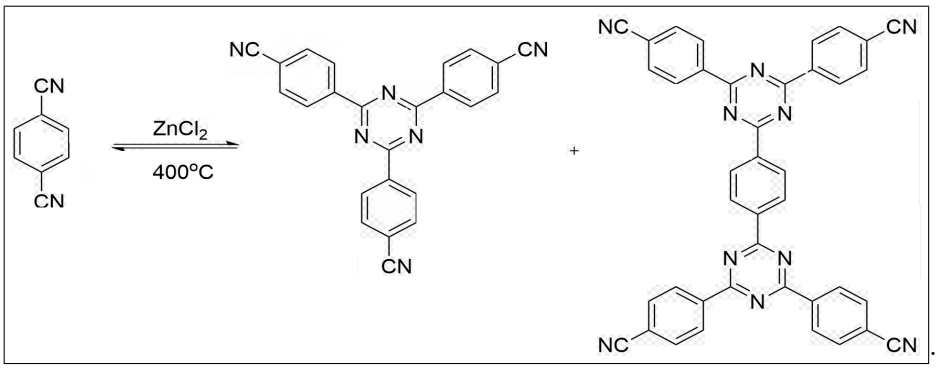

Figure 2.6: Cyano cyclotrimerization reactions occur under ionothermal conditions.

The research performed on CMPs has focused on broadening the range of functional groups that can be incorporated into the frameworks, with the aim to tune the properties of the materials for different applications.
CMPs are currently attracting considerable interest as materials that combine the mechanical stability of polymers with adjustable optoelectronic properties of organic molecules. In fact, species belonging to the family of conjugated polymers have already been exploited for some applications like optoelectronic OLED (Organic Light Emission Diode) for photovoltaic cells and FET transistor. [115, 116]

2.5.4 HyperCrosslinked Polymers (HCPs)

HCPs represent a class of low cost porous materials, which can be prepared mainly by the Friedel-Crafts alkylation reaction. The permanent porosity in HCPs is a result of extensive crosslinking reactions, which prevents the polymer chains from collapsing into a dense, non-porous state. [117]
The crosslinking produces a highly rigid network structure with high thermal stability that is not commonly expected for organic polymers. Combined with their light weight properties, small pore size, micropore volume and high surface areas, HCPs can be considered as promising materials for H_2 and CO_2 storage applications. [118, 119]
According to the synthetic method, HCPs can be produced by the following procedures: [120]

1. intermolecular and intramolecular cross-linking of preformed polymer chains (either linear chains or lightly cross-linked gels).
2. self-condensation of chloromethyl- or hydroxymethylaromatics in the presence of $FeCl_3$.
3. knitting aromatic compounds using cross-linking agents.

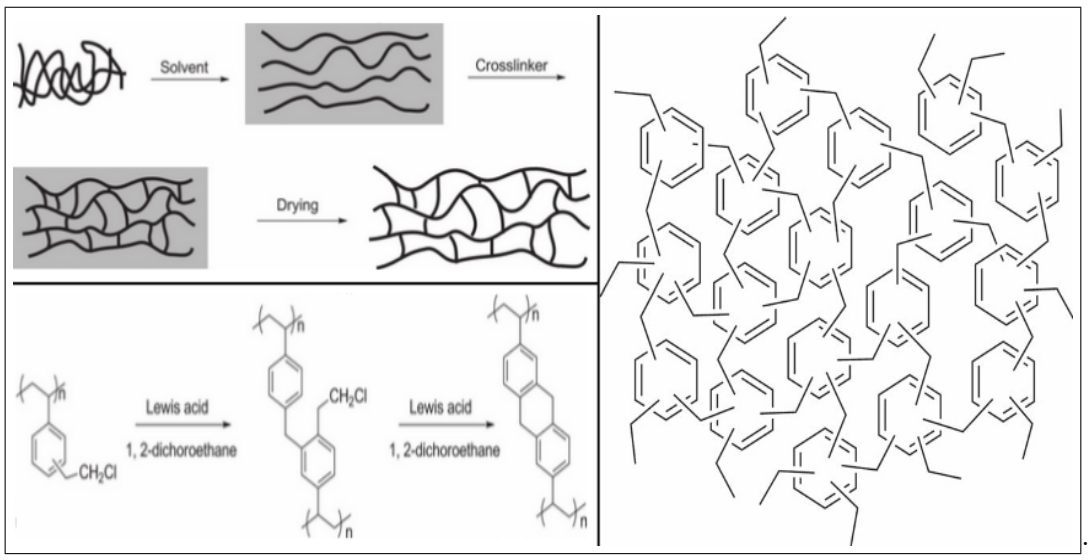

Figure 2.7: Schematic representation of the Hypercrosslinking process, reaction scheme for the synthesis of a HCP polymer prepared from gel poly(divinylbenzene-co-vinylbenzyl chloride) [120] and the final polymer scheme.

In the literature there are many examples of synthesis of HCP. Davankov-type resins are the first type of hypercrosslinked materials, which have been well-studied and are prepared by post-crosslinking of linear polystyrene (PS), poly(vinylbenzyl chloride), or their

pre-crosslinked copolymers with a divinylbenzene (DVB) moiety. [117]
Direct step growth polycondensation of suitable monomers: this is an approach to microporous organic networks that uses bis(chloromethyl) aromatic monomers such as dichloroxylene (DCX), bis(chloromethyl)biphenyl (BCMBP), and bis(chloromethyl) anthracene. [112]
The HCP polymers obtained using these precursors are predominantly microporous and exhibit apparent BET surface areas of up to 1904 m^2/g as measured by nitrogen adsorption at 77 K. [121]
Knitting aromatic compound polymers (KAPs) using an external crosslinking agent.
This procedure has been recently developed and consists in the simple one-step Friedel-Crafts reaction between an aromatic monomer and formaldehyde dimethyl acetal (FDA): in the presence of $FeCl_3$ as catalyst various aromatic monomers can be directly crosslinked to form the highly porous networks (Figure 2.8). [123]

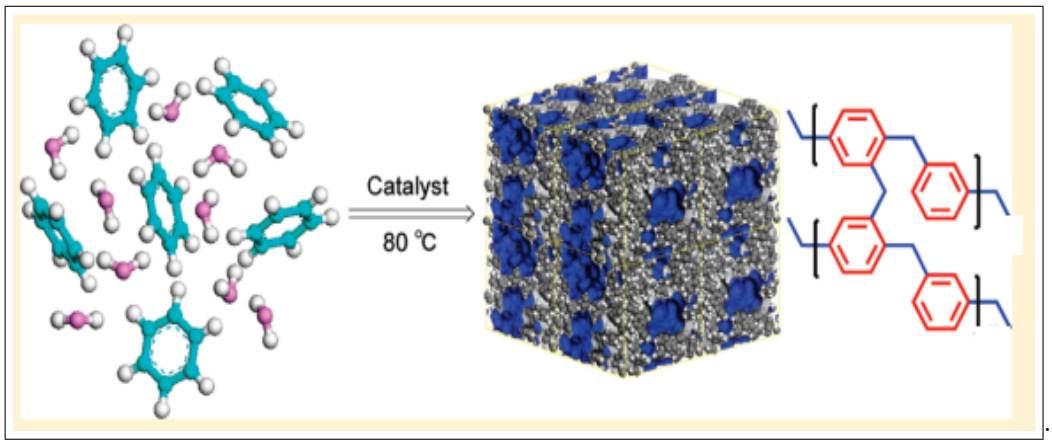

Figure 2.8: Scheme showing the synthetic pathway of HCP polymers using an external crosslinking agent [123].

Also Cooper group demonstrated that this knitting approach can produce networks with surface area of up to 1470 m^2/g when using the tetrahedral monomer, tetraphenylmethane. [124]
This method avoids the need for monomers with specific polymerizable groups and also avoids the use of precious metal coupling catalysts.
Various functional groups can also be easily introduced into the porous frameworks just by choosing the proper monomers.
Based on the combination of large specific surface area and enhanced microporosity, HCPs show good potential for gas storage. [126–129]
The properties of HCPs can be fine-tuned for a specific purpose by post synthetic modification. [122]
This is possible because the hypercross-linking reaction doesn't occur at each possible site, resulting in residual chloromethyl groups being present in the polymeric matrix.
Thus, functional groups, such as amines or alcohols, can be transferred to the polymer matrix by replacing these residual chlorine atoms.
This enables to improve the storage capacity of these materials and extends their application as adsorbents for toxic organic [130] and inorganic contaminants. [4]

2.5.5 Porous Aromatic Frameworks (PAFs)

Porous aromatic frameworks (PAFs) are a family of microporous polyphenylic networks characterized by a three-dimensional, rigid and open-network structures.

The original idea for the synthesis of PAF came from the structure and properties of diamond, in which each carbon atom is tetrahedrally connected to four neighboring atoms by covalent bonds.
Breaking the C-C covalent bond of diamond and inserting rigid phenyl rings allow sufficient exposure of the faces and edges of phenyl rings with the expectation of increasing the internal surface areas.
Ben et al. [21] have proposed, indicating the structure and some of the main characteristics related to the porosity and the hydrogen storage capacity, obtained by the Monte Carlo method, the structures of other materials belonging to the class of PAFs: PAF-301 with one aromatic ring, PAF-303 with three aromatic rings interspersed in CC bond and the PAF-304 with four aromatic rings (Figura 2.9).

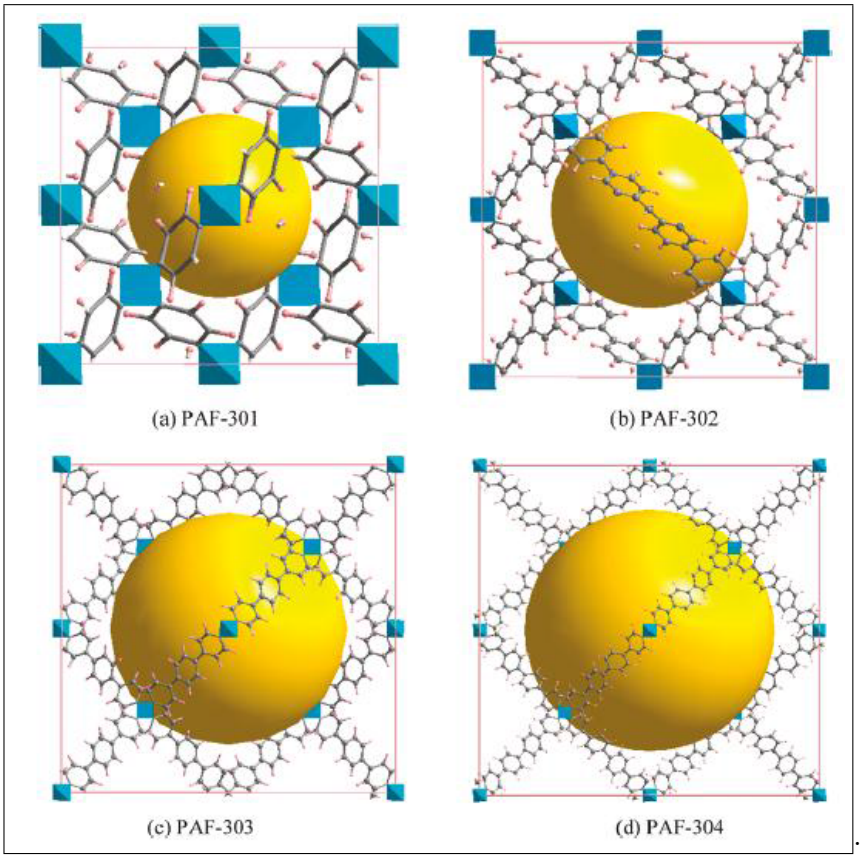

Figure 2.9: Unit cells of PAFs, (a) PAF-301, (b) PAF-302, (c) PAF-303, and (d) PAF-304, derived from topology design and geometry optimization with the force field method. Here, gray and pink spheres represent carbon and hydrogen atoms, respectively, while the blue polyhedron represents the tetrahedrally bonded carbon atoms. In addition, the yellow sphere denotes the pores in 3D PAFs. [21]

The previuos year, in 2009, the same group [131, 132] developed a method to synthesize the first long range ordered porous aromatic framework (PAF) with diamond-like topology (PAF-1 or PAF-302), which had a record surface area (SBET = 5640 m^2/g) at that time and exceptional physicochemical stability via a nickel(0)-catalyzed Yamamoto-type cross-coupling reaction (Figure 2.10).

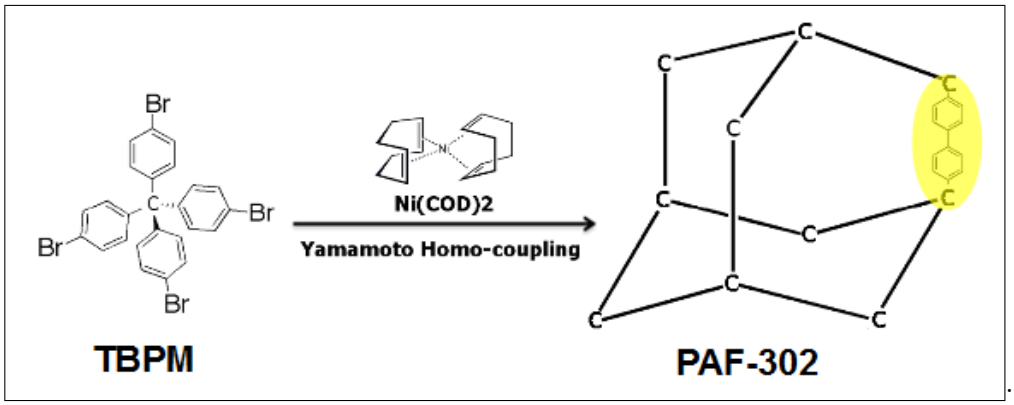

Figure 2.10: Synthesis scheme of the PAF-1 using Yamamoto coupling reaction

For a long time it was thought that the low surface area of porous organic polymers was due to the amorphous structure, but thanks to PAF-1, it has been shown that even non-crystalline materials could reach very high surface areas.
This exceptional surface area, according to Hong-Cai Zhou, [133] is mainly due to three factors:

- The highly efficient Yamamoto reaction helps to eliminate unreacted terms at the monomers and therefore highly connected frameworks are formed. [134]
- The default diamond framework topology, imposed by the tetrahedral monomers, provides widely open and interconnected pores to efficiently prevent the formation of dead space.
- The prevailing robust covalent C-C bond connecting the whole framework leads to a material with exceptionally high thermal and chemical stability.

Compared with other ultrahigh surface area solids such as porous carbons, porous silicas, zeolites, MOF and microporous polymers, PAFs show very high thermal (>450°C) and excellent physicochemical stabilities.They are also characterized by excellent adsorption abilities for CO_2, H_2 and CH_4. [135, 136]
Yamamoto reaction is advantageous as only one type of functionality is required and just a single, halogenfunctionalized monomer can be used to form high molecular weight polyaromatics frameworks.
Compared with other C-C coupling reactions in literature, Yamamoto coupling shows the unexpected ability to eliminate terminal halogen atoms. This makes the reaction unique to prepare ultrahigh porous solids because heavy ending halogen atoms lead to solids with low surface area. [137]
On the other hand, stoichiometric (or excess) quantities of the nickel complex are required because the catalyst is very sensitive. [138]
However, this catalyst is very expansive and toxic.
For these reasons, our experimental group studied the “in situ” preparation of the catalyst and has concerned another type of optimization for the material PAF-302, the use of microwave irradiation as an alternative route to heat source. This technique generally has several advantages including the very fast and homogeneous heating that can result in the reduction of side reactions, cleaner products, and higher yields.
Besides these new preparation appproaches, the optimization of the experimental conditions for the synthesis of PAF-302 in order to obtain reproducible high surface area materials, as well as the reduction of the costs of the synthesis, has been paid to the improvement of the

storage capacity.
A comparative investigation of the physico-chemical properties of the synthesized materials was carried out by a multidisciplinary approach using infrared (IR) and Solid State Nuclear Magnetic Resonance (SS-NMR) spectroscopy and powder X-ray diffraction (PXRD) to evaluate the structural characteristics of the materials and finally Thermal gravimetric analysis (TGA) was used to study the thermal stability of the polymers.
However, the key parameters adopted to demonstrate the success of the synthesized materials are the pore diameter distribution, the pore volume and the surface area measured by N_2 physisorption at 77 K.
In the chapter 4 theoretical calculations concerning the FTIR spectra, pore distributions and capacity storage of gases will be presented and they will be compared to help the interpretation of both spectroscopic and adsorption isotherm results.
The capacity storage of CH_4, H_2 and CO_2 for best materials will be evaluated simulating the adsorption properties of PAF-30n (n = 1-4) at various temperatures, to find the most suitable materials. The theoretical study of these materials has focused, initially, on the optimization of the constituent units of the four PAF and, in particular, on the distance of the C-C bond between the tetrahedral carbon and the carbon of the aromatic ring. Later, the structures of the different PAFs were built with the new coordinates of the cell and they were analyzed two types of interactions:

- Adsorbate-adsorbate interactions

- Adsorbent-adsorbate interactions

The latter refer to the interactions that occur between the gas molecules taken into account and parts of the structure of the PAF, the former, however, are created between the individual molecules of gas, which, tending to repel each other.
The adsorpion was studied ay differnt pressures using the Monte-Carlo method based on the principle of the force fields, to understand the amount of gas that can be stored in each of the four PAF30n considered.
Therefore, the CO_2 adsorption then was simulated in a number of modified PAF-302, with different functional groups (aminomethane, toluene, pyridine, and imidazole) attached to the phenyl chains; different degrees of substitution (25%, 50%, and 100% derivatized rings) were considered. The effects of functionalization and the dependence on the substitution degree are discussed, to determine the most promising materials at low, intermediate, and high pressures.

2.5.6 microPorous Aromatic Frameworks (mPAF)

Recently, a new method for preparing microporous polymers by using formaldehyde dimethyl acetal (FDA) as cross-linking agent to polymerize various aromatic monomers has been reported. [123]
This approach is particularly convenient because it requires mild conditions without the use of expensive reagents, allowing the synthesis of a variety of porous polymers. During their extensive research on organic materials, Cooper and co-workers applied this approach to the polymerization of the rigid aromatic structure of tetraphenylmethane (TPM), obtaining materials with good CO_2 storage properties. [124]
Some collegues of our Department have studied the polymerization based on the Friedel-Crafts TPM /FDA reaction, with the aim of producing good adsorbents also for other gases, mainly methane and hydrogen (Figure 2.11). [141]

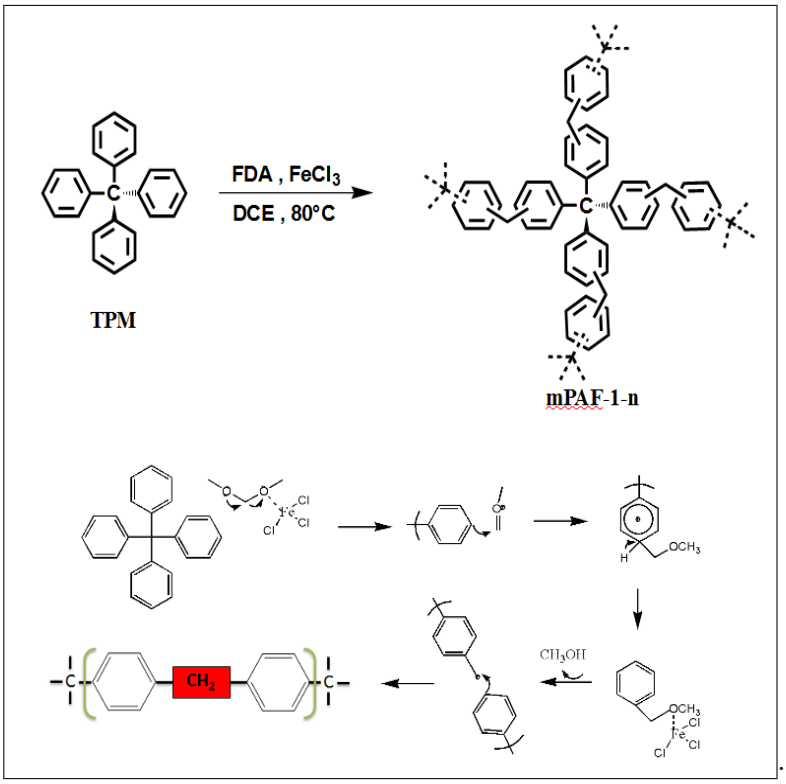

Figure 2.11: Scheme of the synthesis of mPAF. [141]

The synthesis conditions were optimized by investigating how the porosity and the surface area of the final material depend on the reagent stoichiometry, varying the aromatic monomer/cross-linking agent ratio.
The aim was to increase especially the microporous volume, and in particular the fraction of smallest pores, below 10 Å width, which are expected to lead to high gas uptake also at low pressures. [46, 142, 143]
The acronym PAF (Porous Aromatic Framework) is suited for this kind of system, though it was originally proposed for materials obtained by a different route and, more important, with wider pores. To emphasize the role of smaller pores, as pointed out above, we have named this new material mPAF (microPorous Aromatic Frameworks).
To support the characterization of mPAF materials, in this study periodic molecular models will be presented to define networks of tetraphenylmethane moieties connected by methylene bridges in para position.
The atomistic structural model built for the mPAF is different than the PAF model. This is due because the two material natures are different from each other. mPAF is amorphous and it has a structure with different size pores, while the PAF presents a crystalline structure. It wasn't possible to prepare a single structural model for both.
For the following mPAF a sequence monomeric distributed at random was built, on the contrary, the synthesis of PAF leads to a regular structure and to a monomeric sequence uniform in space.
In chapters, different periodic polymer models, which have been applied to various types of monomers, will be discussed. For each monomer a different degree of crosslinking was used.
The study was extended to the evaluation of some of the considered systems and different side groups, not provided in the reaction of reference, were added. Such groups are derived from secondary reactions that occur during the various stages of the synthesis experimental. In fact, the characterization of the material surface carried out FT-IR spectroscopy showed

the presence of the above-mentioned side groups which have led to further investigations modeling.
At first, the Ar adsorption isotherm at 87 K and the N_2 adsorption isotherm at 77 K, simulated with the Monte Carlo technique and the force field described in the chapter 4, will be compared to the adsorption isotherm of experimental mPAF, which showed the largest specific surface area among the experimental samples.
The capacity storage of CH_4, H_2 and CO_2 for the theoretical models compared with the experimental sample will be evaluated.

3 Theoretical elements

3.1 Quantum mechanics theory

3.1.1 The Schrödinger Equation

Most ab-initio methods for the theoretical study of polyatomic systems are based on the time-independent form of the famous Schrödinger equation:

$$\hat{H}\Psi = E\Psi \tag{3.1}$$

with Ψ being the wavefunction of the system, E the energy and $\hat{H}$ the Hamiltonian operator, which is defined as

$$\hat{H} = \hat{T} + \hat{V} \tag{3.2}$$

$\hat{T}$ and $\hat{V}$ being the kinetic and potential energy operators, respectively. In atomic units, the kinetic energy operator is defined as:

$$\hat{T} = \sum_{j=1}^{o} -\frac{1}{2}\nabla_j^2 + \sum_{k=1}^{n} \frac{1}{2m_k}\nabla_k^2 \tag{3.3}$$

where j and k indicize electrons and nuclei, respectively, o and n are respectively the number of electrons and nuclei, ∇_j^2 and ∇_k^2 are the second derivatives with respect to the x, y and z coordintes of the j^{th} and k^{th} nucleus and m_k is the mass of the k^{th} nucleus.

The kinetic energy operator in the absence of external electric or magnetic fields is defined as

$$\hat{V} = \frac{1}{2}\sum_{i,j}{}' \frac{1}{r_{i,j}} - \frac{1}{2}\sum_{j,k} \frac{Z_k}{r_{j,k}} + \frac{1}{2}\sum_{k,l}{}' \frac{Z_k Z_l}{r_{kl}} \tag{3.4}$$

with i and j being the electron indices, k and i nuclei indices, Z_k the charge of the k^{th} nucleus, e the fundamental electric charge and r the distance between two particles. Substituting for 3.4 and 3.3 in 3.2 the extended form of the Hamiltonian is obtained:

$$\hat{H} = \sum_{j=1}^{o} -\frac{1}{2}\nabla_j^2 + \sum_{k=1}^{n} -\frac{1}{2m_k}\nabla_k^2 + \frac{1}{2}\sum_{i,j}{}' \frac{1}{r_{i,j}} - \frac{1}{2}\sum_{j,k} \frac{Z_k}{r_{j,k}} + \frac{1}{2}\sum_{k,l}{}' \frac{Z_k Z_l}{r_{kl}} \tag{3.5}$$

3.1.2 The Born-Oppenheimer Approximation

In a polyelectronic system, the Schrödinger Equation cannot be solved analytically and it therefore becomes necessary to make certain approximations: in this frame, the Born-Oppenheimer approximation plays a central role in Computational Chemistry. The Born-Oppenheimer approximation involves the separation of the movement of electrons and nuclei, thus redefining the wavefunction as the product of two functions:

$$\Psi(q, Q) = \psi(q\|Q)\phi(Q) \tag{3.6}$$

with q and Q being the set of electronic and nuclear coordinates, respectively, $\Psi(q,Q)$ the wavefunction, $\psi(q\|Q)$ a function of q depending parametrically on Q and $\phi(Q)$ a function of nuclear coordinates. Functions $\psi(q\|Q)$ are eigenfunctions of the electronic Hamiltonian H_{el}:

$$\hat{H}_{el}\psi(q\|Q)_k = E_k(Q)\psi(q\|Q)_k \tag{3.7}$$

where k is the index of the eigenfunctions, and the respective eigenvalues, of $\hat{H}_{el}$:

$$\hat{H}_{el} = \sum_{j=1}^{o} \frac{-1}{2}\nabla_j^2 + \frac{1}{2}\sum_{i,j}{}' \frac{1}{r_{i,j}} - \frac{1}{2}\sum_{j,k}\frac{Z_k}{r_{j,k}} = \sum_{j=1}^{o}\hat{h} + \frac{1}{2}\sum_{i,j}{}'\frac{1}{r_{i,j}}. \tag{3.8}$$

It should be noted that any change of Q will result in a change of H_{el} as well and, consequently, of $E_k(Q)$. It is now necessary to define functions $\phi(Q)$: these are eigenfunctions of $(\hat{T}_n + E_k(Q))$, with $\hat{T}_n$ as the nuclear kinetic energy operator. $\hat{T}(Q)$ is proportional to $\frac{\partial^2}{\partial Q^2}$: in the context of the Born-Oppenheimer approximation, integrals relative to $\frac{\partial^2}{\partial Q^2}$ are discarded.

3.1.3 The Wavefunction

An exact definition of the wavefunction is:

$$\Psi = \sum_i c_i\psi_i \tag{3.9}$$

where the ψs make up a complete base and the cs are numerical coefficients that weigh each base functions. Though mathematically correct, this definition is of little practical value for the purpose of solving the Schrödinger equation. In 1928, the physicist Douglas Hartree proposed to address this problem by defining the wavefunction as a product of functions:

$$\Psi = \prod_{i=1}^{n}\phi_i \tag{3.10}$$

where functions ϕ are the molecular spinorbitals and n is the number of electrons. It quickly became evident though how this definition was not consistent with the Pauli Exclusion Principle, a mathematical requirement of which is the antisymmetricity of the wavefunction with respect to the exchange of two electrons. An antisymmetric definition of the wavefunction was later introduced by John Slater:

$$\Phi_S = \frac{1}{\sqrt{N!}}\begin{vmatrix} \phi_1(\vec{X_1}) & \phi_1(\vec{X_2}) & \dots & \phi_1(\vec{X_n}) \\ \phi_2(\vec{X_1}) & \phi_2(\vec{X_2}) & \dots & \phi_2(\vec{X_n}) \\ \vdots & \vdots & \ddots & \vdots \\ \phi_n(\vec{X_2}) & \phi_n(\vec{X_2}) & \dots & \phi_n(\vec{X_n}) \end{vmatrix} \tag{3.11}$$

where $\{\vec{X_i}\}$ is the set of spatial and spin coordinates of the wavefunction. This function is called the Slater Determinant. It is important to observe that in this definition, a significant approximation is implicit: by expressing Ψ as a product of functions, electronic repulsion is treated for each electron as the interaction with an average spherical potential of all other n-1 electrons.

It is now necessary to define ϕs. These are defined as a linear combination of hydrogen-like atomic orbitals, centered on the nuclei, similarly to what was observed in the wavefunction Ψ in 3.9:

$$\phi_i = \sum_i c_i \chi_i \tag{3.12}$$

again, c_i is a numerical coefficient that weighs the contribution of the ith orbital, χ_i.

It must be considered that a wavefunction is required to satisfy certain mathematical conditions imposed by its physical meaning. One such requirement is set by the Born Interpretation, which states that:

$$\int |\Psi|^2 dxdydz = 1 \tag{3.13}$$

this interpretation assigns to the square modulus of the wavefunction the meaning of probability density, implicitly restricting the set of possible functions to finite functions. Recalling the form of the kinetic energy operator as expressed in TOTO, it becomes evident that the wavefunction also needs to be continuous and doubly derivable, due to the presence of the ∇^2 operator.

3.1.4 The Hartree-Fock Method

One of the first techniques developed to solve the Schrödinger Equation is the Hartree-Fock method. This procedure is based on the Variational Theorem, which guarantees that by applying the Hamiltonian operator to any arbitrary trial function Φ, the relative energy eigenvalue E will always be greater than the energy of the ground state E_0, or equal to E_0 if $\Phi = \Psi$. An important consequence of this theorem is that in order to find the best approximation for Ψ it is sufficient to minimize the energy with respect to Φ.

An important part of the Hartree-Fock method is the Fock operator, $\hat{F}$:

$$\hat{F} = \hat{h} + \hat{J} - \hat{K} \tag{3.14}$$

where $\hat{J}$ is the Coulomb operator and $\hat{K}$ is the exchange operator:

$$\hat{J} = \sum_i \hat{J}_i = \sum_i \sum_{j \neq i} \int \phi_j^*(\vec{x_j}) \frac{1}{r_{ij}} \phi_j(\vec{x_j}) \phi_i(\vec{x_i}) d\vec{x_j} \tag{3.15}$$

$$\hat{K} = \sum_i \hat{K}_i = \sum_i \sum_{j \neq i} \int \phi_j^*(\vec{x_j}) \frac{1}{r_{ij}} \phi_i(\vec{x_j}) \phi_j(\vec{x_i}) d\vec{x_j} \tag{3.16}$$

The Fock operators initially built with trial spinorbitals and is then applied to the spinorbitals themselves:

$$\hat{F}\phi_i = \epsilon_i \phi_i \tag{3.17}$$

ϵ_i is minimized on the coefficients of the basis functions χ, iterating the definition of $\hat{F}$ and its application to the spinorbitals, until an arbitrarily defined convergence criterion is met. Spinorbitals thus obtained are then reemployed to generate a new Slater determinant, to which the relevant operators are applied to calculate the observables of interest. The whole process can be expressed in matrix form using the Roothaan equation:

$$\mathbf{FC} = \boldsymbol{\epsilon}\mathbf{SC} \tag{3.18}$$

where $\mathbf{F}$ is the Fock matrix, with elements $F_{ij} = \int \phi_i^*(1) \hat{f}(1) \phi_j(1) d(r_1)$, $\mathbf{C}$ is the basis function coefficients matrix, with c_{ij} as the coefficient of the ith basis function in the expansion of the jth molecular orbital, $\boldsymbol{\epsilon}$ is the diagonal matrix of the energies of the single orbitals and

S is the overlap matrix, with $S_{ij} = \langle \phi_i | \phi_j \rangle$. Expressed in this form, the problem can be solved by diagonalizing the coefficients matrix.

3.1.5 Density Functional Theory

In 1964, Hohenberg and Kohn proved that all the properties of a system can be expressed as a function of its elctronic density $\rho(\vec{x})$, therefore E = E$[\rho(\vec{x})]$, and that the Variational Theorem is valid for E$[\rho(\vec{x})]$. To calculate the energy of a system from $\rho(\vec{x})$, Kohn and Sham introduced the equation that was later named after them, which treats electrons as independent of each other and subject to a potential defined in such a way as to make the electronic density of the system equal to that of the ground state,

$$E[\rho(\vec{r})] = T[\rho(\vec{r})] + \int \rho(\vec{r}) v(\vec{r}) + E_{ee} \tag{3.19}$$

where $T[\rho(\vec{r})]$ is the electron kinetic energy, $\int \rho(\vec{r}) v(\vec{r})$ is the interaction with an external potential and E_{ee} is the electron-electron interaction. The latter is defined as

$$E_{ee}[\rho(\vec{r})] = \frac{1}{2} \int \frac{\rho(\vec{r})\rho(\vec{r'})}{|r - r'|} d\vec{r} d\vec{r'} + E_{XC}[\rho(\vec{r})] \tag{3.20}$$

with $\int \frac{\rho(\vec{r})\rho(\vec{r'})}{|r-r'|} d\vec{r} d\vec{r'}$ as the coulomb interaction between two electrons and $E_{XC}[\rho(\vec{r})]$ which includes exchange and correlation.

Electron densities are calculated by integrating over the molecular orbitals:

$$\rho(\vec{r}) = \sum_i |\phi_i(\vec{r}_i)|^2 \tag{3.21}$$

where each orbital ϕ_i is an eigenfunction of the Kohn-Sham operator:

$$(-\frac{1}{2}\nabla_i^2 + \hat{v}(\boldsymbol{r})_{KS})\phi_i = \epsilon_i \phi_i. \tag{3.22}$$

$\hat{v}(\boldsymbol{r})_{KS}$ is defined as

$$\hat{v}(\boldsymbol{r})_{KS} = -\sum_k \sum_i \frac{Z_k}{r_{ik}} + \sum_i \hat{J}_i + V_{XC} \tag{3.23}$$

with i and k being the electron and nucleus indices, respectively. We have thus introduced V_{XC}, the exchange-correlation potential:

$$V_{XC} = \frac{\delta E_{XC}}{\delta \rho} \tag{3.24}$$

Knowing ρ and $E_{XC}[\rho]$, it is now possible to calculate the energy of the ground state. Unfortunately, the exchange-correlation potential of real physical systems is not known. To solve this problem, several techniques have been developed: the treatment of electrons as independent particles allows to include the V_{XC} of a gas of independent electrons, which is known. This way of handling $E_{XC}[\rho]$ is known as the Local Density Approximation (LDA) and it generally gives good results with periodic systems and has therefore been widely employed in solid state physics. This type of functional does not generate reliable results for most systems of chemical interests, as the distrubiotion of the electron density is considerably different from that of the electron gas model. Better results can be obtained by including the density gradient $\nabla\rho(\vec{r})$: these are known as Generalized Gradient Approximation (GGA) functionals. It should be noted that, while there is only one LDA functional, many GGA

functionals can be defined, as the function that describes the electron density gradient is defined arbitrarily: it can be designed to accurately describe the asymptotic properties of a system, ensuring that the energy of two fragments at infinte distance from each other is the same as the energy of the bound fragments, or empirically, by fitting a set of experimental data. A further development of GGA functionals is the inclusion of part of the Hartree-Fock exchange $\hat{K}$, defined using the eigenfunctions of the Kohn-Sham operator:

$$v_{xc}[\rho] = (1-\alpha)v_x + \alpha\hat{K} + v_c[\rho] \tag{3.25}$$

where v_x is the exchange potential and $v_c[\rho]$ is the correlation potential. Functionals of this type are called hybrid. An example of such a functional is the popular B3-LYP, in which 25% of Hartree-Fock exchange is used.

3.1.6 Basis Functions

The choice of a set of basis functions that describe atomic orbitals is a fundamental step in the setup of an ab-initio calculation: using a complete basis set, made of infinite functions, would produce the true wavefunction Ψ and the true value of its observables. Obviously this is not possible in practice to use infinite basis functions, so it becomes necessary to use incomplete basis sets, which will result in approximations that will generally be more refined as the numer of basis functions is increased. A basis set must always have at least a number of functions equal to the number of electrons of the system: this is called the minimal basis set.

Historically, the first basis functions used were those proposed by Slater, called Slater Type Orbitals (STO), which have the following form:

$$\chi^{STO}_{n,l,m}(r,\theta,\phi) = Nr^{n-1}e^{-\zeta r}Y_{l,m}(\theta,\phi) \tag{3.26}$$

where n, l and m represent the three quantum numbers, N is a normalization factor, r θ and ϕ are polar coordinates and ζ is a constant for each element that accounts for the shielding between electrons. Though these provide a good description of atomic orbitals, in computational practice STOs are seldom used. Much more common are Gaussian Type Orbitals (GTO)

$$\chi^{GTO}_{n,l,m}(r,\theta,\phi) = Nr^{2(n-1)}e^{-\alpha r^2}Y_{l,m}(\theta,\phi) \tag{3.27}$$

their form allows four center integrals to be treated as two center integrals, resulting in reduced computational costs.

3.1.7 Basis Set Superposition Error

In a system composed of two fragments A and B which form adduct AB, the addition energy could be calculated from the exact energies of the monomers and the adduct:

$$\Delta E = E_{AB} - E_A - E_B. \tag{3.28}$$

Normally, the energy of fragments A and B and adduct AB are unknown and must therefore be calculated, using the methods described earlier in this chapter by assigning basis set a to fragment A and basis set b to fragment B. During the calculation of the energy of the adduct, the atoms of each fragment have the basis set of the other fragment as well as their own. This difference leads to an overestimation of the addition energy between the two monomers: the change in energy due to the increase of the basis set involves only the adduct (E_{AB} in

eq. 3.28) while terms E_A and E_B are calculated with two smaller basis sets. This difference is called Basis Set Superposition Error (BSSE). [175]

A way to correct this error consists of the calculation of energies of single monomers using both basis sets, with a centered on the positions of atoms in monomer A and b centered on the positions of atoms in monomer B, but without including the other monomer in the calculation. The energy of the monomers is then expressed as:

$$\Delta E = (E_{AB}^{ab} - E_A^a - E_B^b) + (E_A^a - E_A^{ab}) + (E_B^b - E_B^{ab}) \tag{3.29}$$

where the apices idicate the basis set and the indices specify the species (monomers or adduct). This method is known as Counterpoise Correction (CC).

3.1.8 Monte Carlo method

The Monte Carlo method is, essentially, a calculation technique for evaluation of definite integrals. In particular, within statistical mechanics, the Monte Carlo method allows to evaluate efficiently the average value of an observable property in a system with many coordinates, knowning the density of the system state probability. [145] Considering the following problem: given a observable function *F(q)*, defined in relation to a set of coordinates (classic): *q = (q1; q2; : : : qN)^{tr}*.
The coordinates q represent one state of the system, which we assume it to be described in the context of the canonical ensemble, which represents a measure of probability of microscopic states of the system. [146] The total energy of the system, E:

$$E = V(q) + T = V(q) + \frac{1}{2} p m^{-1} \tag{3.30}$$

where, *p = (p1; p2; : : : pN)^{tr}* is the vector of the generalized moments, while m is the generalized matrix of masses (which can also be a function of q).
The average value of the observable $\bar{F}$ is:

$$\bar{F} = \frac{\int dq \int dp F(q) exp[-E(q,p)/k_B T]}{\int dq \int dp exp[-E(q,p)/k_B T]} \tag{3.31}$$

The configurational integral in dq is extended to the system volume.
Integrating respect to p moments, it remains the expression that involves only potential energy of the system:

$$\bar{F} = \frac{\int dq F(q) exp[-V(q)/k_B T]}{dq exp[-V(q)/k_B T]} = \frac{\int dq F(q) exp[-V(q)/k_B T]}{Q} \tag{3.32}$$

where, Q is the configurational canonical partition function. The Monte Carlo method is precisely dedicated, at least in its standard applications, to the numerical calculation of expressions similar to (4.3). The idea at the basis of the method is the following: "it is determined a set or a representative sample of points, generated randomly within the phase space of the system; They must be replaced by the exact integrals in the numerator and in the denominator of (4.3) with approximate amounts that depend on the sample points." It obvious that the adopted sampling criteria are crucial to select the representative sample of the points, which must be able to explore or to represent efficiently the phase space of the overall system. The choice of a representative sample of the phase space of the system could be carried out just generating a random sequence of points. It is clear, however, that, in general, this choice will not be very efficient in the case where a generic potential *V(q)* is considered. Therefore it would be appropriate to generate points in phase space or configurations that

maximize integrating exp(-ΔE/k$_B$T), basically, system configurations at low energy and high probability. Sampling should take into account the Boltzmann distribution of the energy system; this procedure (also called *importance sampling*) is implemented efficiently by the so-called scheme Metropolis. [147, 148]
The Metropolis scheme can be described as follows:

- given some initial system status *q1*, using a stochastic selection criterion, based on a partially random choice, a new configuration q$_{test}$ is generated;
- to calculate the difference energy ΔE = E (q$_{test}$) - E (*q1*): if the difference is less than zero, i.e, the energy of the test configuration is less than the previous one, the test configuration is accepted becoming part of representative sampling, *q2* = q$_{test}$;
- If ΔE>0, configuration *q2*=q_{test} is accepted in the sample only if exp(-ΔE/k$_B$T) is greater than a random number ϵ, uniformly distributed in the range; otherwise, the test configuration is rejected and you keep the previous configuration, *q2*=*q1*. In practice, the new configuration is accepted with a probability given by the Boltzmann factor exp(-ΔE/k$_B$T);
- given the new configuration *q2*, a new configuration of the sample will be generated restarting from point 1.

Therefore the Metropolis scheme does not choose at random configurations, but they are weighted, taking into account the Boltzmann factor, exp(-ΔE/k$_B$T). Once you have generated a sufficiently large number of M configurations, you get the average value of a property *F(q)* as an unweighted average of all sample configurations:

$$\bar{F} = \frac{1}{M} \sum_{j}^{M} F(q_j) \tag{3.33}$$

Moreover, the Monte Carlo method according to the scheme Metropolis is based on the idea that the sampling constitutes a pseudo-dynamics of the system, namely that the succession of configurations is obtained on the basis of a temporal evolution, or trajectory, defined in the configurational space of the system.
The evolution time is naturally given by the real dynamics of the system, which would be equivalent to a simulation of molecular dynamics, but it has the ability to maintain unchanged some fundamental properties for the equilibrium properties calculation of the system.

3.1.9 Force Fields

The methods of quantum chemistry allow the determination of the geometric characteristics and energy of molecules known or not yet synthesized. Unfortunately, they are extremely costly in terms of computing time and computational load, becoming in some cases prohibitive for very large systems (organic macromolecules or biological).
If the information to look for is structural (geometric) or energetic, and not electronic, one can resort to the methods of molecular mechanics (or empirical force fields), which are based on simple models in which the molecules are treated as if they were composed by masses and springs and their interactions are governed by the laws of classical mechanics. Thus they are able to produce relatively quickly information also for biological macromolecular systems. For these reasons they may be used as basis for subsequent calculations of highest quantum level. The two methods are also different consequences of the Born-Oppenheimer separation of the nuclear and electronic motion. [149]

In quantum mechanical calculations, starting with a given nuclear geometry, the best distribution of the electrons in the potential generated by cores will be determined. With the molecular mechanics, on the contrary, it's studied the position of the cores in the field generated by the electrons. Electrons are not explicitly considered and their camp is actually calculated, but rather represented a "potential effectively" treated according to classical mechanics. Quantum mechanics explicitly examines the electrons of a system and a large number of particles must be considered, making the calculations particularly long and laborious. The methods of molecular mechanics (or force fields) ignore the motion of electrons and calculate the energy as a function of the nuclear coordinates. This allows to use with success the molecular mechanics even in systems that contain a high number of atoms and in some cases the use of force fields can provide extremely accurate answers.
The molecular mechanics is based on an extremely simple model: the molecules are treated as if they were composed of masses and springs and it uses the laws of classical mechanics to treat the different interactions that occur in the real molecule according to a model that is empirically parameterized. A main concept on which the force field parameters are based is the transferability, developed and tested to a relatively small number of model cases can be used to study much larger molecules. [150]
The construction of a force field consists in two parts:

- The choice of the functional form that describes the energy of the system. This choice is based on the assumption that the potential energy of a molecule can be represented as a sum of terms associated respectively with the various types of molecular deformations (variations in bond lengths and valence and torsion angles) or atom-atom interactions. The steric energy calculated from the sum of these terms is the additional energy associated with the deflections of the structure with respect to an ideal situation where all the geometric elements are in a reference state.

- The choice of parameters in the functional form. This choice is based on the assumption that the parameters needed to calculate the molecular energy can be derived from the information obtained from small molecules (lengths and bond angles) and these are transferable to large systems.

Most of the force fields currently used to model molecules or clusters of atoms and molecules can be represented as the sum of four contributions, relatively simple, which describe the intra and intermolecular forces within the system: [151]

$$V_{tot}(r) = V_{stretching} + V_{bending} + V_{torsion} + V_{no-bonded} \tag{3.34}$$

Force fields more sophisticated may have additional terms, but invariably contain these four components. A particular feature of this representation is that the changes in specific internal coordinates (such as bond lengths, angles, the link rotations, or movements of atoms relative to the displacement of others) can be attributed to individual terms.
Two force fields can have an identical functional form despite having very different parameters, and force fields with different functional forms can give results with an comparable accuracy. A force field is generally designed to predict the properties and must be parameterized. The force fields are empirical, there isn't a "correct form" for a force field.
Specifically, the individual contributions to a force field are:

$$V_{stretching} = k(r - r_o)^2 \tag{3.35}$$

The first term in equation ($V_{stretching}$) describes interactions between bounded pairs of atoms and it is represented by a potential that gives variation of energy depending on the deviation

of the bond length from its reference value.
The simplest approach to describe this term consists in using Hooke's law. The energy varies with the square of the variation from the reference value of the bond length r_o.

$$V_{bending} = k(\theta - \theta_o)^2 \tag{3.36}$$

For terms of bending, functional forms are used similar to those of bond stretching, needing three atoms to define the angle. Even here the contribution of each corner is characterized by a force constant k and by a reference value θ_0. It requires less energy to deflect an angle from its equilibrium value than that required to stretch or compress a bond and the force constants are proportionately smaller.

$$V_{torsion} = \sum_{n=0}^{N} \frac{V_n}{2}[1 + cos(n\omega - \gamma)] \tag{3.37}$$

The third term in equation ($V_{torsion}$) is the torsional potential that describes how the energy varies upon rotation of the links. Torsional potentials are expressed as a series expansion of cosines, where ω is the angle of twist.
V_n in the equation is often referred to the height of the barrier.
Stretching and bending of the bonds are degrees of freedom rather rigid,in fact a significant amount of energy needs to cause substantial deformation from the reference values.
Changes in the structure and relative energies are due to the torsional term and to the non-bonding terms. The existence of the rotational barriers around chemical bonds is critical to understanding the structural properties of molecules and conformational analysis.

$$V_{no-bonded} = V_{Electrostatic} + V_{VdW} \tag{3.38}$$

The last term, no-bonded term, takes into account the interactions between pairs of atoms that are in different molecules or that are located in the same molecule but they are separated by at least three links. In the force field the term no-bonded is usually represented using a Coulomb potential for electrostatic interactions and a Lennard-Jones potential for van der Waal interactions.

$$V_{Electrostatic} = \sum_{i=1}^{N_A} \sum_{j=1}^{N_B} \frac{q_i q_j}{4\pi\epsilon_0 r_{ij}} \tag{3.39}$$

The electronegative elements attract greater electrons then the less electronegative element, giving an unequal charge distribution in the molecule. These fillers are introduced to reproduce the electrostatic properties of the molecule. If the charges are restricted to the center of the core, they are often reported as partial atomic charges. Then, The electrostatic interactions between two molecules (or between different parts of the same molecule) are calculated as a sum of interactions between pairs of point charges using Coulomb's law, where N_A and N_B are the number of point charges in the two molecules.
Electrostatic interactions don't take into account all the interactions between the atoms that there aren't tied into a system. [152, 153]

$$V_{vdW} = 4\epsilon[(\frac{\sigma}{r})^{12} - (\frac{\sigma}{r})^{6}] \tag{3.40}$$

The best known of the functions of the Van der Waals potential is the function of Lennard-Jones 12-6, which contains two adjustable parameters:

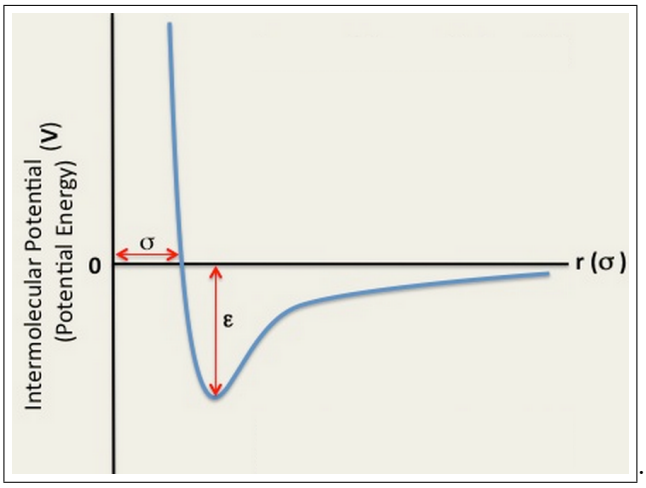

Figure 3.1: σ and ϵ parameters in a Lennard-Jones potential hole.

The Lennard-Jones potential 12-6 contains two adaptable parameters: the "collision diameter" σ (corresponding to a separation between the atoms such that the interaction energy is zero) and the depth of the potential hole ϵ. The number of binding interactions grows linearly with the size of the molecule and consequently grows computing work for the terms of the force field that don't include no-bonded interactions.
The number of non-bonding interactions depends, approximately, by the square of the number of atoms in the system (a molecule with 1000 atoms has about 500000 terms for non-bonding interactions). Therefore it's common to introduce a limit value of distance over which the interactions between atoms are not considered (cutoff).
In theory, infinity force field that describe endless situatuions can be realized with the characteristics explained above.
In Materials Studio, there are four main models of standard force fields, which can be used or customized: Compass, Cvff, PCFF and Dreiding.

- **Compass** (Condensed-phase Optimized Molecular potentials for atomistic Simulation Studies) [155] is an "ab-initio" force field, because many parameters come from ab-inito calculations. As well as CVFF And PCFF, COMPASS belongs to the second generation of force fields, and has been parameterized with a wide range of experimental observables for organic compounds containing H,N,O,S,P, halogens, cations of alkali metals, and other important divalent metal cations. COMPASS is the official force field implemented in Materials Studio that was configured and validated by providing the properties of molecules, both isolated, both in the condensed phase, with an accuracy comparable to obtained experimental data. Consequently, this force field allows an accurate calculation of the structural, conformational, vibrational, and thermo-physical properties for a wide range of isolated molecules and in condensed phase.
  Unfortunately the parameters of this force field can't be modified.

- **Cvff** (consistent-valence forcefield) [156] is suitable for the analysis of small organic molecules and crystals, but also for peptides and proteins. However, it is primarily aimed to the study of binding energies, although it provides good accuracy even with the vibrational energies.

- **Pcff** [157] is based on force field CFF91, extended in order to have a wide and sophisticated description of organic and inorganic polymers, metals and zeolites. It's useful

for polycarbonates, melamine resins, polysaccharides, as well as carbohydrates, lipids and nucleic acids. It's very useful for: cohesive energy, mechanical properties, thermal properties and compressibility.

- **Dreiding** is useful for predicting structures and dynamics of organic, biological, and main-group inorganic molecules. The philosophy in DREIDING is to use general force constants and geometry parameters based on simple hybridization considerations rather than individual force constants and geometric parameters that depend on the particular combination of atoms involved in the bond, angle, or torsion terms. Thus all bond distances are derived from atomic radii, and there is only one force constant each for bonds, angles, and inversions and only six different values for torsional barriers. Parameters are defined for all possible combinations of atoms and new atoms can be added to the force field rather simply. Mayo S.L. et al. [158] report the parameters for the "nonmetallic" main-group elements (B,C,N,0,F columns for the C,Si,Ge and Sn rows) plus H and a few metals (Na,Ca,Zn,Fe). The accuracy of the DRElDlNG force field is tested by comparing with (i) 76 accurately determined crystal structures of organic compounds involving H,C,N,0,F,P,S, and Br, (ii) rotational barriers of a number of molecules, and (iii) relative conformational energies and barriers of a number of molecules. Recently Dreiding forcefield was used to predict gas adsorption in MOFs and COFs materials. [159]
  For our simulations, we modified the Dreiding Force Field [143] which is widely used to simulate intermolecular host-guest interactions; at the first, our modified force field was tested first for various gases, simulating a formal adsorption in an empty box and computing the compressed gas density at different temperatures. The results were compared with the experimental data. [160]

3.2 Computational approach

During this work different methods, modeling programs or packages within them, have allowed the structural modeling of porous materials and they will be described to understand and to examine the behavior of isotherms within the models.

3.2.1 Sorption

Sorption is a module (or package) of the graphics modeling program Materials Studio, in a series of Grand Canonical Monte Carlo (GCMC) simulations, which studies the interactions between the atoms through the method of the force fields and through the Monte Carlo method.
Sorption provides a solution for the prediction of molecular adsorption in a adsorbent framework, with a three-dimensional periodic structure, typically a microporous crystal as a zeolite, or a surface like an oxide of a metal. [154] An advanced simulation is combined with sophisticated modeling tools of the structure; These allow you to:

- predict adsorption isotherms;
- model the effects of structural changes, ion exchange, differing charge distributions and substitutional disorder on sorbing properties;
- study the behavior of pure components and mixtures in molecular sieves;
- quantify the effects of temperature and pressure of the system;

- understand the fundamentals of the mechanism of adsorption on the atomic level, identifying the preferential adsorption sites;
- interpret results through graphical representations and analysis;

The knowledge of these fundamental properties is often essential for the description of the many problems of industrial interest. For example, the adsorption isotherms are necessary to describe the diffusion of molecules through the membranes, even if the experimental data are often deficient. Moreover, the results obtained by molecular modeling may allow a better understanding of data is not easily available through experiment. Sorption offers four different ways to simulate the adsorption equilibrium:

- *Fixed loading* : determines the preferential binding site and determines the energy for a fixed number of molecules absorbed;
- *Fixed pressure*: provides the amount of adsorption at a given pressure;
- *Henry constant*: calculates the load limit, with the pressure that tends to zero;
- *Adsorption Isotherm*: involves the amount of adsorption in a pressure range at constant temperature;

For this study, we used the last procedure.

3.2.2 Amorphous Cell

Amorphous Cell [223] is a package of the graphic modeling program Materials Studio and it's a comprehensive set of model construction, simulation, and analysis tools for predicting properties of amorphous systems.
The behavior of amorphous materials is critical to products such as plastics, glasses, foods, and chemicals. Researchers studying amorphous polymers, for example, seek to optimize their mechanical behavior, the transport of molecules through the system, and their surface and interface interactions.
These properties impact the polymer's performance in applications such as separation processes, packaging, and drug delivery.
Amorphous Cell is a suite of computational tools that allow to construct representative models of complex amorphous systems and predict key properties. Observing the relation between system structure and properties, a more thorough understanding of the important molecular features can be obtain, allowing for a better design of new compounds or new formulations.
The methodology of Amorphous Cell construction is based on an extension of well established methods for generating bulk disordered systems containing chain molecules in realistic equilibrium conformations. [161]
Other features include provision for construction of arbitrary mixture systems containing any combination of small molecules and polymers, in addition to special capabilities for producing ordered nematic mesophases and slabs of amorphous material suitable for use in creating models of interphases and confined fluids, as would be required to study adhesion, lubrication, and shear viscosity.
Simulation parameters can set, including system composition and density, and Amorphous Cell constructs a periodic model of the system.
The program interfaces with the Discover simulation product to perform structure minimization and further extend the range of available simulation and analysis options.
The main features of this software are:

- Model construction using a modified Markov process [162] with bond conformational probabilities chosen to account for both intramolecular and intermolecular non-bonded interactions
- Optional energy minimization of the bulk model
- Molecular dynamics simulations at constant temperature and density, or under other commonly encountered conditions such as constant temperature and pressure, to yield predictions of PVT relations
- Flexible protocols for applying complex simulation strategies, including:
  - Confined shear simulation for study of lubrication and viscosity. [163]
  - Poling to study electric polarization and dielectric behavior.
  - Temperature cycling protocol for studying response to heating and cooling cycles.
  - Hybrid Monte Carlo alternative to traditional molecular dynamics simulation. [164]
- Powerful analysis tools to examine many properties of the resulting structures, including:
  - Cohesive energy density/solubility parameter. [165]
  - All aspects of molecular/chain geometry (either global, or localized within specified. chemical groupings) over a dynamics trajectory chain.
  - Configurational statistics for properties such a end-to-end distances and radii of gyration.
  - X-ray or neutron scattering curves.
  - Atom-atom pair correlation functions. [166]
  - Gas/small molecule diffusivities (via mean-square atom displacements or velocity autocorrelation functions).
  - Infrared spectra and dipole correlation functions.
  - Elastic stiffness coefficients. [167]
  - Surface properties.

In this study this package was used to present models of polymers, initially assembled with the software "Polymatic", aggregates in a periodic system with the final density required.
In later chapter, these costructed models are used to reproduce the porous characteristics of the experimental material.
In this way the adsorption of various gases inside them was simulated and their performance were studied.

3.2.3 Polymatic

Polymatic is a generalized structure generation methodology for amorphous polymers by a simulated polymerization technique. The capabilities of the methods are examinated through application to six linear, glassy polymers ranging in functionally, polarity and rigidity.
Validation of the methodology is provided by comparison of the simulations and experiments for a variety of structural, adsoprtion and thermal properties, all of which showed excellent agreement with available experimental data.

The first task for simulations is obtaining an initial structure of the system. For well-ordered and crystalline materials, on the one hand, reference structures can be obtained in a rather straighforward manner by methods such as X-ray crystallography.
For amorphous materials, on the other hand, this is a non-trivial problem, requiring generation of an ensemble of structures that provide the proper statistical description of material properties of interest. [174]
The main software benefits are:

- the algorithm can be applied in nearly the same fashion to polymers of any connectivity, whether they are linear or networked.
- it alleviates many of the steric hindrance issues often experienced for bulky and rigid structures.
- make qualitative conclusions about important processing parameters as the approach can mimic, to some extent, the synthetic route.

Therefore, multistep processes can be examined, such as the generation of crosslinked polymers by first forming linear polymer chains followed by a second reaction to form crosslinks.

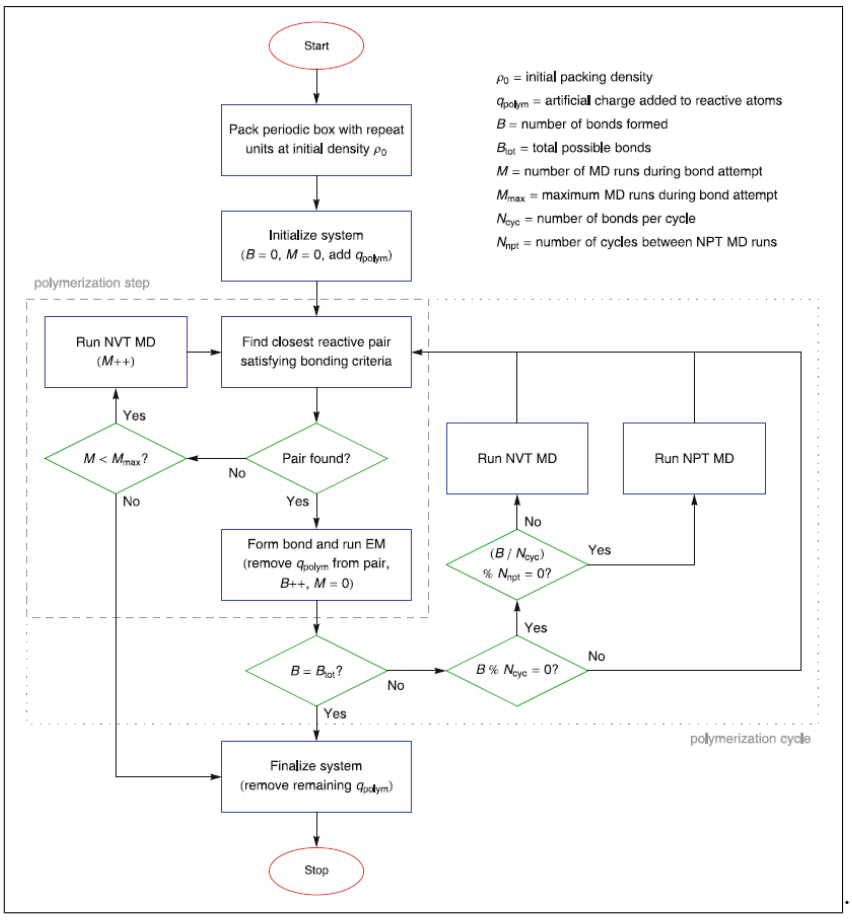

Figure 3.2: Flowchart of the Polymatic simulated polymerization algorithm. The start and stop steps are displayed in ovals, processing steps in rectangles, and conditional steps in diamonds. A polymerization step is enclosed in a dashed box, while a polymerization cycle is outlined in a dotted box.

Other possibilities include polymerization in confined spaces, or around fillers as in nanocomposites or mixed matrix membranes. These examples illustrate the flexibility possible with simulated polymerization methods.
Abbott et al., [171] focused on the development of a generalized simulated polymerization algorithm that can be implemented for many amorphous polymers.
The algorithm is based on initial work performed on a hypercrosslinked polymer, but has been updated and extended for use with a variety of other systems.
The basic structure of the simulated polymerization algorithm is as follows:

1. Initial structures are obtained by a random packing of repeat units into a box under periodic boundary conditions at an initial density, *q0*. The chemical structures of the repeat units are defined in the way they would exist in the polymer with reactive atoms identified as those to be bonded during polymerization steps. The system is initialized for polymerization, such as by the optional addition of artificial charges, q_{polym}, on reactive atoms.

2. A polymerization step is performed:
   - The pair of reactive atoms closest in proximity that meets all bonding criteria is selected.
   - A bond is formed between the atoms such that the proper polymeric structure is obtained, and an energy minimization is performed to relax the newly formed bond. If artificial charges were added, they are removed from the bonded pair at this time.
   - If no pair meeting all bonding criteria is found, a molecular dynamics simulation is performed and a polymerization step attempted again. This is repeated up to M_{max} times until a bond is accepted.

3. N_{cyc} polymerization steps are performed according to step 2 to compose one cycle. At the end of the cycle, a short molecular dynamics step (NVT or NPT) is carried out to relax any remaining stresses in the system, as well as to allow structural rearrangement of the configuration. Multiple equilibration types can be defined and alternated throughout the process, such as by running NVT steps with the inclusion of an NPT step every N_{npt} cycles.

4. Cycles of polymerization steps are successively repeated until B_{tot} bonds are formed or until no pair meeting the bonding criteria is identified within the M_{max} molecular dynamics simulations.

Several criteria can be set to determine if a bond is added between a reactive pair. Since the chemical reactions are not directly considered in these classical simulations, bonding criteria are imposed to prevent unreasonable or unrealistic structural configurations and high levels of stress upon bond formation, which are unlikely to be adequately relaxed during energy minimization and molecular dynamics simulations.
These are applied in a way to ensure that the simulated reactions n these types of approaches result in reasonable structures. Several examples of bonding criteria are implemented in the code.
The first is a cutoff radius, r_{cutoff}, which defines the maximum distance two reactive atoms can be from one another to allow bond formation.
These distances are typically set between 4 and 10 Å, [169–171] but are sometimes increased up to larger values near the end of polymerization to allow for a greater completion. [172,173]

Care must be taken when choosing large cutoffs to prevent the formation of unreasonable bond lengths that would not be properly minimized. Another bonding criterion is imposed to prevent intramolecular bonds during formation of linear polymers. Without this restriction, the construction of networked and looped structures is allowed.
In order to maintain a relaxed structure throughout the simulated polymerization, energy minimization and molecular dynamics steps are included. While energy minimizations provide initial relaxation of the newly formed bond, molecular dynamics offers a more thorough relaxation (and possible compression/decompression) of the structure to minimize any large stresses introduced by bond formations, as well as to allow fluctuations of the structural configuration.
The types of relaxations implemented in approaches in the literature vary greatly in frequency, length, and ensemble/conditions. In the provided code, an energy minimization is carried out after every bond formation to immediately reduce the stretched bond to an appropriate length.
In this work, starting from suitable monomers, polymers were obtained with high degree of crosslinked, recreating the experimental synthesis conditions.
The results of the polymerization process will be shown in later chapters.
The polymer was then added into Amorphous Cell, the package of Materials Studio that allow you to rearrange the structure in the space making it regularly, as it can be appreciated in the next section. This step is the connection link between the theoretical polymer and the experimental one. In fact, the resulting periodic structure affects the density of the material, of which the value is known for the experimental material.
Therefore it is possible to set the parameters of the modeling to obtain a polymer with a density comparable to experimental material. By doing so, it is given an index that allow us to understand how far from the target we are.

4 Computational details and results: PAFs

4.1 Introduction

In the previous chapters the synthesis and characterization of various materials were discussed, especially for the Porous Aromatic Frameworks (PAFs).
These polymers show a good chemical and thermal stability, with a pore distribution characterized by a predominant microporosity.
It is well established that CH_4, H_2 and CO_2 as well as N_2 and Ar, fill the microporosity at low pressure. Gas sorption is a very important part of the physical characterization for insoluble porous polymer networks and it gives an indication of the applicability of the materials for different fields such as energy applications (e.g. on-board storage of H_2 and CH_4 for transportation technologies) or for environmental purposes (e.g. carbon dioxide capture).
The storage of these three gases normally requires materials with high surface area and high pore volume, which has to be microporous.
The micropores are important for the gas storage due to the overlap of the potential fields from both sides of the pore walls. They are characterized by higher affinity towards gases and thus higher uptake capacity comparing to pores with larger diameter. [185]
As a consequence, it has been demonstrated that there is a reliable correlation between gas adsorption capacities and the porous texture of porous materials: CO_2 and H_2 storage requires narrow micropore volume ($\leq$ 7 Å), [159] while for CH_4, micropores with a pore size around 11 Å are more relevant. [63, 186]
In general, a good correlation of the total micropore volume, including both the ultramicroporosity (size lower than 0.7 nm) and supermicroporosity (size between 0.7-2.0 nm) [187] product useful materials for different pressure ranges.
The suitability of an adsorbent for gas storage application can be evaluated from two different points of view:

- based on its capacity on a gravimetric basis (adsorption per gram of adsorbent), where textural properties (surface area, porosity and pore size distribution) are the main parameters that control the adsorption. [188–190]
- depending on its capacity per liter of adsorbent (on a volumetric basis, the most suitable way to express the results from a storage application point of view), in which not only the textural properties but also the density can affect the gas uptake. [186, 191, 192]

Another important relationship between pore size and gas storage pressure should be taken in consideration: narrow pores are important to store gas at low pressures, since, when the pressure is low, it is necessary to have greater host-guest interactions between gas molecules and pore walls. On the other hand, in case of high pressures, pores with large diameter and high surface area and large pore volume become very important.
The capacity storage reported in this thesis is also supported by experimental data, which are the main subject of the work that the Dr.ssa Mina Errahali is doing in my own Department.
In this chapter, the comparison between experimental and computational results on the storage capacity of selected materials will be shown.
In particular, the aims of this PhD chapter is:

- Modeling the structures of the PAF-30n starting from the structure of the diamond with molecular building blocks CH_3-$(Ph)_n$-CH_3 (n= 1-4)
- Developing the force fields which best represent the guest-guest and host-guest interactions for the gases taken into account.
- Comparing the data found through the simulation of the isotherms within the PAF-30n with the free gas equation of the state.
- Comparing the CH_4, CO_2 and H_2 uptakes at different temperatures and pressures in the PAF-30n to evaluate the interaction between the framework and the adsorbed gases.
- Evaluating the pore distribution obtained from argon adsorption at 87 K and from nitrogen adsorption at 77 K of the PAFs materials to obtain a more reliable characterization of the microporsity of this material.
- Comparing the computational results, made on optimized structures, with those obtained from experimental measurements.

The gas uptake measurements have been performed by Dr. M. Thommes of the Quantachrome instruments, who measured the Argon physisorption along with methane and hydrogen uptakes at high pressure;

4.2 Initial Structure

In this study the ability of PAF-30n (n = 1-4) to adsorb various gases at different pressures and at temperatures ranging from 77 to 323 Kelvin will be explored.
The PAF-30n can be modeled starting from the structure of the diamond and replacing each C-C covalent bond with one or more phenyl groups.

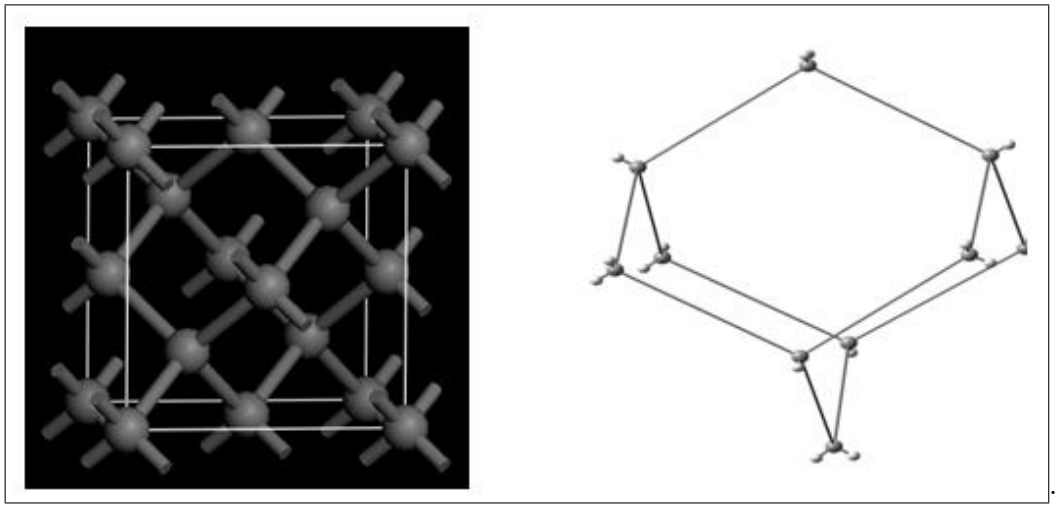

Figure 4.1: Diamond shape of the sp_3 carbon forming the structure.

The resulting solids retain the three-dimensional geometry, although decrease the local symmetry of the group P1, and increases considerably the empty space inside the skeleton aromatic in which is formed a network of micro or mesopores.
The unit cell, from which successively all the PAF-30n are constructed, is, geometrically, very

complicated, but can be shown, with a good approximation, considering the structure formed by a octahedron and four distorted tetrahedra.

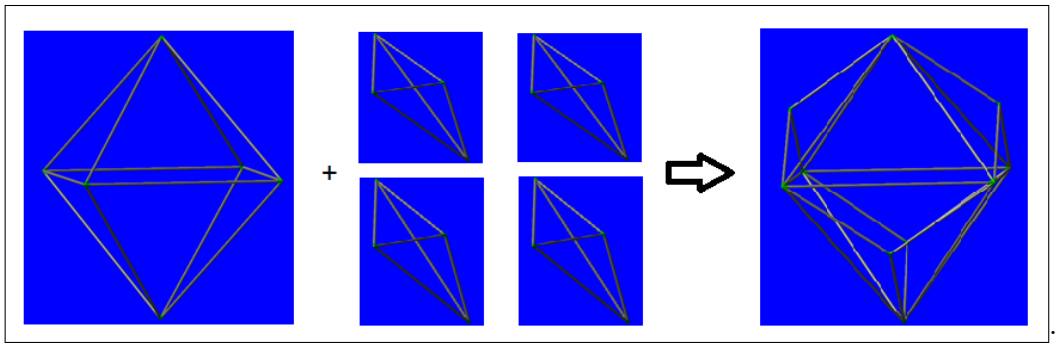

Figure 4.2: Unit cell geometry of PAF-30n.

Once created the elementary cells, the periodic structure of the model has been built up:

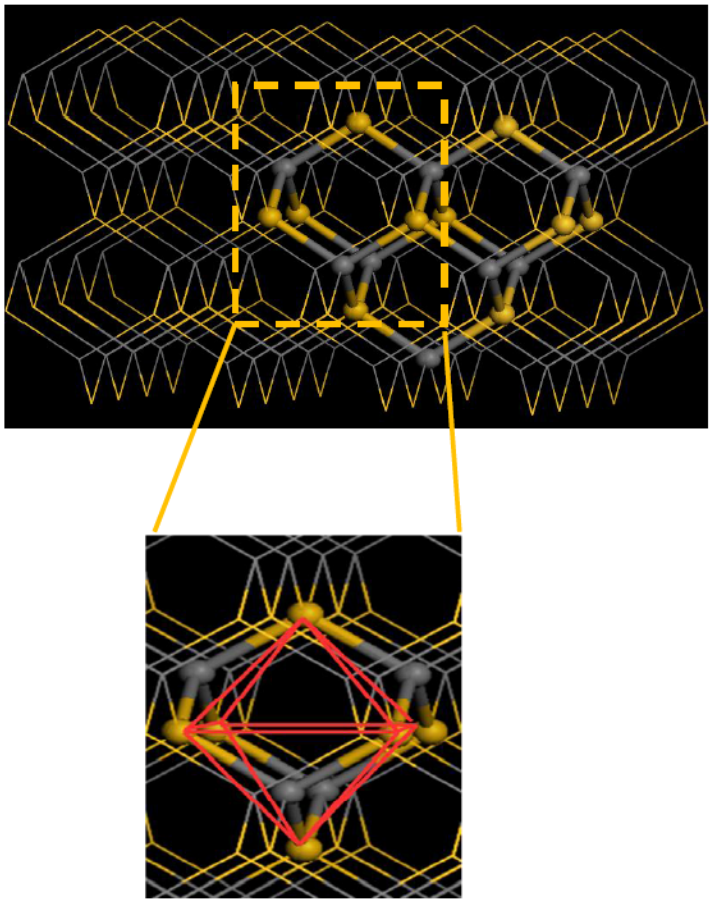

Figure 4.3: Periodic structure resulting to Figure 4.2.

The CIF file that has subsequently originated the structures of the PAF-30n has been so modified: the P1 symmetry was fixed and the distance between two carbon atoms found through the ab initio calculations was exactly the distance between the methyl groups of the optimized molecules.

4.3 The computational method

The first step to tackle the study of PAF was to choose the most appropriate method of calculation to obtain the best optimization of their structure and this happens, first of all, by optimizing the geometry of the dimethyl-diphenyl. Subsequently, it relates, for each functional, the value of the dihedral angle formed between two phenyl with the experimental value. [168]

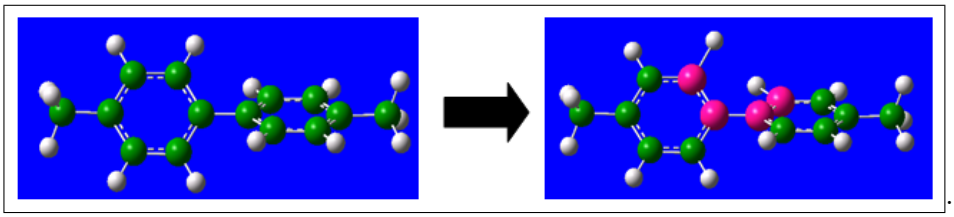

Figure 4.4: Dihedral angle calculated by different calculation methods.

Method Used	Angle
Experimental value	44.40^0
DFT-B3LYP	37.60^0
DFT-BLYP	36.21^0
DFT-PBE	35.26^0
DFT-PBE0	37.61^0
MP2	42.96^0
MOPAC	56.13^0

The pure functional BLYP and PBE and the hybrid functional B3LYP and PBE0 exploit the DFT method, MOPAC is a semi-empirical method, while MP2 is a post Hartree-Fock method.
The MP2 level is confirmed as the most reliable, and it was chosen for all the successive ab initio calculations, in agreement with previous modeling of polyaromatic frameworks. [21,131]
To check the stability of results, the MP2 optimization of 4,4-dimethylbiphenyl was repeated with a larger basis set, namely, 6-311+G(2d,2p), including the counterpoise correction of the Basis Set Superposition Error (BSSE) [175] with the Gaussian 09 program, [176] with negligible variations of the geometrical parameters. The gas molecules were also optimized at the MP2/6-311+G(2d,2p) level.
Generally, MP2 is considered more reliable than various DFT methods, although occasionally, with a clear choice of functional basis, the results of the latter can be more reliable, but DFT methods fail to properly describe the properties of some specific systems.
In fact, the systematic overestimation of the electron delocalization in planar conjugated systems and the systematic underestimation of the Van der Waals interactions are the two factors that probably had a negative impact on our study.

4.4 PAF-30n(1-4) structures

The polyphenyl fragments optimized were inserted between each pair of neighboring C-C, using the graphical interface GaussView.
The fragments were rigidly rotated to delete all contacts between hydrogen atoms.

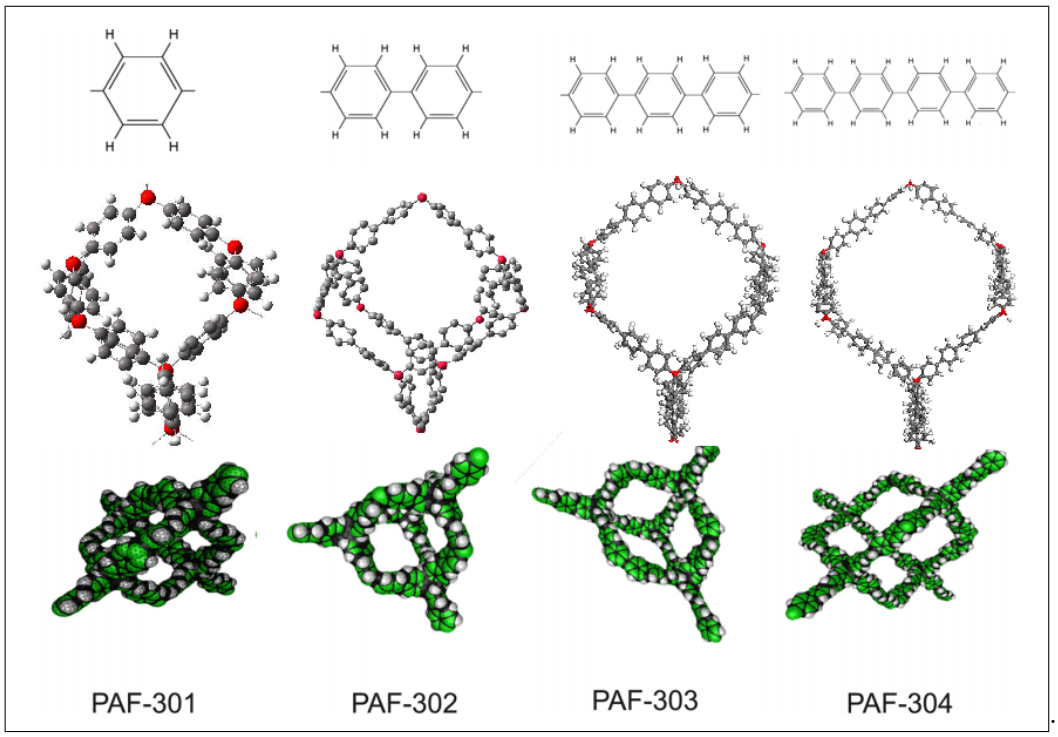

Figure 4.5 Top to bottom: aromatic building block, tridimensional structure of the unit cell, and skeletal volume defined as a collection of atomic spheres by the GEPOL procedure for the PAF-30n, n = 1-4.

4.4.1 Structural and Textural Properties

	unit cell formula	unit cell volume (Å^3)	density (g cm^{-3})	specific volume (cm^3 g^{-1})	unit cell skeletal volume (Å^3)	porous volume fraction	specific porous volume (cm^3 g^{-1})	specific surface area (m^2 g^{-1})
PAF-301	$C_{104}H_{64}$	2614	0.835	1.20	1306	0.50	0.60	5227
PAF-302	$C_{200}H_{128}$	13300	0.316	3.16	2475	0.81	2.58	5550
PAF-303	$C_{296}H_{192}$	37189	0.167	5.99	3679	0.90	5.39	5626
PAF-304	$C_{392}H_{256}$	81284	0.101	9.90	4861	0.94	9.31	5692

Table 1: The structural properties of the PAF-30n models

The skeletal volume and the effective surface area were estimated by the GEPOL procedure implemented in G09, which is used in another context to define the solute-solvent boundary in polarizable continuum models.
Increasing the number of aromatic rings, the PAF density decreases: the values reported in Table 1 are referred to ideal crystalline materials, and can be used as a benchmark to evaluate the degree of crystallization in actual synthesis.
The porous fraction grows markedly along the series.

Ben et al. have modeled the first three members of the series and synthesized PAF-302 [131] and they predicted very similar porous volume fractions (0.41, 0.78, and 0.88 for PAF-301, 302 and 303, respectively).
They also simulated the adsorption of N_2, to estimate the BET surface area of PAF-301 and 302, and found 1880 and 5640 m^2/g, respectively. The latter value agrees very well with the GEPOL result reported in Table 1, while for PAF-301, the two approaches provide very different values: this is probably due to the small size of the PAF-301 pores, which does not allow the formation of N_2 monolayers.
One can observe that GEPOL specific surface areas grows very slowly along the series: in fact, both the unit cell surface area and molecular weight grow almost linearly when a new phenyl ring is added to the aromatic chains and the two effects balance in the definition of specific areas.

4.5 Lennard-Jones potential and standard forcefield

Once identified the quantum method best describing the properties of interest, the suitable force field (FF) was searched.
For the guest-guest interactions, the benchmark is the equation of state of the gas taken into account. [160, 177]
On the contrary, the interactions between gases and the porous framework atoms, i.e., hydrogen, aromatic sp^2 and sp^3 carbon atoms, were evaluated and the classical energies provided by the different FF were compared with MP2/6-311+G(2d,2p) results, including the counterpoise correction for the basis set superposition error (BSSE), for gas-benzene and gas-diphenyl methane couples: the energy was scanned with the intermolecular distance, keeping the geometry of the fragments fixed, with several orientations.
In many cases the standard forcefields inside Materials Studio software present a low affinity with the state equation of the considered gas and with the MP2 level which was decided to use as benchmark.
So, for the various gases below described, we have changed Lennard - Jones σ and ϵ parameters, described in the previous chapter, to simulate as well as possible the interactions within the real matrix.

4.6 Fugacity coefficients

The key quantity in GCMC simulations is the chemical potential, depending on temperature and fugacity. To compare GCMC results with experimental measures, one has to convert fugacities into pressures, in the entire pressure range of interest.
The distinction between fugacities and pressures, sometimes neglected in the literature on simulated adsorptions, is particularly important when high pressures are reached as in the present case.
For the all gases studied, we computed the gas fugacity coefficients $\Phi(P,T)$ at the desired conditions through the formula:

$$\Phi(P,T) = \int_O^P \frac{Z(P',T)-1}{P'} dP' \tag{4.1}$$

where Z is the compression factor, obtained from the experimental molar volumes at the temperature established for the measurement.

The data at the various temperatures and pressures were taken from ref. [160] and based on the equation of state reported in ref. [178].

4.7 Gas uptake capacity

The isotherms describe the absolute adsorption, i.e., the density of the gas that would be stored in a container filled by the adsorbent. The storage capacity is often discussed, especially in the experimental literature, in terms of other, strictly related quantities: the excess and the effective adsorption.
The former is the difference between the absolute adsorption and the amount of gas that would occupy a volume equal to the porous volume of the material at the same pressure and temperature (thus expressing the excess gas that is adsorbed due to the gas/adsorbent interactions); the latter is the difference between the absolute adsorption and the quantity of gas that could be stored in the same container without the adsorbent.
Thus, with $n_{ads} = n$(T, P) the density of the gas adsorbed in PAF-30n, $\rho_{free} = \rho$(EOS, T, P) the density of the free gas and f_{pore} the material porous fraction, the effective adsorption is:

$$n_{eff} = n_{ads} - \rho_{free} \tag{4.2}$$

and the excess adsorption is:

$$n_{exc} = n_{ads} - f_{pore} \cdot \rho_{free} \tag{4.3}$$

N_{eff} could also be negative, if the use of the adsorbent actually lowered the storage with respect to the compressed free gas, due to the large material skeletal volume. While the absolute adsorption capacity for a type I isotherm reaches the saturation value at high pressures and then remains constant, the excess and the effective adsorption isotherms don't possess a plateau at high pressure but a maximum and with further increase of hydrogen pressure the excess uptake decreases. This occurs because the gas saturates the pores but at the same time the external gas density is further increasing. The excess adsorption is zero when the gas density and the adsorbed density are equal.

4.8 Isosteric Heat

The ability of a material as gas adsorber depends on the interactions that are established between the gaseous molecules and the material surface, mainly inside the pores. Such ability is effectively measured by the adsorption enthalpy change, also called isosteric heat of adsorption (Q_{st}), which can be obtained through the Clausius-Clapeyron equation at different gas uptakes:

$$Q_{st} = -\Delta \bar{H}_{ads} = -R \left(\frac{\partial \ln f}{\partial (1/T)} \right)_{n_{exc}} \tag{4.4}$$

where n_{exc} is the excess adsorbed density and f is the fugacity of the free gas in equilibrium with n_{exc}. It is worthy to note that excess isotherms indicate the quantity of gas that is adsorbed as a consequence of gas-surface interactions, thus exceeding the gas that would be stored inside the pores if no interactions were present, and this is directly related to Q_{st}.
In practice, the simulations were repeated at 273, 298 and 323 K for various gases; at different temperatures, different values of free gas fugacities were needed to obtain the same n_{exc}.
Then Q_{st} was computed as the slope of the line fitting the values of ln(f) versus 1/T, for each selected value of n_{exc}.

4.9 Pore Size Analysis

N_2 and Ar physisorption measurements were carried out at 77 K and 87 K, respectively, in the relative pressure range from 1 x 10^{-6} to 1 P/P_0 and to choose the best pore model for PAF-302 materials, all kernels implemented in ASiQWin Quantachrome software were applied.
The most widely used procedure to describe pore distributions are modern microscopic methods based on statistical mechanics such as density functional theory (DFT). [46]
Applying the DFT approach allows calculating the equilibration density profile for all locations in the pore. The equilibrium density profiles are obtained by minimizing a free-energy functional, which is the grand potential or grand free energy for a pore system in equilibrium with a bulk phase (i.e. the situation when an adsorption experiment is performed).
This free-energy potential consists also of terms that describe the attractive and repulsive parts of the fluid-fluid and fluid-wall interactions. Difficulties are associated with a proper description of fluid-fluid interactions and different DFT-approaches were suggested during the last decade, as for instance the so-called Local Density Functional Theory (LDFT) and the Non-Local Density Functional Theory (NLDFT).
The LDFT approach is often used, but is not able to produce the strong oscillation characteristics of a fluid density profile at a solid fluid interface, which leads, in particular for narrow micropores pores, to an inaccurate description of the sorption isotherms, and correspondingly to an inaccurate pore size analysis.
In contrast, the Non-Local Density Functional Theory and the Monte Carlo Computers simulation techniques provide a more accurate structure of a fluid confined to narrow pores.
The application of methods based on NLDFT allows one to describe the adsorption and phase behavior of fluids in pores at a molecular level to obtain an accurate pore size distribution over the complete micro/mesopore range. [213] Recently, a novel approach has been suggested to account for the effect of roughness of porous surfaces, the so-called quenched solid density functional theory (QSDFT), which considers quantitatively the surface geometrical inhomogeneity in terms of a roughness parameter. [214]
The new QSDFT method leads to a significant improvement in the accuracy of DFT pore size distribution analyses of disordered carbon materials from low temperature nitrogen adsorption isotherms.
In contrast to the previous NLDFT models that assumed flat, structureless graphitic pore walls, the QSDFT method takes explicitly into account the effects of surface roughness and heterogeneity. [216]
These DFT methods are currently widely used for the interpretation of experimental data, and the pore size distribution (PSD) calculation from adsorption isotherms is now featured in a recent standard by the International Standard Organization ISO (ISO-15901-3 2007).
For these two gases, which are generally used for the determination of the porosimetry, the method with the lowest fitting error is considered, taking into account the Applicable Pore Diameter Range. [215]
Obviously the porosimetry comparison between the simulated and experimental isotherm within the material was accomplished with the same calculation model.
As an example, we present in figure 4.6 the kernels applied to the material PAF-302: the figure shows pore distributions obtained on different surfaces (carbonaceous or zeolite / silica) and different geometries.
In the inset of the figure 4.6 the relative percentages of fitting error are also reported, which indicates the percentages of deviation between the experimental isotherms and those calculated by the model used.

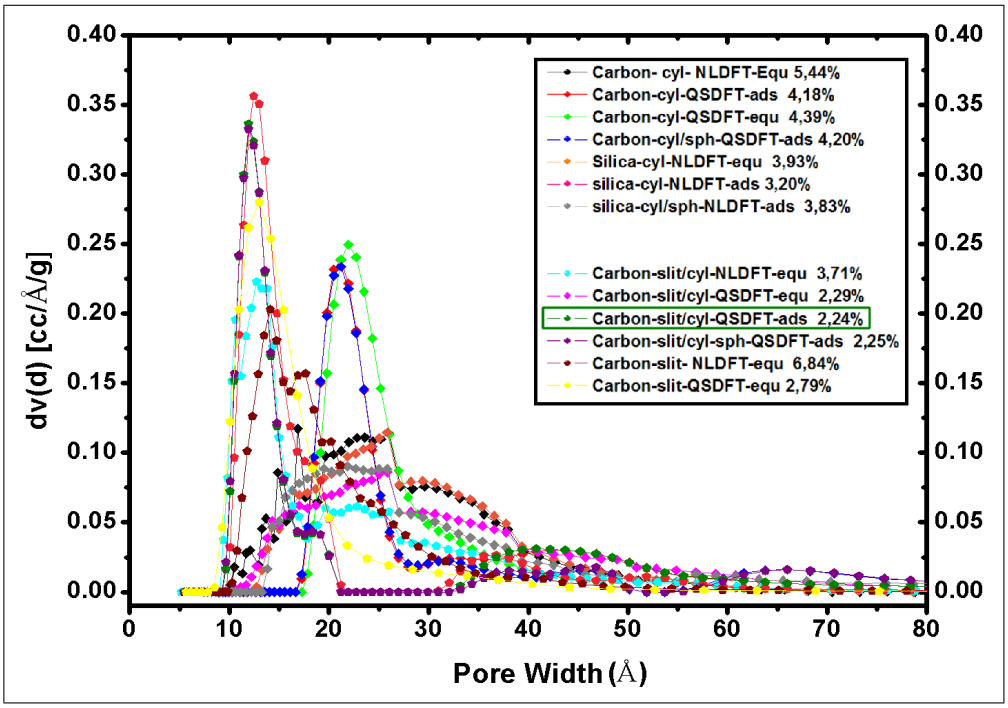

Figure 4.6: Experimental pore distributions obtained from N_2 adsorption isotherm at 77 K on PAF-302. NLDFT and QSDFT models were applied considering carbon and silica surface with different pore geometries. Inset shows the fitting error for each model

The comparison shows that the lowest fitting error (2.24 %) is given by using the model QSDFT applied on carbon and with hybrid slit/cylindrical geometry.

4.10 Simulated Adsorption Isotherms in PAF-30n

The computational adsorption isotherms of N_2, Ar, CH_4, H_2 and CO_2 were simulated with Monte Carlo technique and compared to the corresponding experimental isotherms.
Initially, the nitrogen and argon adsorption isotherms at 77 and 87 K will be shown, focusing in particular on PAF-302, the only member of the PAF-30n family actually synthesized so far.
The simulated isotherms and the experimental uptakes obtained by our physical-chemistry group of our department will be compared.
The difference of the adsorption densities of the considered materials led to the porosimetric determination of the structures.
Then, data on the methane adsorption will be presented. An extensive analysis of the behavior of isotherms within the considered materials was made, in addition to a vibrational study of PAF-302, the most promising material from the family of PAF-30n, to investigate the structure of the porous framework and interactions with adsorbed methane.
Afterwards the H_2 and the CO_2 isotherms have been simulated at different temperatures and at different pressures.
Finally, the CO_2 adsorption in a large group of functionalized PAF-302, varying the nature and the concentration of functional groups, will be investigated to suggest the best candidates for carbon dioxide capture and storage.

4.10.1 Nitrogen and Argon

N_2 physisorption measurements were performed at 77 K to investigate the porosity of PAF-30n structures and the density of gaseous nitrogen was computed at different pressures and at different temperatures, by simulating a formal adsorption in an empty box, and compared with the equation of state (EOS).
At first, at room temperature:

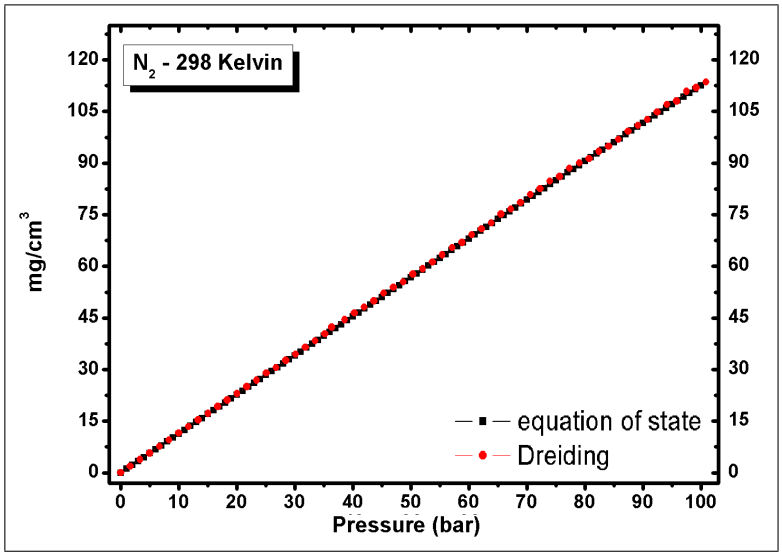

Figure 4.7: Density (mg/cm^3) of gaseous nitrogen computed at 298 K, compared to the EOS.

One can see how the simulated formal adsorption with the parameters of the standard Dreiding forcefield agrees well with the equation of state therefore the guest-guest parameters weren't modified.
The evidence is the comparison with other temperatures:

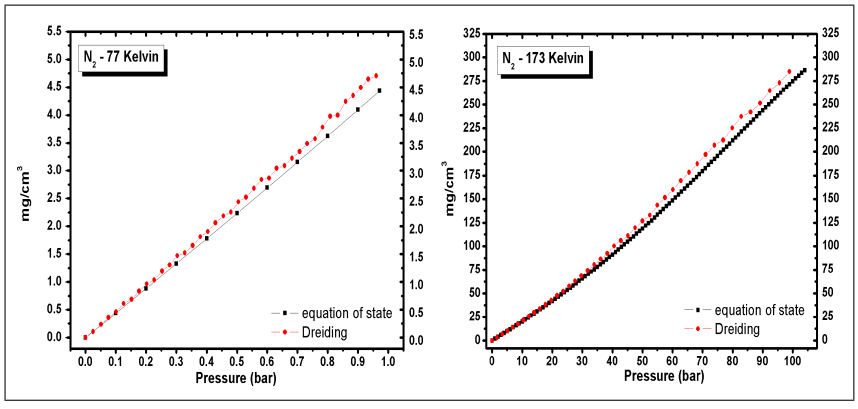

Figure 4.8: Density (mg/cm^3) of gaseous nitrogen computed at 77 K and at 173 K, compared to the EOS.

On the contrary, it was necessary to modify the parameters regarding the host-guest interactions.
Any energy interactions between nitrogen and PAF fragments are shown in Figure 4.9.

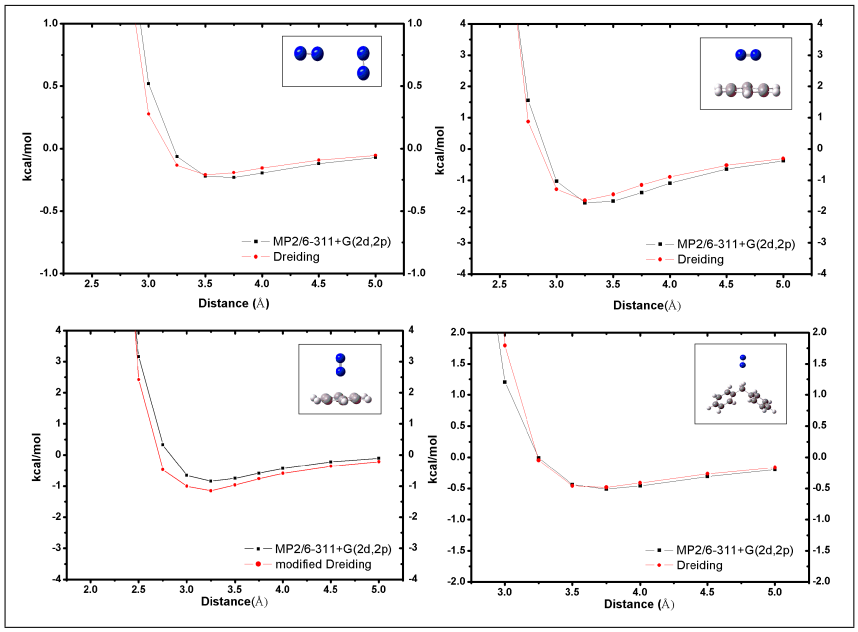

Figure 4.9: Interaction energy between methane and methane and benzene and diphenyl-methane molecules computed at MP2 level and with different FF.

The resulting forcefield has this modified parameter:

Atom Type	Dreiding Symbol	D (kcal/mol)	σ (Å)
Aromatic C sp^2	C_R	3.3983	0.1943

Table 2: FF parameter used in the modified nitrogen force field.

The other FF parameters are the same as in standard Dreding forcefield.
Initially the simulated nitrogen adsorption was compared with the isotherm in PAF-302 measured in our experimental group:

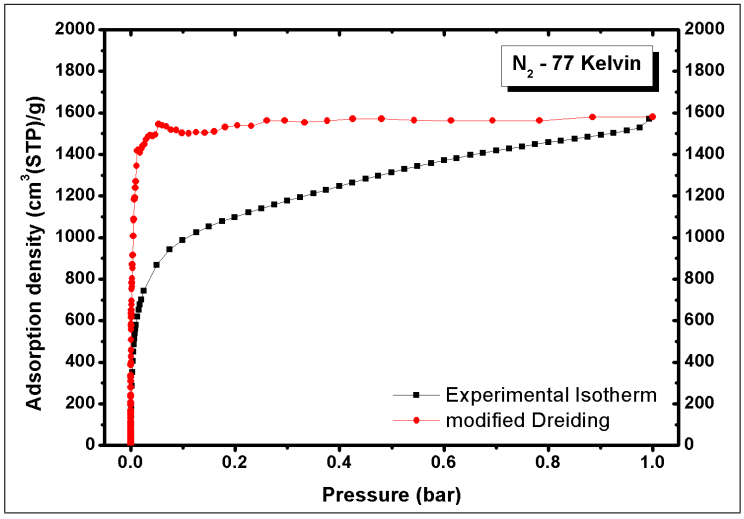

Figure 4.10: Experimental (black squares) and theoretical (red spheres) N_2 physisorption at 77 K on PAF-302.

Simulated and experimental isotherms are in agreement at very low pressures indicating a similar intensity of the host-guest interactions when the gas is preferentially adsorbed in the

smallest pores. The PAF-302 model has an idealized crystalline structure and such differences are likely due to the presence of defects in the real sample.

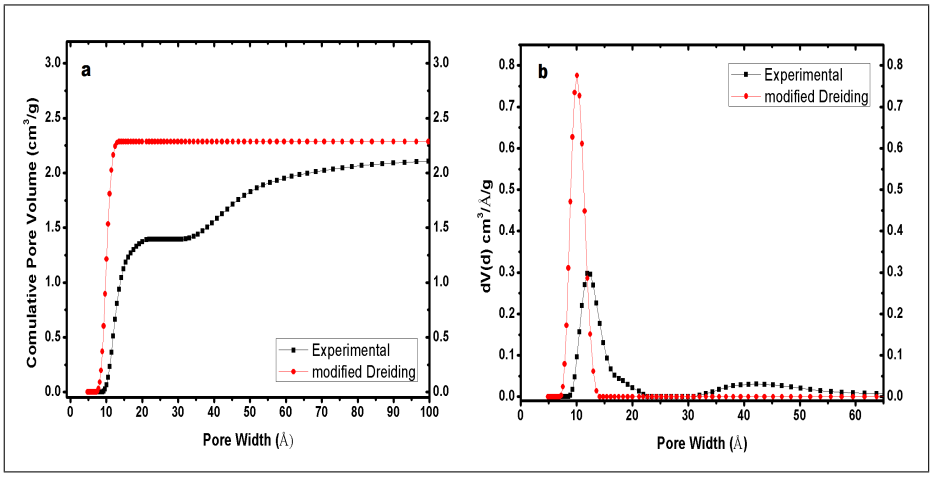

Figure 4.11: Experimental and simulated isotherm of Nitrogen at 77 K: Cumulative Pore Volume(a) and Pore Size Distribution(b)

The pore sizes were calculated using the quenched solid density function (QSDFT) applied on carbon surface with slit/cylindrical pore geometry. The model chosen is the one that gave the lower fitting error, as shown in section 4.9.
Looking at the pore size distribution (figure 4.11b), it can be seen that the theoretical curve (red spheres) presents mainly a single family of micropores at 10.7 Å, while the experimental curve (black stars) shows the main family of pores at 11.9 Å.
A comparison between the different distributions of pore in the PAF-30n models will be discussed using N_2 adsorption, suitable for mesoporous structures, which have PAF-303 and PAF-304. [227]
The FF chosen is the same described above for the comparison between experimental and theoretical PAF-302.

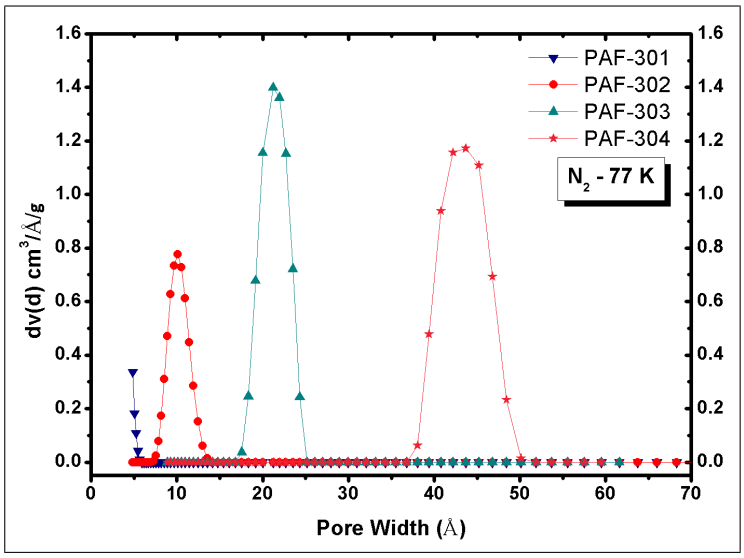

Figure 4.12: Comparison of PAF-30n pore size distribution: blue pentagon PAF-301, red circle PAF-302, light blue triangle PAF-303 and pink star PAF-304.

Figure 4.12 shows a good agreement with the pore size determined by Lan et al.. [21]
PAF-303 and PAF-304 have a substantially mesoporous structures. This property leads to a low gas - benzene interaction due to the high free volume.
On the contrary, PAF-301 presents only ultramicroporosity. This feature, related to the surface area, allows to provide good adsorption at low pressures, due to the high density of aromatic residues, even though it's the cause of the rapid saturation when the pressure increases.
PAF- 302 has a single family of pores centered in the microporous region and at first sight this material seems to have the best combination of surface and micropores.
It is well known that the use of nitrogen for the characterization of microporous materials has some drawbacks. Indeed, compared to nitrogen, argon adsorption may reveals a much more straightforward correlation between pore size and the pressure at which micropores are filled, because nitrogen is a diatomic molecule with a quadrupole moment while argon has no dipole or quadrupole moment and is much less interacting with the solid, allowing to provide a more accurate description of the porous structure of a material.
However, in order to obtain much more accurate data of pore distribution and to compare the pore size dsitribution resulting of two gases, Ar physisorption measurement at 87 K was carried out on four considered PAF, considering at first, like in the nitrogen discussion, the comparison between the experimental and theoretical PAF-302.
For Ar, we used an adapted version of PCFF force field [157] because the standard Dreiding force field hasn't implemented the van der Waals parameter as regard the argon atom.
Argon parameters were slightly modified to reproduce the free gas density at 87 K in the 0-1 bar pressure range and at 298 K in the 0-100 bar pressure range.

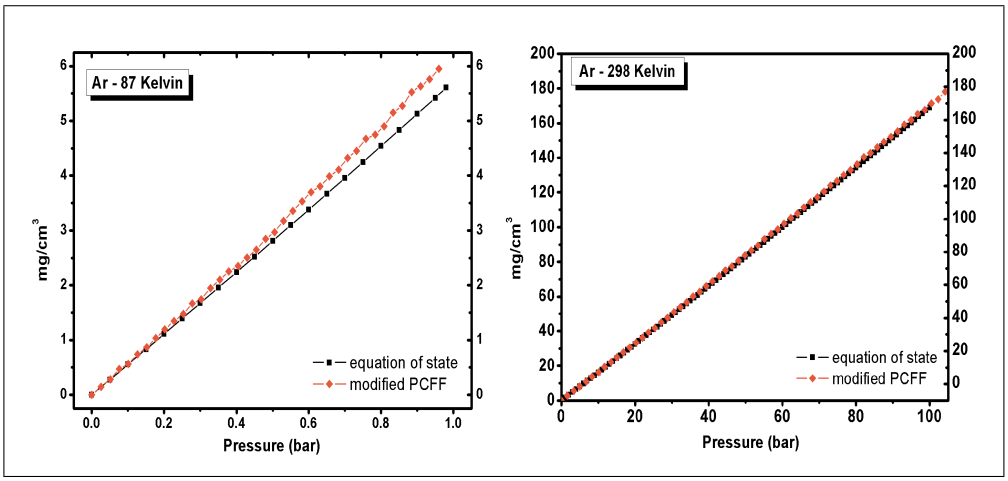

Figure 4.13: Density (mg/cm^3) of gaseous argon computed at different temperatures, compared to the EOS.

Afterwards, as in the case of the developed nitrogen force field described above, the parameters have been verified to provide a good agreement with high level quantum mechanical calculation, at MP2 level with 6-311+G(2d,2p) basis set, including counterpoise correction for BSSE, and then, the same calculation level was used to evaluate the interactions between argon and the porous framework atoms, as shown in Figure 4.14.

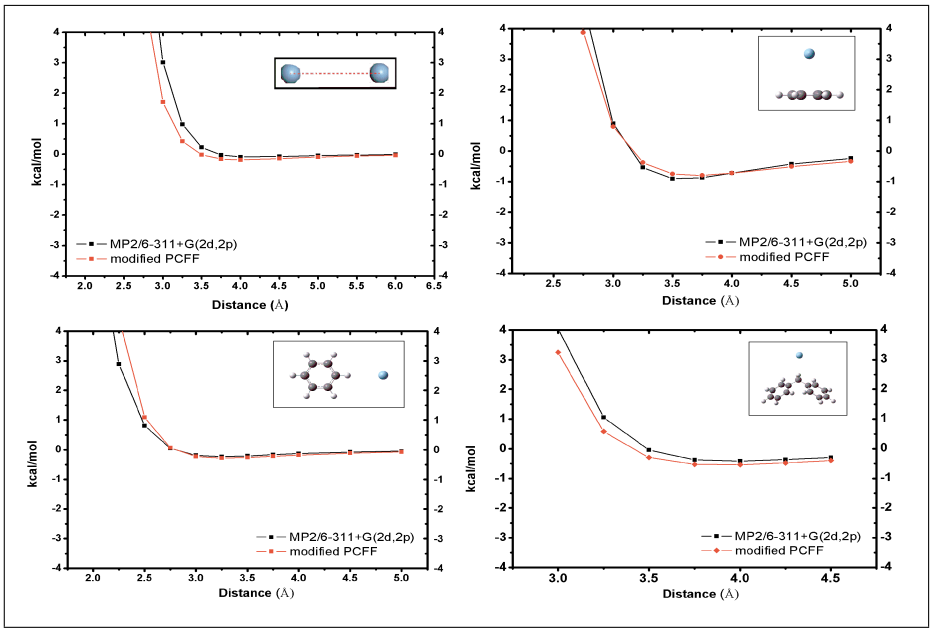

Figure 4.14: Interaction energy (kcal/mol) of Argon atom with aromatic residues in the indicated configurations.

The parameters of the final modified forcefield are:

Atom Type	Dreiding Symbol	D (kcal/mol)	σ (Å)
Argon	ar	3.98	0.1864
Aromatic C sp^2	cp	4.01	0.064

Table 3: FF parameters used in the modified argon force field.

The other FF parameters are the same as in standard PCFF and implemented for instance in Materials Studio package.
Initially the argon adsorption was simulated only in PAF-302 and the result was compared with the isotherm in PAF-302 measured in our experimental group:

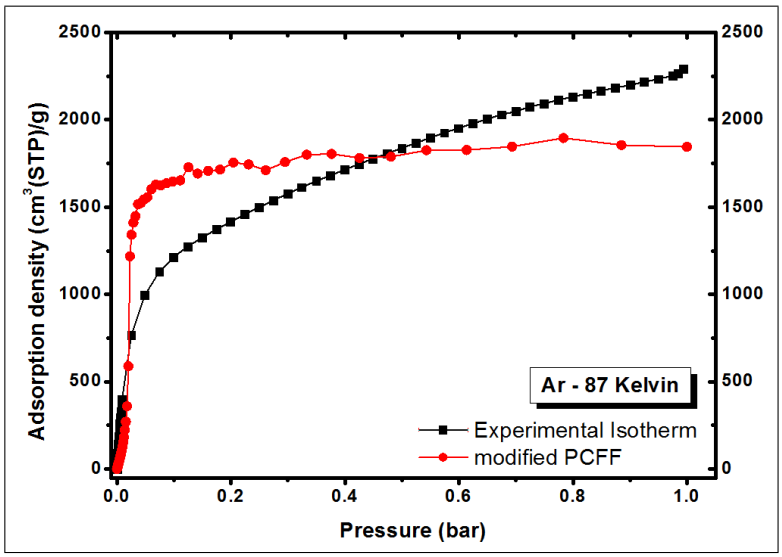

Figure 4.15: Experimental (black squares) and theoretical (red spheres) Ar physisorption at 87 K on PAF-302.

Applying the multipoint BET method in the range 0.049-0.2 P/P_0, the experimental specific surface area was 4563 m^2/g, a somehow lower value that reported by Ben et al.. [21]
The computational curve obtained on a perfectly crystalline system gives a value of 5500 m^2/g, and this suggests that the material synthesized in our lab has some defects in the framework, i.e. it is not perfectly crystallized.
The experimental curve also shows a Langmuir-type profile, however the saturation is reached much more progressively and only at P/P_0 close to 1. This is a clear indication that both micropores and mesopores are present in our material: indeed, the mesoporosity leads to a hysteresis loop in the desorption branch which closes only at very low pressures.
The calculated isotherm has a Langmuir profile with only micropores, as expected from the simulated structure model.
In Figure 4.16 the Cumulative Pore Volume and the Pore Size Distribution confirm the previous analysis.

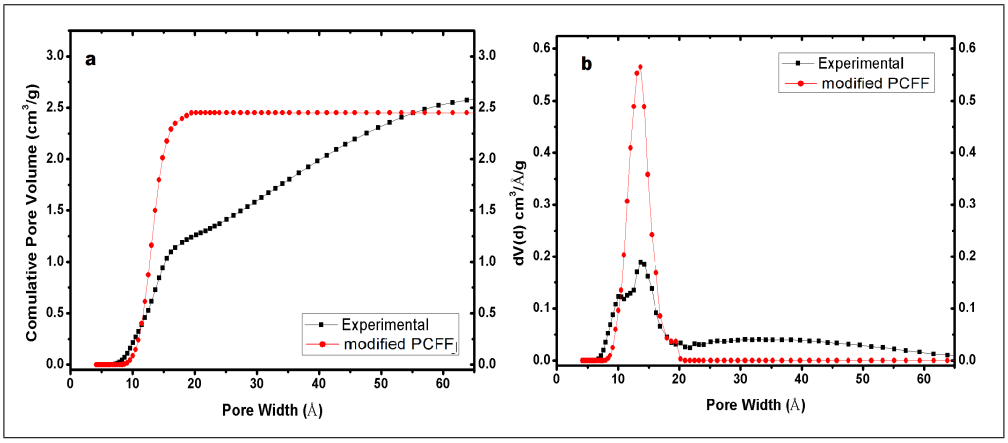

Figure 4.16: The results of Cumulative Pore Volume(a) and Pore Size Distribution(b) for the experimental and simulated isotherm of Argon at 87 K.

The pore sizes were calculated using the non-local density function (NLDFT) applied on zeolite / silica surface with cylindrical pore geometry. The model chosen is the one that gave the lower fitting error, i.e. 0.161% for the experimental sample and 0.155% for the theoretical one.
Looking at the pore size distribution (figure 4.16b), it can be seen that the theoretical curve (red spheres) presents mainly a single family of micropores at 13.6 Å, while the experimental curve (black stars) shows the main family of pores at 13.6 Å with a shoulder at 10 Å which represents 13% of the micropores (table 4).

Sample	SSA BET (m^2/g)	Total Pore volume (cc/g)	Micropore volume		
			<10Å	10<Å<20	Total
Exp. PAF-302	4562.87	2.89	0.16	1.1	1.26
Calc. PAF-302	5500	2.48	0.044	2.41	2.45

Table 4: Theoretical and experimental textural data obtained from Ar physisorption at 87 K.

The small difference in the pore size between calculated and experimental results is due to the fact that at the theoretical level an ideal structure is considered, while the synthesized material is characterized by a defective structure with two families of micropores and a small part of mesopores.
The experimental total pore volume is higher than the theoretical value, due to the presence of mesopores in the synthesized material, whose fraction is ca. 66% of the total volume, whereas in the ideal structure practically all empty space is due to micropores.
The same differences between the theoretical model and the experimental sample, found in the porosimetry of the PAF-302 through argon, are evident in the porosimetric study with nitrogen.
Comparison between the pore distribution obtained from nitrogen and argon adsorption isotherms at 77 and 87 K is interesting (figure 4.17).

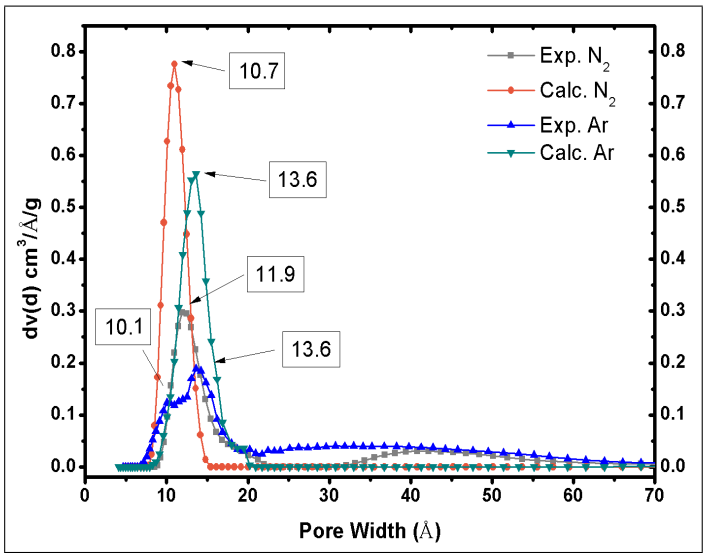

Figure 4.17: Pore distribution of PAF-302 from nitrogen (77 K) and argon (87 K) adsorption isotherms.

Indeed, analyzing the comparison between the two gas porosimetries, the size of the micropores is comparable between the theoretical model and the experimental one using the same gas.
The average families of pores, obtained by the two gases (10.7 Å and 11.9 Å for N_2 and from 10 Å to 13 Å for Ar) are very similar.
The comparison between the nitrogen and argon measurements showed the reliability of results from nitrogen physisorption in this case. This was expected since nitrogen measures reliably the supermicropores, as reported in literature. [46]
The exceptionally high surface area and pore volume combined with an excellent stability make PAF-302 a very attractive candidate for gas storage applications, particularly for CH_4, H_2 and CO_2 storage for on-board mobile applications.

4.10.2 Methane

Methane is used as a fuel in the form of compressed natural gas (CNG) and there is a strong need for efficient adsorbents for methane, [28,133] able to substantially increase the loading at high pressures, thus improving the capacity of the existing tanks, or to reduce the operating pressure at the same gas loading, in both cases with an important economic impact.

In this section, the ability of PAF-30n to adsorb methane was explored.
First of all, the density of gaseous methane at 298 K was computed at different pressures, by simulating a formal adsorption in an empty box, with different force fields, and compared with the equation of state (EOS).
As shown in Figure 4.18, the densities computed with all four standard FF deviate from the EOS at high pressures, though COMPASS performs better than CVFF, PCFF and Dreiding.

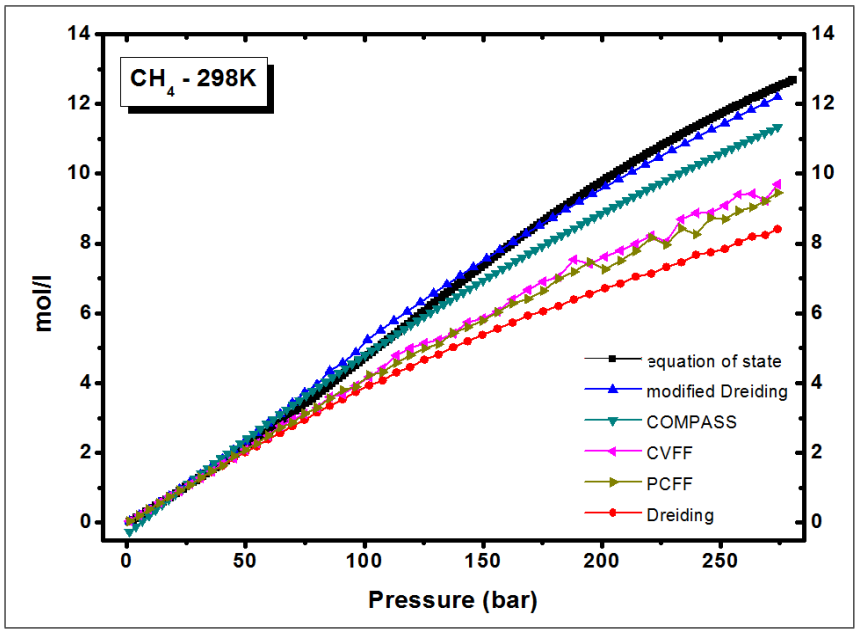

Figure 4.18: Density (mol/l) of gaseous methane computed with different force fields, compared to the EOS.

It has been decided to modify Dreiding in order to improve the agreement with the EOS because it is known that Dreiding forcefield has good coverage for organic molecoles, indeed it is often used to study the gas storage within a solid matrix [179, 180] and, moreover, it is freely available, user friendly and it can be used with other computational packages. However, the reliability of the new parameters about C_3 (sp carbon) and O_2 (oxigen) of the carbon dioxide was also confirmed by comparing the formal "adsorption" in a empty box with the equation of state at 273 Kelvin and 323 Kelvin.

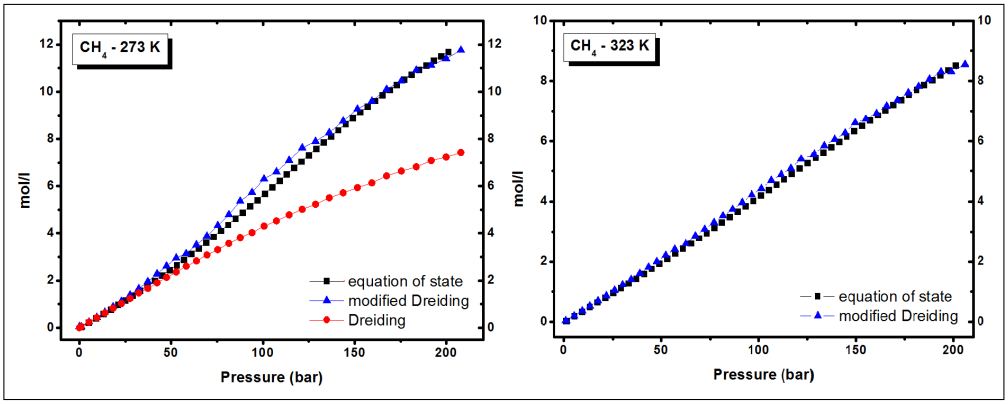

Figure 4.19: Density (mol/l) of gaseous methane computed at different temperatures, compared to the EOS.

Afterward, the parameters choosen to reproduce the free gas density have been verified to provide a good agreement with high level quantum mechanical calculation, at MP2 level with 6-311+G(2d,2p) basis set, including counterpoise correction for BSSE, as shown in Figure 4.20(a).
The same calculation level was used to evaluate the interactions between methane and the porous framework atoms, i.e., hydrogen, aromatic sp^2 and sp^3 carbon atoms, for CH_4-benzene and CH_4-diphenyl methane couples: the energy was scanned with respect to the intermolecular distance, keeping the geometry of the fragments fixed, with three orientations, with the results illustrated in Figure 4.20.

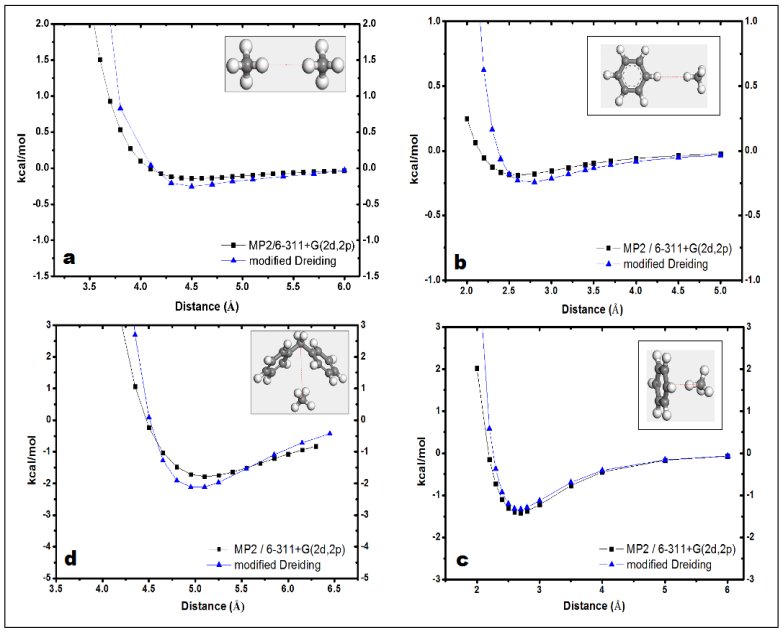

Figure 4.20: Interaction energies between methane-methane(a), methane-benzene, normal to the benzene ring plane (c) and aligned with benzene C-H (b), and methane-diphenyl-methane (d).

Therefore, the parameters of the final modified forcefield are the following:

Atom Type	Dreiding Symbol	D (kcal/mol)	σ (Å)
CH_4 carbon	C_3	3.8983	0.1451
Hydrogen	H_	3.195	0.0152
Aromatic C sp^2	C_R	3.3989	0.1449
Aromatic C sp^3	C_31	3.8983	0.0951

Table 5: FF parameters used in the modified force field.

The Lennard-Jones parameters used in the following calculations are collected in Table 2: the other FF parameters are the same as in standard Dreiding FF and implemented for instance in Materials Studio package. [154]
Other FF have been proposed recently to model the methane adsorption in porous materials: Wang [181] has modified some OPLS [182] parameters and used a single-site model for methane, with parameters taken from TraPPE FF, [183] to simulate the adsorption in MOFs, obtaining a generally good agreement with experimental data. Mendoza-Cortes et al. [184] followed a procedure similar to ours, fitting Lennard-Jones parameters to MP2 calculations to simulate the adsorption isotherms in COFs.

The density of methane adsorbed in crystalline PAF-30n and in equilibrium with the free gas at various pressures was evaluated with GCMC simulations, exploiting the modified Dreiding force field described above, and taking into account the fugacity coefficients obtained from the EOS.

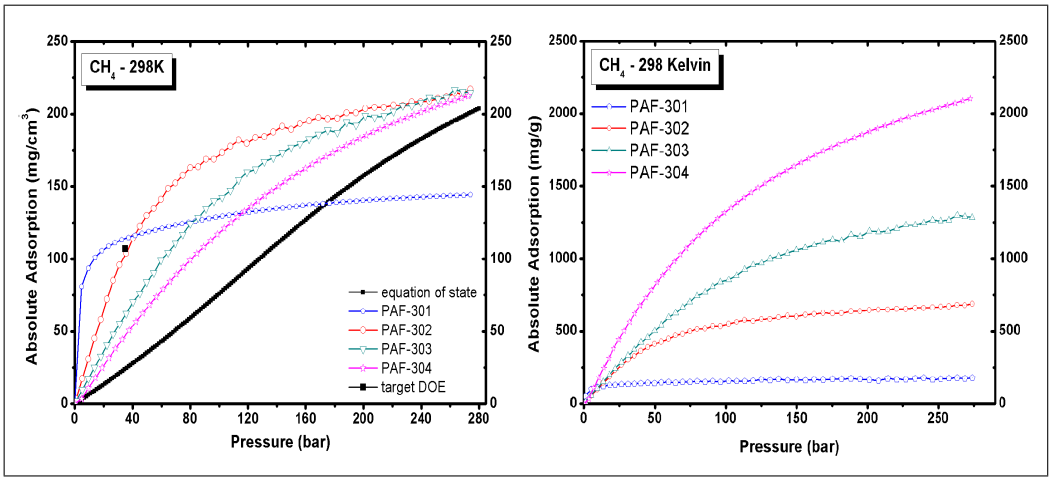

Figure 4.21: GCMC adsorption isotherms of methane in PAF-30n at 298 K. The adsorption densities are expressed in the volumetric and gravimetric terms. The density of free gaseous methane (from EOS) is shown for comparison. The black square indicates the storage target proposed by DOE at 35 bar, 298 K.

In figure 4.21, the simulated adsorption isotherms at 298 K are reported in volumetric and gravimetric densities for PAF-30n, n=1-4, along with the corresponding density of the free gas. The gravimetric values where reported because usually the gravimetric data are more common in the literature and easier to obtain but somehow misleading. The lighest materials are favored in comparison.
Volumetric uptakes are more directly comparable, as they depend on the actual porosity and specific surface area of the materials.
All the obtained volumetric data were compared with the density of free gaseous methane (from EOS) and with a single reference value, equal to 150 cm^3/cm^3 (107 mg/cm^3) at 35 bar; In fact, this is the current objective that the United States Department of Energy (US DOE) stands reaching for the adsorption of methane with ANG technology.
The literature and the same Department are somehow confusing about this target: the value was set in 1997 to 150 cm^3 (STP)/cm^3, [55] and updated from 180 to 263 in the years later, but recent analysis [56] showed that it may be difficult, if not impossible, to reach the last DOE targets for natural gas storage using nanoporous materials and the study suggests that those targets are unrealistically high.
For this reason the first value was taken into account to compare the mathane adsoprtion uptake.
This value was overcome by the PAF-301, which gave a value of 0.114 mg/cm^3 and the PAF-302 almost meets the target fixed by DOE with 103 mg/cm^3 at 35 bar of pressure.
Analysing the volumetric adsorptions for each individual materials:

- **PAF-301**: This material has a rapid adsorption within 20 bar and then a plateau up to 280 bar. This behavior is indicative of a material that quickly reaches saturation due to the small size of its pores; In fact, there are strong interactions between PAF-301 and methane already at low pressures. Subsequently, the curve doesn't change since

the material isn't capable of adsorbing more methane, indeed, even around 170 bar, it shows a worst performance than free methane density.
However, the high initial adsorption, between 0 and 1 bar, appears to be very attractive and will be studied more carefully further.

- **PAF-302**: It shows a fairly steep slope at low pressures, up to about 80 bar, which subsequently decreases, maintaining an adsorption increase, although less marked.
  Above 100 bar there isn't a real plateau, even if, comparing line with that of methane shipping, PAF-302 has a greater methane density, at equal pressure; the difference between PAF-301 and PAF-302 lies in the different size distribution of the cavities, as shown in the next section.

- **PAF-303**: For this type of PAF, performance is rather scarce. Surely the adsorption is positive, there is an improvement compared to the curve of the free methane, but much lower than the two PAFs previously investigated and even below the DOE reference value.

- **PAF-304**: It has a very similar trend as PAF-303, although, at the same pressure, it has lower adsorption values. Also for this case, the reason is the dimension of the cavities, greater than PAF-303.

All the considered materials adsorb CH_4 very efficiently at low and moderate pressures (below 120 bar), and PAF-301 provides good adsorption at low pressures, due to the high density of aromatic residues, but it has a very fast saturation. This is due to the absence of enough free volume within the structure and moreover this material, potentially useable for automoctive applications at low pressure in competition with liquefied petroleum gas (LPG), still presents considerable experimental difficulties in the synthesis. PAF-302 exhibits the best behavior over the entire considered range of pressures, except in the initial step ($P \leq 40$ bar) where it's outperformed by PAF-301.
To confirm the adsorption's behaviors of the four considered PAF30n, the temperature effect on CH_4 adsorption was evaluated by repeating the simulations at 273 and 323 K as shown in figure 4.22.

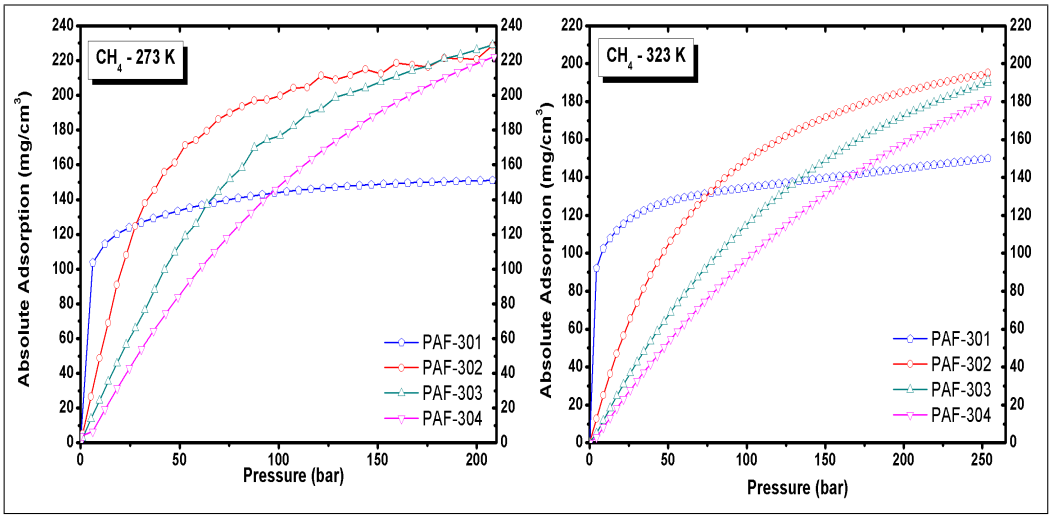

Figure 4.22: Absolute adsorption isotherms (mg/cm^3) in PAF-30n at 273 and 323 Kelvin.

Even for the temperatures of 273 and 323 Kelvin, the behavior for the adsorption of methane within the PAF-30n is almost identical, except in the case of saturated PAF-301.

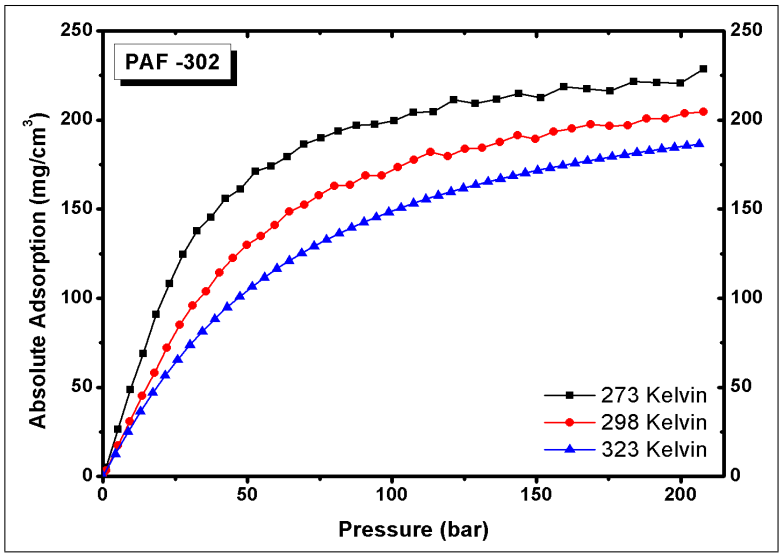

Figure 4.23: PAF-302 isotherms at different temperatures.

This can be seen even better in Figure 4.12 where, in this precise case with the PAF-302, you can see how the adsorption of methane has the same trend for all three curves, but it is clear how the adsorption is greatly influenced by the temperature, especially at low pressures; for instance, at 27 bar the adsorbed density in PAF-302 passes from 124 mg/cm^3 at 273 K to 84 mg/cm^3 at 298 K, to 68 mg/cm^3 at 323 K.
As described at the beginning of the chapter, to understand in an immediate way the difference with the compressed gas, the storage capacity is discussed in terms of excess and effective adsorption, shown in Figure 4.24 at the temperature of 298 Kelvin.

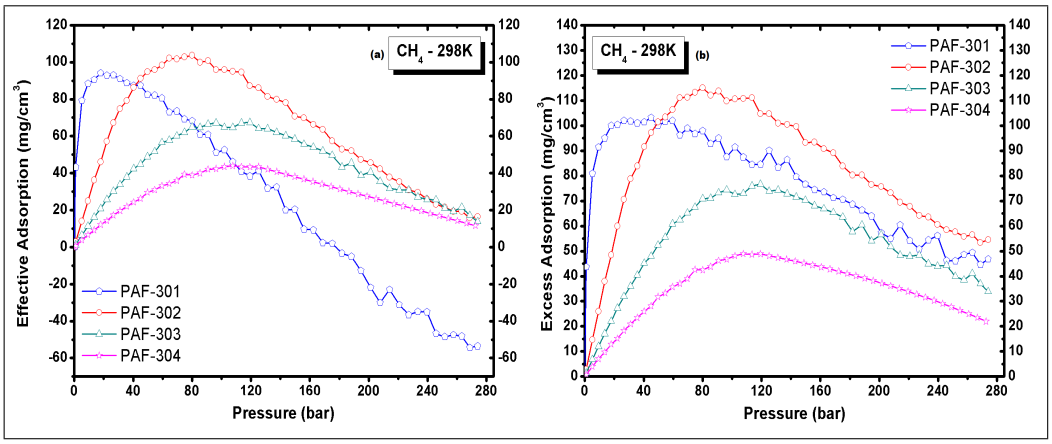

Figure 4.24: Effective (a) and excess (b) adsorption isotherms of methane in PAF-30n at 298 K.

The largest gain respect the compressed gas is obtained with PAF-302, whose maximum effective adsoprtion (n_{eff}) falls at 80 bar; here, the storage density is increased to 162,94 vs

59,17 mg/cm^3 in the free gas, with a gain factor of 2.75.
The storage density is also increased by the other materials, though to a lesser extent: n_{eff} has a maximum at 17.79 bar for PAF-301 (density gain factor 7.94), at 119.3 bar for PAF-303 (1.72) and at 125.2 bar for PAF-304 (1.43).
At the largest pressure considered, 274 bar, the methane density in PAF-302 is still 8.5% higher than the corresponding free gas density (217.1 vs 200 mg/cm^3).
In Figure 4.25, the simulated and experimental adsorption isotherms of CH_4, these latter estimated by the experimental group present in my department, adsorbed on PAF-302 at 298 K and up to 200 bar, are reported:

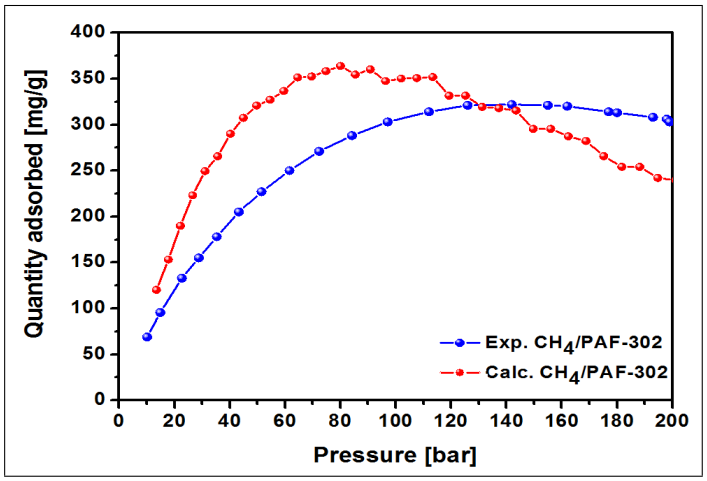

Figure 4.25: Experimental and theoretical excess storage capacity of CH_4 adsorbed on PAF-302 at 298 K and up to 200 bar.

Obviously these thereoretical results are referred to ideal crystalline materials, while PAF materials synthesized and characterized until now are highly disordered: then, lower adsorbed densities have to be expected in actual operative conditions, but these idealized results show the upper limit that can be approached when improving the crystallinity of the samples.
The methane adsorption in PAF-302 has been studied experimentally, at 273 K and for pressures up to 1 atm, in a paper recently pubblished. [10]

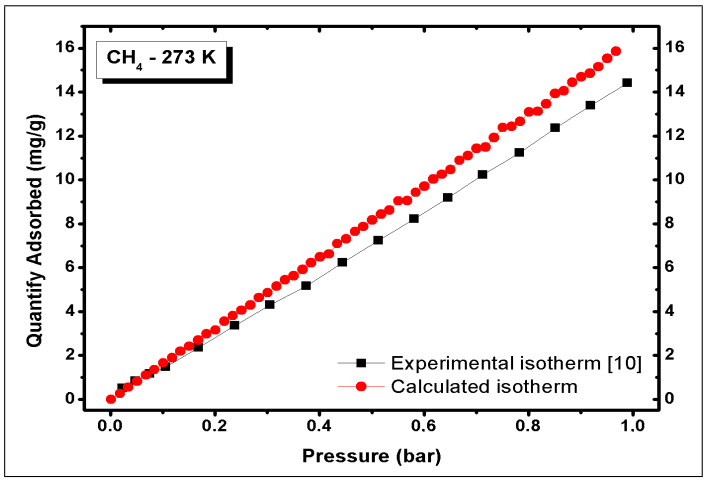

Figure 4.26: Simulated and experimental gravimetric CH_4 adsorption in PAF-302 at 273 K.

Simulated and experimental isotherms are in good agreement at low pressure, and show discrepancies at higher pressures. Such differences are likely due to the ideal crystalline structure of the model PAF-302, in contrast to the probable presence of defects in the real samples.
In fact, an incomplete or defective polymerization during PAF synthetis can lead to a different pore distributions within the structure, as it will be demonstrated in the next section analyzing the porosimetry of the considered materials by studying the adsorption isotherms of argon and nitrogen.
The presence of mesopores in the synthesized material causes the shift of the experimental adsorption maximum at high pressures (140 bar) in contrast to the calculated curve (80 bar), representative of an "ideal" material that contains only micropores.
The comparison between the storage capacity of PAF-302 and those of selected materials reported in literature is now discussed. A large number of results can be found for methane adsorption in porous materials belonging to the class of activated carbons, metal organic frameworks (MOF), and covalent organic frameworks (COF), which have been proposed for this kind of application much earlier than PAFs materials.
In table 6, CH_4 gravimetric uptakes of different microporous materials are reported:

Material	SSA_{Bet} ($m^2\ g^{-1}$)	T (Kelvin)	P (bar)	Excess CH_4 Uptake ($mg\ g^{-1}$)	Ref.
PAF - 302 (Model)	5519	298	35	265	this work
			80	362	
PAF - 302 (Experimental)	4563	298	35	178	this work
			140	322	
PAF - 1	5600	298	35	185	[137]
MOF-210	6240	298	80	264	[90]
HKUST - 1	1270	298	35	200	[195]
PCN-14	1753	290	35	181	[34]
PCN-68	5109	298	100	390	[193]
PPN-4	6461	295	55	269	[135]
COF - 102 (Model)	4360	298	100	271	[194]
COF - 102 (Experimental)	3620	298	35	188	[7]
COF - 103 (Model)	4640	298	100	258	[194]
COF - 103 (Experimental)	3530	298	35	175	[7]
ZIF – 8	1813	270	62	100	[197]
Maxorb-A	3100	298	40	211	[63]

Table 6: Properties and CH_4 uptake of selected porous materials.

The comparison of PAF-302 with the best adsorbing materials confirms that PAF-302 is a very promising material for methane storage over a wide range of pressure. The maximum adsorption is reached only at very high pressure, 140 bar with an uptake of 322 mg/g for the

experimental sample and 80 bar with an uptake of 365 mg/g for the computational model. Since the simulations provide an upper limit for the expected gas uptake, they can also be used to evaluate the "ideality" of actual samples.
Althought a more reliable comparison can only be made if the pore size distribution for all materials is known, Table 6 clearly shows that the gas storage capacity of a material is strongly dependent by SSA.
In the case of gas storage at high pressure, the specific surface area is important because it reveals how much porosity a material has. A higher surface area means that a larger volume of gas can be stored.
However, for high storage capacity other parameters such as the presence of pores comparable to the size of the adsorbed gas and the presence of heteroatoms or metals, which contributes to increase the interaction forces between gas and framework, are relevant.
From the comparison between PAFs and other materials, it can be seen how the presence of metals (MOF, PCN, PPN) and hetero atoms (COF and carbon) combined with the presence of pores with suitable size greatly affects gas uptake.
Adsorption is an exothermic process, as a consequence of the surface/molecule interactions: the excess density in the pores depends on such energy gain, which is effectively measured by the isosteric heat of adsorption, Q_{st}.

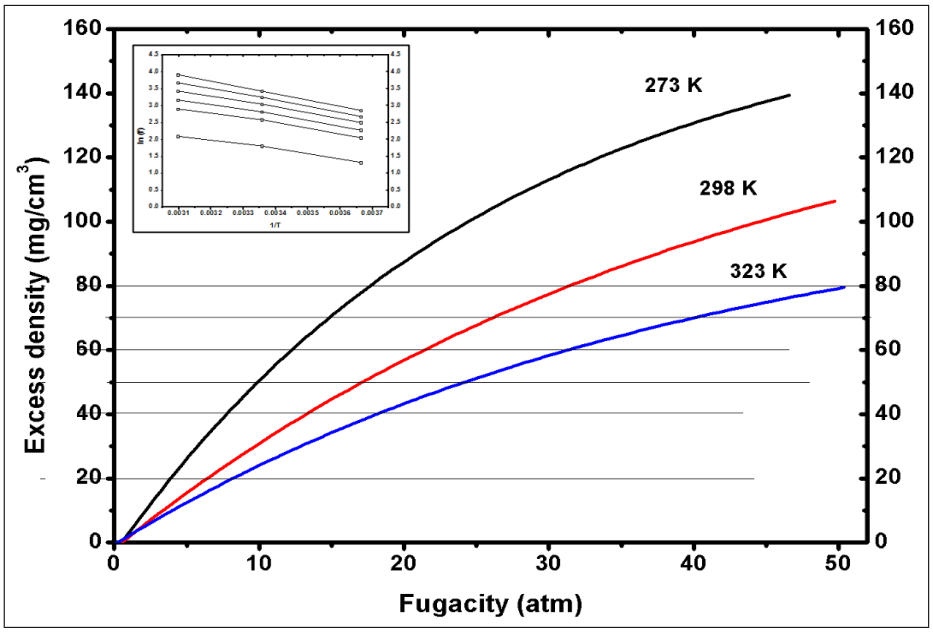

Figure 4.27: Excess adsorbed density of methane in PAF-302 at 273 (black line), 298 (red line) and 323 (blue line) K. The horizontal lines indicate the fugacities of the free gas in equilibrium with various excess densities at all the temperatures. Inset: the data used to estimate Q_{st} from eq 2 at various methane loadings.

To apply eq 5.4, the excess isotherms are measured or simulated at different temperatures, reporting the fugacities corresponding to constant loadings, as illustrated in Figure 4.27; Q_{st} is properly defined for low surface coverages, in any case before the maximum in the excess isotherms.

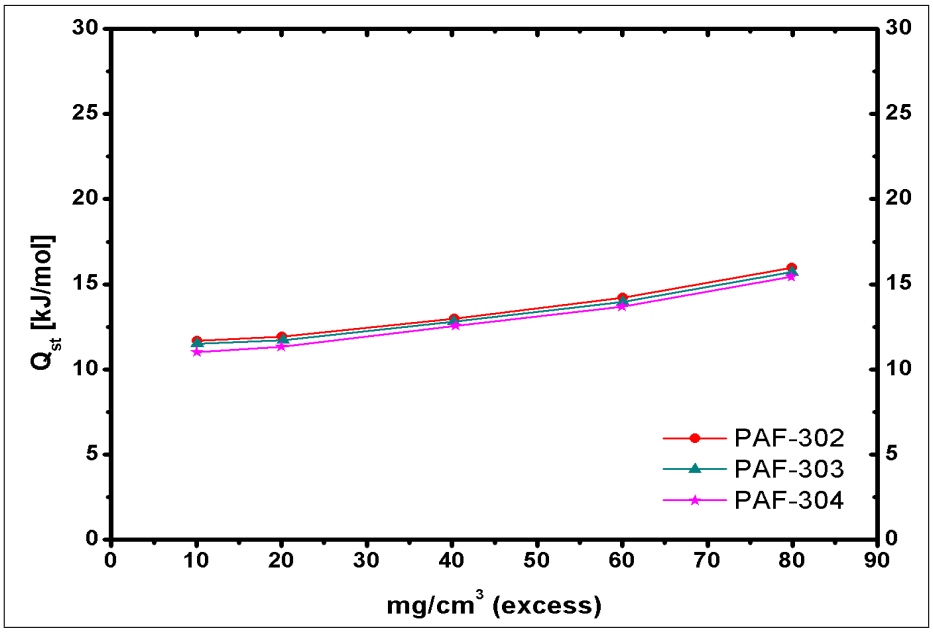

Figure 4.28: . Isosteric heat of adsorption for PAF-30n at different methane loadings.

In Figure 4.28, the isosteric heat is reported as a function of the gas loading for PAF-302, 303, and 304 (PAF-301 saturates so quickly at low pressure that it is difficult to obtain reliable data at different temperatures).
The three materials exhibit very similar Q_{st} values up to an excess loading of about 80 mg/cm^3, reflecting the similarity in the gas/surface interactions.
PAF-302 heat is slightly larger, however, likely due to the possibility for single gas molecules to interact with two aromatic rings bonded to the same aliphatic carbon at a favorable angle; this possibility is comparatively smaller in PAF-303 and 304, which contain longer, linear polyphenyl chains.
For very low n_{exc}, the heats of adsorption in PAF-304, 303, and 302 are 10.9, 11, and 11.2 kJ/mol, respectively (increasing above 16.1 kJ/mol for PAF-302 at high surface coverage): these values can be compared with the heats measured in microporous carbons and zeolites, ranging from 12.10 to 25.52 kJ/mol [28] or in PCN-14, around 30 kJ/mol. [79]
Considering materials with higher area, the initial Q_{st} is around 12.2 kJ/mol in MOF-5 and 12.0 in ZIF-8 (see Table 3).

4.10.3 FTIR, Raman and Theoretical Combined Study

FTIR and Raman spectroscopies, along with ab initio calculations, are employed to describe the PAF-302 vibrational features and investigate the interactions of methane with the surface of the porous framework.
Upon adsorption, methane vibrational modes are shifted due to the host-guest interactions with the surface: several studies have been performed on zeolites, [205] silica [206, 207] and oxides [208] but only few works have been done on carbon-based adsorbents such as activated carbon and C_{60} fullerenes. [209, 210]
The vibrational spectra of the polymer have been interpreted by comparison with the spectra of tetrakis(4-bromophenyl) methane (TBPM), the precursor used in the PAF-302 synthesis.

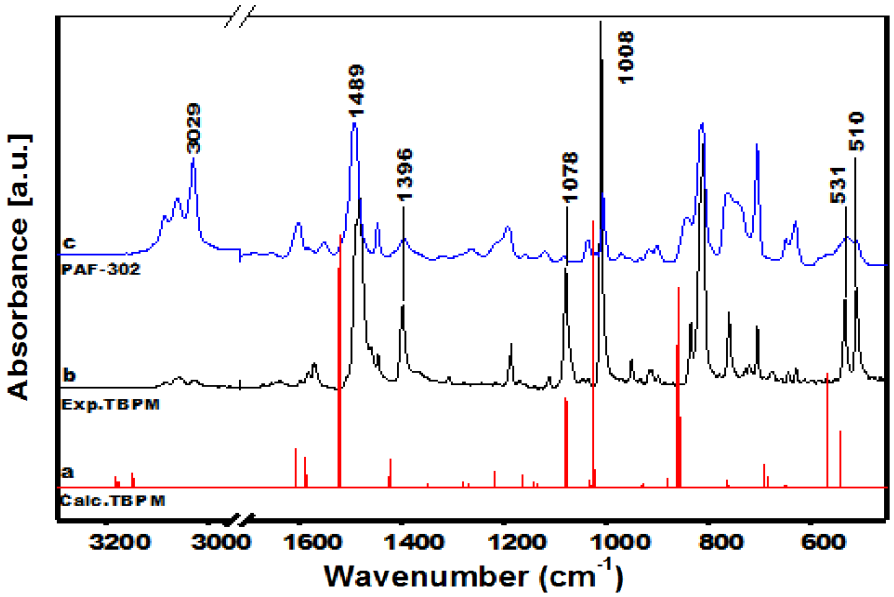

Figure 4.29: FTIR spectra in the region 3300-450 cm^{-1} of: (a) DFT spectrum of TBPM calculated in harmonic approximation at the MP2/6-311+G(2d,2p) level; (b) and (c) experimental spectra of TBPM and PAF-302 in the KBr pellet, respectively.

TBPM vibrational bands were assigned by comparison with a theoretical spectrum calculated at the MP2/6-311+G(2d,2p) level: the main components are listed in Table 4.
From the data reported in table 7 and figure 4.29, one can see that the theoretical (a) and experimental (b) TBPM spectra are in good agreement, presenting only a small shift due to the harmonic approximation adopted for the calculated spectrum.

Vibrational mode	TBPM Calc. Freq. [cm^{-1}]	TBPM Exp. Freq [cm^{-1}]	PAF-302 Exp. Freq. [cm^{-1}]
Stretch aromatic C-H	3183, 3176, 3147	3083(vw), 3057(vw), 3026 (vw)	3085(w), 3059(m), 3029(s)
Ring quadrant stretch	1605-1583	1603-1555	1621-1531
Semicircle stretch pair	1520, 1420	1481(s), 1396 (m)	1489(s), 1394 (w)
In plane C-H bend	1215	1185	1190
C-Br stretch	1077	1078 (m)	1081 (vw)
Ring C-C bend + C-H bend + C-Br stretch	1024	1008 (vs)	1005 (m)
Ring and C-H out of plane bend	861, 761	810(s), 759	812(m), 761
In plane ring bend	689	702	703
Out of plane quadrant ring bend + C-Br bend	566, 541	531(m), 510(m)	557-497 (w)

$vs = very strong, s = strong, m = medium, w = weak and vw = very weak$

Table 7: IR vibrational modes of the TBPM calculated spectrum compared to those of the TBPM and PAF-302 experimental spectra.

The FTIR spectrum of TBPM generally shows sharp bands because of the crystalline nature of the compound. Three very weak bands are found in the high-frequency region at 3085, 3059, and 3029 cm^{-1} , which are assigned to the CH stretching vibrations of the aromatic

rings on the basis of the calculated spectrum and in agreement with the literature [211, 212]. Likewise, based on the computed spectrum, in the low-frequency region the bands falling at 1481 and 1396 cm^{-1} involve semicircle stretching pair modes of the aromatic rings. The band at 1078 cm^{-1} is an almost pure C-Br stretching mode, whereas the intense and sharp band at 1008 cm^{-1} is assigned to the C-C bending of the aromatic rings coupled with C-H bending and C-Br stretching vibrations.
At lower frequencies the bands with medium intensity at 531 and 510 cm^{-1} are assignable to the out-of-plane quadrant ring bending deformations somehow coupled with the C-Br deformation.
These results have allowed us to assign with more precision the IR bands of the PAF-302 polymer (Figure 4.29c). The comparison between PAF-302 and TBPM spectra shows that in general the bands of the polymer become broader, change in intensity, and slightly shift in the position. Indeed, after the polymerization reaction the high-frequency band intensity largely increases due to the change of the local dipole moment related to the aromatic ring asymmetric CH stretching.
Furthermore, the bands at 1396, 1008, 531, and 510 cm^{-1} assigned to the aromatic ring stretching and bending (the last three being coupled to C-Br vibrations) undergo a drastic reduction in their intensities in the PAF-302 polymer: it can be thus inferred that the dipole moment of these modes is strongly influenced by the presence of bromine atoms in the TBPM precursor.
The main fingerprint of the polymerization is, however, related to the band at 1078 cm^{-1} due to the C-Br vibration, which diminished to an undetected level in the PAF-302 spectrum, suggesting essentially complete reaction of the starting TBPM. The PAF-302 Raman spectrum (Figure 4.30) was also interpreted with the help of both the computed and the experimental TBPM spectra.

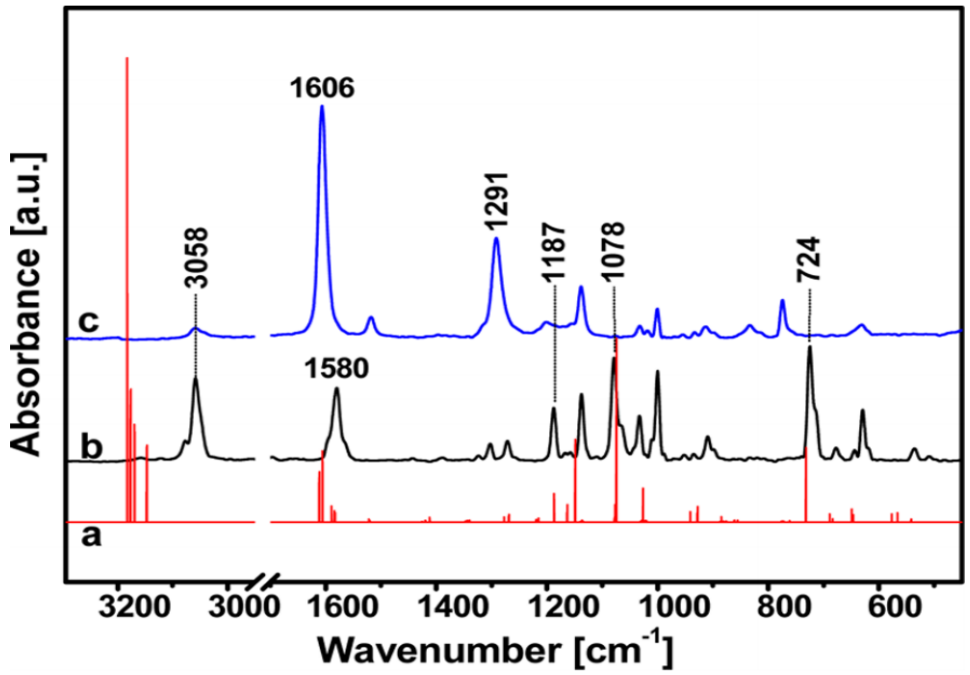

Figure 4.30: Raman spectra in the region 3300-450 cm^{-1} of: (a) DFT spectrum of TBPM calculated in harmonic approximation at the MP2/6311+G(2d,2p) level; (b) and (c) experimental spectra of TBPM and PAF-302, respectively.

Table 8 summarizes the assignments of the main vibrational modes.

Vibrational mode	TBPM Calc. Freq. [cm^{-1}]	TBPM Exp. Freq [cm^{-1}]	PAF-302 Exp. Freq. [cm^{-1}]
stretch aromatic C–H		3088–3031	3074–3039
ring quadrant stretch		1580(s)	1606(vs), 1517(w)
ring sextant stretch	1269	1271	–
C–C biphenyl bond stretch	–	–	1291
asym. C–C quaternary carbon stretch	1187	1187(m)	1201(vw)
sym. C–C quaternary carbon stretch	1150	1137	1138
C–Br stretch	1076	1078(s)	–
ring C–C bend + out-of-plane CH bend	1027	1000(m)	1000(w)
in-plane quadrant bend + C–Br stretch	732	724(s)	–
in-plane quadrant bend	646	630(m)	630(w)

$vs = very strong, s = strong, m = medium, w = weak and vw = very weak$

Table 8: Raman vibrational modes of the TBPM calculated spectrum compared to those of the TBPM and PAF-302 experimental spectra.

In the high wavenumber region the TBPM spectrum (Figure 4.30, curve b) is characterized by an intense broad absorption at 3058 cm^{-1} with an evident weaker band at 3076 cm^{-1} and a shoulder at lower wavenumber.
The bands in this region can be easily assigned to the C-H stretching vibrations of the aromatic rings on the basis of the calculated spectrum (Figure 4.30, curve a). At low frequency, the TBPM spectrum shows a band at 1580 cm^{-1} due to the ring quadrant stretching, whereas the peaks at 1187 and 1137 cm^{-1} are due to the asymmetric and symmetric stretching of the quaternary carbon, respectively.
As in the infrared spectrum, the strong band at 1078 cm^{-1} is assigned to the C-Br stretching, whereas at lower frequencies the band at 724 cm^{-1} is due to the in-plane quadrant bending of the aromatic ring coupled to C-Br stretching.
The comparison between PAF-302 and TBPM spectra (Figure 4.30, curves c and b, respectively) at high frequency shows a significant decrease in the intensity of the bands referred to C-H stretching vibrations in agreement with the fact that upon polimerization the symmetry of the TBPM is removed and the C-H stretching vibrations become asymmetric (strong IR activity). Remarkably, in the low frequency region, the bands at 1078 and 724 cm^{-1} of the precursor, assigned to vibrations involving the bromine atoms, are absent in the spectrum of the polymer PAF-302, indicating a complete polymerization in full agreement with the IR results.
Another mark of the polymerization, only present in the Raman spectrum, is given by the intense band at 1291 cm^{-1}, which is absent in the precursor: it has been assigned to the stretching of the C-C bond which is formed after the coupling between the aromatic rings.
The methane/PAF system was studied by considering the possible local symmetry of methane molecules interacting with the porous network. PAF-302 polymer is characterized by a 3D structure where methane can interact simultaneously with faces and edges of phenyl rings, and monodentate (local C_{3v} symmetry) and bidentate (local C_{2v} symmetry) configurations of methane molecules are possible.

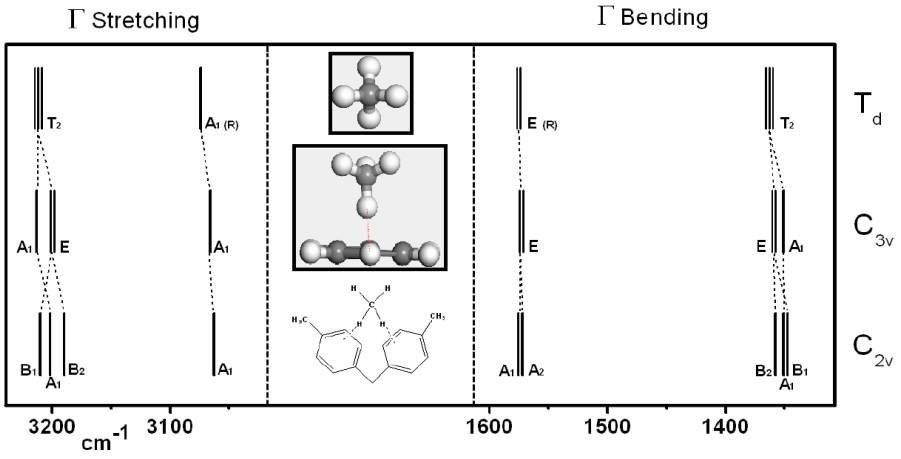

Figure 4.31: Representation of the theoretical stretching and bending harmonic frequencies of free CH_4 (T_d symmetry) p-xylene - methane (C_{3v} symmetry) and di-tolylmethane-methane (C_{2v} symmetry) structures.

Figure 4.31 shows the theoretical stretching and bending harmonic frequencies of free CH_4 (T_d symmetry) p-xylene-methane (C_{3v} symmetry) and di-tolylmethane-methane (C_{2v} symmetry) structures: after the adsorption of methane the forbidden modes (that would be normally detected only by Raman spectroscopy) may become observable in the infrared spectra because of surface interactions.
Difference spectra after gas adsorption on PAF-302 were examined, in order to reveal bands of adsorbed methane or deuterated methane possibly masked by the structural bands of the material. [141]
To correlate the information from FTIR spectra with the interactions experienced by the single methane molecules, it is of great interest to evaluate the actual number of gas molecules adsorbed in PAF-302 pores at the various pressures.
The adsorption isotherms were simulated at different temperatures in the range 87-115 K. The isotherms, for pressures up to 0.020 bar, are reported in Figure 4.32.

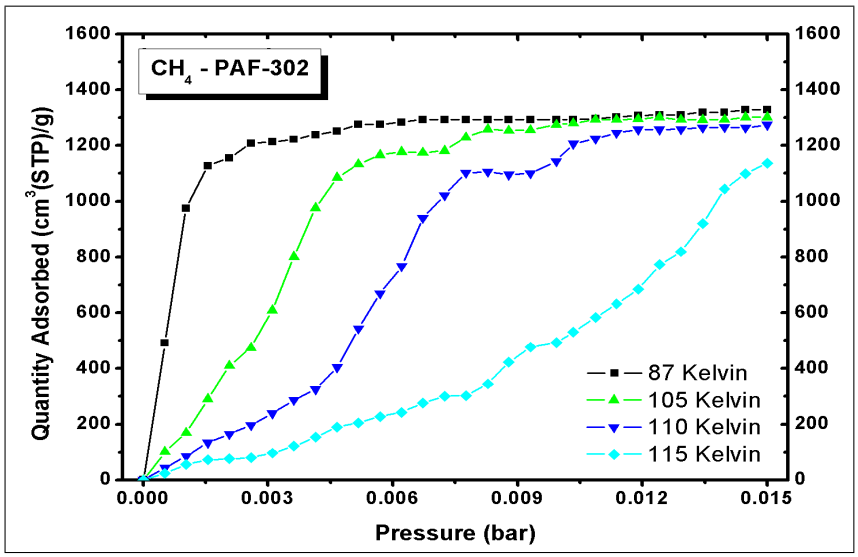

Figure 4.32: Adsorption isotherms of CH_4 on PAF-302 at different temperatures: the isotherms were simulated with GCMC method.

At 110 K the unit cell of model PAF-302 contains about 10 molecules at 0.001 bar and 140 molecules at saturation, above 0.010 bar.
These quantities have to be reduced by around 20% in the actual sample, whose specific area is ca. 4200 m^2/g, compared to ca. 5500 m^2/g of the ideal material used in GCMC simulations.
Considering that the PAF-302 unit cell contains 4 sp_3 carbon atoms, or equivalently 8 biphenyl moieties, estimating methane molecules/ biphenyl ratio approximately 1 at 0.001 bar and 14 at saturation.
On the basis of these results, the spectra recorded after adsorption indicate multiple interactions between methane and the PAF surface, where one or two phenyl rings (i.e., monodentate or bidentate adducts, respectively) are involved.

4.10.4 Hydrogen

As discussed in chapter 2, hydrogen, as a viable energy carrier, may play an important role in future energy plans. Widespread adoption of hydrogen as a vehicular fuel depends critically upon the ability to store hydrogen on-board at high volumetric and gravimetric densities, as well as on the ability to extract/insert it at sufficiently rapid rates.
Therefore, we attempted to explore the performance of hydrogen storage in the whole class of PAF-30n to understand if these materials can be considered good candidates for hydrogen storage.
At first the FF was tested first for gaseous H_2, simulating a formal "adsorption" in an empty box and computing the compressed gas density at 298 K and at 77 K.
These two temperatures are important: at 77K, the hydrogen is used as an aid for the porosimetric determination of the material and lately to store significant amounts of gaseous hydrogen in the crystalline compounds to facilitate the development of technologies related to the use of hydrogen, while usually at 298 K the hydrogen is stored in hydrogen tanks. The results were compared with the hydrogen EOS at the same temperature, in an identical manner to the other gas.

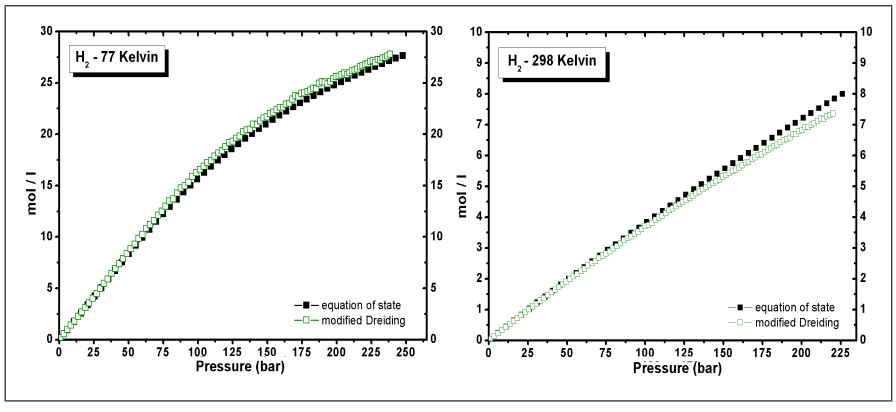

Figure 4.33: Density (mol/l) of gaseous hydrogen at 77 K and 298 K.

Host-guest interactions were considered next, comparing classical and MP2 intermolecular energies for the H_2-benzene couple along some different orientations. The reliability of the new parameters was also confirmed by comparing the trend of H_2-H_2(4.34a) intermolecular energies with the modified FF and by Gaussian 09 at the MP2 level, with obviously correction of BSSE.

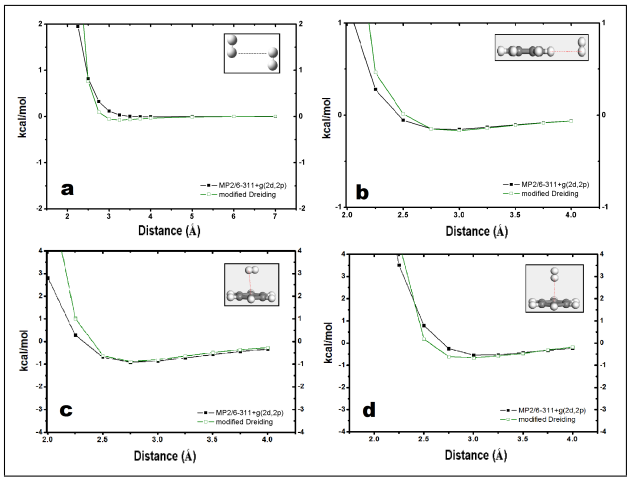

Figure 4.34: Guest-guest(a) and host-guest(b-c-d) interaction energies.

Therefore, the parameters of the final modified forcefield are the following:

Atom Type	Dreiding Symbol	D (kcal/mol)	σ (Å)
H of H_2	H_A	3.30	0.021
Aromatic C sp^2	C_R	3.09	0.33

Table 9: FF parameters present in the modified force field.

The other FF parameters are the same as in standard Dreiding and implemented for instance in Materials Studio package. In Figure 4.35, the simulated adsorption isotherms at 298 K are reported separately for every PAF-30n.

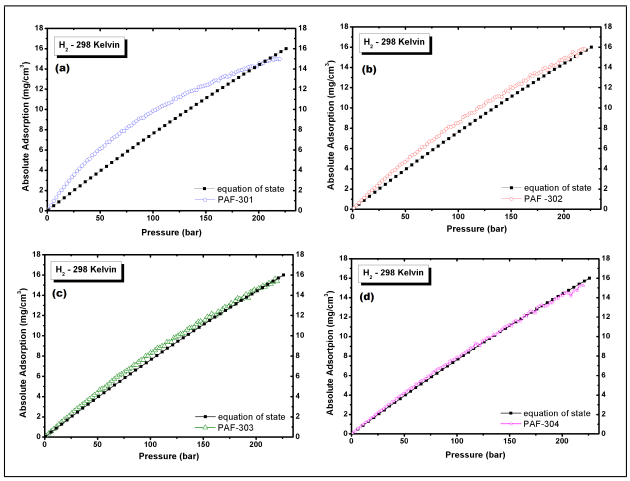

Figure 4.35: GCMC adsorption isotherms of hydrogen in PAF-301(a), PAF-302(b), PAF-303(c) and PAF-304(d). The density of free gaseous hydrogen (from EOS) is shown for comparison.

The resulting uptake isn't as satisfactory by comparing the equation of state, but it's something we expected. Indeed the hydrogen adsorption on PAF-302 is an exothermic process due to weak van der Waals interactions, which lead to very low heat of adsorption in the range 3 to 7 kJ/mol. [10]
So, to obtain significant amounts of H_2 uptake, the measurement is usually performed at 77 K.
The results are shown in Figure 4.36:

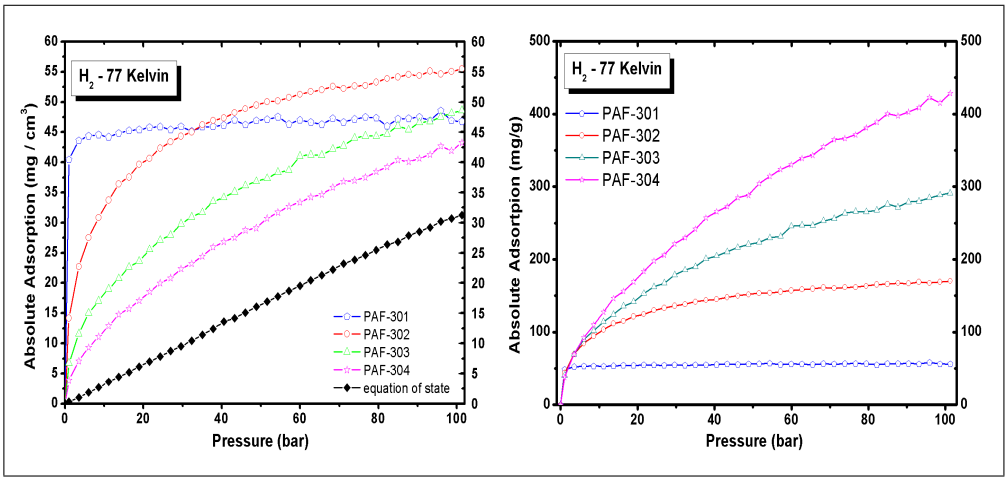

Figure 4.36: To the left GCMC adsorption volumetric isotherms of hydrogen in PAF-30n and equation of state for comparison. To the right GCMC adsorption gravimetric isotherms.

At this temperature, only PAF-301 is completely saturated.
All of the considered materials adsorb hydrogen very efficiently at low and high pressure. PAF-302, looking the absolute adsorption, exhibits the best trend, except in the initial step ($P \leq 25$ bar) where PAF-301 performs better, likely due to the smaller pore size, shown above in the pore size distribution, which amplifies the host-guest interactions but leads to a faster saturation.
Simulated excess and effective adsorptions for PAF-30n at 298 K are reported in Figure 4.37.

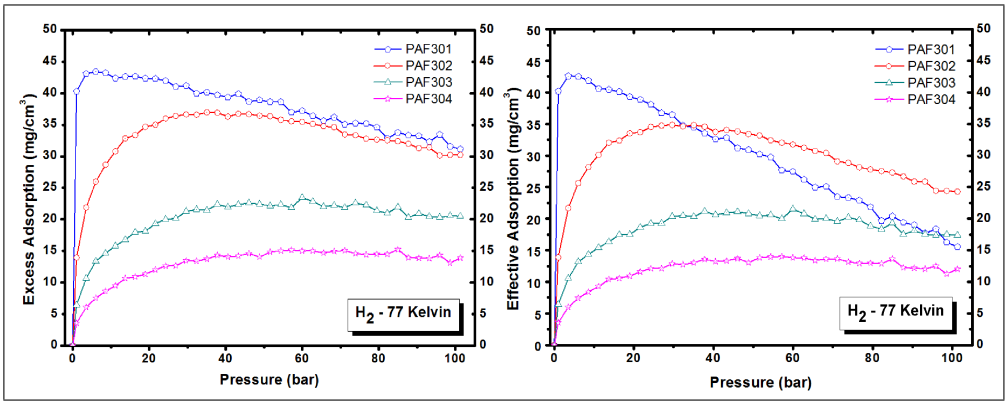

Figure 4.37: Excess and effective adsorption isotherms of hydrogen in PAF-30n at 77 Kelvin.

The results obtained in the excess isotherms show the importance of the ultramicropores which are present in the PAF-301 for the hydrogen adsorption in the pressure range between 0 and 100 bar.
In fact, although the pressure range increase and the PAF-302 exceeded the values of excess adsorption of PAF-301, it is clear how the pores of this material have a great importance in the adsorption of hydrogen, even greater than the other gas taken into account.
As regards the largest gain respect to the compressed gas, PAF-301 has maximum effective adsorption at 6 bar. Here the storage density is increased to 42.4 vs 0.95 (mg/cm^3) in the

free gas.
PAF-302 has a maximum at 35 bar with 34.8 (mg/cm^3) and at the largest pressure considered, 100 bar, the hydrogen density in PAF-302 is still 75% higher than the corresponding free gas density.
In Figure 4.38, the simulated and experimental adsorption isotherms of H_2, these latter estimated by the experimental group present in my department, adsorbed on PAF-302 at 77 K and up to 100 bar, are reported:

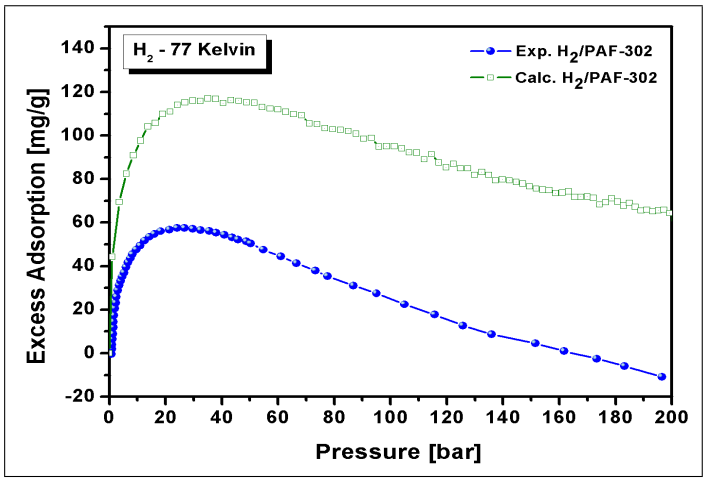

Figure 4.38: Experimental (blue spheres) and theoretical (green empty squares) excess storage capacity of H_2 adsorbed on PAF-302 at 77 K and up to 200 bar.

The experimental and calculated curves show the same trend but with different storage capacity: the synthesized material shows a maximum value of 57 mg/g at 25 bar, while the calculated curve reaches the maximum at 35 bar and 115 mg/g, a value double of the experimental one.
The behavior of the material in the experimental and theoretical hydrogen and methane storage is very different and mainly depends on the pore distribution.
Despite the difference in the total pore volume, the experimental and theoretical methane uptake lead to very similar storage capacity. This confirms the role of mesoporosity.
Regarding hydrogen, the capacity storage is strongly correlated to the amount of very small pores.
The synthesized material stores half of the amount predicted, as the microporous total volume is half of the theoretical value as shown in the table 7.
An important consideration about the experimental and theoretical comparison, just described in the case of methane, is the poor crystallinity of the synthesized material which presents a smaller area that reduces the interactions with gas, and a less porous structure that increases the material bulk density, making the comparison with theoretical results even less favorable.
Recently, the hydrogen adsorption in PAF-302 has been studied both theoretically and experimentally, especially at 77 K. Lan et al. [21] simulated hydrogen adsorptions on PAF-302 model through a forcefield based on a Morse potential. The interaction energies between H_2 and PAFs were calculated by performing a series of single-point energy calculations and calibrating their results predicted with a experimental hydrogen isotherm [131] in PAF-302 at 77 Kelvin by a multiscale method.
They simulated H_2 storage in every PAF-30n structure, each of them with similar structural and textural properties of our models.

So, in the same article simulated isotherms at 298 Kelvin can be compared as they were experimental, as shown in Figure 4.39

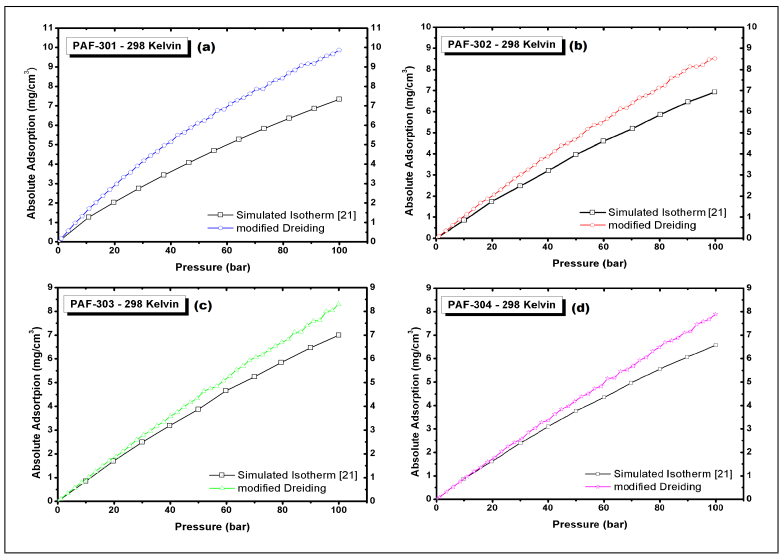

Figure 4.39: Comparison between literature and simulated isotherms for PAF-301(a), PAF-302(b), PAF-303(c) and PAF-304(d)

Comparing their results at 298 K and our simulated isotherms at the same temperature, the values are comparable in a wide range of pressure, considering the data of Lan et al. coming from a material that has structural defectivity with respect to our ideal models.
More results have been obtained for the H_2 in other porous material, including MOF and COF, as shown in Table 10, where gravimetric uptake are reported for some of the best performing materials.

Material	SSA_{Bet} ($m^2\,g^{-1}$)	T (Kelvin)	P (bar)	Excess H_2 Uptake ($mg\,g^{-1}$)	Ref.
PAF - 302 (Model)	5519	77	35	113	this work
			100	92	
PAF - 302 (Experimental)	4563	77	30	58	this work
PAF - 1	5600	77	50	75,5	[137]
5wt%Li@PAF-1	2620	77	50	99	[204]
MOF-210	6240	77	55	86	[90]
PCN-14	1753	77	30	46	[34]
PCN-68	5109	77	28	73	[193]
PPN-4	6461	77	55	91	[135]
COF - 102	3620	77	35	72	[7]
COF - 103	3530	77	35	70	[7]
KUA6	3808	77	30	57	[203]

Table 10: H_2 excess gravimetric uptake in different materials.

Although the PAF-301 has adsorption density greater than PAF-302, it was decided to not compare it with other porous materials because PAF-301, as explained above, presents synthesys problems.
These data show that PAF-302 is a very promising material for hydrogen storage and this is even more appealing taking into account the high termal and hydrotermal stability exhibited by PAFs.

4.10.5 Carbon dioxide

The ever-growing energy demand, largely satisfied by the combustion of fossil fuels, caused an escalated global CO_2 emission, which became the major cause of global warming.
Besides the attempts to reduce anthropogenic emissions, it has been proposed to control atmospheric CO_2 concentration removing the gas from the air through carbon capture and storage (CCS) techniques, whose study is strongly supported by governments and scientific institutes.
Also for this gas, we perform Grand Canonical Monte Carlo (GCMC) simulations to explore the ability of several members of the PAF family to adsorb gaseous carbon dioxide at pressures ranging from 0 to ca. 60 bar and temperatures of 273, 298, and 323 K.
For our simulations, we modified the Dreiding Force Field, which is widely used to simulate intermolecular hostguest interactions.
The FF was tested first for gaseous CO_2, simulating a formal adsorption in an empty box and computing the compressed gas density at 298 K. The results were compared with the experimental data from EOS.
Carbon and oxygen partial charges were estimated with the Mulliken method from a MP2 calculation on isolated CO_2 molecule and kept unaltered in all of the simulations.

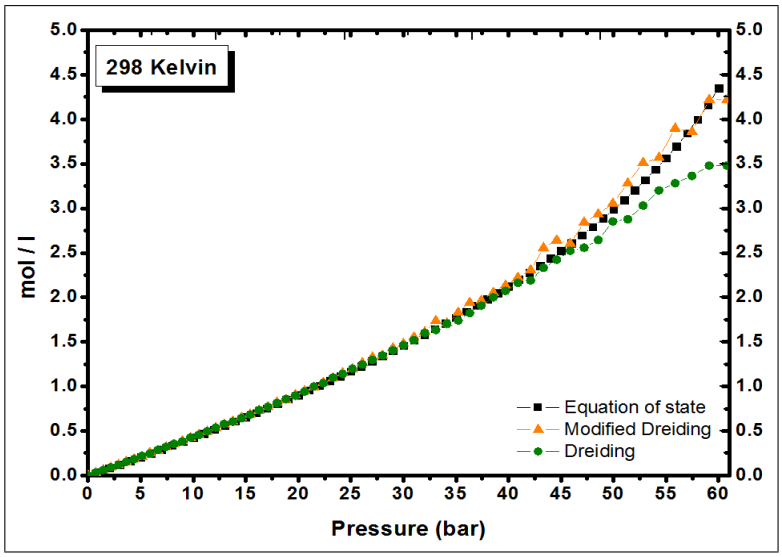

Figure 4.40: Simulated and experimental CO_2 density at 298 K. Circle, green: standard Dreiding FF; triangle, orange: modified FF; square, black: experimental.

The standard FF provides densities somehow too low, so that the Lennard-Jones parameters for carboxylic C and O (C_1 and O_2 in Dreiding notation, respectively) were slightly modified to make them more attractive.

However, the reliability of the new parameters about C_3 (sp carbon) and O_2 (oxigen) of the carbon dioxide was also confirmed by comparing the formal "adsorption" in a empty box with the equation of state at 273 Kelvin and 323 Kelvin.

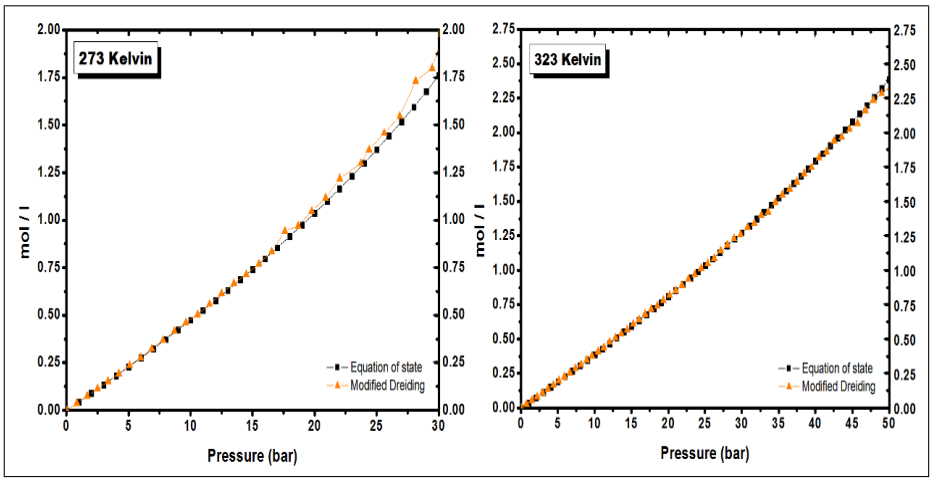

Figure 4.41: Simulated and experimental CO_2 density at 273 K and 323 K.

New parameters were also validated by comparing the trend of CO_2-CO_2 intermolecular energies computed by Forcite with the modified FF and by Gaussian 09 at the MP2 level, with correction of the BSSE, along two different orientations, as shown in Figure 4.42.

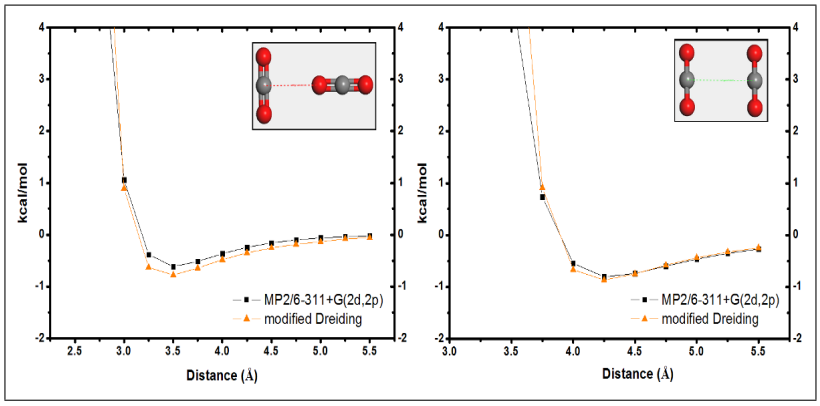

Figure 4.42: CO_2-CO_2 interaction energy (kcal/mol) computed with the modified FF (triangle, orange) and at MP2/6-311+G(2d,2p) level (square, black), including the correction of the BSSE. Rigid scans in the indicated orientations.

Host-guest interactions were considered next, comparing classical and MP2 intermolecular energies for the CO_2-benzene couple along different orientations.
Because Mulliken charges for the aromatic moiety were markedly unstable and orientation-dependent, we chose to set aromatic carbon and hydrogen partial charges to zero, and only use Lennard-Jones parameters for computing hostguest interactions.
Keeping C_1 and O_2 parameters previously optimized, the LJ parameters for aromatic carbon (C_R in Dreiding notation) were adjusted to obtain a satisfatory fit of classical and ab initio curves, as reported in Figure 4.43(a-b-c) and we verified that this FF also reproduces well the CO_2-toluene interactions, Figure 4.43(d).

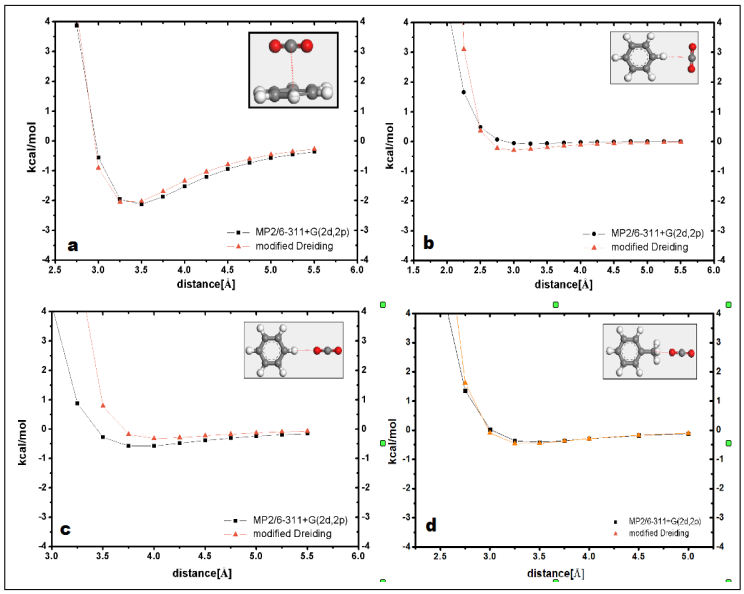

Figure 4.43: Host-guest interaction energy (kcal/mol) computed with the modified FF(triangle, orange) and at MP2-6-311+G(2d,2p) level (square, black).

The Lennard-Jones parameters used in the following calculations are collected in Table 11:

Atom Type	Dreiding Symbol	D (kcal/mol)	σ (Å)	q (a.u.)
carbonxylic carbon	C_1	3.7770	0.079	0.6032
carbonxylic oxigen	O_2	3.1830	0.125	-0,3016
aromatic carbon	C_R	3.8000	0.138	

Table 11: FF parameters used in the modified force field. For all the other atom types the standard Dreiding LJ parameters were used.

The GCMC volumetric and gravimetric simulated adsorption isotherms at 298 K, along with the density of the free gas at the same pressures, are reported in Figure 4.44.

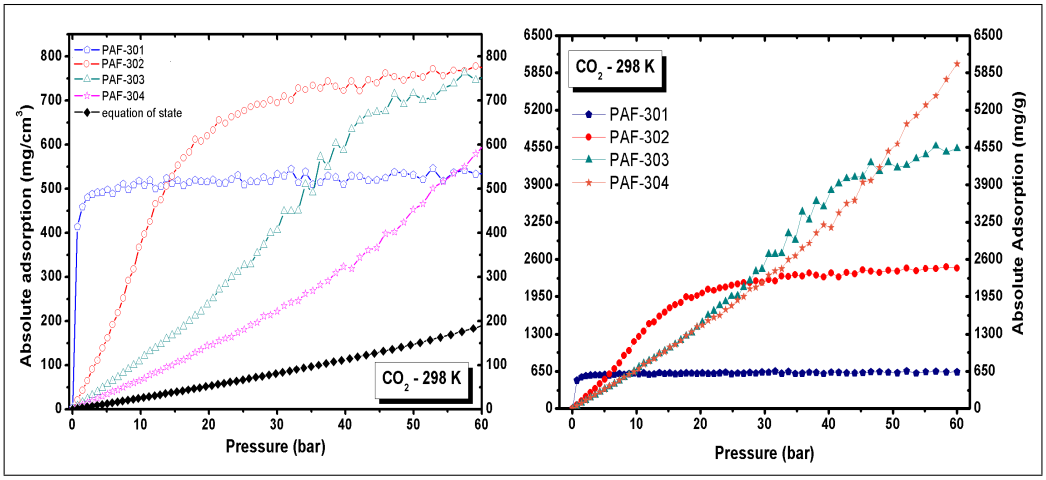

Figure 4.44: CO_2 adsorbed density (absolute volumetric adsorption, mg/cm^3) at 298 K. Blue pentagone, PAF-301; red circle, PAF-302; light blue triangle, PAF-303; orange star, PAF-304; black square, experimental density of the compressed gas;

All of the considered materials adsorb carbon dioxide very efficiently at low and high pressure. PAF-302 exhibits the best behavior, except in the initial step (P $\leq$ 15 bar) where PAF-301 performs better, likely due to the smaller pore size (with an average pore diameter of 8 Å, PAF-301 is close to the boundary between micro- and ultramicroporous materials), which amplifies the host-guest interactions but leads to a faster saturation.
Overall PAF-302, as already shown in previous gases, presents the best combination of large surface area and microporosity.
Simulated excess and effective adsorptions for PAF-30n at 298 K are reported in Figure 4.45.

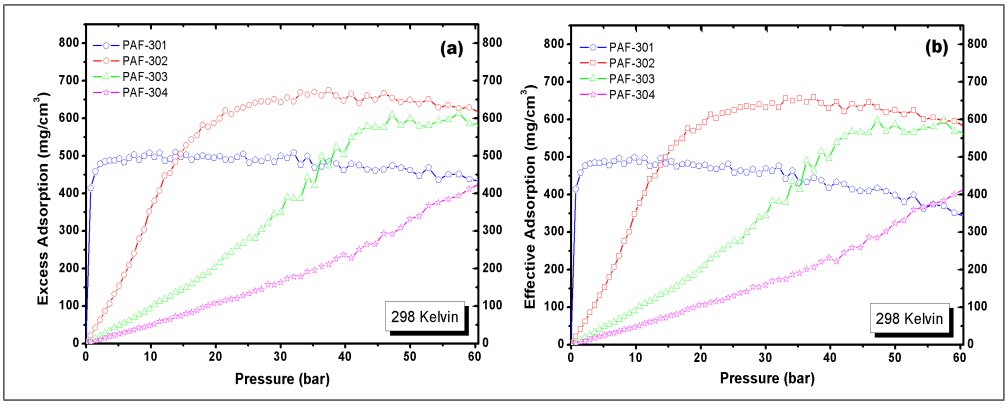

Figure 4.45: Excess(a) and effective(b) CO_2 adsorbed density (mg/cm^3) at 298 K.

At this temperature, the largest gain with respect to the compressed gas is obtained with PAF-302, whose maximum n_{eff} occurs at 37.4 bar, where the storage density is increased from 84.0 to 659.4 mg/cm^3 with a gain factor of 7.8 with respect to the free gas.
The storage density is enhanced by the other materials too, although to a lesser extent: maximum n_{eff} occurs at 9.8, 45.9, and 59.1 bar for PAF-301 (gain factor 28.5), PAF-303 (5.3), and PAF-304 (2.5), respectively. At the largest pressure considered, 60.8 bar, the carbon dioxide density in PAF-302 is still more than three times the corresponding free gas density (579.1 vs 191.4 mg/cm^3).
The temperature effect on CO_2 adsorption was evaluated by repeating the simulations at 273 and 323 K on all of the PAF-30n; in figure 4.46 different adsorptions in PAF-302 are shown:

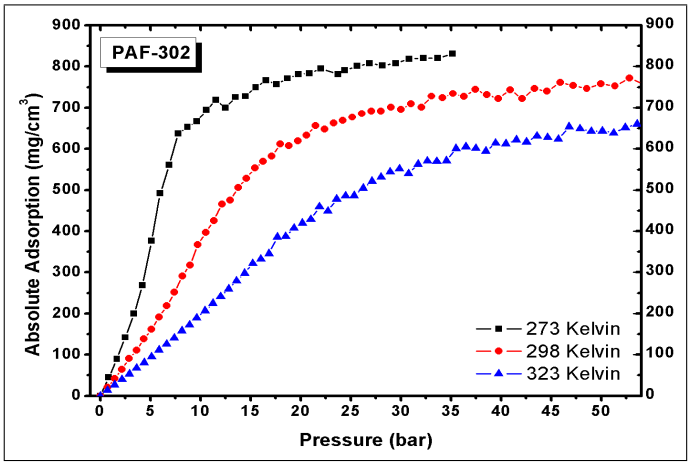

Figure 4.46: Absolute adsorption isotherms (mg/cm^3) in PAF-302 at 273, 298 and 323 K. Square, black: 273 K; circle, red: 298 K; triangle, blue: 323 K;

The adsorption is greatly influenced by the temperature, especially at low pressures; for instance, at 14.2 bar the adsorbed density in PAF-302 passes from 727.9 mg/cm^3 at 273 K to 528 mg/cm^3 at 298 K, to 297.9 mg/cm^3 at 323 K.
Recently, the carbon dioxide adsorption in PAF-302 has been studied experimentally at different temperatures, [10,131,198] and in figure 4.47, our volumetric theoretical predictions were compared in the pressure range between 0 and 1 bar at 273 K.

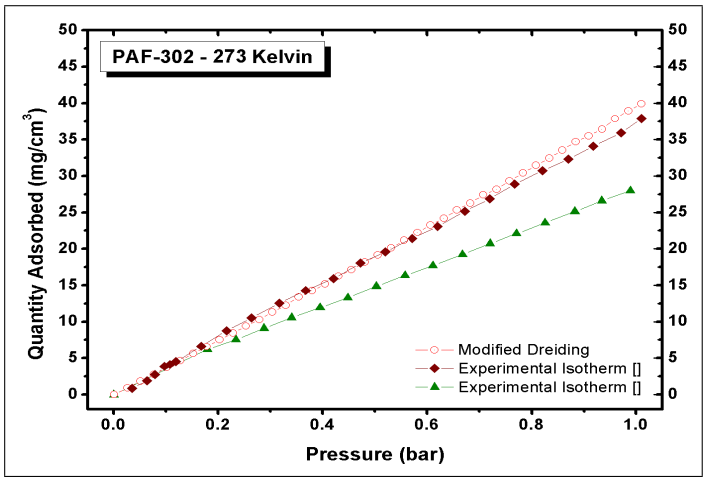

Figure 4.47: Simulated and experimental volumetric CO_2 adsorption in PAF-302 at 273 K at low pressure.

Moreover, in Figure 4.48, the theoretical excess isotherm at 298 K is compared to the experimental curve measured in a sample of PAF-302.

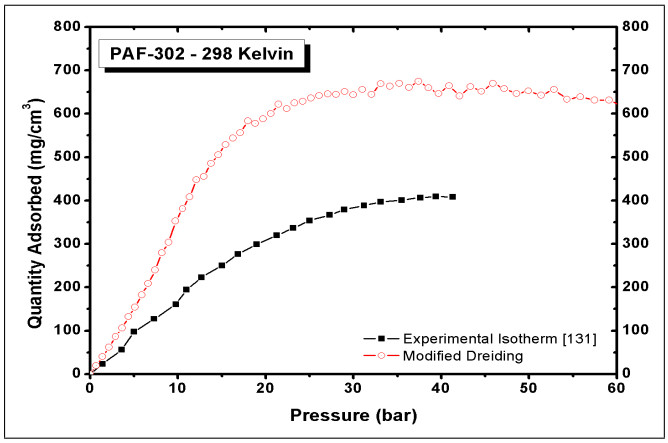

Figure 4.48: Simulated and experimental volumetric CO_2 adsorption in PAF-302 at 298 K at high pressure.

Simulated and experimental isotherms are in good agreement at low pressure, and show increasing discrepancies at higher pressures. Such differences are likely due to the ideal crystalline structure of the model PAF-302, in contrast to the probable presence of defects in the real samples.
In fact, an incomplete or defective polymerization during PAF synthesis can lead to a smaller active area, and to a partial obstruction of pores; because crystalline PAF-302 seems to be ideally suited for gas adsorption, as noted above, any modification of the structure is likely to lower the uptake, especially at high pressure.
It is also interesting to compare our simulations to the theoretical results of Yang et al.. [199]

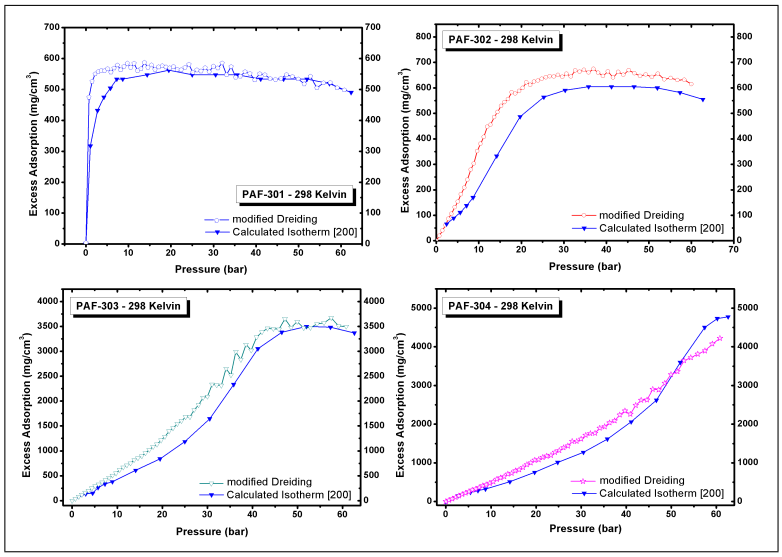

Figure 4.49: Comparison with other theoretical simulations.

At 50 bar and 298 K, our computed CO_2 uptakes are systematically larger. Actually, in ref. [200] the force field was chosen to fit the experimental CO_2 uptake in PAF-302 reported by Ben et al. [131]
The force field used in this simulation, on the contrary, was modified as explained above to fit experimental guest-guest and ab initio host-guest interaction energies. We have just commented the discrepancies with the experimental uptakes in terms of nonideality of the actual samples; in our view, GCMC simulations on perfect PAF crystals can be considered as upper bounds for the adsorption behavior of real materials, provided reliable force fields are used.
More results have been obtained for the CO_2 adsorption in other porous materials, including metal organic frameworks (MOF) and covalent organic frameworks (COF), as shown in Table 10, where gravimetric uptakes are reported for some of the best performing materials.

Material	SSA_{Bet} ($m^2\ g^{-1}$)	T (Kelvin)	P (bar)	Excess CO_2 Uptake ($mg\ g^{-1}$)	Ref.
PAF - 302	5519	298	10	1164	this work
			37	2142	
			50	2040	
PAF - 1	5600	298	37	1291	[137]
MOF-210	6240	298	50	2437	[90]
COF - 102 (Model)	4434	298	10	749	[194]
COF - 102 (Experimental)	3620	298	55	1200	[7]
COF - 103	3530	298	55	1190	[7]
Li-COF-102	5005	298	10	1012	[199]
ACB-5	3537	298	18	909	[200]
MIL-100V	1203	298	10	440	[201]
Nu-Bai12	1327	298	20	873	[202]

Table 12: CO_2 excess gravimetric uptake in different materials

The data in Table 12 clearly show that PAF-302 can be an exceptional adsorber for CO_2; for instance, its excess uptake at 298 K and 50 bar in PAF-302 is predicted to be as high as 2072 mg/g, among the best results reported so far.
The ability of a material as a gas adsorber depends on the interactions that are established between the gaseous molecules and the material surface, mainly inside the pores.

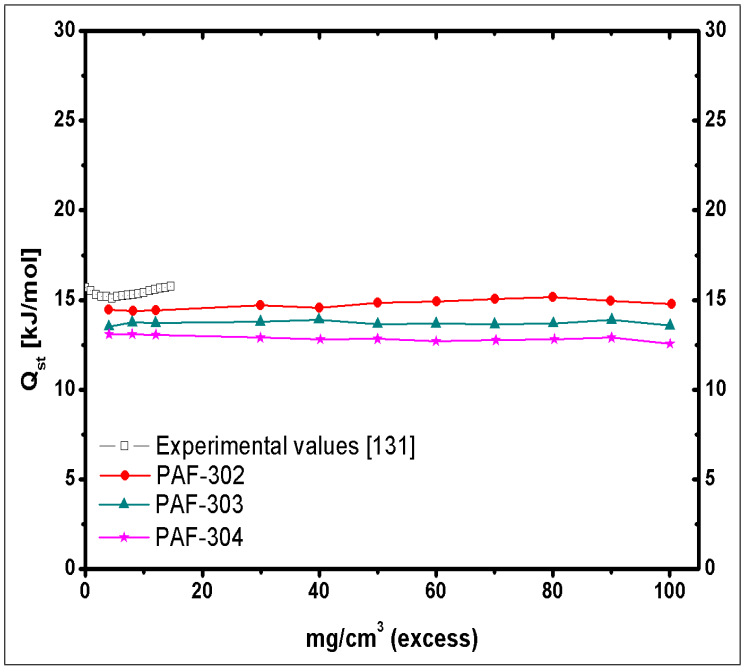

Figure 4.50: Adsorption isosteric heat (kJ/mol) for PAF-30n and comparison with experimental values for PAF-302.

In Figure 4.50, the isosteric heat is reported as a function of the gas loading for PAF-302, 303, and 304 (PAF-301 saturates so quickly at low pressure that it is difficult to obtain reliable data at different temperatures).
The three materials exhibit very similar Q_{st} values up to an excess loading of about 40 mg/cm^3, reflecting the similarity in the gas/surface interactions.
Simulated Q_{st} for PAF-302 can also be compared to experimental values. The comparison shows that our model is in very good agreement with the measures reported by Ben et al. [10]
In conclusion, as shown for the other gases, the present simulations show how all the modeled PAFs exhibit a very high affinity for the carbon dioxide, with adsorbed densities always larger than compressed gas density and how the PAF-302 has an enormous potential as CO_2 adsorber in a large pressure range.

4.10.6 Functionalized PAF-302: CO_2 adsorption

Although PAFs are relatively new materials, their performances in gas adsorption have been deeply studied with various techniques.
Some works have pointed out that the adsorption of methane, hydrogen, and CO_2 can be enhanced by a suitable derivatization of the parent PAF-302 (the only member of the PAF-30n family actually synthesized so far).
The proposed functionalizations include the postsynthesis lithiation, the treatment with sulfonic acid/lithium sulfonate, and also the carbonization (possibly with KOH activation). [204]

The last approach leads to a partial collapse of the PAF structure with the formation of ultramicropores besides the usual PAF-302 micropores.
The best results, at least at low pressure, were obtained in PAF-302 functionalized with NH_2CH_2 moieties. [198]
Experimentally, these materials can be prepared starting from precursors tetrabromo phenylmethane (TBPM), properly functionalized, as in this specific case of the PAF-302-CH_2-NH_2, through the "de novo synthesis" and a post-synthesis deprotection, as summarized in Figure 4.51.

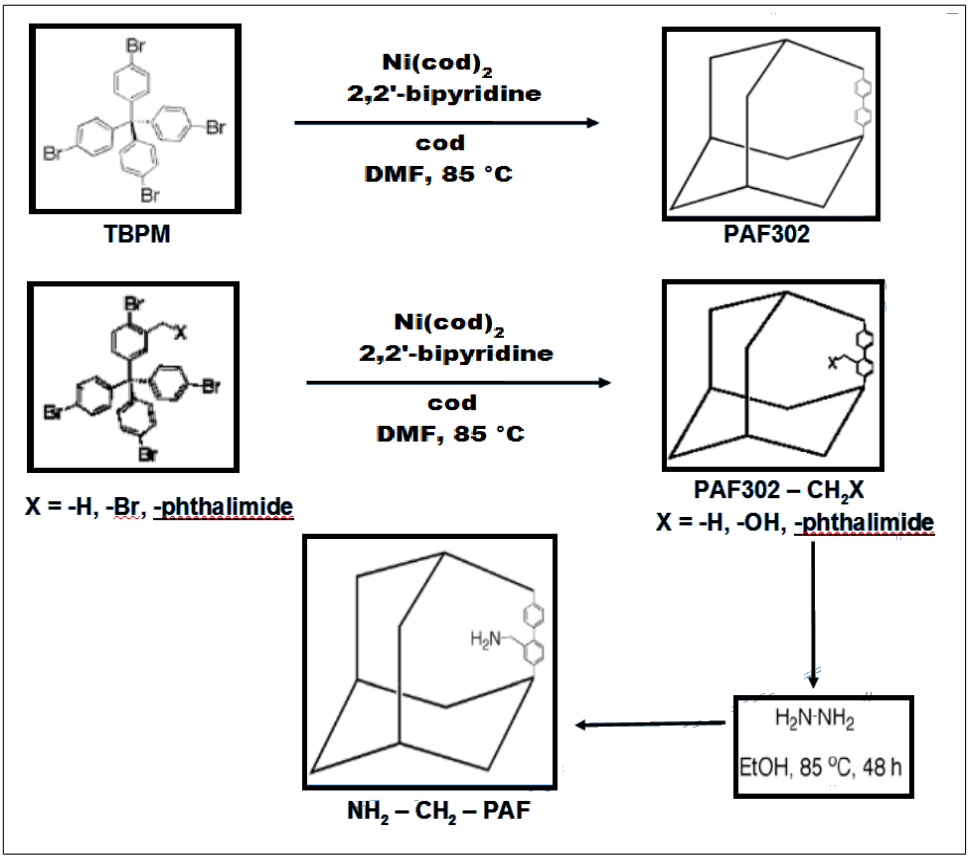

Figure 4.51: the de novo synthesis from different precursors of PAF-302, PAF-302CH_3, PAF-302-CH_2OH and PAF-302-CH_2-phthalimide (X = H, OH, or phthalimide, respectively) from the corresponding functionalized tetrakis(4-bromophenyl) methane tetrahedral building units and the post-synthesis deprotection of PAF-302-CH_2-phthalimide with hydrazine to give PAF-302-CH_2-NH_2.

Besides, recent calculations predicted that the addition of polar moieties (tetrahydrofuran-like rings fused with the biphenyl rings) should improve the gas loading markedly. [180]
In addition, a rich literature exists about the effect of functionalized ligands on CO_2 adsorption in metalorganic frameworks, which has evidenced the very promising effects of aromatic and amino-aromatic moieties, thanks to enhanced polar interactions. [218–220]
Therefore, we decided to simulate the adsorption in several modified PAF-302, first adding aminomethyl and tolyl groups, then using other moieties that somehow combine these functional groups, including imidazole (Imi) and pyrimidine (Pyr).
The complete list of functional groups is reported in Figure 4.52.

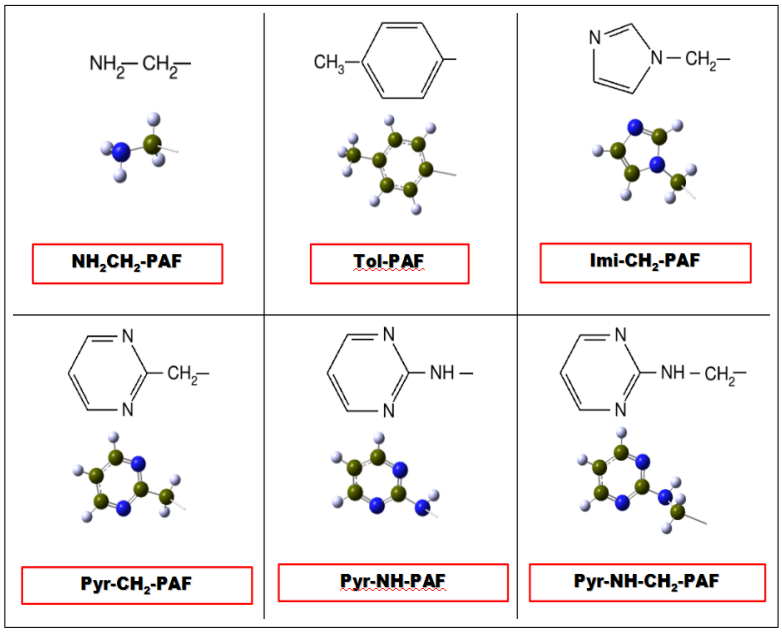

Figure 4.52: Functional groups attached to biphenyl chains in PAF-302. Lewis structure, ball-and-stick model, and name of the corresponding functionalized PAF-302 are indicated for each group.

Besides the nature of the attached group, the degree of functionalization is also an important parameter. PAF-302 is usually synthesized by Yamamoto coupling from tetrakis(pbromophenyl)methane, so that when one, two, or four phenyl rings are derivatized in the reactant, functionalized PAF-302 with 25%, 50%, or 100% modified aromatic rings are obtained, respectively. Since the PAF-302 unit cell contains 16 biphenyl linkers, R-PAF(25%), (50%), and (100%) have 8, 16, and 32 functional groups in the unit cell, as shown in Figure 4.53.

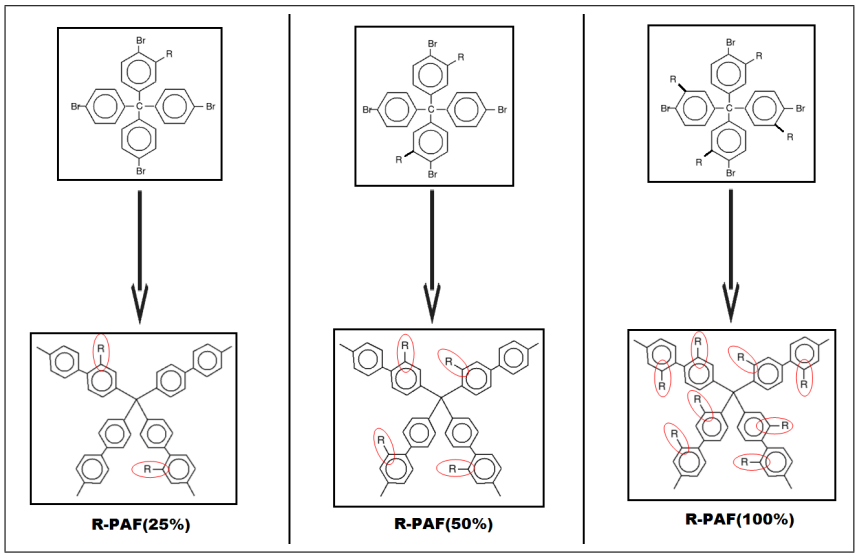

Figure 4.53: Substituted tetrakis(p-bromophenyl)methane giving rise to PAF-302 with one,two or four functional groups per biphenyl chain, on average and derivatized PAF-302 lattice with one-fourth (25%), one-half (50%), and all (100%) phenyl rings are created.

The unit cell parameters and the atomic coordinates for all of the substituted PAF-302 were optimized with the Materials Studio Forcite module. Some structural properties, requiring a measure of the skeletal density of the simulated materials, were estimated using the GEPOL procedure and the structural data for all of the optimized simulated materials are listed in table 13.

	unit cell formula	unit cell volume (Å^3)	density (g cm^{-3})	specific volume (cm^3 g^{-1})	unit cell skeletal volume (Å^3)	porous volume fraction	specific porous volume (cm^3 g^{-1})	specific surface area (m^2 g^{-1})
Tol-PAF(25)	$C_{256}H_{176}$	12914	0.418	1.79	3243	0.75	1.79	5414
Tol-PAF(50)	$C_{312}H_{224}$	12913	0.511	1.96	4057	0.69	1.34	5177
Tol-PAF(100)	$C_{424}H_{320}$	12501	0.719	1.39	5659	0.55	0.76	4643
NH2-CH2-PAF(25)	$C_{208}N_8H_{152}$	13033	0.352	2.84	2717	0.79	2.25	5473
NH2-CH2-PAF(50)	$C_{216}N_{16}H_{176}$	13032	0.382	2.62	2946	0.77	2.03	5381
NH2-CH2-PAF(100)	$C_{232}N_{32}H_{224}$	12856	0.447	2.24	3536	0.73	1.62	5133
Imi-CH2-PAF(25)	$C_{232}N_{16}H_{160}$	13073	0.403	2.48	3177	0.76	1.88	5219
Pyr-CH2-PAF(25)	$C_{240}N_{16}H_{160}$	13102	0.414	2.41	3218	0.75	1.82	5252
Pyr-NH-PAF(25)	$C_{232}N_{24}H_{152}$	13034	0.417	2.40	3174	0.76	1.81	5215
Pyr-NH-PAF(50)	$C_{264}N_{48}H_{176}$	12975	0.515	1.94	3840	0.70	1.37	4874
Pyr-NH-PAF(100)	$C_{328}N_{96}H_{224}$	13085	0.699	1.43	5199	0.60	0.86	4290
Pyr-NHCH2-PAF(25)	$C_{240}N_{24}H_{168}$	13026	0.432	2.32	3325	0.74	1.72	5177
Pyr-NHCH2-PAF(50)	$C_{280}N_{48}H_{208}$	12895	0.547	1.83	4342	0.66	1.21	5113
Pyr-NHCH2-PAF(100)	$C_{360}N_{96}H_{288}$	12918	0.766	1.31	5819	0.55	0.72	4361

Table 13: Structural parameters for the simulated PAFs.

Considering these new functionalized groups in the structure, the force field described above for the CO_2 adsorption has been adjusted. Classical and MP2 energies were compared for CO_2 interacting with phenyl-CH_2-R (R = NH_2, imidazole, pyrimidine).
In the Figure 4.54 some energy configurations are presented:

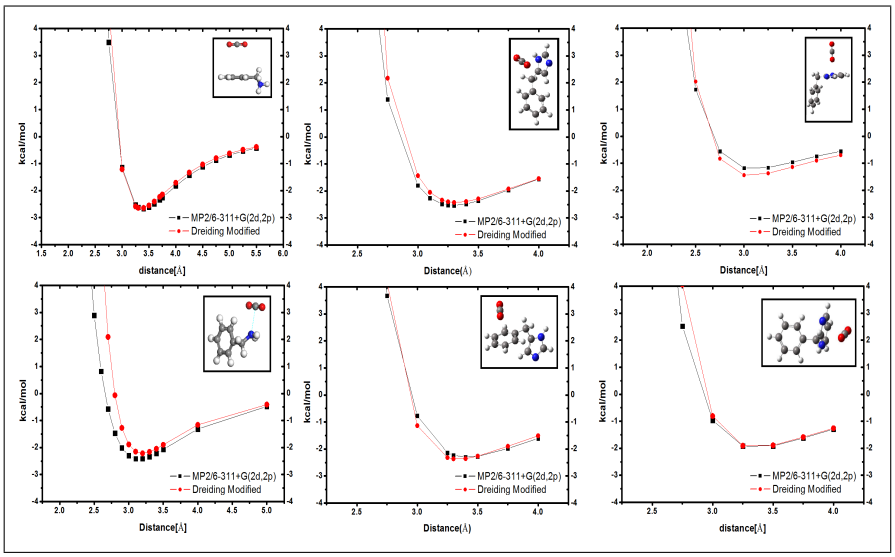

Figure 4.54: CO_2 - functionalized fragments interaction energy (kcal/mol) computed with the modified FF (circle, red) and at MP2-6-311+G(2d,2p) level (square, black), including the correction of the BSSE.

The modified parameters are listed in Table 14.

Atom Type	Dreiding Symbol	D (kcal/mol)	σ (Å)
amino nitrogen	N_3	3.0621	0.5774
amino hydrogen	H_A	2.8550	0.0350
heterocyclic nitrogen	N_R	3.6621	0.0974

Table 14: FF parameters used in the modified force field for the functionalized PAF-302. The parameters for the carbon and oxigen of carbon dioxide and for the aromatic carbon are the same described in the last section. For all the other atom types the standard Dreiding LJ parameters were used.

As was already noted, suitable functionalizations are expected to increase the CO_2 adsorption in PAF markedly, at least at low pressure.
All the adsorptions of the functionalized PAF-302 with 25% substitution degree (i.e., with 8 functional groups per unit cell) are shown in Figure 4.55 and in Figure 4.56; the curves for the unmodified PAF-302 are also shown for comparison.

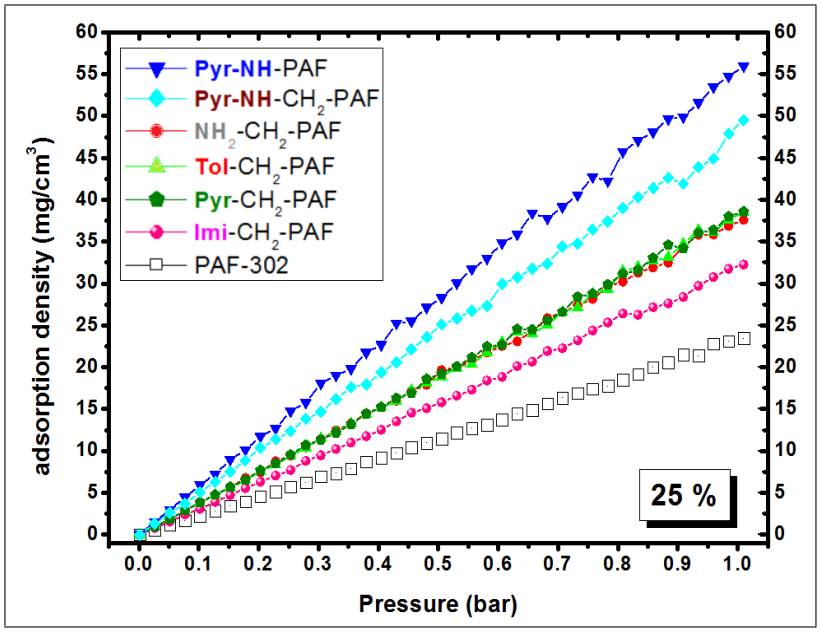

Figure 4.55: CO_2 adsorbed density in functionalized PAF-302 at low pressure at 298 K, with 25% substitution. Empty black squadre, unmodified PAF-302; purple sphere, Imi-CH_2-PAF; red circle, NH_2-CH_2-PAF; light green triangle, TolPAF; green pentagon, Pyr-CH_2-PAF; light blue diamond, Pyr-NH-CH_2-PAF; blue triangle, Pyr-NH-PAF.

Between 0 and 1 bar at 298 Kelvin, it is observed that all the functionalized materials have a greater adsorption capacity then unmodified PAF-302 and in particular, the best adsorption material is Pyr-NH-PAF-302 that is more than 2.5 times higher than in the unmodified system.
The second and third best performances are provided by Pyr-NH-CH_2-PAF and Pyr-CH_2-PAF (with loadings 2.25 and 1.75 times higher than in PAF-302), clearly indicating that pyrimidine is the most promising functional group for this kind of application.
Tolyl and aminomethyl groups enhance the adsorption to a good extent, too, proving almost as efficient as Pyr-CH_2-PAF in this pressure range; on the other hand, imidazole group

provides quite a poor performance.
The picture is quite different when high pressures are considered, as shown in Figure 4.56.

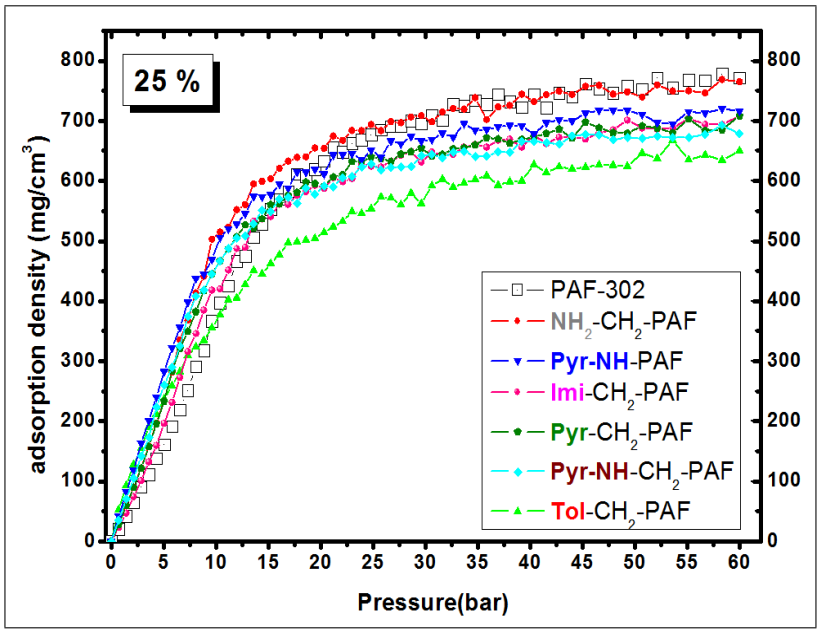

Figure 4.56: CO_2 adsorbed density in functionalized PAF-302 at high pressure at 298 K, with 25% substitution.

On the contrary, at low pressures where the functionalized material adsorbed more than PAF-302, looking at high pressures, only the NH_2-CH_2-PAF can almost equate the performance of adsorption of the unmodified material.
Apparently at higher pressure, when the adsorbed gas density grows, the available porous volume becomes more important than the strength of gas-surface interactions, which predominates at low pressure. Indeed, as seen in the Table 13, PAF-302 and NH_2-CH_2-PAF have the largest specific porous volume in the series, that is, 2.58 and 2.25 cm^3/g, while none of the other materials exceeds 1.90 cm^3/g.
This analysis is confirmed by the cumulative pore volume and by the pore size distributions (Figure 4.57) of the best models at the two range of pressure:

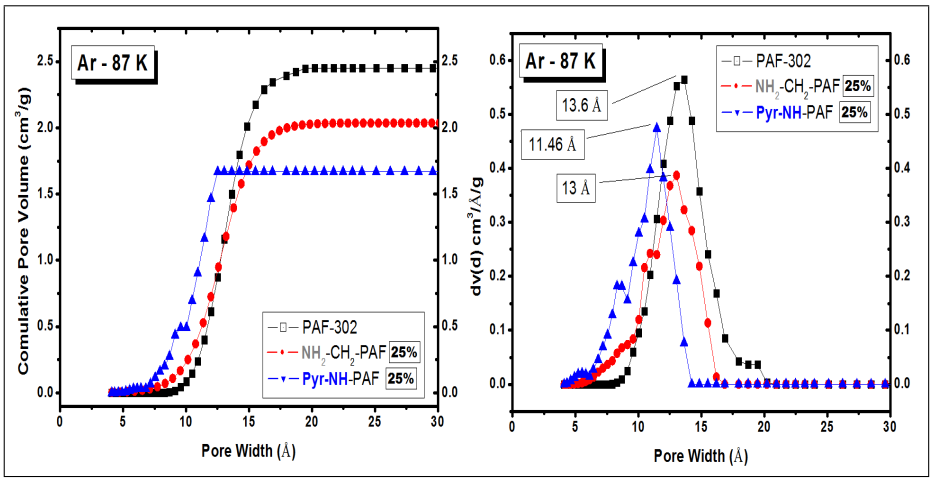

Figure 4.57: Cumulative pore volume and pore size distributions: (empty black square) PAF-302, (red circle) NH_2-CH_2-PAF and (blue triangle) Pyr-NH-PAF.

Cumulative pore volume (CPV) and pore size distribution curves for the functionalized PAF-302 materials were determined from appropriately fitting density functional theory (DFT) models.
As for the study of the argon adsorption described in the section 4.10.1, the lowest fitting error is obtained by the NLDFT model applied on silica/zeolite surfaces with cylindrical pores.
The best adsorbent materials at low pressure, Pyr-NH-PAF, along the entire pressure range, NH_2-CH_2-PAF, and at high pressure, PAF-302 were compared to understand their different porosimetries, which have allowed their performances.
The data of surface area and porosity of the materials are shown in table 15.

Model	SSA_{Bet} ($m^2\ g^{-1}$)	Density (g/cm^3)	Total Pore Volume (cm^3/g)	Micropore Volume (cm^3/g)	
				<10 Å	10 <Å<20
PAF-302	5550	0,315	2,451	0,087	2,364
NH_2 - CH_2 - PAF - 302 (25%)	5473	0,352	2,037	0,220	1,810
Pyr - NH - PAF -302 (25%)	5215	0,414	1,669	0,490	1,179

Table 15: BET surface area and pore size distribution obtained from Ar physisorption measurements at 87 K.

The Pyr-NH-group occupies a lot of free volume within the material and the size of the pores decreases drastically.
However, the strong interaction between this functional group with the gas and the presence of ultramicroporosity, which passes from 0.087 in the case of PAF-302 to 0.490, allows rapid adsorption, although there is a fast saturation which disadvantages the CO_2 storage at pressures greater than 15 bar.
The decrease of the total pore volume is in accordance with the decrease of the surface area.
On the contrary, the material NH_2-CH_2-PAF has a pore distribution most similar to PAF-302, with an average pore size around 13 Å, although the ultramicroporous volume increases compared to the PAF-302.
The microporous volume of this functionalized material allows a good gas storage along the entire pressure range.
In Figure 4.58, the simulated excess adsorptions in NH_2-CH_2-PAF are compared to the experimental results presented in ref. [199]

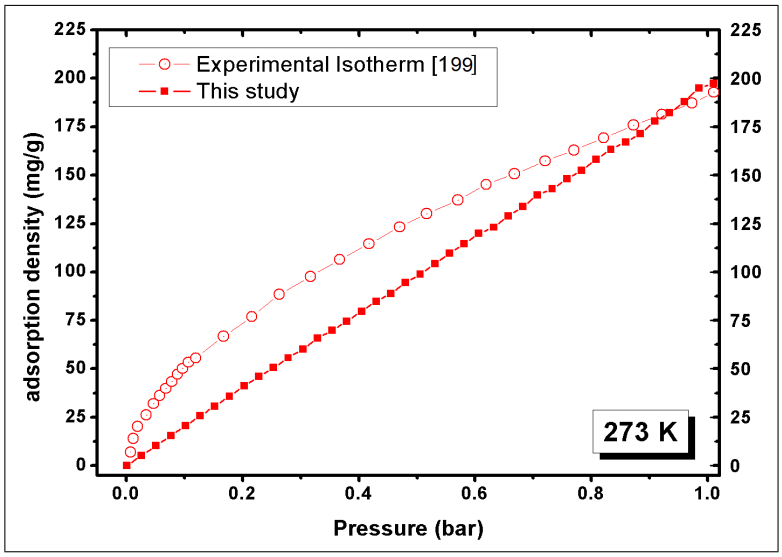

Figure 4.58: Comulative pore volume and pore size distributions: (red square) NH_2-CH_2-PAF model; (empty red circle) experimental NH_2-CH_2-PAF;

The agreement is quite good, although the measured isotherm grows more steeply at very low pressure, and starts bending as in near-saturation regime at 1 bar, while the simulated curve is almost linear in this pressure range.
The former behavior is quite typical of ultramicroporous materials, as seen for instance in the simulated isotherms in PAF-301, and it could be explained by an imperfect polymerization leading to a lower porous volume than in the ideal crystalline material.

	Specific surface Area (m^2/g)	Density (g/cm^3)	Rif.
PAF-302 Exp.	4100	0,34	[199]
PAF-302	5500	0,315	this work
NH_2-CH_2-PAF Exp.	1363	0,7	[199]
NH_2-CH_2-PAF	5473	0,352	this work

Table 16: Comparison between our models and Garibay et al. [198] structural properties.

NH_2-CH_2-PAF surface area measured in ref. [199] was an average from at least two indipendent experiments and the value is 1363 m^2/g (to be compared to 4100 m^2/g for the starting PAF-302), with a corresponding reduction, of the porous volume from 2.73 to 0.74 cm^3/g and a 2 Å decrease of the dominant pore diameter.
Comparing this data with the ideal structural properties listed in Table 16, the changes can't be explained simply by the steric hindrance of the added functional group, but they are likely due to a partial collapse of the crystalline structure.
Increasing the degree of functionalization (i.e., passing to materials with 16 and 32 functional

groups per unit cell), the adsorption isotherms for some of the models seen before were simulated and they are shown at low pressures (Figures 4.59) and at high pressures (Figure 4.60). At low pressure the CO_2 uptake is higher than in standard PAF-302.

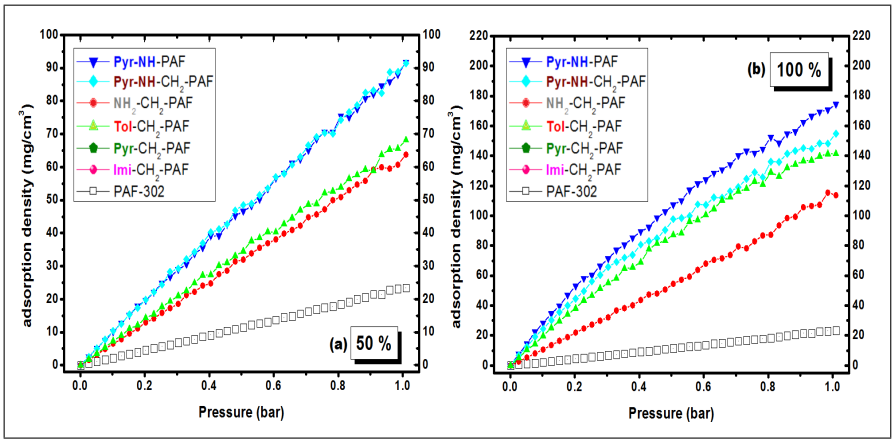

Figure 4.59: CO_2 adsorbed density, in absolute volumetric adsorption, at low pressures in functionalized PAF-302 at 298 K, with (a) 50% substitution and (b) 100% substitution.

With 50% functionalization degree, Pyr-NH-PAF adsorb up to 6.7 times more gas than PAF-302, reaching an adsorbed density of 187 mg/cm^3 at 1 bar, while NH_2-CH_2-PAF and Tol-PAF present a gain factor of about 4.6.
In the 100% derivatized material, the trend is even more evident, with uptakes 8.5-10.5 times higher than in PAF-302. At 1 bar the best performing material is Pyr-NH-PAF(100%), which adsorbs 305 mg/cm^3, although its isotherm shows a near-saturation bending.
At higher pressures the porous volume becomes determinant.

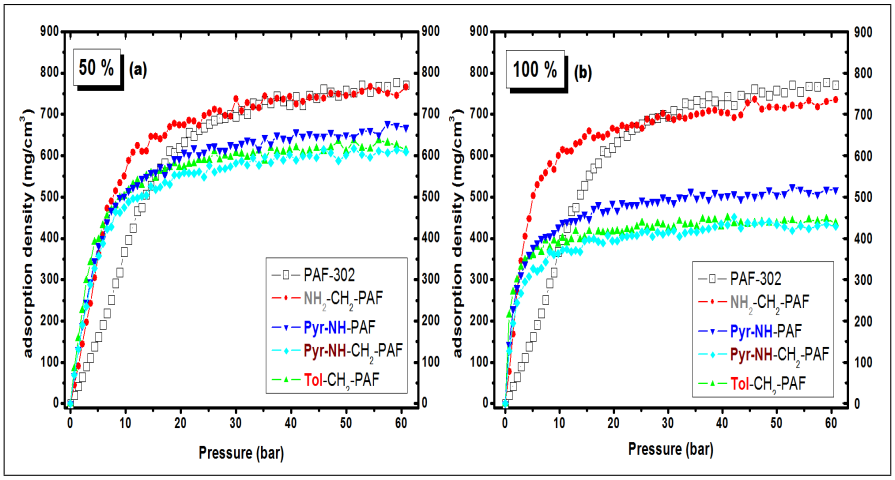

Figure 4.60: CO_2 adsorbed density, absolute volumetric adsorption, at high pressures in functionalized PAF-302 at 298 K, with (a) 50% substitution and (b) 100% substitution.

Above 25 bar the unmodified PAF-302 is able to adsorb more gas than the functionalized counterparts, both at 50% and at 100% substitution degree.
The pore size distribution explains these behaviors by the functionalized models at different pressures, as shown in Figure 4.58 taking into consideration the case of Pyr-NH-PAF.

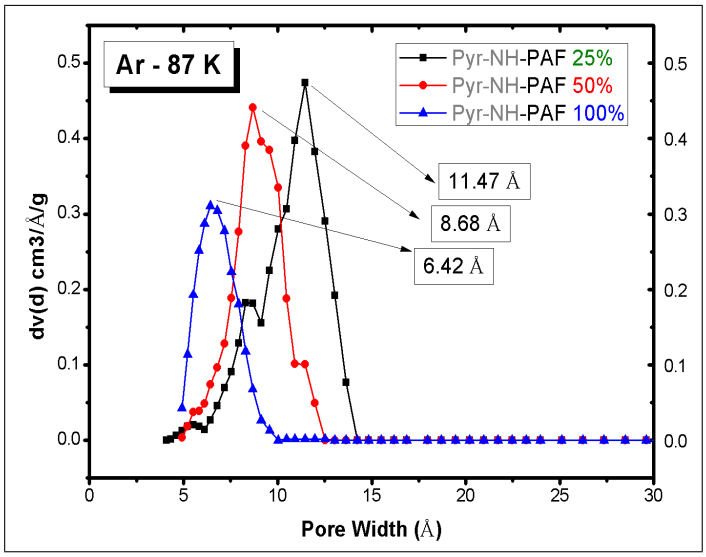

Figure 4.61: Pore size distribution for the Pyr-NH-PAF model at different fuctionalization degrees: black square 25%, red circle 50% and blue triangle 100%.

The increase of the functionalization degree is proportional to the decrease of the free volume within the models.
In fact, the pore size decreases, the affinity of the material with CO_2 increases at low pressures, but at the same time the saturation of the material occurs rapidly.
However, NH_2-CH_2-PAF performs almost equally well at high pressure, besides being clearly more efficient than PAF-302 at intermediate pressure (120 bar).
In the Table 17, the total volumetric and gravimetric comparison, for all the models discussed in this section, is shown:

Material	1 bar	Carbon dioxide Absolute adsorption		10 bar	Carbon dioxide Absolute adsorption		40 bar	Carbon dioxide Absolute adsorption	
	T (K)	(mg / cm^3)	(mg/g)	T (K)	(mg / cm^3)	(mg/g)	T (K)	(mg / cm^3)	(mg/g)
PAF-302	**298**	**42**	**131**	**298**	**397**	**1261**	**298**	**744**	**2361**
Tol-PAF 25%	298	74	177	298	377	902	298	627	1499
Tol-PAF 50%	298	135	265	298	517	1011	298	620	1213
Tol-PAF 100%	298	240	334	298	401	558	298	450	627
NH_2-CH_2-PAF 25%	**298**	**71**	**202**	**298**	**515**	**1463**	**298**	**732**	**2079**
NH_2-CH_2-PAF 50%	298	129	338	298	589	1541	298	725	1899
NH_2-CH_2-PAF 100%	298	270	605	298	615	1375	298	703	1573
Imi-CH_2-*PAF* 25%	298	57	143	298	420	1043	298	677	1680
Pyr-CH_2-PAF 25%	298	74	188	298	467	1186	298	673	1708
Pyr-NH-PAF 25%	298	109	261	298	516	1212	298	678	1624
Pyr-NH-PAF 50%	298	186	361	298	505	1000	298	657	1276
Pyr-NH-PAF 100%	298	307	439	298	439	628	298	503	720
Pyr-NH-CH_2-PAF 25%	298	97	224	298	467	1082	298	666	1543
Pyr-NH-CH_2-PAF 50%	298	188	345	298	488	893	298	589	1077
Pyr-NH-CH_2-PAF 100%	298	265	347	298	372	485	298	432	564

Table 17: Comparison between functionalized PAF-302 models.

The resulting data show that functionalized PAFs, especially the groups of Pyr-NH-PAF could be the most promising materials for applications at low or atmospheric pressure (for instance, postcombustion CO_2 separation and capture), while at high pressures (as required, for instance, in massive gas storage) unmodified PAF-302 is preferable.
A very good compromise is represented by NH_2-CH_2-PAF at high substitution degree, whose performance is close to the best in the whole pressure range.

4.11 Conclusion

In this part of the work, the performances of the PAF-30n have been evaluated, through GCMC simulations, by measuring N_2, Ar, CH_4, H_2 and CO_2 adsorption capacities of the material at several temperatures and in a wide range of pressure.
First of all, the structural properties of four types of PAF-30n were examined. The PAF-30n can be modeled starting from the diamond structure replacing each C-C covalent bond with one or more phenyl groups. The skeletal volume and the effective surface area were estimated by the GEPOL procedure implemented in Gaussian 09.
After explaining some aspects of the analysis of adsorption isotherms, the gas storage of all the gases was simulated with Monte Carlo technique and compared to the corresponding experimental isotherms, when possible.
Force fields employed in the simulations were optimized to fit the correct behavior of the free gas in all the pressure range and to reproduce the gasphenyl interactions computed at high quantum mechanical level (post HartreeFock).
The pore distributions were investigated by applying nonlocal density and quenched state solid functional theory analysis (NLDFT and QSDFT, respectively) to the adsorption isotherms of Ar at 87 K and N_2 at 77 K (the former being more suited for pore widths less than 10 Å).
The results allowed to describe the experimental sample defectivity compared with our theoretical ideally cristalline model and to understand the differences between each kind of material of the PAF-30n family. Indeed, the good performance at low pressure of the PAF-301 can be attributed to the abundance of ultramicropores.
Then methane was studied and all the examined materials showed a high affinity for methane, ensuring a larger storage than simple compression in all the conditions.
PAF-301 exceeds the target proposed by U.S. Department of Energy at 35 bar for methane storage in low-pressure fuel tanks and PAF-302 almost meets the target fixed.
Moreover, a vibrational study about the interactions of methane with the surface of the porous frameworks was presented. The precursor, tetrakis(4-bromophenyl) methane (TBPM), and the polymer were studied with FTIR and Raman spectroscopies to investigate the structure of PAF-302, whereas the system after methane adsorption was studied by FTIR, also varying the CH_4 loading, to get some hints on the strength of the interactions with adsorbed methane.
Theoretical calculations of the harmonic frequencies of TBPM, methane, and methane/aromatic model systems were performed at high theory level (MP2 with extended basis set) to support the assignment of vibrational bands and to estimate the interactions causing the observed frequency shifts upon methane adsorption.
The analysis shows that the polymerization process is essentially complete and that the adsorbed CH_4 molecules interact with two phenyl rings and finally, a GCMC approach was used to simulate the methane adsorption isotherm in the conditions adopted for FTIR experiments.
The hydrogen storage is strongly correlated to the amount of very small pores and in the range of pressure taken into account, the ultramicroporosity of the PAF-301 makes this material better in the excess adsorption than PAF-302.

Finally the adsorption isotherms of CO_2 were studied and PAF-302, which shows the best combination of specific area and microporosity, has an effective predicted uptake of 660 mg/cm^3, one of the highest uptakes reported so far, and it is one of the best candidate for the CO_2 storage.
Even better results can be obtained by a suitable functionalization of PAF-302; different chemical groups, which can be actually included in PAF synthesis, have been tested to find the most promising ones and support the synthetic efforts. Also, the degree of functionalization has been considered, modeling materials with 25%, 50%, and 100% substituted phenyl rings.
The results show that functionalized PAF-302 improves the CO_2 uptake dramatically at low pressure. The most efficient functional group is pyrimidine, especially using NH linker, which increases the adsorbed gas density at 1 bar by 2.5, 6.7, and 10.5 at 25%, 50%, and 100% substitution degree, respectively.
On the other hand, at higher pressures the larger porous volume of unmodified PAF-302 becomes determinant, and the latter material provides the best performance; however, NH_2-CH_2-PAF, especially at high substitution degree, proved to be almost as efficient as PAF-302.

5 Computational details and results: mPAF

5.1 Introduction

Hyper-Crosslinked Polymers (HCPs) are a class of low cost porous organic networks easily prepared through Friedel-Crafts reaction. The permanent porosity in HCPs is a result of extensive crosslinking reactions of aromatic units, which prevents the polymer chains from collapsing into a dense, nonporous state. [121]
The extensive crosslinked nature of the materials confers them high thermal stability that is not commonly expected for organic polymers. The stability, combined with high surface areas and simple, cost-effective and easy to scale-up preparation, make HCPs highly promising materials for fuel gas storage (methane and hydrogen) and carbon dioxide capture applications. [120]
Our experimental group, as explained in the previous chapters, has explored the polymerization based on the Friedel-Crafts TPM / FDA reaction, with the aim of producing good adsorbents also for various gases and as for the naming, the acronym PAF (porous aromatic framework) is suited for this kind of system, though it was originally proposed for materials obtained by a different route and, more important, with wider pores.
The synthesis conditions were optimized by investigating how the porosity and the surface area of the final material depend on the reagent stoichiometry, varying the aromatic monomer/cross-linking agent ratio.
The aim was to increase especially the microporous volume, and in particular the fraction of smallest pores, below 10 Å width, which are expected to lead to high gas uptake also at low pressures, [46] but in addition to the main coupling mechanism other side reactions due to the presence of excess of Lewis acid and FDA are possible.
The narrow distribution of ultramicropores suggests that a part of the material is regularly polymerized, indicating the presence of ordered islands surrounded by less regular and amorphous regions.
The aims of this PhD chapter to support the characterization of mPAF materials were focused on:

- Defining periodic molecular models as a network of tetraphenylmethane moieties connected by methylene bridges in para position.
- Building an ideal crystal structure to confirm the pore size of the regularly polymerized material.
- Building amorphous models with different core networks to recreate the polycristalline structure of the material.
- Analyzing the porosimetry of the models with functional groups from other side reactions within the structure.
- Comparing computational results, made on optimized structures, with those obtained from experimental measurements.

5.2 Synthesis and characterization: quick review

A new method for preparing microporous polymers by using formaldehyde dimethyl acetal (FDA) as crosslinking agent to polymerize various aromatic monomers has been reported. [123]
During their extensive research on organic materials, Cooper and co-workers applied this approach to the polymerization of the rigid aromatic structure of tetraphenylmethane (TPM) obtaining materials with good CO_2 storage properties. [124]
Our experimental group has applied the Friedel-Crafts reaction using formaldehyde dimethyl acetal (FDA) to crosslink various tetrahedral aromatic monomers in order to get different microporous polymers.
The reaction mechanism concerning the use of the FDA linker agent can be described in this way:

- Lewis acid attacks the FDA with the formation of an oxocarbenium ion.
- Electrophilic aromatic substitution reaction between the intermediate and the aromatic ring results in the formation of a resonance stabilized carbocation. The carbocation intermediate loses a proton and the aromaticity is restored.
- The resulting ether undergoes rapid cleavage with iron chloride to give methanol and the carbocation intermediate, which undergoes a further electrophilic aromatic substitution generating a methylene bridge between two aromatic rings.

In addition to the main coupling mechanism other side reactions due to the presence of excess of Lewis acid and FDA are possible (Figure 5.1):

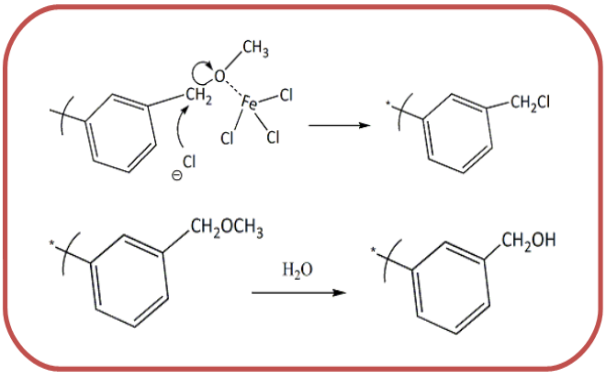

Figure 5.1: Reaction mechanism for the side products formed during the synthesis of the HCP polymers by Friedel-Crafts reaction.

The presence of these entrapped impurities is also demonstrated by IR spectroscopy and SS-NMR. [141]
The experimental research work was focused on the optimization of the Friedel-Crafts synthetic conditions: the ratio between the monomer TPM and the linker FDA was changed in order to optimize the porous properties of the polymers.
Because Friedel-Crafts alkylation is unselective under the conditions employed, substitution on the aromatic rings cannot be easily controlled. However, by changing the amount of electrophile, some degree of control over polymerization rate and cross-linking extent could be achieved.
The experimental group focused their study on understanding how different synthetic conditions and reagent ratios can influence the microscopic structure of the materials modulating

both porosity and surface area that are the main features controlling gas loading by physisorption on a porous structure.
Indeed, different reaction conditions, which in principle could modulate the substitution of the aromatic residues from partial to extensive substitution, were explored. In particular all reaction parameters were kept constant except the amount of catalyst and FDA employed as crosslinking agent.
Ideal reaction conditions should exist to grant regular and extended polymerization giving narrow pore size and large surface areas.
This material obtained with this specific Friedel-Crafts synthesis is cheaper and more efficient for an industrial application. In fact, this method led to the deposition of an European patent in collaboration with OMB Saleri and SOL Group companies. [224] The mPAF polymer with the highest surface area and ultramicropore volume was further optimized, in terms of porosity and gas storage capacity, using thermal treatment at a temperature of 380 °C for 16 h.
A comparative investigation of the physico-chemical properties of the prepared polymers was carried out using elemental analysis, FTIR, SS-NMR, PXRD, TGA and N_2 physisorption at 77 K. [141]
The FTIR and SS-NMR show the presence of bands characteristic indicating a predominant 1,4-substitution and the polymer porosity was analyzed by adsorbing gas at low temperature and this analysis clearly shows the porosimetric differences between PAF-302 and MPAF, as shown in Figure 5.2.

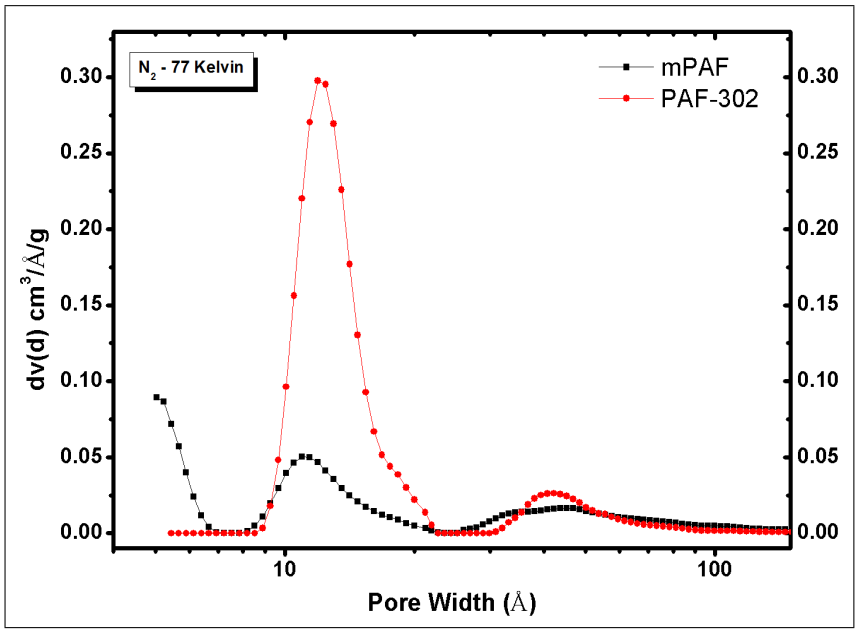

Figure 5.2: Comparison between mPAF and PAF-302. Pore Size Distributions have been obtained by N_2 adsorption.

The pore sizes were calculated using the quenched state density function (QSDFT) applied on carbon surface with slit/cylindrical pore geometry.
The mPAF materials show several families of pores, namely, micropores at 5 and 12 Å and mesopores broadly distribuited over 25 Å.
Although there is a strong decrease of the family of supermicropores, between 10 and 20 Å, mainly in the material PAF-302, the presence of ultramicropores in mPAF makes this polymer very interesting for adsorption of gases, especially at low pressures.
In fact, at low pressures, the favorable trend storage evidenced by the PAF-301, a material

which presents, on the contrary of the mPAF, enormous problems of synthesis, could be approached by this polymer.

Polymer	SSA (m^2/g)	PV (cc/g)	MPV (cc/g)	Density (g/cc)
mPAF	1528	1.04	0.42	**0.53**
PAF-302	4563	2.89	1.26	**0.29**

Table 18: Total pore volume (PV) calculated at P/P_0, Total micropore volume (MPV) up to 20 Å and the density values are obtained from helium pycnometry measurements at room temperature.

The total microporous volume due to pore families corresponding to 5 Å and 20 Å is 0.42 cm^3/g.
A very broad signal is observed above 30 Å and it's attributed to several kinds of mesopores. The total porous volume results in 1.04 cm^3/g and the skeletal density of mPAF was estimated to be about 1.22 g/cm^3 by helium adsorption at room temperature.
This result, along with the porous volume reported above, leads to an apparent density of 0.53 g/cm^3 for this sample.
Table 18 indicates how the suitable pore size, surface area and stability against moisture make these porous materials good candidates for gas storage and separation, especially at low pressures.

Material	Elemental analysis (%)		EDX analysis (%)		
	C	H	Cl	O	Fe
mPAF	88.46	5.60	0.15	5.66	0.13

Table 19: Elemental and EDX analysis of the mPAF material.

However, the elemental analysis (Table 19) showed that the experimental material contain 5-6% of elements other than the expected C and H, as also reported in the literature for analogous polymeric systems. [121, 221]
EDX data reports that small amounts of chlorine, oxygen, and iron are present in the material probably because of side reactions and residues of catalyst.
Polyalkylation of the aromatic rings occurs in excess of FDA, the formation of chloromethyl or hydroxymethyl groups would arise in the presence of chloride ions or traces of water when there is no possibility to cross-link with another TPM unit.
The presence of a narrow distribution of ultramicropores suggests that a part of the material is regularly polymerized, indicating the presence of ordered islands surrounded by less regular and amorphous regions, probably due to the presence of impurities caused by side reactions.

5.3 Models Construction Scheme

To support the characterization of mPAF material, which has a strongly amorphous structure and a synthesis uncomparably cheaper than PAF-302, periodic molecular models were defined as networks of tetraphenylmethane moieties connected by methylene bridges in para position, as shown in Figure 5.3.

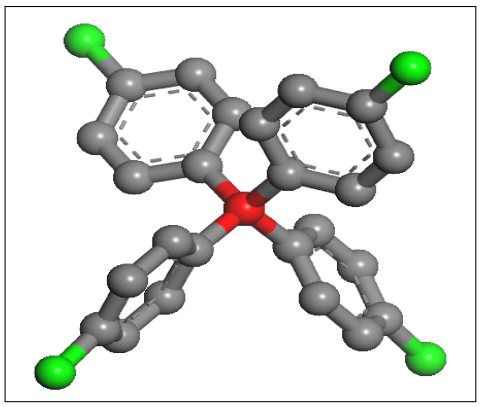

Figure 5.3: Every phenyl of TPM, with a tetra substituted carbon (red atom), has a CH_2 bridge (green atoms).

However, in the experimental sample not completely hypercrosslinked, the phenyl of TPM cannot be crosslinked with a CH_2 bridge and therefore computational models were created with a different intersystem crossing and a different crystalline rate.
The main structures used to model structure and porosity of MicroPorous Aromatic Frameworks are:

- Fully Hypercrosslinked Model (FHM)
- Random Branched Polymer (RBP)
- Random Core/Shell Polymer (RCSP)
- Random Hybrid Polymer (RHP)
- Random Hydrid Polymer with defective groups (RHP_CH_2OH)

Basically all computational models, except in the case of FHM, have followed a common costruction scheme as follows:

* Define the initial monomer with branching points
* Build random polymers with POLYMATIC procedure
* Build amorphous periodic solid with Amorphous Cell (one of Materials Studio packages)

5.3.1 Define Monomer

Starting from an initial monomer, connection points are defined. A binding site may be used as the branching point and must be defined as "head" or "tail". Obviously the polymerization process will take place with the formation of the bond between an head atom and a tail atom.

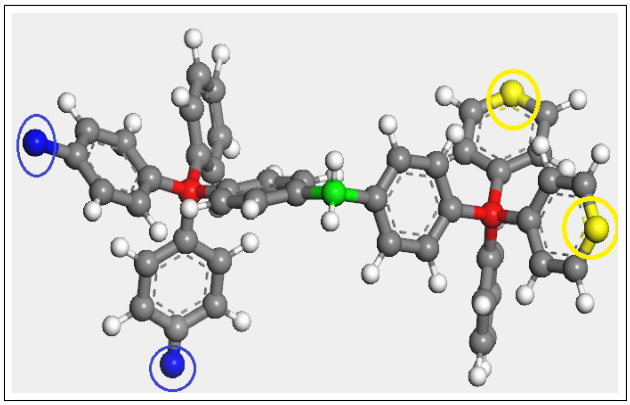

Figure 5.4: Example of initial monomer: red atoms, tetra substituted carbon of TPM, green atom, already formed CH_2 bridge carbon, blue atoms, head carbons, and yellow atoms, tail carbons.

In Figure 5.4, in addition to the carbon already described above, the head atoms and a tail atoms are highlighted. The blue atoms are carbons of CH_2 bridge, while the yellow atoms are carbons of the aromatic ring, the head-tail bond acceptors.

5.3.2 POLYMATIC, random polymeric procedure

The simulation models of all polymers in this PhD work were generated using the open source POLYMATIC simulated polymerization code based on molecular dinamics calculations. A procedure recently defines how to form random polymers or copolymers from any monomer. Polymatic is a set of codes for the generation of amorphous polymers by a simulated polymerization algorithm. The main task of Polymatic is to perform polymerization steps within a system based on a number of defined bonding criteria. It works in conjunction with a simulation package to perform energy minimization throught the CVFF force field and molecular dynamics simulations during the polymerization.

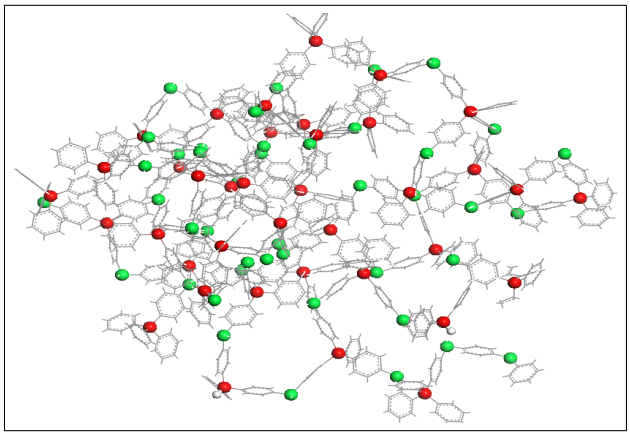

Figure 5.5: Example of polymerization with POLYMATIC procedure: red atoms, tetra substituted carbon of TPM, and green atoms, already formed CH_2 bridge carbons.

In Figure 5.5 an example of polymerization with POLYMATIC procedure is presented. The repeat units were designed in such a way that the resulting polymer was accurate and simulating the synthetic route with a number as greater as possible of inital monomers.

In fact, the software has a limit beyond which the calculations become too expensive computationally. This limit doesn't allow the creation of macroporous models.
The cut-off in which the atoms can link was set, bonds were formed in cycles along with energy minimization and molecular dynamics steps were performed in LAMMPS to produce a well-relaxed initial structure of the polymeric materials at low density.
After the simulated polymerization, the structures were compressed and equilibrated using a step molecular dynamics protocol, which has been utilized for effective structure generation of a wide variety of amorphous materials.

5.3.3 Amorphous periodic solid with Amorphous Cell

Amorphous Cell is a suite of computational tools that constructs representative models of complex amorphous systems and predicts key properties.
The methodology of Amorphous Cell construction is based on an extension of well-established methods for generating bulk disordered systems containing chain molecules in realistic equilibrium conformations.
Initially the polymer from POLYMATIC is optimized with the COMPASS force field to prevent any excessive proximity between the atoms.
Then, the final step is the assembly of the polymer at the same density of the experimental material, i.e 0.53 g/cm^3, building an amorphous periodic solid.

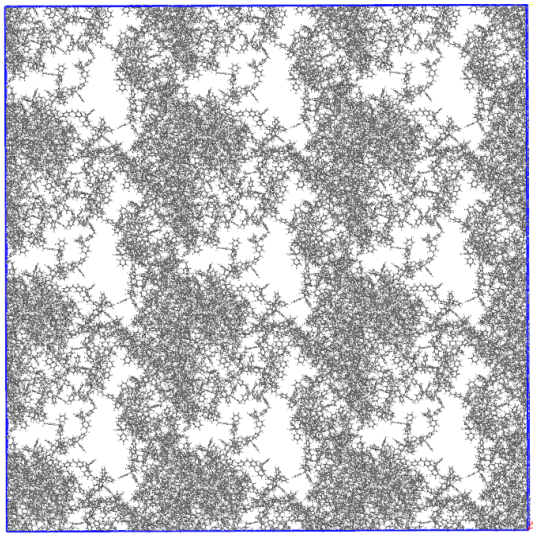

Figure 5.6: Example of amorphous periodic solid.

The polymer thus assembled can be used to obtain reliable GCMC gases simulations within the matrix.

5.4 Cross-linked Index and Crystalline Rate

The first model, FHM, is fully hypercrosslinked, i.e all the phenyls of tetraphenylmethane are connected to another phenyl with a CH_2 bridge as if the polymerization reaction was completed, as shown in the 2D ideal structure in Figure 5.7.

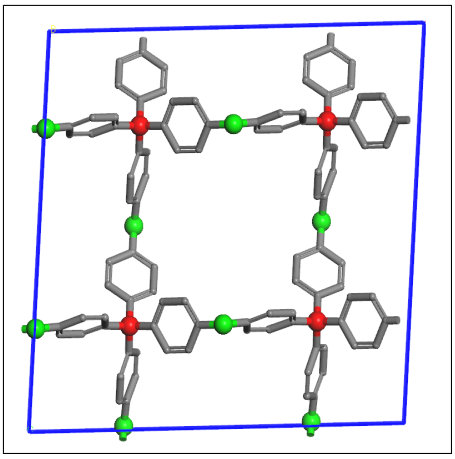

Figure 5.7: 2D representation of complete hypercrosslinked structure showing the sp^3 carbon atoms belonging to TPM (red) and FDA (green).

This model was used as a reference to describe the other models with two different properties:

- Cross-linked Index

$$CI\% = \frac{CH_{2(Amorphous)}}{CH_{2(Crystalline)}} * 100 \tag{5.1}$$

So, as Figure 5.7 shows, in a crystalline figure for every TPM fragment there are two CH_2 bridges.
$CH_{2(Amorphous)}$ is the number of CH_2 bridges present in the polymer considered while $CH_{2Crystalline}$ would be the number of CH_2 in the structure if the material were fully crystalline as in the case of FHM model.

- Crystalline Rate

$$CR\% = \frac{{}_4TPM +_3 TPM}{{}_{Tot}TPM} * 100 \tag{5.2}$$

In polymers not completely hypercrosslinked, not all tetraphenylmethanes are fully connected with their neighbors and the crosslinked branching can end in one or more phenyls of the TPM, as shown in Figure 5.8.

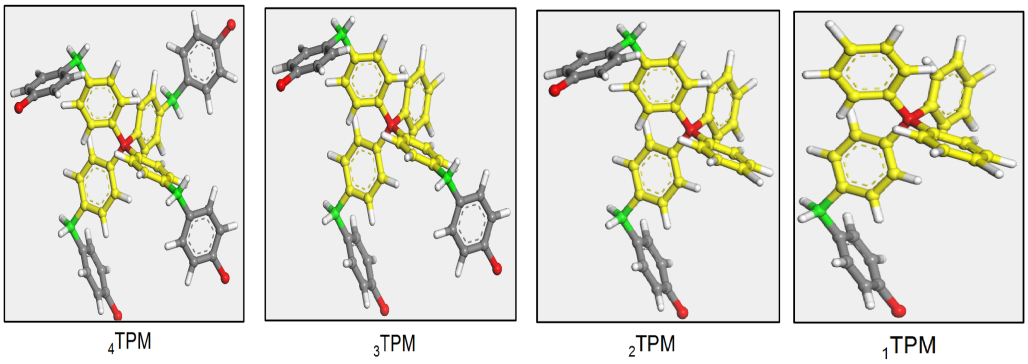

Figure 5.8: Four crosslinked cases of crosslinking that may occur during polymerization.

Therefore, unlike experimental sythesis, for computational polymerization, to control the branching of the different fragments, tri substituted ($_3$TPM) and tetra substituted ($_4$TPM) TPM can be considered to analyze the crosslinked degree of the computational models.
So, the Crystalline Rate is the sum of tetra substituted and tri substituted TPM divided by the number of total TPM.
Obviously the FHM has 100% in both properties.

5.5 mPAF Structures

5.5.1 Fully Hypercrosslinked Model (FHM)

The first model was built starting from the polyaromatic diamond network of PAF-301, described in the previous chapter, and replacing two aromatic rings with H in every second sp^3 carbon.

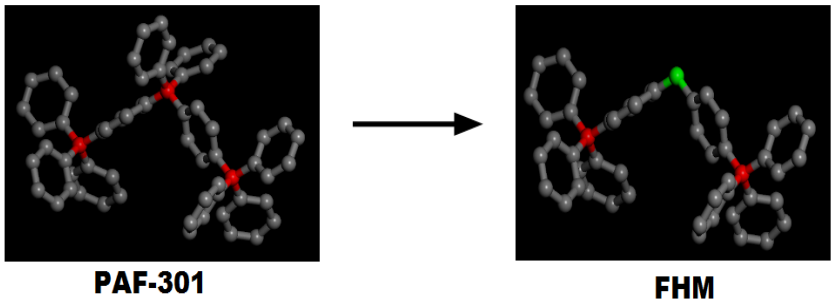

Figure 5.9: The structure's change from PAF-301 to mPAF.

The resulting structure was optimized at the density functional theory (DFT) level with the plane-wave code PWSCF, using the Perdew-Burke-Ernzerhof (PBE) functional and 120 Ry energy cutoff; the periodic lattice is triclinic with P1 symmetry (i.e., no point group symmetry is imposed to leave the largest flexibility to the atoms inside the unit cell).

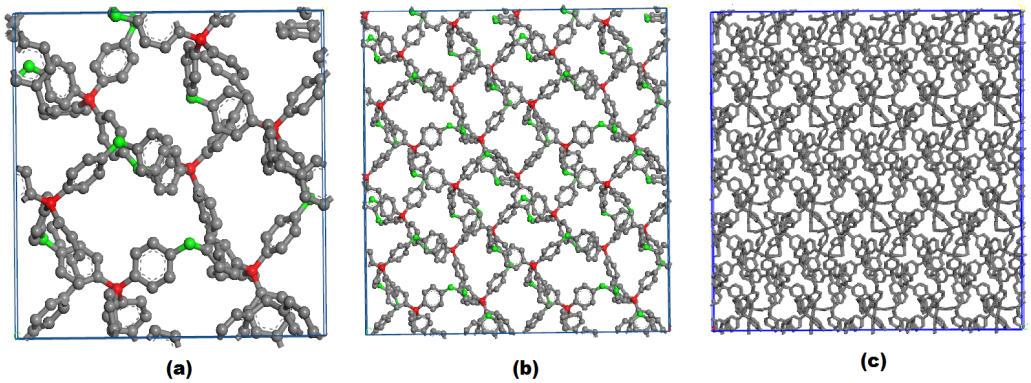

Figure 5.10: Optimized periodic structure of model FHM. (a) Unit cell, showing the sp^3 carbon atoms belonging to TPM (red) and FDA (green); (b) 2 x 2 x 1 supercell and (c) 1 x 3 x 5 supercell highlight the 3D channel structure.

The unit cell with a volume of 21.1 nm^3 and a cell formula of $C_{216}H_{160}$ is reported in Figure 5.10 and it's clear how, especially in Figure 5.10(c), this crystalline pattern appears, already

at first sight, very dense with regular ultramicropores that can hardly afford a good gas adsorption at high pressures.
The procedure of construction for FHM is different from other models. In this case, to check that the ultramicropores come from a complete polymerization during the synthesis process, the crystalline pattern was not changed further and the resulting density is 0.87 g/cm^3.
In fact, a high density of crystalline pattern suggests that the experimental material has a good part of ultramicropores, the same highlighted in the FHM.
The amorphous part, not crystallized due to gaps created by the failure of the total crosslinking of the experimental sample, led to the lowering of density.
This analysis is confirmed by the porosimetric study made through the N_2 adsorption at 77 kelvin, simulated with Monte Carlo techniques.
The simulations were performed by PAF force fields because they can be used safely for mPAF. The kind of atoms and the expected interactions are the same in the two classes of materials.

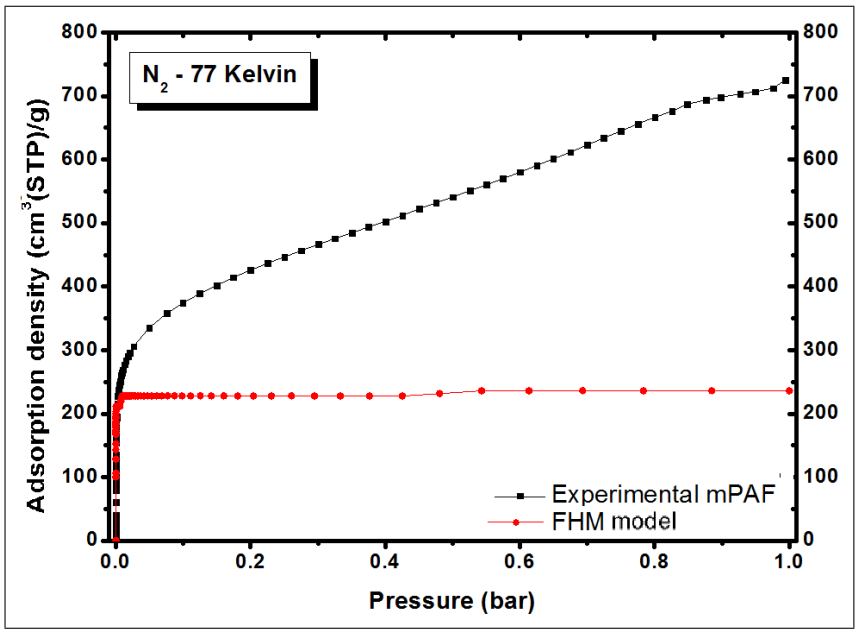

Figure 5.11: Simulated (red circles) and experimental (black squares) N_2 adsorption isotherms at 77 K for the FHM model.

In Figure 5.11, the N_2 adsorption isotherm at 77 K, simulated with Monte Carlo technique is compared to the adsorption isotherm of experimental mPAF.
At very low pressure the two curves are in very good agreement indicating a similar intensity of the host-guest interactions when the gas is preferentially adsorbed in the smallest micropores.
At slighty higher pressures, the simulated adsorption is smaller than in the experiment because all the specific volume in the model material is ultramicroporous (unlike in the experimental sample).
On the other hand, at pressures around 1 mbar the model pores are saturated, whereas the experimental isotherm keeps growing as the gas fills larger and larger pores.
The model is an idealized picture of the mPAF crystal, with no defects and perfectly regular cross-linking in para position; as a result, only one family of micropores is expected in the model.

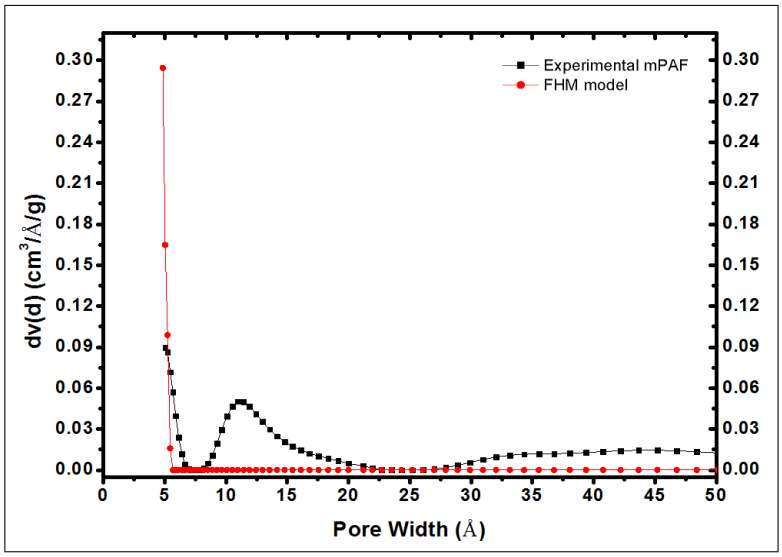

Figure 5.12: Pore size distribution calculated with QSDFT method for carbon slit/cylindrical pores on simulated and experimental adsorption isotherms.

The QSDFT procedure was applied to the simulated isotherm in the same conditions as for the experimental curve.
As shown in Figure 5.12, the agreement between the simulated and experimental pore distributions is very good in the region of ultramicropores; in fact, a narrow ultramicropore distribution around 5.04 Å width is found, in very good agreement with the smallest pores found for the experimental sample (i.e., 5.04 Å).
The different heights of the peaks relating to the ultramicropores are due to the presence in the FHM model of one pore family, while the real sample contains different porous families.
The main porosimetric properties of this model are summarized in Table 20.

	SSA_{BET} (m^2/g)	Microporous Volume (cm^3/g)		Total Pore Volume (cm^3/g)	CI%	CR%
		7 Å	20 Å			
mPAF Exp.	1527.66	0.145	0.42	1.042		
FHM	1036.38	0.467	0.467	0.467	100	100

Table 20: Comparison of the main porosimetric properties between experimental mPAF sample and FHM model.

The Cumulative Pore Volume shows how the FHM model is a ultramicroporous model. Indeed, as explained above, all of the pore volume is within the family of ultramicropores which are located at values lower than 7 Å.
These porous properties clarify the strong adsorption at very low pressures by the model FHM and the subsequent rapid saturation with the formation of a plateau, due to the absence of pores with a dimension greater than 7 Å.
In conclusion, on the basis of the above discussion, we believe that the most regular and ordered fraction of mPAF material is well described by this model structure and the FHM model demonstrates the presence of structural ultramicropores in the experimental sample that are derived from the complete hypercrosslinking of the material during the synthesis process.

5.5.2 Random Branched Polymer(RBP)

Once defined the model that describes qualitatively the ultramicropores, the next target of this PhD work was to obtain a computational atomistic model as similar as possible to the experimental sample in the whole family of micropore and, possibly, of mesopore.
So, a random amorphous polymer starting from a monomer consisting of two tetraphenylmethanes joined by a CH_2 bridge was created, as shown in Figure 5.13.

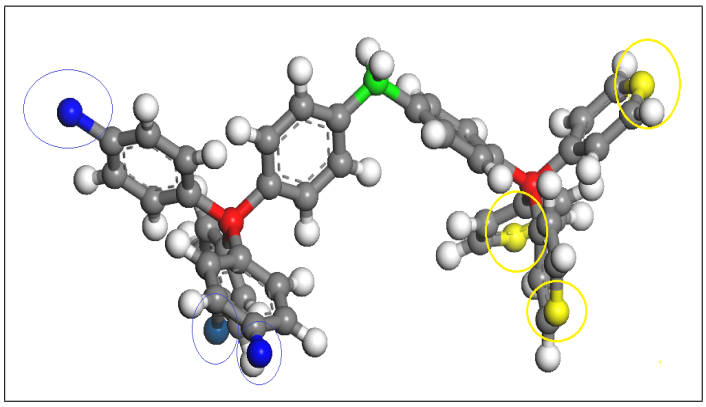

Figure 5.13: First starting monomer: two tetraphenylmethanes joined by a CH_2 bridge. Green atom is the already formed CH_2 bridge, red atoms are the tetra substituted carbons and blue and yellow atoms are the heads and the tails, which are the connection points to form the final polymer.

At the beginning, to generate this model, repeat units, called "heads" and "tails" are defined as they have to appear in the polymer structure.
To give the highest possible freedom to POLYMATIC procedure, three connection points indicated as "head" and three connection points indicated as "tail" have been defined.
One hundred monomers were packed between them and a cut off, which defines the maximum distance that two reactive atoms can be to allow bond formation, was set at 7 Å in the recommended range suggested in the procedural manual.

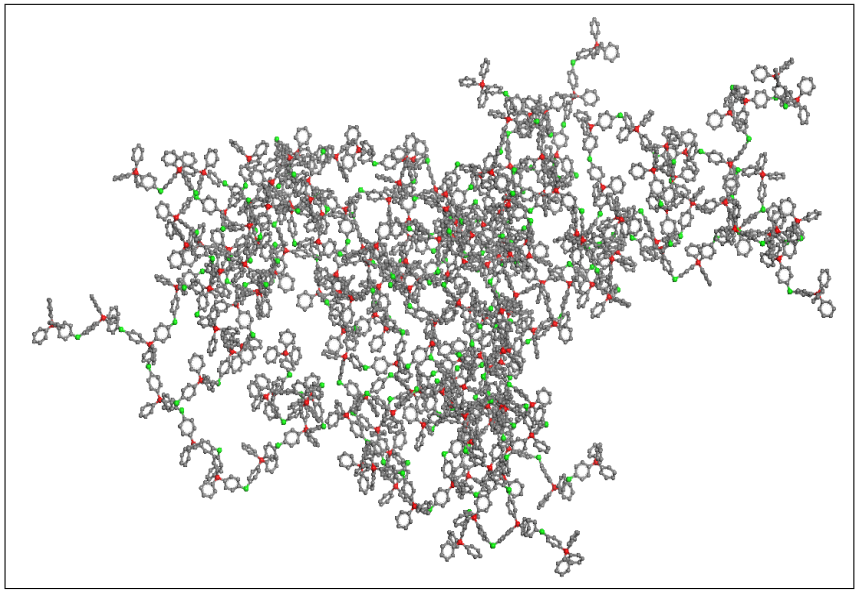

Figure 5.14: Random final POLYMATIC polymer starting to 100 monomer units.

Bonding criteria are imposed to prevent unreasonable or unrealistic structural configurations and procedures to help the system to find the energy minimization.
The resulting polymer is shown in Figure 5.14.
The polymer, before described, already optimized through the molecular dynamic procedures of POLYMATIC, was then assembled through the Amorphous Cell package within the Materials Studio program.
In this way the computational material has been made periodic in space assembled with a density equal to the experimental material.
The periodic structure can be used to simulate the adsorption isotherm of nitrogen at 77 K to determine the porosimetry of the model.

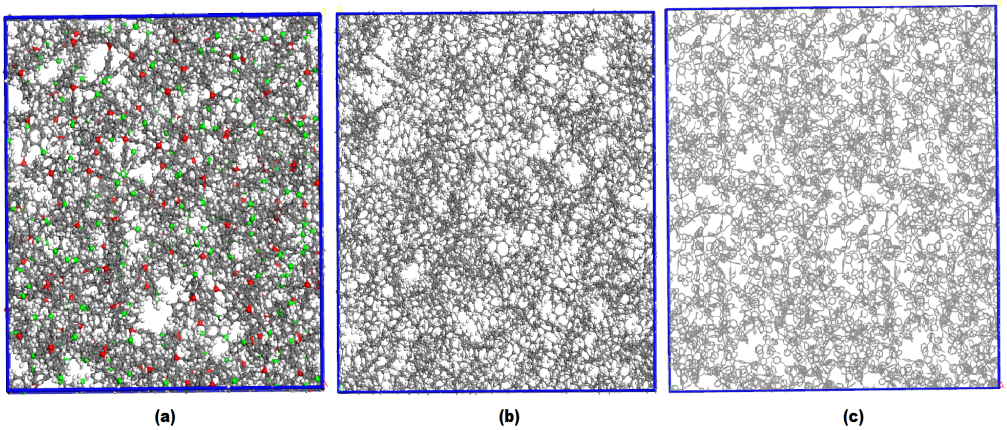

Figure 5.15: Optimized periodic structure of RBP model. (a) Unit cell, showing the sp^3 carbon atoms belonging to TPM (red) and FDA (green); 2 x 2 x 1 supercell (b) and 1 x 2 x 2 supercell (c) highlight the 3D channel structure. H_2 atoms are not shown.

In figure 5.15(a) the unit cell of the RBP model with a volume of 194.38 nm^3 and with a cell formula formed by $C_{5300}H_{4202}$ is indicated.

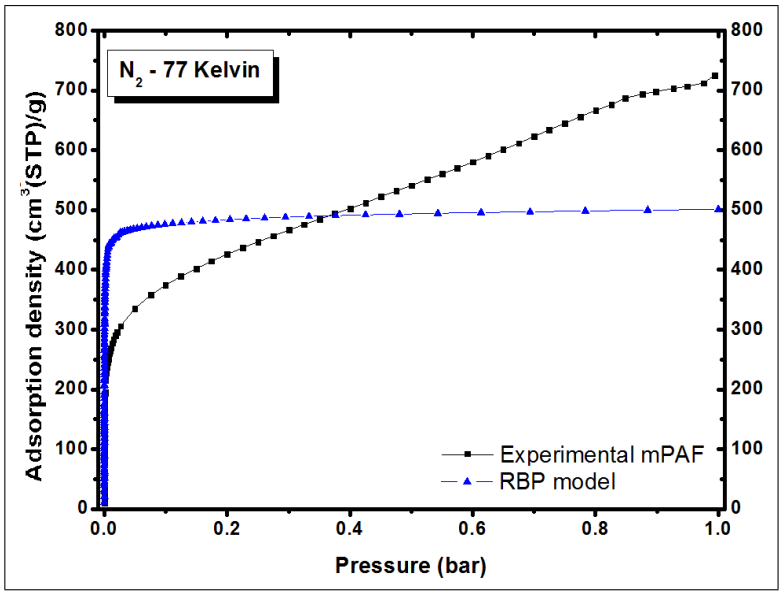

Figure 5.16: Simulated (blue triangles) and experimental (black squares) N_2 adsorption isotherms at 77 K in the RBP model.

In figure 5.15(b) and (c), the model is shown highlighting different space dimensions in the two representations, which outlines the three-dimensional structure of the material.
The pores visually appear several but with narrow cavities.
The adsorption isotherm of N_2 was simulated to study the cumulative pore volume and the pore size distributions within the computational structure.
This first model has a different adsorption than FHM computational structure.
The choice of the initial monomer caused a greater formation of micropores, which led an increase of the initial nitrogen adsorption.
However, the "knee" in the adsorption curve seems a little less accentuated than that in the FHM model but the presence of ultramicropores is still largely predominant, which causes the rapid plateau at low pressures.

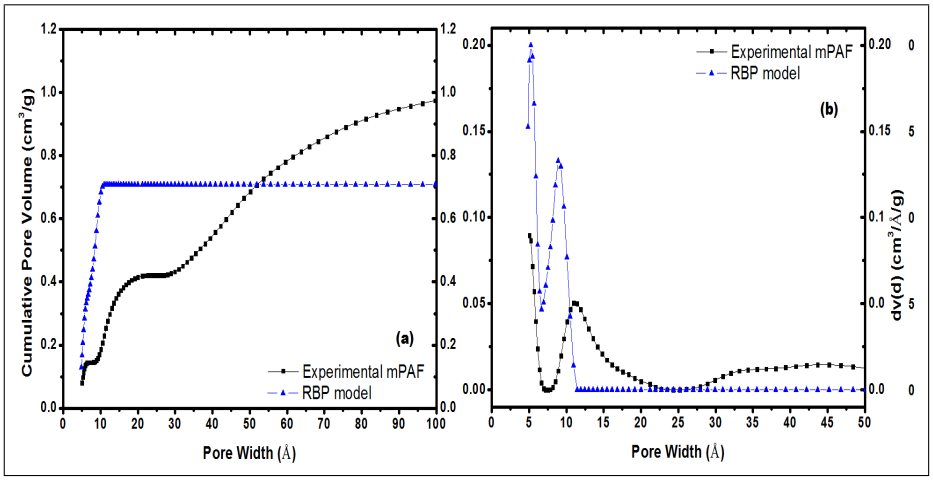

Figure 5.17: Comparison of Cumulative Pore Volume (a) and Pore Size distributions (b) between experimental sample (black squares) and RBP model (blue triangles).

As shown in Figure 5.17(b), there is a family of ultramicropores with a diameter smaller than 7 Å, which is consistent with the latest model and the experimental material.
The possibility of a polymerization not totally hypercrosslinked led to the formation of a second non structural family of pores, within the computational structure.
This consideration allows, in a preliminary manner, to imagine a real structure composed to a pore structural family and other families due to the aggregation of the different crystalline portions between them.

	SSA_{BET} (m^2/g)	Microporous Volume (cm^3/g)		Total Pore Volume (cm^3/g)	CI%	CR%
		7 Å	20 Å			
mPAF Exp.	1527.66	0.145	0.42	1.042		
RBP	1976.04	0.375	0.711	0.711	49.75	23.5

Table 21: Comparison of the main porosimetric properties between experimental mPAF sample and RBP model.

Table 21 indicates how the ultramicroporous volume in the RBP model is smaller than the FHM model.
However the Crosslinked Index and the Crystalline rate denote an excessive crosslinking possibility given to the initial fragment and the final structure is scarcely tidy.
Indeed most of the TPM has terminal phenyls and in this way the CR% has dramatically decreased.
However, the structure thus created, analizing the Cumulative Pore Volume in Figure 4.17 (b), has formed a family of ultramicropores lower than that seen in the FHM model, but still greater than the experimental mPAF sample.
This suggests that the assumption made previously with crystal crosslinked cores connected together to form either a ultramicroporous structural family and other porous aggregation families is correct.

5.5.3 Random Core/Shell Polymer (RCSP)

The next step was to provide a model with a crystalline crosslinked core packed with other crystalline cores.
In this way the value of the CR% compared to the RBP material should increase lowering the ultramicroporous portion.
Thus a frame formed by a heart made with nine tetraphenylmethanes linked by CH_2 bridges is created, as shown in Figure 5.18.

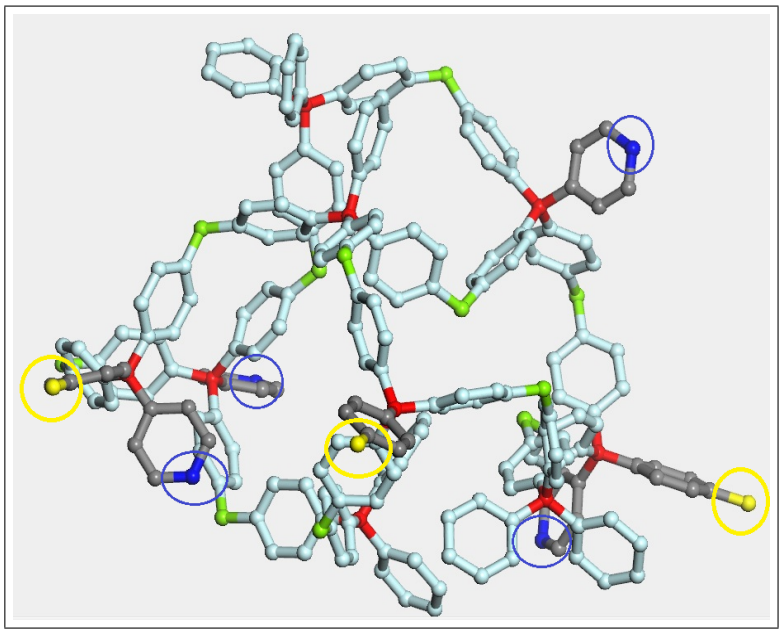

Figure 5.18: Starting monomer: nine tetraphenylmethanes joined by CH_2 bridges (green atoms). Red atoms are the tetra substituted carbons and blue and yellow atoms are the heads and the tails, which are the connection points to form the final polymer. The light blue atoms form the pattern's core.

The cage core is surrounded by phenyls with head or tail terminal atoms which allow the formation of the final polymer through their packing.
Fifteen monomers were packed between them and the same cut off used for the RBP model was defined.
The POLYMATIC procedure generates the polymer shown in Figure 5.19:

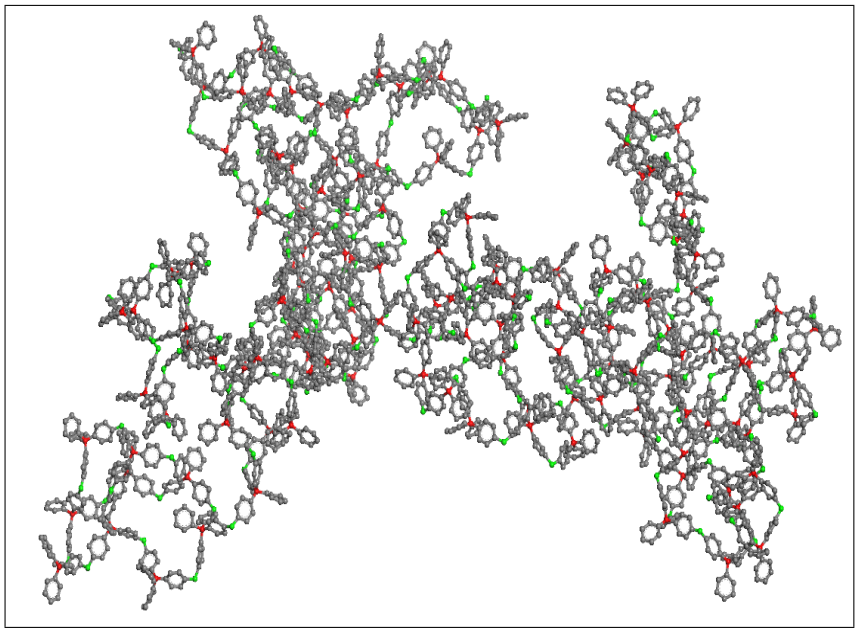

Figure 5.19: RCCFP model generates with the POLYMATIC procedure.

So, the final polymer already optimized by the POLYMATIC procedure is a packing of core/shell and the next step was to assemble the polymer through the Amorphous Cell package to the density of 0.53 cm^3/g, the same estimated for the experimental sample.
The periodic structure was used to simulate the adsorption isotherm of nitrogen at 77 K to determine the model's porosimetry.

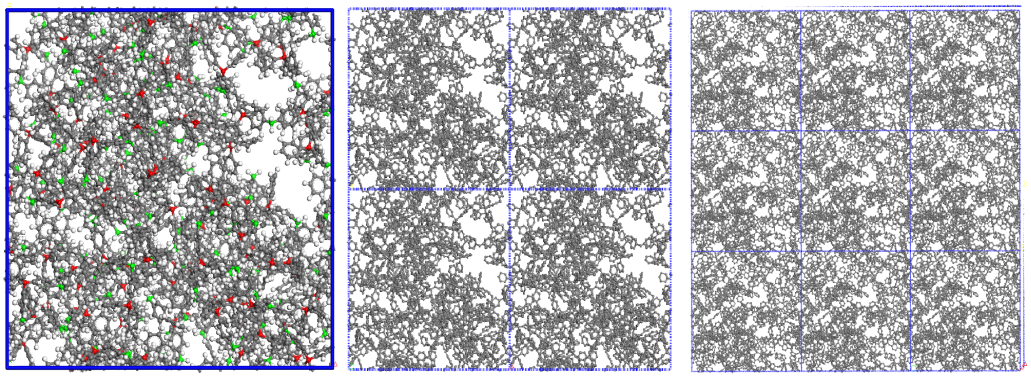

Figure 5.20: Optimized periodic structure of RCSP model. (a) Unit cell, showing the sp^3 carbon atoms belonging to TPM (red) and FDA (green); 2 x 2 x 1 supercell (b) and 1 x 3 x 3 supercell (c) highlight the 3D channel structure. H_2 atoms are not shown.

Figure 5.20(a) indicates the unit cell of RCSP model with a volume of 142.27 nm^3 and with a cell formed by $C_{3554}H_{2700}$.
The different representations show how the initial monomer has defined a final structure with pores larger than the previous model. Visually, more free volume seems to be than in RBP model althought the densities for the two computational materials are the same.
The adsorption isotherm of N_2 was simulated to study the pore size distributions and the Cumulative Pore Volume of the RCSP model.

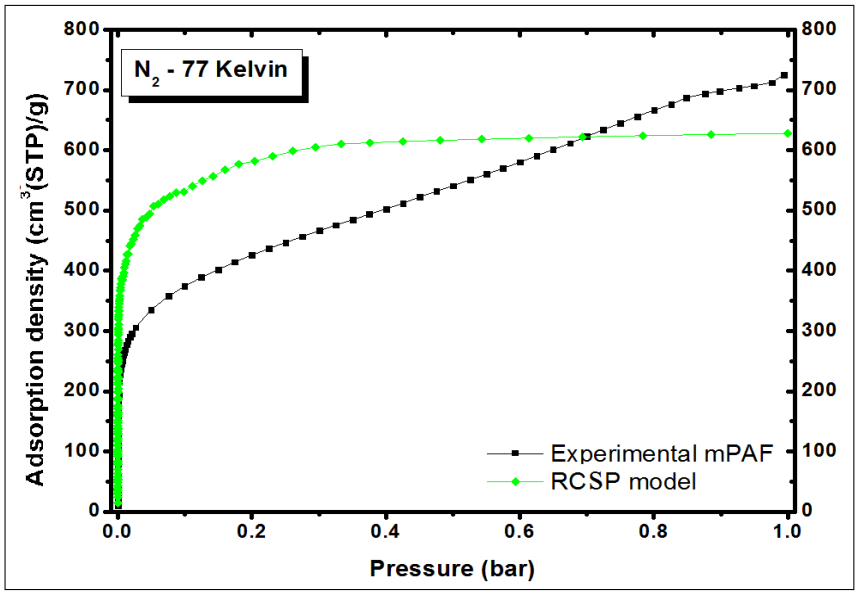

Figure 5.21: Simulated (green diamonds) and experimental (black squares) N_2 adsorption isotherms at 77 K in the RCSP model.

The RCSP shows a fairly steep slope at lower pressures to 0.1 bar, then decreases, maintaining an increase in the adsorption, though less evident.
Over the 0.4 bar you have a real plateau due to the absence of macropores within the model. However, the behaviors of the adsorption curves are still too far. The explanation can be given analyzing the figure 5.22.

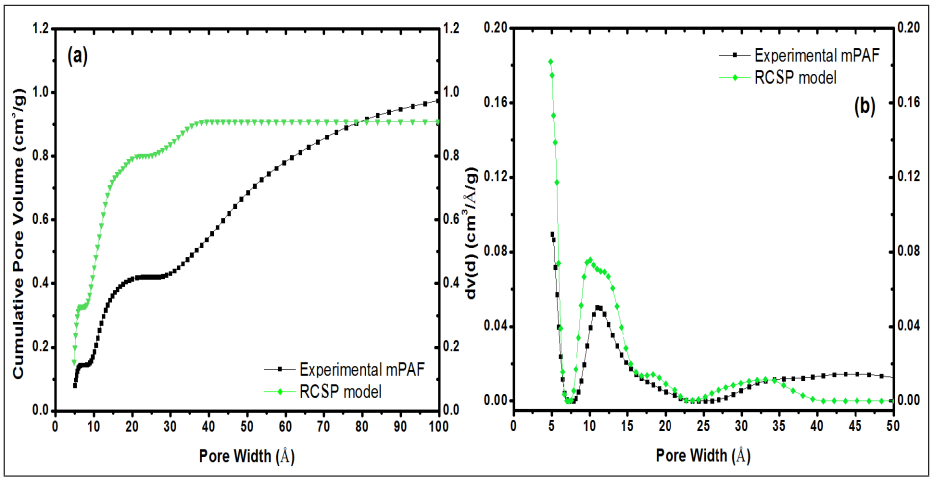

Figure 5.22: Comparison of Cumulative Pore Volume (a) and Pore Size distributions (b) between experimental sample (black squares) and RCSP model (green diamonds).

As shown in Figure 5.22(b), the agreement between the simulated and experimental pore distributions is good in the whole region of micropores.
In fact the model has a ultramicroporous family below 7 Å and moreover, in the supermicroporous region, between 7 and 20 Å for the computational model the same pore size distribution of the experimental sample was generated.
An important novelty, however, is the formation of aggregation pores not only in the supermicroporous region, but also in the region of macropores between 20 and 40 Å.

However, the amount of micropores, especially in the region less than 7 Å, is still too high quantitatively, as it shown in the porosimetric comparison in Table 22.

	SSA_{BET} (m^2/g)	Microporous Volume (cm^3/g)		Total Pore Volume (cm^3/g)	CI%	CR%
		7 Å	20 Å			
mPAF Exp.	1527.66	0.145	0.42	1.042		
RCSP	2167.42	0.328	0.792	0.908	66.3	54.07

Table 22: Comparison of the main porosimetric properties between experimental mPAF sample and RCCBP model.

The amount of micropores from the Cumulative Pore Volume, as shown in Figure 5.22(a), in the model RCCFP is 0.328 cm^3/g in the region of ultramicropores and 0.792 cm^3/g in the region of supermicropores.
An excessive amount with respect to the experimental sample is still evident.
The percentage of CI% and CR% increased, confirming the validity of our model, because the crystalline cores contains obviously more tetra and tri substituted TPM than the RBP model, which is a complete amorphous structure.

5.5.4 Random Hybrid Polymer (RHP)

The next step was to define quantitatively the ultramicroporous part of the material, still excessive in the model RCSP.
In this way, the RHP computational polymer was created combining each crystal-like core with non-crosslinked connecting chains.

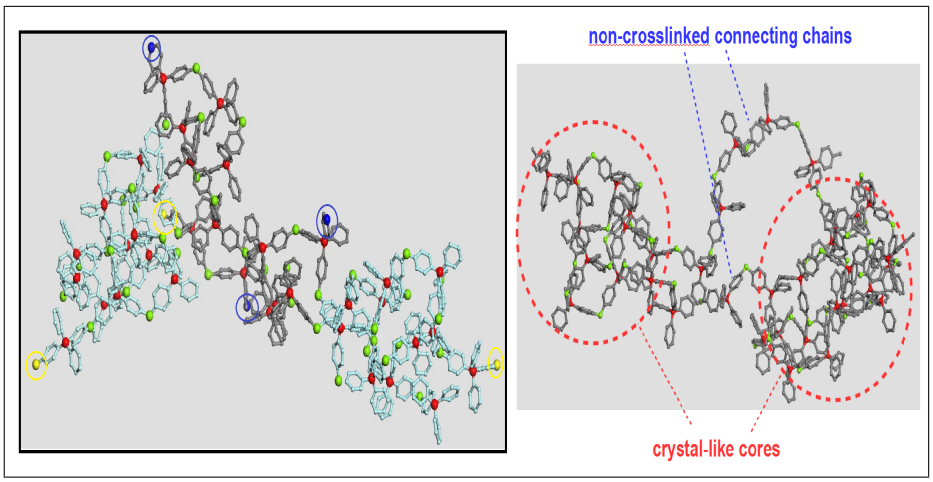

Figure 5.23: Starting monomer: two crystal-like core connected with non-crosslinked chain. Tetra substitued carbons (red atoms), CH_2 bridges (green atoms), head atoms (yellow carbons) and tail atoms (blue carbons). The light blue atoms form the crystal-like core.

As shown in figure 5.23, the heads and the tails in the initial fragment were defined both on the crystal-like core and in the non-crosslinked connecting chains, to enable connections by

core-core or chain-chain packaging, which may have occured in the experimental sample. Seven monomers were packed between them and the same cut off used for the previous models was defined.
The POLYMATIC procedure generates the computational polymer shown in Figure 5.24:

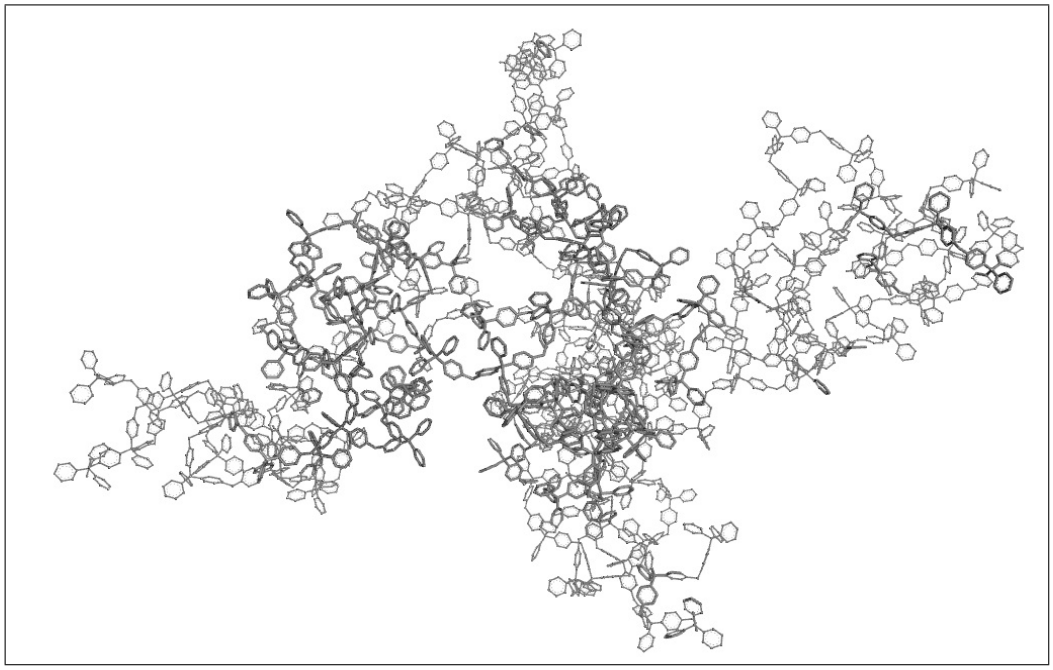

Figure 5.24: RHP model generates with the POLYMATIC procedure.

So, the polymer packed was assembled at the same experimental density through the package of Materials Studio, Amorphous Cell, using the COMPASS force field.
The resulting periodic structure is shown in Figure 5.25:

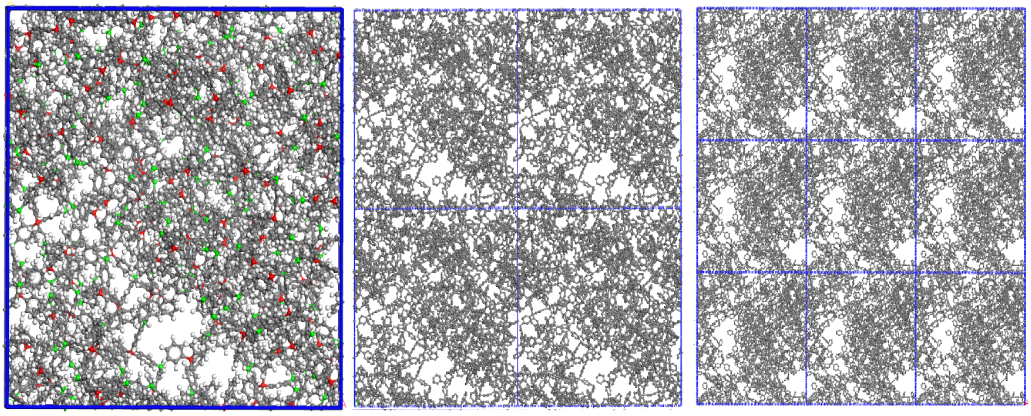

Figure 5.25: Optimized periodic structure of RCSP model.(a) Unit cell, showing the sp^3 carbon atoms belonging to TPM (red) and FDA (green); 2 x 2 x 1 supercell (b) and 1 x 3 x 3 supercell (c) highlight the 3D channel structure. H_2 atoms are not shown.

Figure 5.25(a) indicates the unit cell of RHP model with a volume of 188.73 nm^3 and with a cell formed by $C_{4713}H_{3600}$.

A visual analysis of the different representations shows how this model has pores with different dimensions.
Indeed, there are distinct large free volumes in some part of the space where the polymer is present.
The adsorption isotherm of N_2 was simulated in order to study the pore size distributions and the CPV of the RHP model.

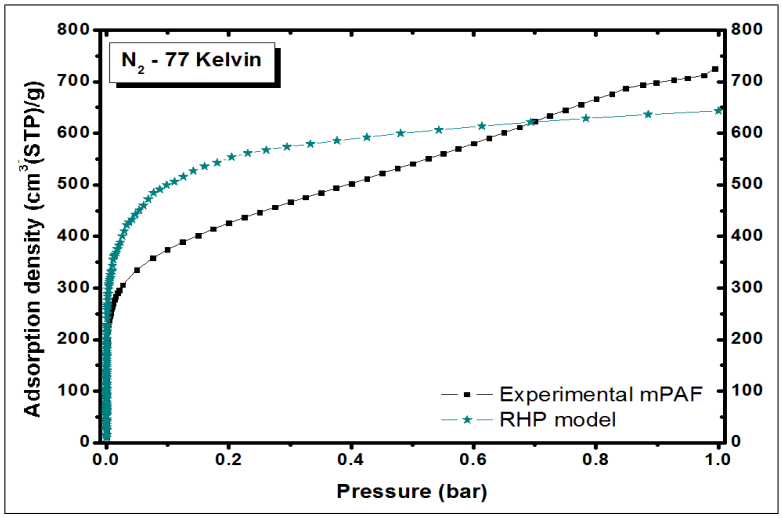

Figure 5.26: Simulated (blue stars) and experimental (black squares) N_2 adsorption isotherms at 77 K in the RHP model.

Figure 5.26 shows a good agreement between the computational and experimental adsorption.
The isotherm of the RHP model is obviously still characteristic of the materials almost entirely microporous, but the sudden adsorption is not quick, and a "knee" is no longer present.
This trend indicates that the ultramicroporous family is quantitatively diminished.

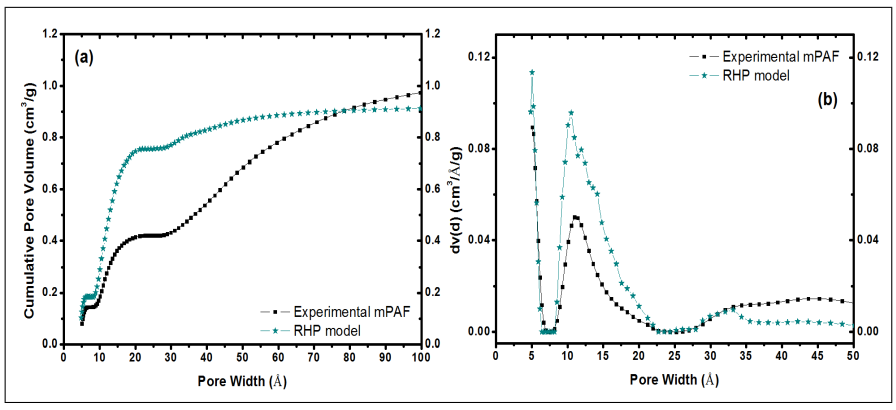

Figure 5.27: Comparison of Cumulative Pore Volume (a) and Pore Size distributions (b) between experimental sample (black squares) and RHP model (blue stars).

The considerations expressed above are confirmed both the Cumulative Pore Volume, Figure 5.27(a), both the Pore Size Volume, Figure 5.27 (b).
The model has roughly the same amount of ultramicropores present in the experimental mPAF, as Table 23 indicates, reinforcing that the initial model consists of crystal-core and non-crosslinked chains.

	SSA_{BET} (m^2/g)	Microporous Volume (cm^3/g)		Total Pore Volume (cm^3/g)	CI%	CR%
		7 Å	20 Å			
mPAF Exp.	1527.66	0.145	0.42	1.042		
RHP	2002	0.184	0.746	0.927	59.17	46.67

Table 23: Comparison of the main porosimetric properties between experimental mPAF sample and RCSP model.

The result is very satisfactory because a model with the same amount of structural ultramicropores, from the regularly polymerized part, of the experimental sample was realized.
The CR% and the CI% indeces decrease compared to the previous model because the non-crosslinked chains present in the RHP model are poorly hypercrosslinked and there are a lot of terminal phenyl in these chains.
The last step was to introduce in the model the polymeric functional groups of other side reactions that may decrease the amount of aggregate supermicropores and mesopores, plugging the cavities.

5.5.5 Random Hybrid Polymer with defective groups (RHP_CH_2OH)

As explained in section 5.2, in addition to the main coupling mechanism other side reactions due to the presence of excess of Lewis acid and FDA are possible.
The elemental analysis showed that small amounts of chlorine, oxygen and iron are present in the material and probabily they have a role in the stopping of the hypercrosslinked polymerization, forming the polymeric chains and hindering the complete crosslinked process.
Moreover, these defects obstruct porous cavities decreasing the adsorbent performance of the material.

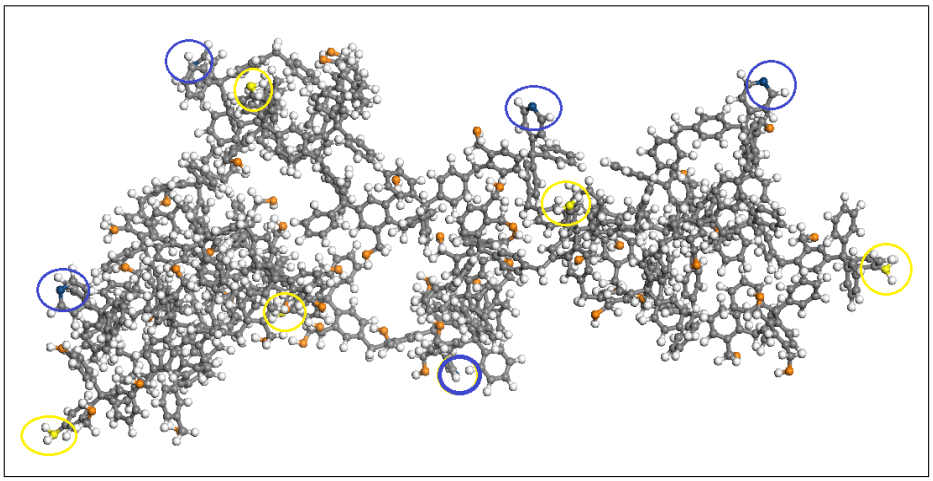

Figure 5.28: Starting monomer: two crystal-like core connected with non-crosslinked chain of which 6% by weight is oxygen (orange atoms) added throught CH_2 defective group. Head atoms (yellow carbons) and tail atoms (blue carbons).

So, to investigate the complete structure of the synthesized polycrystalline material and to analyze the change of performance of the model with defective groups, the percentages of

chlorine and iron were added to the oxygen amount and a RHP model with a 6% by weight were created.
The oxygen atoms were added in the functional CH_2OH group which is a possible mechanism of an other side reaction.
The RHP_CH_2OH computational polymer was created starting from this monomer (Figure 5.28) and not only adding to the final RHP polymer the CH_2OH groups. In this way, the structure has been optimized considering the steric hindrance of the defective groups.
The defective groups were connected in a homogeneous way in the structure to recreate the experimental conditions.
Six monomers were packed between them and the same cut off used for the previous models was fixed to help the POLYMATIC procedure.
The resulting computational polymer is shown in Figure 5.29:

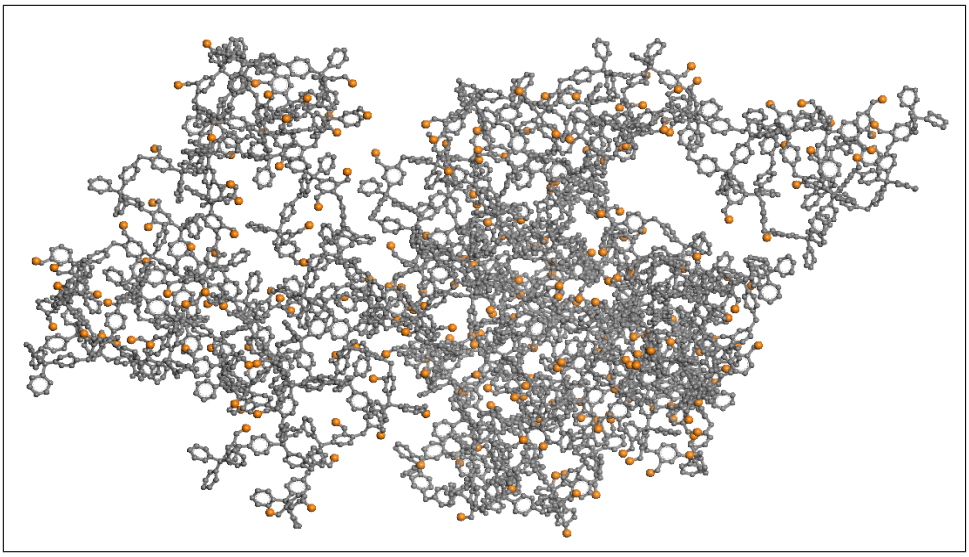

Figure 5.29: RHP_CH_2OH model generates with the POLYMATIC procedure.

The optimized polymer throught Amorphous Cell, a package of Materials Studio, was assembled using the COMPASS force field.
The result of this process is the modeling of a periodic structure, as shown in Figure 5.30.

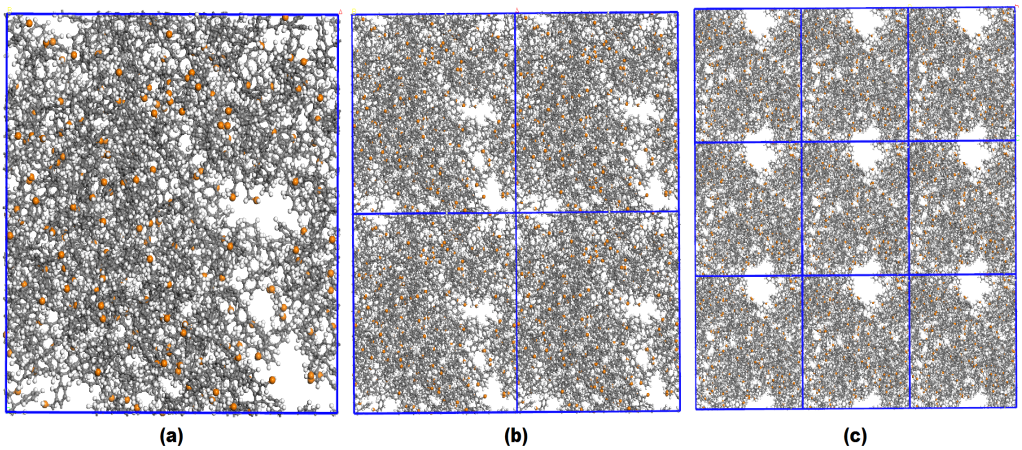

Figure 5.30: Optimized periodic structure of RCSP_CH_2OH model.(a) Unit cell, showing the orange oxygen atoms; 2 x 2 x 1 supercell (b) and 1 x 3 x 3 supercell (c) highlight the 3D channel structure. H_2 atoms are not shown.

Looking at the different representations, it's clear how in this model there are less free volume than in the RHP model without CH_2OH groups.
However an empty space probably belonging to an aggregate macroporous pore (Figure 5.30(c)) was generated.
Figure 5.30(a) indicates the unit cell of RHP_CH_2OH model with a volume of 211.53 nm^3 and with a cell formed by $C_{4954}H_{4080}O_{240}$. The other features, useful to calculate the later data storage, of this model are shown in Table 24.

	unit cell formula	unit cell volume (Å^3)	density (g cm^{-3})	specific volume (cm^3 g^{-1})	unit cell skeletal volume (Å^3)	porous volume fraction	specific porous volume (cm^3 g^{-1})
RHP_CH_2OH	$C_{4954}H_{4080}O_{240}$	211348	0.53	1.89	79183	0.625	1.18

Table 24: The structural properties of the RHP_CH_2OH model.

Considering these new functionalized groups in the structure, the force fields described above have been controlled.
Force fields and MP2 energies were compared to study the interactions between some gases and phenyl-CH_2-OH.

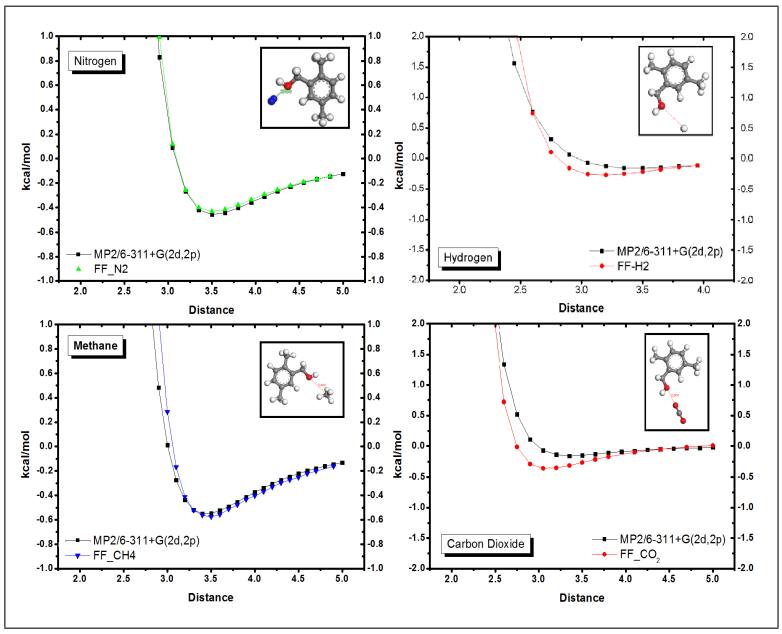

Figure 5.31: Gases - functionalized fragments. Interaction energy (kcal/mol) computed with the modified FF and at MP2/6-311+G(2d,2p) level (black squares), including the correction of the BSSE.

The interaction energies of various gases with the default parameters regarding the atoms of CH_2OH group, implemented within used force fields, were compared with the interaction energies from the MP2/6-311+G(2d,2p) level, including the BSSE correction.
The host-guest energies for the different gases well agree and therefore the parameters of the force fields weren't changed.

At first, the adsorption isotherm of N_2 was simulated to study the porosimtric features of the RHP_CH_2OH model.

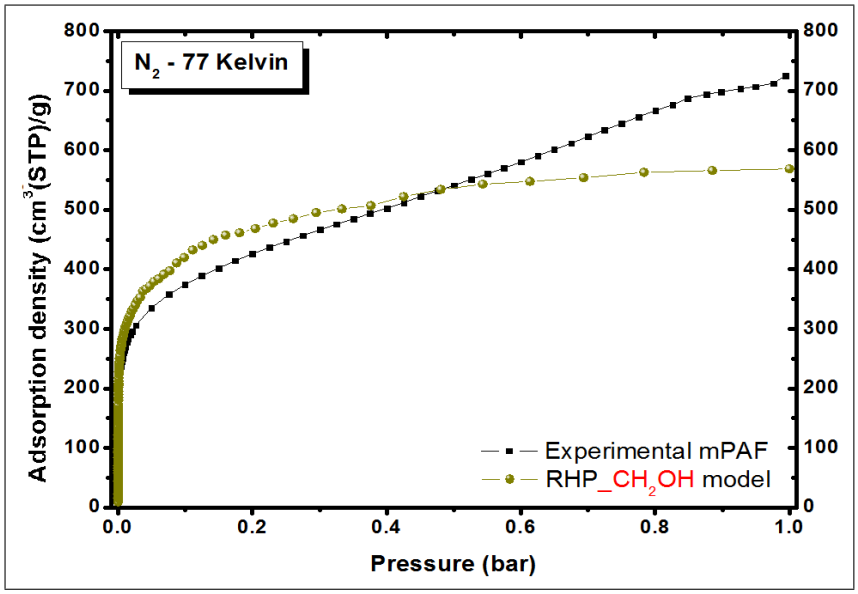

Figure 5.32: Simulated (yellow spheres) and experimental (black squares) N_2 adsorption isotherms at 77 K in the RCSP_CH_2OH model.

Figure 5.32 shows a excellent agreement between the computational and experimental adsorption, especially at low pressures where the micropores are responsible of the adsorbent behavior.
The computational curve of this model doesn't show a real evident plateau and compared to the RCSP adsorption, it's clear how the microporous family is quantitatively diminished.

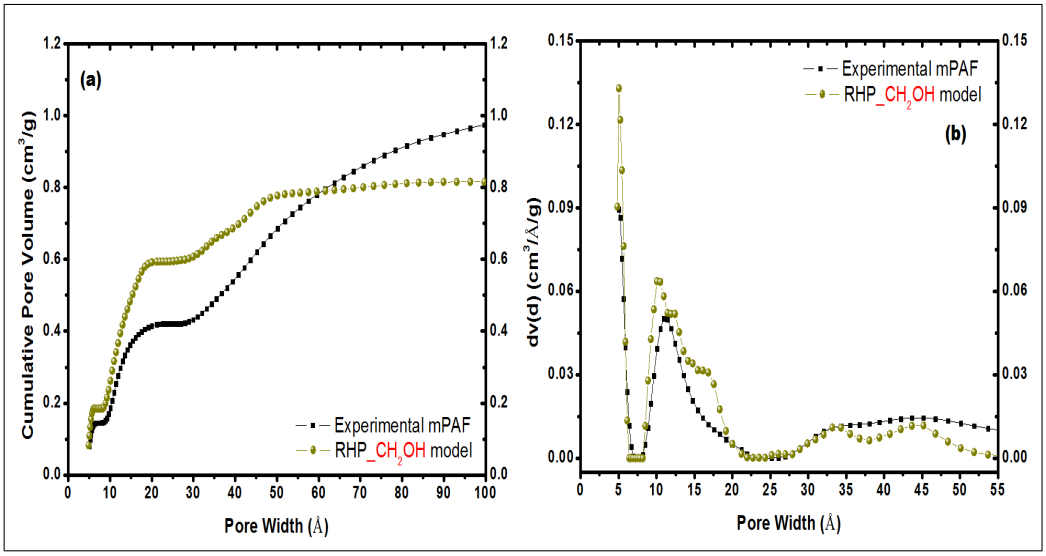

Figure 5.33: Comparison of Cumulative Pore Volume (a) and Pore Size distributions (b) between experimental sample (black squares) and RHP_CH_2OH model (yellow spheres).

The addition of the groups due to secondary reactions caused the lowering of the amount of supermicropores within the material plugging the cavity.

The ultramicroporous region increased slightly and this increase is due to some supramicroporous cavities which, obstructed by some defective groups, became ultramicroporous.
The macroporous area is due to the particular material's packaging.

	SSA_{BET} (m^2/g)	Microporous Volume (cm^3/g)		Total Pore Volume (cm^3/g)	CI%	CR%
		7 Å	20 Å			
mPAF Exp.	1527.66	0.145	0.42	1.042		
FHM	1036.38	0.467	0.467	0.467	100	100
RBP	1976.04	0.375	0.711	0.711	49.75	23.5
RCSP	2167.42	0.328	0.792	0.908	66.3	54.07
RHP	2002	0.184	0.746	0.927	59.17	46.67
RHP_CH_2OH	1774.14	0.186	0.592	0.818	59.44	47.22

Table 25: Comparison of the main porosimetric properties between experimental mPAF sample and all computational models analized in this chapter.

The values confirm the excellent agreement between the experimental material and the RHP_CH_2OH model in the microporous region.
Looking at the SSA_{BET}, this last model has the closest specific surface area compared to the experimental mPAF, further confirming the validity of the model.
The similar CI% and CR% between RHP and RHP_CH_2OH models show that even if the two polymers were created by two different starting monomers and with two indipendent procedures, the final computational structures are structurally adequate each other.
Thus, the differences between the two models are caused only by the presence of defective groups in the RCSP_CH_2OH model. In conclusion a variety of computational approaches have been adopted for the modeling and for the optimization of structures and the RHP_CH_2OH is the model which is closest to the porosimetric features of the real sample.
Therefore, this latest model is a good structural atomistic model, which will be taken into account to compare computational results of some gases with those obtained from experimental measurements.

5.6 Simulated Adsorption Isotherms in mPAF model

Monte Carlo simulations were performed to study methane, carbon dioxide and hydrogen adsorption in the mPAF model structure described above.
The comparison between the computational model and the experimental sample was made to analyze the adsorption behaviors with CO_2 and CH_4 gases.
Moreover, hydrogen adsorption was simulated, not carried out at the experimental level, to estimate the performance of the material mPAF with this gas also.
In figure 5.34 the theoretical excess isotherm of CH_4 at 298 K are compared to the corresponding experimental curve.

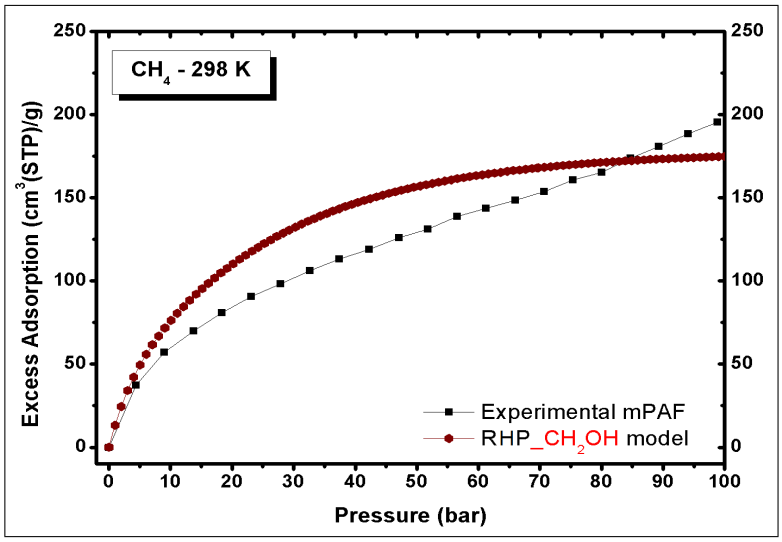

Figure 5.34: Simulated and experimental CH_4 adsorptions at 298 K in the range of pressures between 0 and 100 bar.

As expected, the excess adsorption isotherms present the same trend analyzed in the N_2 adsorption.
From 0 to 5 bar, the two curves are overlaid because the amount of ultramicropores are pratically the same, in fact at 4.39 bar the CH_4 adsorptions in the mPAF and in the model are 37.45 cm^3/g and 44.01 cm^3/g, respectively.
From 5 to 80 bar, the mesoporous cavities have an important rule and the little greater amount of the RHP_CH_2OH compared to the real sample (0.592 cm^3/g and 0.42 cm^3/g, respectively, seen in the Table 24) causes a shift between two adsorption curves.
As expected, the two curves intersect at a certain pressure because the computational model has less total pore volume than the real material. In fact, the computational atomistic models created with the previously described procedure don't allow to form the large mesopores and, therefore, the adsorption in the computational model reaches saturation plateau which doesn't occur in the experimental sample, much more mesoporous.

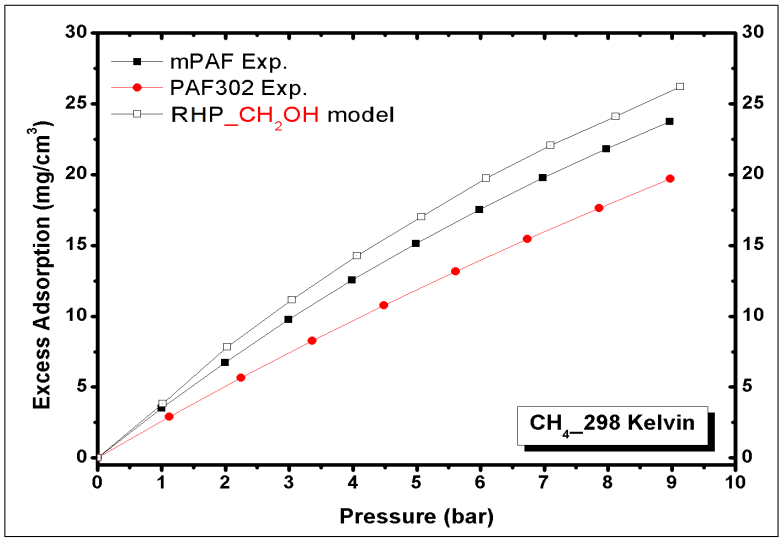

Figure 5.35: Simulated and experimental CH_4 adsorptions at 298 K in the range of pressures between 0 and 9 bar.

It is interesting to observe that at 9 bar and 298 K the volumetric CH_4 uptake in mPAF exceeds that of PAF-302: as shown in Figure 5.35, despite the lower specific surface area (1528 m^2/g for mPAF and 4563 m^2/g for PAF-302), the volumetric adsorption in mPAF is higher than in PAF-302, due also to mPAF higher density (0.53 g/cm^3 than 0.29 g/cm^3).
The methane uptake in the mPAF sample is greater than that in PAF-302.
23.74 mg/cm^3 adsorbed CH_4 in experimental mPAF sample (25.29 mg/cm^3 for the simulated model) agaist the 19.61 mg/cm^3 in the PAF-302.
The adsorption could be greater considering the defective groups inside the experimental mPAF due to other side reactions.
The presence of ultramicropores in the synthesized mPAF material causes the shift of the experimental PAF-302 adsorption that contains especially supermicropores.
For the carbon dioxide adsorption, the comparison of the experimental and theoretical curves for the mPAF is shown in Figure 5.36.

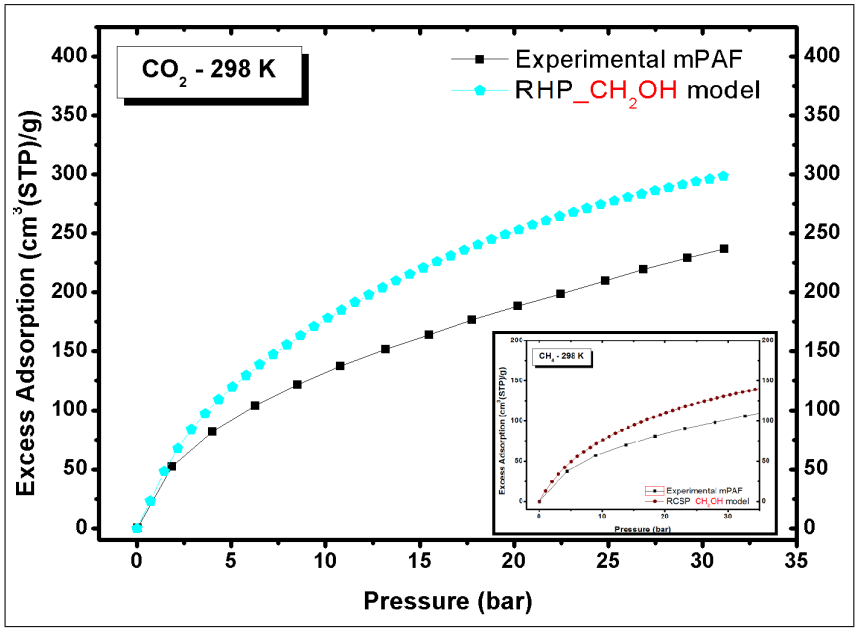

Figure 5.36: Simulated and experimental CO_2 adsorptions at 298 K in the range of pressures between 0 and 10 bar.

The behaviors of these two carbon dioxide uptakes for the experimental sample and for the computational model which has the closest microporous structure are the same seen for the methane uptake.
Indeed, at low pressures, up to 5 bar, the two adsorptions are very similar, with a little difference for the already discussed excessive ultramicroporosity in the computational structure.
From 5 bar to 30 bar, the rule most important for the gas adsorption was determined by the mesoporosity and the computational material, as seen in the previous section, has a greater amount of this porous family which causes different uptakes with respect to the real sample.
However, the ratio between the adsorption trends of the carbon dioxide, in the same range or pressures, is the same analyzed for the methane adsorptions, as shown in the inset in Figure 5.36.
In this case, the CO_2 storage in the experimental sample of PAF-302 wasn't measured and therefore it can not be compared with that in the mPAF. On the contrary, for the hydrogen adsorption, the experimental H_2 adsorption in the mPAF wasn't realized.
Therefore, the simulated isotherm in the RHC_CH_2OH model can predict the adsorption in

the real sample, inquiring the comparison of the hydrogen's adsorption in the sythetisized PAF-302.
Simulated and experimental H_2 uptakes at 77 K in the range of pressures between 0 and 10 bar are shown in Figure 5.37:

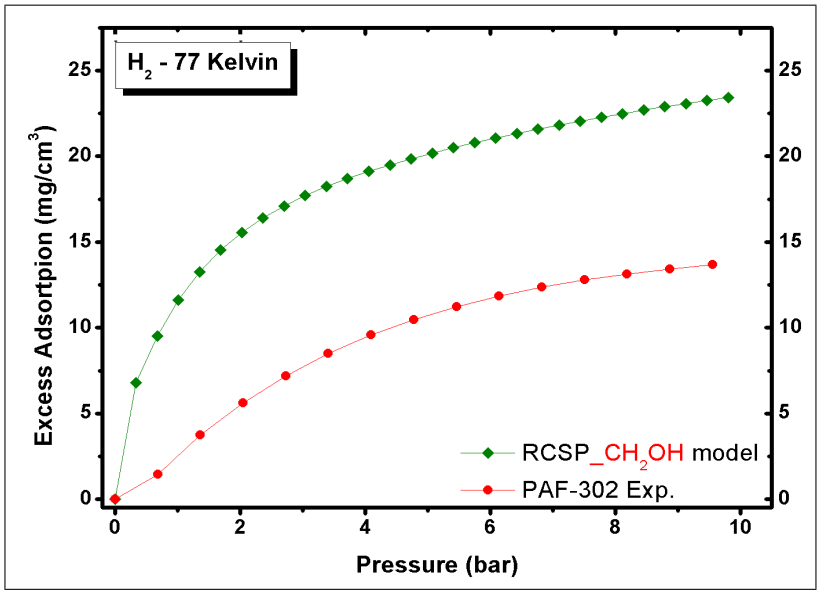

Figure 5.37: Simulated and experimental H_2 adsorptions at 77 K in the range of pressures between 0 and 10 bar.

The results obtained in the excess adsorption show the relevance of the ultramicropores which are present in the mPAF model. In fact, as alreeady seen for the PAF-301 in the previous chapter, the adsorption amount of hydrogen, even more than for the other gases, is related to the presence within the material of ultramicroporosity.
The simulated adsorption in the computational model provides an idea how the hydrogen adsorption should be in the experimental sample, considering the good agreement between the behaviors of uptake in the two structures for other gases.
The storage capacity of PAF-302 and of mPAF synthesized in our laboratory and the mPAF model are compared to these selected materials reported in literature.

Sample	CO_2 (mg/cm^3)	CH_4 (mg/cm^3)	H_2 (mg/cm^3)	Ref
	298 K 10 bar	298 K 10 bar	77 K 10 bar	
RHP_CH_2OH	174	25.3	23.5	this work
mPAF **Exp.**	141	23.9		our exp. Group
PAF-302 **Exp.**		19.6	13.7	our exp. Group
COF-102	189.2	24.9	21.5	[7]
MOF-210	81.3	13.8	11.7	[90]
MOF-205	180	22	20.9	[90]
PPN-4	127	19	17	[135]
HKUST-1		9.7		[225]

Table 26: Excess uptakes of methane, carbon dioxide and hydrogen at different temperatures at 10 bar.

A large number of results at low pressures can be found for methane, carbon dioxide and hydrogen adsorption in porous materials belonging to the class of activated carbons, metal organic frameworks (MOF), and covalent organic frameworks (COF), which have been proposed for this kind of application much earlier than PAFs materials.
Some of the materials reported in table 26 have been described in Chapter 1, belonging to the classes of metal organic frameworks (MOF-210, MOF-205, HKUST-1) and covalent organic frameworks (COF-102) and the gravimetric uptakes are reported.
The data in Table 26 clearly show that mPAF at low pressures can be an exceptional adsorber for various gases and these results confirmed the importance of ultramicropores for the gases adsorption at low pressures and established how the better absorption at low pressures is proportional to the amount of ultramicropores present in the material.
This is even more appealing if one takes into account, for an industrial application, that the obtained materials with Friedel-crafts synthesis are cheaper and more efficient at low pressures than the porous aromatic frameworks.
In fact, this method has led to the deposition of a European patent [226] and the material was called UPO (UPO stands for Universita' Piemonte Orientale), submitted in collaboration with SOL Group.

5.7 Conclusion

Hyper-cross-linked aromatic polymers were produced by a FriedelCrafts reaction between TPM and FDA, providing an easy and low-cost route toward efficient adsorbents for carbon dioxide, methane and hydrogen.
Theoretical models were developed to reproduce the most regular and ordered fraction of mPAF, with TPM units connected in a arrangement by methylene groups in para position in the ultramicroporous region, and to develop on a computational model which reproduces the various regions of porosity of the experimental sample.
As for the previous study PAF-302, simulated isotherms of nitrogen were used to define the cumulative pore size and the pore size distributions and they were analyzed with the same software tool used for the experimental adsorption.
A variety of computational approaches were adopted for the modeling and for the optimization of materials structures:

- Crystalline model has confirmed the regularly and ordered polymerized fraction due to the complete hypercrosslinked process.
- Amorphous model has consolidated the idea of the formation of aggregate pores by incomplete hypercrosslinking of the material.
- Core/shell model has showed that as in the real material, crystalline regions are present, which are formed from highly crosslinked cores and supermicroporous porosity caused by the aggregation of these cores.
- Hybrid model has recreated with good agreement the pore size distributions of the experimental sample in the microporous and in the mesoporous parts.
- Defective model has demonstrated the role of the groups due to side reactions during the synthesis improving agreement between the model and the real system.

Thus, when classical models are used for the optimization of structures, forcefields are usually sufficient to obtain reliable structures throught the study of simulated adsorption isotherms

which need a careful parameterization of the interaction energies.
Monte Carlo simulations with some forcefields suitable for the gases were performed to study methane, carbon dioxide and hydrogen adsorption in the defective model which has the pore size distribution most similar to the real material.
The uptakes are in good agrement with the experimental values, especially at low pressures, confirming the good description particularly of the mPAF microporous fraction.
The results and the simulations show that mPAF has a very high potential as gas adsorber at low pressures compared with other microporous materials and the good performance can be attribuited to the abundance of ultramicropores.
These data have become more important because another important advantage of this material compared to PAFs is connected to the cost of the synthesis: on a laboratory scale PAF-302 costs in our laboratories, around 340 €/g while mPAF-1 costs 5 €/g and a cost of 0.12 €/g has been estimated in a pilot scale.
Therefore, materials obtained with Friedel-Crafts synthesis are cheaper and more efficient for an industrial application and they are extremely interesting as gas adsorbers.

6 General Conclusion

In this PhD thesis we have treated: i) the modeling of new microporous organic materials, characterized and synthetized by one experimental group at our department, and ii) the identification of their gas storage properties.
Two classes of porous materials with different porosity were optimized to this purpose: Porous Aromatic Frameworks (PAF) and microPorous Aromatic Frameworks (mPAF).
In both cases, the adsorption of gases in these newly developed classes of porous materials has been modeled with Grand Canonical Monte Carlo, GCMC simulations, in oder to estimate the potential of these materials and to enhance the performance in gas capture and storage, at different temperatures and in a wide pressure range.
GCMC simulations were simulated with purposely modified versions of Dreiding force fields were adopted.
The Lennard-Jones parameters for the gas-gas and gas-solid van der Waals interactions were modified, to reproduce the experimental density of the free gas and to match high level quantum mechanical calculations on model systems.
The difference between fugacity and pressure was properly taken into account.
Initially, four PAF-30n were considered (n = 1-4 being the number of phenyl rings connecting the sp^3 carbons in the diamond-like structure).
The porosity of the materials has been investigated and all the structures are predicted to adsorb various gases very efficiently, with densities much higher than the compressed gas.
PAF-301, whose small pores and relatively high density of aromatic groups enhance the gas-surface interactions, should be the best performing material at low pressures, while the PAF-302 exhibits the best behavior over the entire pressure range, providing the best combination of specific area and microporosity.
A vibrational study about the interactions of methane with the surface of the porous frameworks was presented. A simple model based on the symmetry reduction passing from gaseous to adsorbed methane allowed us to predict the structure of the vibrational bands upon adsorption: the calculations on the molecular models provided an estimate of the expected frequency shifts. On the basis of these results, the spectra recorded after adsorption indicate multiple interactions between methane and the PAF surface, where one or two phenyl rings (i.e., monodentate or bidentate adducts, respectively) are involved.
Moreover, PAF-302 was computationally functionalized to improve the CO_2 storage. All the functionalized PAF-302 improves the CO_2 uptake at low and room pressures and, in summary, PAF-302 and functionalized PAF-302 are extremely promising materials for CO_2 capture and storage; among the different functional groups, pyrimidine is predicted to provide the highest uptakes at low and atmospheric pressure, while unmodified PAF-302 is expected to be the most efficient at high pressure. A very good compromise can be NH_2-CH_2-PAF, performing well in the whole pressure range.
A second class of materials studied in this thesis are Hyper-Crosslinked Polymers (HCPs), a class of low cost porous organic networks easily prepared by Friedel-Crafts reaction.
MicroPorous Aromatic Frameworks (mPAF) have been produced by Friedel-Crafts reaction between tetraphenylmethane (TPM) and formaldehyde dimethyl acetal (FDA), with an easy and low-cost synthetic route.
In optimal conditions, the resulting materials are characterized by high surface area and high

micropore volume with predominance of pores size $\leq$ 7 Å.
Theoretical models have been developed to model the various regions of porosity of the experimental sample.
Simulated N_2 adsorption isotherms have been used to define the cumulative pore size and the pore size distributions and these have been analyzed with the same software tool used for the adsorption in laboratory.
Several structural models have been proposed for mPAF: in each model the N_2 adsorption was simulated by GCMC and compared to the experiment.
So, we could propose a model comprising crystalline as well as amorphous regions, and inclusing damling groups due to side reactions, which reproduces quite well the experimental behavior.
The adsorption capacities of CH_4, H_2 and CO_2 gases in mPAF material have been compared with PAF materials, where it's possible, and with other porous materials at different temperatures and pressures.
The methane storage has showed the most interesting results. In fact, at 10 bar of pressure, 23.74 mg/cm^3 CH_4 in experimental mPAF sample (25.29 mg/cm^3 for the computational model) have been adsorbed against 19.61 mg/cm^3 in the PAF-302.
The present measures show that mPAF materials have an enormous potential as gas adsorbers at low pressures and in the next research steps, convenient changes will be designed to improve the performance of adsorption in this material.
In conclusion, we have shown how fruitful can be the strong collaboration between experimental measures and theoretical simulations in the field of materials chemistry.
Hopefully, these results will improve the use of theoretical methods as a tool for the design and the characterization of new functional materials, side by side with classical physical-chemistry methoods.

Bibliography

[1] Dyer, A.; An Introduction to Zeolite Molecular Sieves (Wiley, Chichester, **1988**).

[2] Holderich, W.; Hesse, M. and Numann, F.; Zeolites: Catalysts for Organic Syntheses. *Angew. Chem. int.* **1988**, 27, 226-246.

[3] McKeown, N. B.; Budd, P. M.; Polymers of intrinsic microporosity (PIMs): organic materials for membrane separations, heterogeneous catalysis and hydrogen storage. *Chem. Soc. Rev.* **2006**, 35, 675-683.

[4] Li, B.; Su, F.; Luo, H. K.; Liang, L.; Tan, B.; Hypercrosslinked microporous polymer networks for effective removal of toxic metal ions from water. *Microporous and Mesoporous Mater.* **2011**, 138, 207-214.

[5] Du, X.; Sun, Y.; Tan, B.; Teng, Q.; Yao, X.; Su, C.; Wang, W.; Trgers base-functionalised organic nanoporous polymer for heterogeneous catalysis. *Chem. Commun.* **2010**, 46, 970-972.

[6] Dang, D.; Wu, P.; He, C.; Xie, Z.; Duan, C.; Homochiral metal-organic frameworks for heterogeneous asymmetric catalysis. *J. Am. Chem. Soc.* **2010**, 132, 14321-14323.

[7] Furukawa, H.; Yaghi, O. M.; Storage of Hydrogen, Methane, and Carbon Dioxide in Highly Porous Covalent Organic Frameworks for Clean Energy Applications. *J. Am. Chem. Soc.* **2009**, 131, 8875-8883.

[8] McKeown, N. B.; Gahnem, B.; Msayib, K. J.; Budd, P. M.; Tattershall, C. E.; Mahmood, K.; Tan, S.; Book, D.; Langmi, H. W. and Walton, A.; Towards Polymer-Based Hydrogen Storage Materials: Engineering Ultramicroporous Cavities within Polymers of Intrinsic Microporosity. *Angew. Chem.* **2006**, 118, 1836-1839.

[9] Wood, C. D.; Tan, B., Trewin, A.; Su, F.; Rosseinsky, M. J.; Bradshaw, D.; Sun, Y.; Zhou, L. and Cooper, A. I. Microporous Organic Polymers for Methane Storage. *Adv. Mater.* **2008**, 20, 1916-1921.

[10] Ben. T.; Pei. C.; Zhang. D.; Xu. J.; Deng. F.; Jing. X.; Qiu. S.; Gas Storage in Porous Aromatic Frameworks (PAFs). *Energy Environ. Sci.* **2011**, 4, 3991-3999.

[11] Deanna, M. D.; Berend, S.; Jeffrey R. L.; Carbon Dioxide Capture: Prospects for New Materials, *Angew. Chem. Int. Ed.* **2010**, 49, 60586082.

[12] Frota, W.M.; Sa, J.A.S.; Moraes, S.S.B.; Rocha, B.R.P.; Ismail, K.A.R.; Natural gas: The option for a sustainable development and energy in the state of Amazonas. *Energy Policy.* **2010**, 38, 3830-3836.

[13] Jain, I.P.; Hydrogen the fuel for 21st century. *Int. J. Hydrog. Energy.* **2009**, 34, 7368-7378.

[14] Kelly, N.A.; Gibson, T.L.; Cai, M.; Spearot, J.A.; Ouwerkerk, D.B.; Development of a renewable hydrogen economy: optimization of existing technologies. *Int. J. Hydrog. Energy.* **2010**, 35, 892-899.

[15] Nath, K.; Das, D.; Production and storage of hydrogen: Present scenario and future perspective. *J. Sci. Ind. Res.* **2007**, 66, 701-709.

[16] Pasculete, E.; Condrea, F.; Radulescu, C.; Hydrogen and sustainable energy. Research for hydrogen production. *Environ. Eng. Manag. J.* **2007**, 6, 45-49.

[17] U.S. Department of Energy's Energy Efficiency and Renewable Energy Website.(**2010**) `https://www1.eere.energy.gov/hydrogenandfuelcells/storage/current_technology.html`.

[18] Jena, P.; Materials for Hydrogen Storage: Past, Present, and Future. *J. Phys. Chem. Lett.* **2011**, 2, 206-211.

[19] Mao, W. L.; Koh, C. A.; Sloan, E. D.; Clathrate Hydrates under Pressure. *Phys. Today* **2007**, 60, 42-47.

[20] Wang, L.; Yang, R. T.; New Sorbents for Hydrogen Storage by Hydrogen Spillover: A Review. *Energy Environ. Sci.*, **2008**, 1, 268-279.

[21] Lan, J.; Cao, D.; Wang, W.; Ben, T.; Zhu, G.; High-Capacity Hydrogen Storage in Porous Aromatic Frameworks with Diamond-like Structure. *J. Phys. Chem. Lett.* **2010**, 1, 978-981.

[22] Orimo, S.; Nakamori, Y.; Eliseo, J. R.; Zuttel, A.; Jensen, C. M.; Complex Hydrides for Hydrogen Storage. *Chem. Rev.* **2007**, 107, 4111-4132.

[23] Gutowska, A.; Li, L.; Shin, Y.; Wang, C. M.; Li, X. S.; Linehan, J. C.; Smith, R. S.; Kay, B. D.; Schmid, B.; Shaw, W.; Gutowski, M.; Autrey, T.; Nanoscaffold Mediates Hydrogen Release and the Reactivity of Ammonia Borane. *Angew. Chem. Int. Ed.* **2005**, 44, 3578-3582.

[24] Zhao, Y.; Kim, Y.-H.; Dillon, A. C.; Heben, M. J.; Zhang, S. B.; Hydrogen Storage in Novel Organometallic Buckyballs. *Phys. Rev. Lett.* **2005**, 94, 155-504.

[25] Sun, Q.; Wang, Q.; Jena, P.; Kawazoe, Y.; Clustering of Ti on a C_{60} Surface and Its Effect on Hydrogen Storage. *J. Am. Chem. Soc.* **2005**, 127, 14582-14583.

[26] Sun, Q.; Jena, P.; Wang, Q.; Marquez, M.; First-Principles Study of Hydrogen Storage on $Li_{12}C_{60}$. *J. Am. Chem. Soc.* **2006**, 128, 9741-9745.

[27] Thomas, K. M.; Adsorption and Desorption of Hydrogen on Metal-Organic Framework Materials for Storage Applications: Comparison with other Nanoporous Materials. *Dalton Trans*, **2009**, 1487-1505.

[28] Menon, V.C.; Komarneni, S.; Porous Adsorbents for Vehicular Natural Gas Storage: A Review. *Journal of Porous Materials*, **1998**, 5, 43-58.

[29] Makal, T.A.; Li, J.-R.; Lu, w.; Zhou, H.C.; Methane storage in advanced porous materials. *Chem. Soc. Rev.* **2012**, 41, 7761-7779.

[30] Firas, N.R.; Mat, H.B.; Zakaria, Z.; On-board adsorptive natural gas storage: hindrances for commercial applications. *Clean Technol. Transport.* **2001**, 179.

[31] EPA (**2010**). Methane and Nitrous Oxide Emissions from Natural Sources. U.S. Environmental Protection Agency, Washington, DC, USA.

[32] Wegrzyn, J.; Gurevich, M.; Adsorbent storage of natural gas. *Appl. Energy.*, **1996**, 55, 71-83.

[33] Burchell, T.; Rogers, M.; Low pressure storage of natural gas for vehicular applications. *SAE Technol. Pap. Ser.* **2000**, 2001-2205.

[34] Ma, S. Q.; Sun, D. F.; Simmons, J. M.; Collier, C. D.; Yuan, D. Q.; Zhou, H. C.; Metal-organic framework from an anthracene derivative containing nanoscopic cages exhibiting high methane uptake. *J. Am. Chem. Soc.* **2008**, 130, 1012-1016.

[35] DOE MOVE program at https://arpa-e-foa.energy.gov/.

[36] He, Y.; Zhou, W.; Yildirim, T.; Chen, B.; A series of metal-organic frameworks with high methane uptake and an empirical equation for predicting methane storage capacity. *Energy Environ. Sci.* **2013**, 6, 2735-2744.

[37] Wu, H.; Zhou, W.; Yildirim, T.; High-Capacity Methane Storage in MetalOrganic Frameworks M2(dhtp): The Important Role of Open Metal Sites. *J. Am. Chem. Soc.*, **2009**,131, 4995-5000.

[38] Guo, Z.; Wu, H.; Srinivas, G.; Zhou, Y.; Xiang, S.; Chen, Z.; Yang, Y.; Zhou, W.; O'Keeffe M.; Chen, B. A.; MetalOrganic Framework with Optimized Open Metal Sites and Pore Spaces for High Methane Storage at Room Temperature. *Angew. Chem. Int. Ed.* **2011**, 50, 3178-3181.

[39] Amini, H.R.; Reinhart, D.R.; Regional prediction of long-term landfill gas to energy potential. *Waste Manage.* **2011**, 31, 2020-2026.

[40] Mandal, T.K.; Gregory, D.H.; Hydrogen: a future energy vector for sustainable development. *J. Eng. Mech. Eng. Sci.* **2010**, 224, 539-558.

[41] Boden, T.A.; Marland, G.; Andres, R.J.; Global, Regional, and National Fossil-Fuel CO_2 Emissions., Carbon Dioxide Information Analysis Center, Oak Ridge National Laboratory, U.S. Department of Energy, Oak Ridge, Tenn., (USA).

[42] Liu, Y.; Wang, Z. U.; Zhou, H.C.; Recent advances in carbon dioxide capture with metal-organic frameworks. *Greenhouse Gas Sci Technol.* **2012**, 2, 239-259.

[43] Songolzadeh, M.; Ravanchi, M. T.; Soleimani, M.; Carbon Dioxide Capture and Storage: A General Review on Adsorbents. *World Academy of Science, Engineering and Technology.* **2012**, 6, 10-24.

[44] Lu, C.; Bai, H.; Wu, B.; Su, F.; Hwang, J. F.; Comparative study of CO_2 capture by carbon nanotubes, activated carbons, and zeolites. *Energy & Fuels.* **2008**, 22, 3050-3056.

[45] Sing, K.S.W.; Everett, D.H.; Haul, R.A.W.; Moscou, L.; Pierotti, R.A.; Rouquerol, J.; Siemieniewska, T.; Reporting physisorption data for gas/solid systems with special reference to the determination of surface area and porosity. *Pure Appl. Chem.* **1985**, 57, 603-619.

[46] Lowell, S.; Shields, J.; Thomas, M.A.; Thommes, M.; Characterization of porous solids and powders: surface area, pore size and density. *Springer.* **2004**.

[47] Thommes, M.; Physical Adsorption Characterization of Nanoporous Materials. Chemie Ingenieur Technik, **2010**, 82, No. 7.

[48] Thommes, M.; Cychosz, K. A.; Physical Adsorption characterization of nanoporous materials: progress and challenges. *Adsorption*, **2014**, 20, 233-250.

[49] McBain, J. W.; J. Am. Chem. Soc., **1935**, 57(4), 699-700.

[50] Everett, D. H.; The Solid-Gas Interface., **1967**, Dekker: New York.

[51] Rasmussen, C. J.; Vishnyakov, A.; Thommes, M.; Smarsly, B. M.; Kleitz, F.; Neimark, A. V.; Cavitation in metastable liquid nitrogen confined to nanoscale pores. *Langmuir*, **2010**, 26(12), 10147-10157.

[52] Thommes, M.; In Nanoporous Materials, Science & Engineering (Lu, G. Q., Zhao, X. S., Eds.), *Imperial College Press*, **2004**, p 317.

[53] Ravikovitch, P. I.; Neimark, A. V.; Experimental Confirmation of Different Mechanisms of Evaporation from Ink-Bottle Type Pores: Equilibrium, Pore Blocking, and Cavitation. *Langmuir*, **2002**, 18, 9830-9837.

[54] Thommes, M.; Smarsly, B.; Groenewolt, M.; Ravikovitch, P. I.; Neimark, A. V.; Adsorption Hysteresis of Nitrogen and Argon in Pore Networks and Characterization of Novel Micro and Mesoporous Silicas. *Langmuir*, **2006**, 22, 756-764.

[55] Atlanta Gas Light Adsorbent Research Group (AGLARG), Report to U.S. Department of Energy (**1997**).

[56] Simon, C. M.; Kim, J.; Gomez-Gualdron, D. A.; Camp, J. S.; Chung, Y. C.; Martin, R. L.; Mercado, R.; Deem, M. W.; Gunter, D.; Haranczyk, M.; Sholl, D. S.; Snurr, R. S.; Smit, B.; The materials genome in action: identifying the performance limits for methane storage, *Energy Environ. Sci.*, **2015**, 8, 1190-1199.

[57] Lu, G. Q.; Zhao, X. S.; Nanoporous Materials: Science and Engineering. *Imperial College Press*, **2004**.

[58] Celzard, A.; Fierro, V.; Preparing a Suitable Material Designed for Methane Storage: A Comprehensive Report. *Energy & Fuels*, **2005**, 19, 573-583.

[59] Holst, J. R.; Cooper, A. I.; Ultrahigh surface area in porous solids. *Advanced materials*, **2010**, 22, 5212-5216.

[60] Figueiredo, J. L.; Pereira, M. F. R; Freitas, M. M. A.; Orfao J. J. M.; Modification of the surface chemistry of activated carbons. *CARBON*, **1999**, 37, 9, 1379-1389.

[61] Wigmans, T.; Figueiredo, J.L.; Moulijn, J.A.; Carbon and Coal Gasification. *Martinus Nijhoff Publishers*, **1986**, 559-599.

[62] Iovino, P.; Canzano, S.; Capasso, S.; Erto, A.; Musmarra D.; A modeling analysis for the assessment of ibuprofen adsorption mechanism onto activated carbons, *CHEMICAL ENGINEERING JOURNAL*, **2015**, 277, 360-367.

[63] Lozano-Castello, D.; Alcaniz-Monge, J.; Casa-Lillo, M. A.; Cazorla-Amoros, D.; Linares-Solano, A.; Advances in the study of methane storage in porous carbonaceous materials, *Fuel*, **2002**, 81, 1777-1803.

[64] Miyawaki, J.; Kanda, T.; Suzuki, T.; Okui, T.; Maeda, Y.; Kaneko, K.; Macroscopic Evidence of Enhanced Formation of Methane Nanohydrates in Hydrophobic Nanospaces. *J. Phys. Chem. B.*, **1998**, 102 , 2187-2192.

[65] Davis, M. E.; Ordered porous materials for emerging applications. *Nature*, **2002**, 417, 813-821.

[66] Chahine, R.; Bose, T.K.; Low-pressure adsorption storage of hydrogen. *Int. J. Hydrogen Energy*, **1994**, 19, 161-164.

[67] Velu, S.; Ma, X.; Song, C.; Selective adsorption for removing sulfur from jet fuel over zeolite-based adsorbents. *Industrial and Engineering Chemical Research*, **2003**, 42, 5293-5304.

[68] Qiu, W.; Zheng, Y.; Arsenate removal from water by an alumina-modified zeolite recovered from fly ash. *Journal of Hazardous Materials*, **2007**, 148, 721-726.

[69] Corma, A.; Diaz-Cabanas, M. J.; Martinez-Triguero, J.; Rey, F.; Rius, J.; A large-cavity zeolite with wide pore windows and potential as an oil refining catalyst. *Nature*, **2002**, 418, 514-517.

[70] Van Der Waal, J. C.; Van Bekkum, H.; Molecular Sieves, Multifunctional Microporous Materials in Organic Synthesis. *Journal of Porous Materials*, **1998**, 5, 289-303.

[71] Cejka, G.; Corma, A.; Zones, S.; Zeolites and Catalysis Synthesis, Reactions and Applications. *WILEY-VCH Verlag GmbH & Co. KGaA: Weinheim*, **2010**.

[72] Zheng, Y.; Li, X.; Dutta, P.K.; Exploitation of Unique Properties of Zeolites in the Development of Gas Sensors. *Sensors*, **2012**, 12, 5170-5194.

[73] Hyun, S. H.; Song, J. K.; Kwak, B. I.; Kim, J. H.; Hong, S. A.; Synthesis of ZSM-5 zeolite composite membranes for CO_2 separation. *Journal of Materials Science*, **1999**, 34, 3095.

[74] Felderhoff, M.; Weidenthaler, C.; von Helmolt, R.; Eberle, U.; Hydrogen storage: the remaining scientific and technological challenges. *Phys. Chem. Phys.*, **2007**, 9, 2643-2653.

[75] Zhdanov, S. P.; Some Problems of Zeolite Crystallization, *AMERICAN CHEMICAL SOCIETY*, **1974**, 101, 2, 20-43.

[76] Lozano-Castello, D.; Cazorla-Amoros, D.; Linares-Solano,A.; Quinn, D.F.; Influence of pore size distribution on methane storage at relatively low pressure: preparation of activated carbon with optimum pore size. *Carbon*, **2002**, 40, 989-1002.

[77] Zhou, W.; Methane storage in porous metalorganic frameworks: current records and future perspectives. *The Chemical record* (New York, N.Y.), **2010**, 10(3) 200-204.

[78] Petit C.; Bandosz T. J.; The Department of Chemistry, The City College of New York and the Graduate School of the City University of New York, 160 Convent Avenue, New York, USA. *Dalton Trans.*, **2012**, 41, 4027-4035

[79] Ma, S.; Zhou, H.C.; Zhou, H.C.; Gas storage in porous metal-organic frameworks for clean energy applications. *Chemical communications* (Cambridge, England), **2010**, 46(1), 44-53.

[80] Yurum, Y.; Taralp, A.; Veziroglu, T. N.; Storage of hydrogen in nanostructured carbon materials. *Int J. Hydrogen Energy*, **2009**, 34, 3784-3798.

[81] Strobel, R.; Garche, J.; Moseley, P. T.; Jrissen, L.; Wolf, G.; Hydrogen storage by carbon materials. *Journal of Power Sources*, **2006**, 159, 781-801.

[82] Himeno, S.; Komatsu, T.; Fujita, S.; High-Pressure Adsorption Equilibria of Methane and Carbon Dioxide on Several Activated Carbons. *Journal of Chemical Engineering Data*, **2005**, 50, 369.

[83] Sevilla, M.; Fuertes, A. B.; Sustainable porous carbons with a superior performance for CO_2 capture. *Energy & Environmental Science*, **2011**, 4, 1765-1771.

[84] Wegrzyn, J.; Wisemann, H.; Lee, T.; Low pressure storage of natural gas on activated carbon. *SAE Proc. of Annual Automotive Technology Development*, **1992**, 1-11.

[85] Frey, G.; Hybrid porous solids: past, present, future. *Chem. Soc. Rev.*, **2008**, 37, 191-214.

[86] Rosseinsky, M. J.; Recent developments in metal-organic framework chemistry: design, discovery, permanent porosity and flexibility. *Microporous Mesoporous Mater.*, **2004**, 73, 15-30.

[87] Rowsell, J. L. C.; Yaghi, O. M.; Metal-organic frameworks: a new class of porous materials. *Microporous Mesoporous Mater.*, **2004**, 73, 3-14.

[88] Murray, L. J.; Dinc, M.; Long, J. R.; Hydrogen storage in metal-organic frameworks. *Chem Soc Rev.*, **2009**, 38, 1294-1314.

[89] Janiak, C.; Vieth, J. K.; MOFs, MILs and more: concepts, properties and applications for porous coordination networks (PCNs). *New J. Chem.*, **2010**, 34, 2366-2388.

[90] Furukawa, H.; Ko, N.; Go, Y. B.; Aratani, N.; Choi, S. B.; Choi, E.; Yazaydin, A. O.; Snurr, R. Q.; OKeeffe, M.; Kim, J.; Yaghi, O. M.; Ultrahigh porosity in metal-organic frameworks. *Science*, **2010**, 329, 424-428.

[91] Millward, A. R.; Yaghi, O. M.; Metal-organic frameworks with exceptionally high capacity for storage of carbon dioxide at room temperature. *J. Am. Chem. Soc.*, **2005**, 127, 17998-17999.

[92] Chui, S. S. Y.; Lo, S. M. F.; Charmant, J. P. H.; Orpen, A. G.; Williams, I. D. A.; Chemically Functionalizable Nanoporous Material, *Science*, **1999**, 283, 1148-1150.

[93] Dietzel, P. D. C.; Panella, B.; Hirscher, M.; Blom, R.; Fjellvag, H.; Hydrogen adsorption in a nickel based coordination polymer with open metal sites in the cylindrical cavities of the desolvated framework. *Chem. Commun.*, **2006**, 959-961.

[94] Feng X.; Ding X.; Jiang D.; Covalent organic frameworks. *Chem. Soc. Rev.*, **2012**, 41, 6010-6022.

[95] Farha, O.K.; Yazaydin, A.O.; Eryazici, I.; Malliakas, C.D.; Hauser, B.G.; Kanatzidis, M.G.; Nguyen, S.T.; Snurr, R.Q.; Hupp, J.T.; De Novo synthesis of a metal-organic framework material featuring ultrahigh surface area and gas storage capacities. *Nature Chem.*, **2010**, 2, 944-948.

[96] Germain, J.; Frchet, J. M. J.; Svec, F.; Nanoporous polymers for hydrogen storage. *Small*, **2009**, 5, 1098-1111.

[97] Jiang, J. X.; Su, F.; Trewin, A.; Wood, C. D.; Niu, H.; Jones, J. T.; Khimyak, Y. Z.; Synthetic control of the pore dimension and surface area in conjugated microporous polymer and copolymer networks. *Journal of the American Chemical Society*, **2008**, 130, 7710-7020.

[98] Makowski, P.; Thomas, A.; Kuhn, P.; Goettmann, F.; Organic materials for hydrogen storage applications: from physisorption on organic solids to chemisorption in organic molecules. *Energy Environ. Sci.*, **2009**, 2, 480-490.

[99] Ilinitch, O. M.; Fenelonov, V. B.; Lapkin, A. A.; Okkel, L. G.; Terskikh, V. V.; Zamaraev, K. I.; Intrinsic microporosity and gas transport in polyphenylene oxide polymers. *Microporous and Mesoporous Materials*, **1999**, 31, 97-110.

[100] Budd, P.M.; Butler, A.; Selbie, J.; Mahmood, K.; McKeown, N.B.; Ghanem, B.; Msayib, K.; Book, D.; Walton, A.; The potential of organic polymer-based hydrogen storage materials. *Phys. Chem. Phys.*, **2007**, 9, 1802-1808.

[101] McKeown, N. B.; Budd, P. M.; Book, D.; Microporous polymers as potential hydrogen storage materials. *Macromol. Rapid Commun.*, **2007**, 28, 995-1002.

[102] Cote, A. P.; El-Kaderi, H. M.; Furukawa, H.; Hunt, J. R.; Yaghi, O. M.; Reticular synthesis of microporous and mesoporous 2D covalent organic frameworks. *Journal of the American Chemical Society*, **2007**, 129, 12914-12915.

[103] El-Kaderi, H. M.; Hunt, J. R.; Mendoza-Corts, J. L.; Ct, A. P.; Taylor, R. E.; OKeeffe, M.; Designed synthesis of 3D covalent organic frameworks. *Science*, **2007**, 316, 268-272.

[104] Wang, L.; Zhao, J.; Yan, T.; Adsorption of selected gases on metal-organic frameworks and covalent organic frameworks: A comparative grand canonical Monte Carlo simulation. *Journal of Applied Physics*, **2012**, 111, 1126-1128.

[105] Tilford, R. W.; Mugavero, S. J.; Pellechia, P. J.; Lavigne, J. J.; Tailoring microporosity in covalent organic frameworks. *Adv. Mater.*, **2008**, 20, 2741-2746.

[106] Koo, B. T.; Dichtel, W. R.; Clancy, P. A.; Classification scheme for the stacking of two-dimensional boronate ester-linked covalent organic frameworks. *Journal of Materials Chemistry*, **2012**, 22, 17460-17469.

[107] Doonan, C. J.; Tranchemontagne, D. J.; Glover, T. G.; Hunt, J. R.; Yaghi, O. M.; Exceptional ammonia uptake by a covalent organic framework. *Nature Chem.*, **2010**, 2, 235-238.

[108] Assfour, B.; Seifert, G.; Adsorption of hydrogen in covalent organic frameworks: comparison of simulations and experiments. Microporous Mesoporous Mater., **2010**, 133, 59-65.

[109] Li, Y.; Yang, R. T.; Hydrogen Storage in Metal-Organic and Covalent-Organic Frameworks by Spillover. *Langmuir*, **2008**, 54, 269-279.

[110] Chinchilla, R.; Najera, C.; The Sonogashira reaction: a booming methodology in synthetic organic chemistry. *Chem. Rev.*, **2007**, 107, 874-922.

[111] Weder, C.; Hole Control in Microporous Polymers. *Angew Chem.*, **2008**, 47, 448-450.

[112] Jiang, J.X.; Su, F.; Trewin, A.; Wood, C. D.; Campbell, N. L.; Niu, H.; Dickinson, C.; Ganin, A. Y.; Rosseinsky, M. J.; Khimyak, Y. Z.; Cooper, A. I.; Conjugated Microporous Poly(aryleneethynylene) Networks. *Angew Chem.*, **2007**, 46, 8574-8578.

[113] Hasell, T.; Wood, C. D.; Clowes, R.; Jones, J. T. A.; Khimyak, Y. Z.; Adams, D. J.; Cooper, A. I.; Palladium nanoparticle incorporation in conjugated microporous polymers by supercritical fluid processing. *Chem. Mater.*, **2009**, 22, 557-564.

[114] Ren, S.; Dawson, R.; Laybourn, A.; Jiang, J.-x.; Khimyak, Y.; Adams, D. J.; Cooper, A. I.; Functional conjugated microporous polymers. *Polymer Chemistry*, **2012**, 3, 928-934.

[115] Grimsdale, A. C.; Leok Chan, K.; Martin, R. E.; Jokisz, P. G.; Holmes, A. B.; Synthesis of light-emitting conjugated polymers for applications in electroluminescent devices. *Chemical reviews*, **2009**, 109, 897-1091.

[116] Weder, C.; Synthesis, processing and properties of conjugated polymer networks. *Chem. Commun.* **2005**, 43, 5378-5389.

[117] Tsyurupa, M. P.; Davankov, V. A.; Porous Structure of Hypercrosslinked Polystyrene: State of the Art Mini-Review. *React. Funct. Polym.*, **2006**, 66, 768-779.

[118] Mason, C. R.; Maynard-Atem, L.; Al-Harbi, N. M.; Budd, P. M.; Bernardo, P.; Bazzarelli, F.; Clarizia, G.; Jansen, J. C.; Polymer of intrinsic microporosity incorporating thioamide functionality: preparation and gas transport properties. *Macromolecules*, **2011**, 44, 6471-6479.

[119] Dawson, R.; Stevens, L.; Drage, T. C.; Snape, C. E.; Smith, M. W.; Adams, D. J.; Cooper, A. I.; Impact of water co-adsorption for carbon dioxide capture in microporous polymer sorbents. *J. Am. Chem. Soc.*, **2012**, 134, 10741-10744.

[120] Xu, S.; Luo, Y.; Tan, B.; Recent Development of Hypercrosslinked Microporous Organic Polymers. *Macromol., Rapid Commun.*, **2013**, 34, 471-484.

[121] Wood, C. D.; Tan, B.; Trewin, A.; Niu, H.; Bradshaw, D.; Rosseinsky, M. J.; Khimyak, Y. Z.; Campbell, N. L.; Kirk, R.; Stckel, E.; Cooper, A. I.; Hydrogen Storage in Microporous Hypercrosslinked Organic Polymer Networks. *Chem. Mater.*, **2007**, 19, 2034-2048.

[122] Schwab, M. G.; Lennert, A.; Pahnke, J.; Jonschker, G.; Koch, M.; Senkovska, I.; Rehahn, M.; Kaskel, S.; Nanoporous copolymer networks through multiple FriedelCraftsalkylationstudies on hydrogen and methane storage. *J. Mater. Chem.*, **2011**, 21, 2131-2135.

[123] Li , B.; Gong, R.; Wang, W.; Huang, X.; Zhang, W.; Li, H.; Hu, C.; Tan, B.; A New Strategy to Microporous Polymers: Knitting Rigid Aromatic Building Blocks by External Cross-Linker. *Macromolecules*, **2011**, 44, 2410-2414.

[124] Dawson, R.; Stckel, E.; Holst, J.R.; Adams, D. J.; Cooper, A. I.; Microporous Organic Polymers for Carbon Dioxide Capture. *Energy Environ. Sci.*, **2011**, 4, 4239-4245.

[125] Luo, Y.; Li, B.; Wang, W.; Wu, K.; Tan, B.; Hypercrosslinked Aromatic Heterocyclic Microporous Polymers: A New Class of Highly Selective CO_2 Capturing Materials. *Adv. Mater.* **2012**, 24, 5703-5707.

[126] Eddaoudi, M.; Kim, J.; Rosi, N.; Vodak, D.; Wachter, J.; OKeeffe, M.; Yaghi, O. M.; Systematic design of pore size and functionality in isoreticular MOFs and their application in methane storage. *Science*, **2002**, 295, 469-472.

[127] Martn, C. F.; Stckel, E.; Clowes, R.; Adams, D. J.; Cooper, A. I.; Pis, J. J.; Rubiera, F.; Pevida, C.; Hypercrosslinked Organic Polymer Networks as Potential Adsorbents for Pre-Combustion CO_2 Capture. *J. Mater. Chem.*, **2011**, 21, 5475-5483.

[128] Liewellyn, P. L.; Bourrelly, S.; Serre, C.; Vimont, A.; Daturi, M.; Hamon, L.; De Weireld, G.; Chang, J.S.; Hong, D.Y.; Kyu Hwang, Y.; Hwa Jhung, S.; Hwa Jhung, G. F.; High Uptakes of CO2 and CH4 in Mesoporous Metal Organic Frameworks MIL-100 and MIL-101., *Langmuir*, **2008**, 24, 7245-7250.

[129] Pan, B. C.; Xiong, Y.; Li, A. M.; Chen, J. L.; Zhang, Q. X.; Jin, X. Y.; Adsorption of aromatic acids on an aminated hypercrosslinked macroporous polymer. *Reactive & Functional Polymers*, **2002**, 53, 63-72.

[130] Chang, C. F.; Chang, C. Y.; Hsu, K. E.; Lee, S. C.; Holl, W.; Adsorptive removal of the pesticide methomyl using hypercrosslinked polymers. *Journal of Hazardous Materials*, **2008**, 155, 295-304.

[131] Ben, T.; Ren, H.; Ma, S.; Cao, D.; Lan, J.; Jing, X.; Wang, W.; Xu, J.; Deng, F.; Simmons, J. M.; Qiu, S.; Zhu, G.; Targeted Synthesis of a Porous Aromatic Framework With High Stability and Exceptionally High Surface Area. *Angew. Chem., Int. Ed.*, **2009**, 48, 9457-9460.

[132] S. Qiu, G. Zhu, T. Ben (2009) Porous Polymer and synthetic method thereof. Patent: US **2010**/0331436 A1

[133] Lu, W. G.; Yuan, D. Q.; Zhao , D.; Schilling, C. I.; Plietzsch, O.; Muller, T.; Brase, S.; Guenther, J.; Lumel, J.; Krishna, R.; Porous Polymer Networks: Synthesis, Porosity, and Applications in Gas Storage/Separation. *Chem. Mat.*, **2010**, 22, 5964-5972

[134] Trewin, A.; Cooper, A. I.; Porous organic polymers: distinction from disorder?. *Angew. Chem.*, **2010**, 49, 1533-1535.

[135] Yuan, D.; Lu, W.; Zhao, D.; Zhou, H. C.; Highly Stable Porous Polymer Networks With Exceptionally High Gas-Uptake Capacities. *Adv. Mater.*, **2011**, 23, 3723-3725.

[136] Holst, J. R.; Stockel, E.; Adams, D. J.; Cooper, A. I.; High Surface Area Networks from Tetrahedral Monomers: Metal-Catalyzed Coupling, Thermal Polymerization, and Click Chemistry. *Macromolecules*, **2010**, 43, 8531-8538.

[137] Li, Y.; Ben, T.; Zhang, B.; Fu, Y.; Qiu, S.; Ultrahigh Gas Storage both at Low and High Pressures in KOHActivated Carbonized Porous Aromatic Frameworks. *Scientific Reports*, **2013**, 3, 2420.

[138] Lu, W.; Yuan, D.; Sculley, J.; Zhao, D.; Krishna, R.; Zhou, H.; Sulfonate-grafted porous polymer networks for preferential CO_2 adsorption at low pressure. *J. Am. Chem. Soc.*, **2011**, 133, 18126-18129.

[139] Gregg, S. J.; Sing, K. S. W.; Adsorption, Surface Area and Porosity; Academic Press: New York, **1982**.

[140] Ravikovitch, P. I.; Haller, G. L.; Neimark, A. V.; In Mesoporous Molecular Sieves; Amsterdam, **1998**, 117, 77.

[141] Errahali, M., Gatti, G.; Tei, L.; Paul, G.; Rolla, G. A.; Canti, L.; Fraccarollo, A.; Cossi, M.; Comotti, A.; Sozzani, P.; Marchese, L.; Microporous Hyper-Cross-Linked Aromatic Polymers Designed for Methane and Carbon Dioxide Adsorption. *J. Phys. Chem. C*, **2014**, 118, 28699-28710.

[142] Cossi, M.; Gatti, G.; Canti, L.; Tei, L.; Errahali, M.; Marchese, L. Theoretical Prediction of High Pressure Methane Adsorption in Porous Aromatic Frameworks (PAFs). *Langmuir*, **2012**, 28, 14405-14414.

[143] Fraccarollo, A.; Canti, L.; Marchese, L.; Cossi, M.; Monte Carlo Modeling of Carbon Dioxide Adsorption in Porous Aromatic Frameworks. *Langmuir*, **2014**, 30, 4147-4156.

[144] Boys, S. F.; Bernardi, F.; The calculation of small molecular interactions by the differences of separate total energies. Some procedures with reduced errors. *Mol. Phys.* **1970**, 19, 553.

[145] Cashwell E.D.; Everett C.J.; Monte Carlo method, New York, **1959**.

[146] Kroese D.P.; Rubinstein R.Y.; Simulation and the Monte Carlo method, *WILEY*, **2011**.

[147] Metropolis, N.; Rosenbluth, A.; Rosenbluth, M.; Teller, A.; Teller, E.; Equations of state calculations by fast computing machines. *Journal of Chemical Physics*, **1953**, 21, 1087-1091.

[148] Hastings, W.K.; Monte Carlo sampling methods using Markov chains and their applications. *Biometrika*, **1970**, 57(1), 97-109.

[149] Leckband, D.; Israelachvili, J.N.; Intermolecular forces in biology. *Quart. Rev. Biophys.*, **2001**, 34, 105-267.

[150] Lomize A.L.; Reibarkh M.Y.; Pogozheva I.D.; Interatomic potentials and solvation parameters from protein engineering data for buried residues. *Protein Sci.*, **2002**, 11, 1984-2000.

[151] Stone A.; The Theory of Intermolecular Forces, *Science*, **2013**.

[152] Tee L.S.; Gotoh S.; Stewart L. E.; Molecular Parameters for Normal Fluids. Lennard-Jones 12-6 Potential, *Ind. Eng. Chem. Fundamen.*, **1966**, 5 (3), 356-363.

[153] Kong C.L.; Combining rules for intermolecular potential parameters. II. Rules for the LennardJones (12-6) potential and the Morse potential. *J. Chem. Phys.*, **1973**, 59, 2464.

[154] http://accelrys.com/products/datasheets

[155] Sun, H.; COMPASS: An ab Initio Force-Field Optimized for Condensed-Phase Applications Overview with Details on Alkane and Benzene Compounds. *The Journal of Physical Chemistry B*, **1998**, 102(38):, 7338-7364.

[156] Dauber-Osguthorpe, P.; Roberts, V. A.; Osguthorpe, D.; Wolff, J.; Genest, M.; Hagler, A. T. Structure and energetics of ligand binding to proteins: Escherichia coli dihydrofolate reductasetrimethoprim, a drugreceptor system. *Proteins*, **1988**, 4, 31.

[157] Sun H.; Stephen J.; Mumby J.R.; Maple A.; Hagler T.; An ab Initio CFF93 All-Atom Force Field for Polycarbonates, *Journal of the American Chemical Society*, **1994**, 116, 2978-2987.

[158] Mayo, S. L.; Olafson, B. D.; Goddard, W. A.; Dreiding - A Generic Force-Field for Molecular Simulations. *J. Phys. Chem.*, **1990**, 94, 8897-8909.

[159] Duren, T.; Bae, Y. S.; Snurr, R. Q.; Using Molecular Simulation to Characterise Metal-Organic Frameworks for Adsorption Applications. *Chem. Soc. Rev.*, **2009**, 38, 1237-1247.

[160] Lemmon, E. W.; McLinden, M. O.; Friend, D. G.; NIST Chemistry WebBook Nist standard reference database number 69; National Institute of Standards and Technology: Washington, DC, **2011**.

[161] Theodorou, D.N.; Suter, U.W.; Atomistic modeling of mechanical properties of polymeric glasses. *Macromolecules*, **1986**, 19, 139.

[162] Allen, M.P.; Tildesley, D.J.; Computer Simulation of Liquids, *Oxford University Press*, **1987**.

[163] Khane, R.; de Pablo, J.; and Yethiraj, A.; Molecular simulation and continuum mechanics investigation of viscoelastic properties of fluids confined to molecularly thin films. *J. Chem. Phys.*, **2001**, 114(17), 7593-7601.

[164] Mehlig, B.; Heerman, D.W.; Forrest, B. M.; Hybrid Monte Carlo method for condensed-matter systems. *Phys. Rev.*, **1992**, B 45, 679.

[165] Hildebrand, J.H.; Wood, S.E.; The derivation of equations for regular solutions. *J. Chem. Phys.*, **1933**, 1, 817.

[166] Rigby, D.; Roe, R.J.; Molecular dynamics simulation of polymer liquid and glass. II. Short range order and orientation correlation. *J. Chem. Phys.*, **1988**, 89, 5280.

[167] Brown, D.; Clarke, J.H.R.; Molecular dynamics simulation of an amorphous polymer under tension. *Macromolecules*, **1991**, 24, 2075.

[168] Almenningen, A.; Bastiansen, O.; Fernholt, L.; Cyvin, B. N.; Cyvin, S. J.;Samdal, S. J.; *J. Mol. Struct. (theochem)*, **1985**, 128, 59.

[169] Wu, C.; Xu, W.; Atomistic molecular modelling of crosslinked epoxy resin. *Polymer*, **2006**, 47, 6004-6009.

[170] Liu, J.W.; Mackay, M.E.; Duxbury, P.M.; Molecular Dynamics Simulation of Intramolecular Cross-Linking of BCB/Styrene Copolymers. *Macromolecules*, **2009**, 42, 8534-8542.

[171] Abbott, L.J.; Colina, C.M.; Atomistic structure generation and gas adsorption simulations of microporous polymer networks. *Macromolecules*, **2011**, 44, 4511-4519.

[172] Varshney, V.; Patnaik, S.S.; Roy, A.K.; Farmer, B.L.; A molecular dynamics study of epoxy-based networks: cross-linking procedure and prediction of molecular and material properties. *Macromolecules*, **2008**, 41, 6837-6842.

[173] Khare, K.S.; Khare, R.; Directed Diffusion Approach for Preparing Atomistic Models of Crosslinked Epoxy for Use in Molecular Simulations. *Macromol Theory Simul.*, **2012**, 21, 322-327.

[174] Brunauer, S.; Emmett, P.; Teller, E.; Adsorption of gases in multimolecular layers. *J. Am. Chem. Soc.*, **1938**, 60, 309-319.

[175] Boys, S. F.; Bernardi, F.; Calculation of Small Molecular Interactions by Differences of Separate Total Energies - Some Procedures with Reduced Errors. *Mol. Phys.*, **1970**, 19, 553-566.

[176] Frisch, M. J.; Trucks, G. W.; Schlegel, H. B.; Scuseria, G. E.; Robb, M. A.; Cheeseman, J. R.; Scalmani, G.; Barone, V.; Mennucci, B.; Petersson, G. A.; Nakatsuji, H.; Caricato, M.; Li, X.; Hratchian, H. P.; Izmaylov, A. F.; Bloino, J.; Zheng, G.; Sonnenberg, J. L.; Hada, M.; Ehara, M.; Toyota, K.; Fukuda, R.; Hasegawa, J.; Ishida, M.; Nakajima, T.; Honda, Y.; Kitao, O.; Nakai, H.; Vreven, T.; Montgomery, J. A., Jr.; Peralta, J. E.; Ogliaro, F.; Bearpark, M.; Heyd, J. J.; Brothers, E.; Kudin, K. N.; Staroverov, V. N.; Kobayashi, R.; Normand, J.; Raghavachari, K.; Rendell, A.; Burant, J. C.; Iyengar, S. S.; Tomasi, J.; Cossi, M.; Rega, N.; Millam, N. J.; Klene, M.; Knox, J. E.; Cross, J. B.; Bakken, V.; Adamo, C.; Jaramillo, J.; Gomperts, R.; Stratmann, R. E.; Yazyev, O.; Austin, A. J.; Cammi, R.; Pomelli, C.; Ochterski, J. W.; Martin, R. L.; Morokuma, K.; Zakrzewski, V. G.; Voth, G. A.; Salvador, P.; Dannenberg, J. J.; Dapprich, S.; Daniels, A. D.; Farkas, O.; Foresman, J. B.; Ortiz, J. V.; Cioslowski, J.; Fox, D. J.; Gaussian 09, revision D; Gaussian, Inc.: Pittsburgh, PA, **2009**.

[177] Setzmann, U.; Wagner, W. J.; A new equation of State and Tables of Thermodynamic Properties of Methane Covering the Range from the Melting Line to 625 K at Pressures up to 1000 MPa. *Phys. Chem. Ref.*, **1991**, 20, 1061.

[178] Span, U.; Wagner, W.; A New Equation of State for Carbon Dioxide. *J. Phys. Chem.*, **1996**, 25, 1509-1596.

[179] Han, S. S.; Choi, S.-H.; Goddard, W. A.; III. Zeolitic Imidazolate Frameworks as H-2 Adsorbents: Ab Initio Based Grand Canonical Monte Carlo Simulation. *J. Phys. Chem. C.*, **2010**, 114, 12039-12047.

[180] Babarao, R.; Dai, S.; Jiang, J.; Functionalizing Porous Aromatic Frameworks with Polar Organic Groups for High-Capacity and Selective CO_2 Separation: A Molecular Simulation Study., *Langmuir*, **2011**, 27, 3451-3460.

[181] Wang, S.; Comparative molecular simulation study of methane adsorption in metal-organic frameworks. *Energy Fuels*, **2007**, 21, 953.

[182] Rappe, A. K.; Casewit, C. J.; Colwell, K. S.; Goddard, W. A., III; Skiff, W. M.; *J. Am. Chem. Soc.*, **1992**, 114, 100-124.

[183] Martin, M. G.; Siepmann, J. I.; Transferable potentials for phase equilibria. United-atom description of n-alkanes. *J. Phys. Chem. B*, **1998**, 102, 14, 2569-2577

[184] Mendoza-Cortes, J. L.; Han, S. S.; Furukawa, H.; Yaghi, O. M.; Goddard, W. A.; *J. Phys. Chem. A*, **2010**, 114, 108-124.

[185] Lennard-Jones, J. E.; Processes of adsorption and diffusion on solid surfaces. *Trans. Faraday Soc.*, **1932**, 28, 333-359.

[186] Yeon, S.H.; Knoke, I.; Gogotsi, Y.; Fischer, J. E.; Enhanced volumetric hydrogen and methane storage capacity of monolithic carbide-derived carbon. *Microporous Mesoporous Mater.*, **2010**, 131, 423-428.

[187] Alcaiz-Monge, J.; De la Casa-Lillo, M.A.; Cazorla-Amors, D.; Linares-Solano, A.; Methane storage in activated carbon fibres. *Carbon*, **1997**, 35, 91.

[188] Yang, S. J.; Im, J. H.; Nishihara, H.; Jung, H.; Lee, K.; Kyotani, T.; Park, C. R.; General Relationship between Hydrogen Adsorption Capacities at 77 and 298 K and Pore Characteristics of the Porous Adsorbents. *J. Phys. Chem. C*, **2012**, 116, 10529-10540.

[189] Presser, V.; McDonough, J.; Yeon, S.H.; Gogotsi, Y.; Effect of pore size on carbon dioxide sorption by carbide derived carbon. *Energy Environ. Sci.*, **2011**, 4, 3059-3066.

[190] Jorda-Beneyto, M.; Suarez-Garcia, F.; Lozano-Castello, D.; Cazorla- Amoros, D.; Linares-Solano, A.; Hydrogen storage on chemically activated carbons and carbon nanomaterials at high pressures. *Carbon*, **2007**, 45, 293-303.

[191] Jorda-Beneyto, M.; Lozano-Castello, D.; Suarez-Garcia, F.; Cazorla-Amoros D.; Linares-Solano, A.; *Microporous Mesoporous Mater.*, **2008**, 112, 235-242.

[192] Zacharia, R.; Cossement, D.; Lafi, L.; Chahine, R.; Volumetric hydrogen sorption capacity of monoliths prepared by mechanical densification of MOF-177. *J. Mater. Chem.*, **2010**, 20, 2145-2151.

[193] Yuan, D.; Zhao, D.; Sun, D. F.; Zhou, H.C.; An Isoreticular Series of MetalOrganic Frameworks with Dendritic Hexacarboxylate Ligands and Exceptionally High Gas-Uptake Capacity. *Angew. Chem.*, **2010**, 49, 5357-5361.

[194] Zhao, J.; Yan, T.; Effects of substituent groups on methane adsorption in covalent organic frameworks. *RSC Adv.*, **2014**, 4, 15542-15551.

[195] Sun, B.; Kayal, S.; Chakraborty, A.; Study of HKUST (Copper benzene, 3, 5-tricarboxylate, Cu-BTC MOF) metal organic frameworks for CH_4 adsorption: An experimental Investigation with GCMC (grand canonical Monte-carlo) simulation. *Energy*, **2014**, 76, 419-427;

[196] Diring, S.; Furukawa, S.; Takashima, Y.; Tsurouka, T.; Kitagawa, S.; Controlled Multiscale Synthesis of Porous Coordination Polymer in Nano/Micro Regimes. *Chem. Mater.*, **2010**, 22, 4531.

[197] Zhou, W.; Hartman, M. R.; Yildirim, T.; Hydrogen and methane adsorption in metal-organic frameworks: a high-pressure volumetric study, *J. Phys. Chem. C*, **2007**, 111, 16131-16137.

[198] Garibay, S. J.; Weston, M. H.; Mondloch, J. E.; Colon, Y. J.; Farha, O. K.; Hupp, T. H.; Nguyen, S. T.; Accessing Functionalized Porous Aromatic Frameworks (PAFs) through a De Novo Approach., *CrystEngComm*, **2013**, 15, 1515-1519.

[199] Yang, Z.; Peng, X.; Cao, D.; Carbon Dioxide Capture by PAFs and an Efficient Strategy To Fast Screen Porous Materials for Gas Separation. *J. Phys. Chem, C*, **2013**, 117, 8353-8364.

[200] Shao, X.H.; Feng, Z.H.; Xue, R.S.; Ma, C.C., Wang, W.C.; Peng, X.; Cao, D.P.; Adsorption of CO_2, CH_4, CO_2/N_2 and CO_2/CH_4 in novel activated carbon beads: preparation, measurements and simulation, *AIChE J.* **2011**, 57, 3042-3051.

[201] Yang, J.; Wang, J.; Li, L.; Zhang, Z.; Li, J.; *Journal of Colloid and interface science*, **2015**, 456, 197-205.

[202] Zheng, B.; Yun, R.; Bai, J.; Lu, Z.; Du, L.; Li, Y.; Expanded Porous MOF-505 Analogue Exhibiting Large Hydrogen Storage Capacity and Selective Carbon Dioxide Adsorption. *Inorg. Chem.*, **2013**, 52, 2823-2829.

[203] Jorda-Beneyto, M.; Suarez-Garcia, F.; Lozano-Castello, D.; Cazorla- Amoros, D.; Linares-Solano, A.; Hydrogen storage on chemically activated carbons and carbon nanomaterials at high pressures. *Carbon*, **2007**, 45, 293-303.

[204] Konstas, K.; Taylor, J. W.; Thornton, A. W.; Doherty, C. M.; Lim, W. X.; Bastow, T. J.; Kennedy, D. F.; Wood, C. D.; Cox, B. J.; Hill, J. M.; Lithiated Porous Aromatic Frameworks with Exceptional Gas Storage Capacity, *Angew. Chem., Int. Ed.*, **2012**, 51, 6639-6642.

[205] Yamazaki, T.; Watanuki, I.; Ozawa, S; Ogino, Y.; Infrared Spectra of Methane Adsorbed by Ion-Exchanged ZSM-5 Zeolites. *Langmuir*, **1988**, 4, 433-438.

[206] Chen, L.; Lin, L.; Xu, Z.; Zhang, T.; Liang, D.; Interaction of methane with surfaces of silica, aluminas and HZSM-5 zeolite. A comparative FT-IR study. *Catal. Lett.*, **1995**, 35, 245-258.

[207] Kishima, M.; Okubo, T.; Characterization of Microporous Titanosilicate ETS-10 by Infrared Spectroscopy with Methane as a Probe Molecule for Basic Sites. *J. Phys. Chem. B*, **2003**, 107, 8462-8468.

[208] Li, C.; Li, G.; Xin, Q.; FT-IR Spectroscopic Studies of Methane Adsorption on Magnesium Oxide. *J. Phys. Chem.* **1994**, 98, 1933-1938 .

[209] Yoshida, H.; Yamazaki, T.; Ozawa, S.; IR Spectra of CH_4 Physisorbed on an Active Carbon at Low Temperature. *J. Colloid Interface Sci.*, **2000**, 224, 261-264.

[210] Lubezky, A.; Chechelnitsky, L.; Folman, M.; IR spectra of CH_4, CD_4, C_2H_4, C_2H_2, CH_3OH and CH_3OD adsorbed on C_{60} films. *J. Chem. Soc.*, Faraday Trans. **1996**, 92(12), 2269-2274.

[211] Socrates, G.; Infrared and Raman Characteristic Group Frequencies: Tables and Charts, 3rd ed.; John Wiley & Sons Inc: New York, **2004**, 157-161.

[212] Colthup, N. B.; Daly, L. H.; Wiberley, S. E.; Introduction to Infrared and Raman Spectroscopy. Introduction to Infrared and Raman Spectroscopy; *Academic Press: New York*, **1964**, 261-280.

[213] Ravikovitch, P.I.; Vishnyakov, A.; Russo, R.; Neimark, A.V.; Unified approach to pore size characterization of microporous carbonaceous materials from N_2, Ar, and CO_2 adsorption isotherms. *Langmuir*, **2000**, 16, 2311-2320.

[214] Neimark, A.V.; Ravikovitch, P.I.; Lin, Y.; Thommes, M.; Quenched solid density functional theory and pore size analysis of micromesoporous carbons. *Carbon*, **2009**, 47, 1617.

[215] Thommes, M.; Pore Size Analysis by Gas Adsorption. PArt I: Aspects of the application of Density Functional Theory(DFT) and Monte Carlo simulation (MC) for micro/mesopore size analysis, **2010**, www.quantachrome.com. Powder Tech Note 31.

[216] Thommes, M.; Application of QSDFT (Quenched Solid Density Fuctional Theory) - A novel density functional theory for an accurate pore size analysis od disordered porous carbons; **2012**, www.quantachrome.com, Powder Tech Note 40.

[217] Mao, W.; Mao, H.K.; Hydrogen storage in molecular compounds, *CrossMark*, **2010**, 101, 3, 708-710.

[218] Couck, S.; Denayer, J. F. M.; Baron, G. V.; Remy, T.; Gascon, J.; Kapteijn, F.; An Amine-Functionalized MIL-53 Metal-Organic Framework with Large Separation Power for CO_2 and CH_4. *J. Am. Chem. Soc.*, **2009**, 131, 6326-6327.

[219] Torrisi, A.; Bell, R. G.; Mellot-Draznieks, C.; Functionalized MOFs for Enhanced CO_2 Capture. *Cryst. Growth Des.*, **2010**, 10, 2839-2841.

[220] Jing, X.; Zou, D.; Cui, P.; Ren, H.; Zhu, G.; Facile synthesis of cost-effective porous aromatic materials with enhanced carbon dioxide uptake, *J. Mater. Chem. A*, **2013**, 1, 13926-13931.

[221] Luo, Y.; Zhang, S.; Ma, Y.; Wang, W.; Tan, B.; Microporous Organic Polymers Synthesized by Self-Condensation of Aromatic Hydroxymethyl Monomers. *Polym. Chem.*, **2013**, 4, 1126-1131.

[222] Hart, K.; Abbott, L.; McKeown, N.; Colina, C.; Morphology and Molecular Bridging in Comb- and Star-shaped Diblock Copolymers. *Macromolecules*, **2013**, 46, 5371-5380.

[223] Accelrys; Accelrys Software Inc.: San Diego, **2001-2011**.

[224] Patent: A porous organic polymer capable of adsorbing gas and the method of preparing thereof; Applicant: SOL S.p.A., et al.; Inventors: Errahali, M., Gatti, G., Tei, L., Cossi, M., Marchese, L. European application 13425105.7(2013); PCT International extension rif. E0094969 (**2014**).

[225] Peng, Y.; Krungleviciute, V.; Eryazici, I.; Hupp, J. T.; Farha O. K.; Yildirim, T.; Methane Storage in MetalOrganic Frameworks: Current Records, Surprise Findings, and Challenges. *J. Am. Chem. Soc.*, **2013**, 135, 32,11887-11894.

[226] Patent: A porous aromatic hypercrosslinked polymer capable of adsorbing gas and the method of preparing thereof; Applicant: SOL S.p.A.; Inventors: Errahali, M., Gatti, G., Tei, L., Cossi, M., Marchese, L.; **2015**.

[227] Zukal, A.; Thommes, M.; Cejka, J.; Synthesis of highly ordered MCM-41 silica with spherical particles. *Microporous and Mesoporous Mater.*, **2007**, 104, 52-59.

7 Appendix

7.0.1 Papers

- M. Errahali, G. Gatti, L. Tei, G. Paul, G. A. Rolla, L. Canti, A. Fraccarollo, M. Cossi, A. Comotti, P. Sozzani and M. Marchese; Microporous HyperCrossLinked Aromatic Polymers Designed for Methane and Carbon Dioxide Adsorption, 2014, J.Phys.Chem.C, 118(49), 28699-28710.
- M. Errahali, G. Gatti, L. Tei, L. Canti, A. Fraccarollo, M. Cossi and M. Marchese; Understanding Methane Adsorption in Porous Aromatic Frameworks: an FTIR, Raman and Theoretical Combined Study, J.Phys.Chem.C, 2014, 118(19), 10053-10060.
- A. Fraccarollo, L. Canti, M. Cossi and L.Marchese, Monte Carlo Modeling of Carbon Dioxide Adsorption in Porous Aromatic Frameworks, Langmuir, 2014, 30 (14), 4147-4156.
- M. Cossi, G. Gatti, L. Canti, L. Tei, M.Errahali and L. Marchese, Theoretical prediction of high pressure methane adsorption in porous aromatic frameworks (PAFs), Langmuir, 2012, 28, 14405-14414.

7.0.2 Participation in seminars and conferences

- October 2015 Rimini, "Sigma-Aldrich Young Chemists Symposium". Poster Contribution.
- July 2015 Torino, "International Congress of Theoretical Chemists from Latin expression"(CHITEL) 2015. Poster Contribution.
- December 2014 Pisa, "Winter Modeling". Poster Contribution.
- September 2014 Rende(CS), the "XXV National Italian Chemical Company(SCI) Congress". Oral Contribution.
- June 2014 Amantea(CS), 6th Czech-Italian-Spanish Conference on "Molecular Sieves and Catalysis". Poster Contribution.
- March 2014 Napoli, "Crystal school".
- November 2013 Torino, "Nanostructured Interfaces and Surfaces (NIS) Colloquium in CO_2 capture and reactivity with new materials". Oral Contribution.
- June 2013 Alessandria, the "XL National Italian Chemical Company(SCI) Congress". Poster Contribution.
- March 2013 Torino, "National Theoretical and Computational Chemistry Congress". Poster Contribution.
- February 2013 Torino, "Nanostructured Interfaces and Surfaces (NIS) Colloquium. Materials for Hydrogen Storage".

Acknowledgements

At first I would like to thank my supervisor Prof. Maurizio Cossi, who patiently provided the vision, encouragement and advice necessary for me to proceed through this work.
I would like to thank Dr. Alberto Fraccarollo who have helped me with everything, from computational problems and even tooks the time to revise my thesis, which was very much appreciated.
I would like to thank Prof. Leonardo Marchese, Dr. Giorgio Gatti and Dr.ssa Mina Errahali for their helpful discussions and experimental data.
Many thanks go to my friends, colleagues and staff in the University of Eastern Piedmont and in particular to Satiro, Mario, Daniele, Jack, Cuchu, John, Luca, Mazzu, la Cantatrice, Valentina, Chiara, Gabriele, Vittoria and Ivana for their friendship and always being willing to help.
Lastly, a special thanks to company SOL group S.p.A for funding this research.